Dissertation

submitted to the

Combined Faculties of the Natural Sciences and Mathematics

of the Ruperto-Carola-University of Heidelberg. Germany

for the degree of

Doctor of Natural Sciences

Put forward by

Giancarlo Mattia

born in Chieri, Italy

Oral examination: 28/07/2022

Toward a consistent turbulence model for the origin of jet-launching magnetic fields: theoretical and numerical improvements

Referees:

apl. Prof. Dr. Christian Fendt
Prof. Dr. Ralf Klessen

Abstract

Astrophysical jets, consisting of collimated high-speed outflows, are typically found in several astrophysical objects, e.g., young stellar objects, X-ray binaries, gamma-ray bursts, or active galactic nuclei. The formation of collimated outflows requires some common features, such as the presence of a central object, an accretion disk and a large scale magnetic field (whose origin is still unclear).

Regarding the numerical aspects, we compared several solutions of the Riemann problem for ideal relativistic plasma in terms of accuracy and robustness against one – and multidimensional standard numerical benchmarks. We then performed non-ideal Magnetohydrodynamic simulations by employing the PLUTO code in order to investigate how the mean-field dynamo and the magnetic diffusivity affect the disk and jet properties.

At first we have investigated a non-isotropic dynamo toy model in order to disentangle the effect of the different dynamo components on the launching process and on the disk magnetic field. Then, we investigated a disk dynamo that follows analytical solutions of the mean-field dynamo theory, essentially based mainly on the Coriolis number. We thereby confirmed the anisotropy of the dynamo tensor acting in accretion disks, allowing both the resistivity and the mean-field dynamo to be related to the disk turbulence.

Subsequently, we studied the feedback of the generated magnetic field on the mean-field dynamo. We found that a stronger quenching of the dynamo leads to a saturation of the magnetic field at a lower disk magnetization. Nevertheless, we found that, when applying only a dynamo quenching, the overall jet properties do not depend on the feedback model. Finally, we present a feedback model which encompasses a quenching of the magnetic diffusivity. We find that after the magnetic field is saturated the Blandford-Payne mechanism takes place yielding to more collimated yet slower jets. We find strong intermittent periods of flaring and knot ejection for low Coriolis numbers.

Zusammenfassung

Astrophysikalische Jets bestehen aus kollimierten Ausströmungen hoher Geschwindigkeit und sind typischerweise in verschiedenen astronomischen Objekten, wie z. B. jungen stellaren Objekten, Röntgendoppelsternen, Gammablitzen oder aktiven Galaxienkernen, zu finden. Zur Bildung kollimierter Ausströmungen sind einige gemeinsame Eigenschaften erforderlich: ein zentrales Objekt, eine Akkretionsscheibe und ein großräumiges Magnetfeld (dessen Ursprung noch unklar ist) müssen vorhanden sein.

Hinsichtlich numerischer Aspekte haben wir mehrere Lösungen des Riemann-Problems für ideale relativistische Plasmen in Bezug auf ihre Genauigkeit und Robustheit mit ein- und mehrdimensionalen numerischen Standardbezugswerten verglichen. Anschließend führten wir nicht-ideale, magnetohydrodynamische Simulationen mit dem PLUTO-Code durch, um zu untersuchen, wie der mittlere Felddynamo und die magnetische Diffusivität die Eigenschaften von Scheiben und Jets beeinflussen.

Zunächst haben wir ein nicht-isotropes Dynamo-Spielzeugmodell untersucht, um die Auswirkungen der verschiedenen Dynamokomponenten auf den Startprozess und auf das Scheibenmagnetfeld zu entschlüsseln. Anschließend untersuchten wir einen Scheibendynamo, der analytischen Lösungen der mittleren Felddynamo-Theorie folgt. Diese basieren im Wesentlichen auf der Coriolis-Zahl. Damit bestätigten wir die Anisotropie des in den Akkretionsscheiben wirkenden Dynamotensors, sodass sowohl der Widerstand als auch der mittlere Felddynamo mit der Scheibenturbulenz in Verbindung stehen können.

Anschließend untersuchten wir das Feedback des erzeugten magnetischen Felds auf den mittleren Felddynamo. Wir fanden heraus, dass eine stärkere Abdämpfung des Dynamos zu einer Sättigung des Magnetfelds bei einer geringeren Magnetisierung der Scheibe führt. Dennoch hängen die allgemeinen Eigenschaften von Jets nicht vom Feedback-Modell ab, wenn nur eine Abdämpfung des Dynamos angewendet wird. Schließlich präsentierten wir ein Feedback-Modell, das die Abschwächung magnetischer Diffusivität umfasst. Wir stellen fest, dass nach der Sättigung des Magnetfelds der Blandford-Payne-Mechanismus einsetzt, der zu kollimierteren aber jedoch langsameren Jets führt. Bei niedrigen Corioliszahlen treten starke, intermittierende Zeiträume des Aufflackerns und Knotenauswürfe auf.

Contents

List of Figures

List of Tables

.

"It is not our part to master all the tides of the world, but to do what is in us for the succor of those years we are set"

J.R.R. Tolkien

Chapter 1

Introduction

In this chapter we highlight some of the most important discoveries about astrophysical jets. Starting from the observations of jets in different astrophysical environments in Section 1.1, we discuss some of the most important numerical simulations of jets performed in the last decades in Section 1.2. We then outline the main ideas behind dynamo theory in Section 1.3, focusing on the difference between the direct dynamo and the mean-field dynamo approaches. Finally, the outline of this thesis is summarized in Section 1.4.

1.1 Introduction to Astrophysical Jets

Astrophysical jets, which consist of highly-collimated beams of high-velocity material, have been launched from a variety of astrophysical objects, such as young stellar objects (YSOs), micro-quasars (MQ), or active galactic nuclei (AGNs). Since these sources span over orders of magnitude in length, time and energy scales, scientists have looked for common properties in astrophysical jets in order to understand why they are launched and how they are maintained. So far there is a common understanding that jets are launched by systems which include the presence of a central object (S. Komissarov and Oliver Porth, 2021) surrounded by an accretion disk. Furthermore, another fundamental prerequisite for the launching of jets is the presence of a strong magnetic field with a favorable topology (see, e.g., Frank et al. 2014; J. F. Hawley, Fendt, et al. 2015; Pudritz and T. P. Ray 2019). This holds for both non-relativistic and relativistic jets.

1.1.1 Jets from Young Stellar Objects

A jet launched by a YSO was first discovered (inadvertently) by Burnham (1890). It was described as a small elongated star within a small condensed nebula. Nowadays we know that the variations in the nebula are caused by the winds launched by a T Tauri star (which was discovered by Hind 1852). A few decades later, Herbig (1950), Herbig (1951), Herbig (1952), Haro (1952), and Haro (1953) have independently performed observations on several T Tauri stars, detecting strong emission lines of H, O and S elements. Such emission lines can be attributed to stars (which are now called Herbig-Haro stars) characterized by an accretion disk around them (Dopita, Schwartz, and Evans, 1982) and strong supersonic outflows in the form of winds and jets (Schwartz, 1975; Schwartz, 1977; Snell, Loren, and Plambeck, 1980).
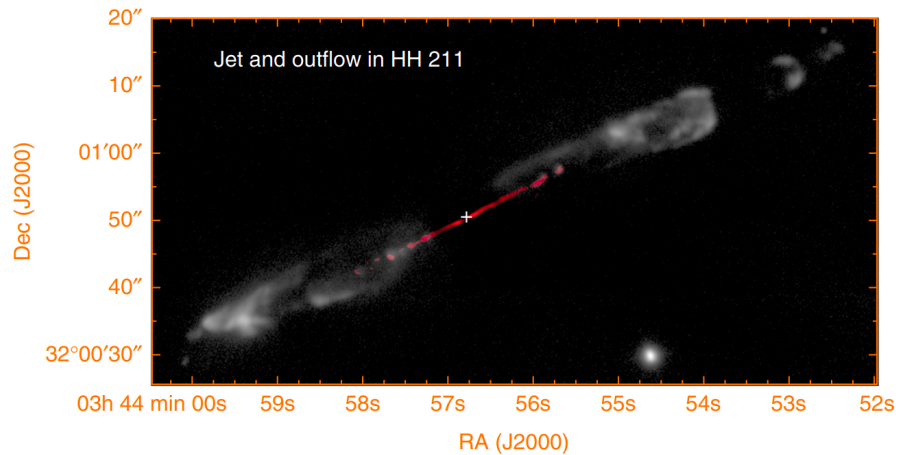
FIGURE 1.1: Highly collimated jet from HH 211. Credit: Lee et al. (2018).

However, the discovery of four T-Tauri stars with jet-like structures star happened only one year later (Mundt and Fried, 1983).

It became clear very soon that these outflows from YSOs were not driven by the radiative pressure provided by the central star (Bally and Lada, 1983), especially since the outflows have been found to be collimated already in the vicinity of the object (Takano et al., 1984). Moreover, a clear correlation between the mass of the circumstellar structure and the jet power has been found and confirmed by Lada (1985) and Cabrit and Andre (1991).

Today the link between YSO outflows and accretion disks around stars is clearer, and so is the relation between the accretion and the ejection processes (see, e.g., T. P. Ray and Ferreira 2021). Disks and outflows have been detected near low (Bally, Reipurth, and C. J. Davis, 2007; Bally, 2007), intermediate (Watson et al., 2007) and high (Davies et al., 2010) mass pre-main sequence stars. The typical velocities measured for such outflows range from $100 - 500$ km s^{-1} (Hartigan et al., 2001; T. Ray et al., 2007).

More precise observations (e.g., Lee et al. 2018, see Figure 1.1) showed that such outflows can propagate from up to several parsecs to beyond the size of the molecular cloud associated to the young star (Reipurth, Bally, and Devine, 1997; Curiel et al., 2006; Bally, Walawender, and Reipurth, 2012; Qiu et al., 2019).

1.1.2   Jets from Active Galactic Nuclei

AGN jets (like Cygnus A, see Figure 1.2), and more generally relativistic jets, are mostly detected in the radio band because of synchrotron emission (Shklovskii, 1953). The first observed AGN (NGC 1068, described as a "spiral nebula with a diffuse nucleus") was documented by Fath (1909), while the first observation of an AGN jet was performed by Curtis (1918), who observed the galaxy M87. Because of the development of radioastronomy (Jansky, 1933), early radio surveys (e.g., the 3C catalogue, Edge et al. 1959) were able to successfully detect several AGN jets and their sources.
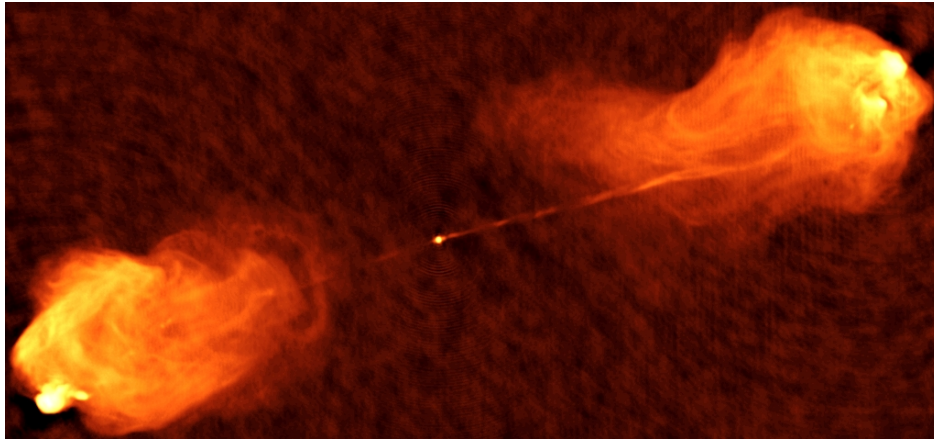
FIGURE 1.2: Image of Cygnus A at 5 GHz. Credit: Carilli and Barthel (1996).

By studying NGC 1068, along with other galaxies with "an exceeding luminous stellar or semistellar nucleus", Seyfert (1943) proposed the existence of a gravitational potential well in the center of the AGNs. This class of object has been later defined as "Seyfert Galaxies": AGNs characterized by broad emission lines confined in an extremely compact nucleus (Woltjer, 1959). Seyfert galaxies represent the largest fraction of AGNs in the local universe (Maiolino and Rieke, 1995; Ho, Filippenko, and Sargent, 1997).

For the sake of convenience, the AGNs have been divided into two categories: the radio-quite AGNs have extremely weak or no jets, while the radio-loud AGNs show jets that extend up to the Mpc scale and whose luminosity dominates the source at radio wavelenghts. In the latter category fall blazars, whose observed fluxes (Schmidt, 1963; Hughes, 1965; Schmitt, n.d.; Punch et al., 1992) show variations that can act on the timescale of minutes.

Another large subset of AGNs consists of quasars, which can be both radio quiet and radio loud. While they usually appear as point sources, they emit almost uniformly from the X-ray band to the far-infrared. The first observations of a quasar, were performed by Schmidt (1963) and Hazard, Mackey, and Shimmins (1963) toward 3C 273. Radio-loud quasars have been found to be 10 times less numerous than their radio-quiet counterparts (Sandage, 1965). In the unification scenario of radio-loud AGNs, blazars and quasars are considered as normal radio galaxies observed at some peculiar angles to the line of sight (Antonucci and Ulvestad, 1985; Urry and Padovani, 1995). A similar model has been applied in order to provide unification of radio-quiet Seyfert galaxies.

The majority of AGN jets reaches Lorentz factors of $\Gamma \sim 10 - 20$ (Lister and Marscher, 1997; Lister, Cohen, et al., 2009; Homan, 2012); however in some extreme cases the Lorentz factor can reach values of $\Gamma \sim 40$ (Jorstad et al., 2005).

1.1.3 Other Types of Astrophysical Jets

Relativistic jets can be observed also within our galaxy, more precisely in binary systems of stellar mass black holes and neutron stars (Mirabel and Rodríguez, 1994). Such systems are called X-Ray Binaries (XRB) since they were originally detected
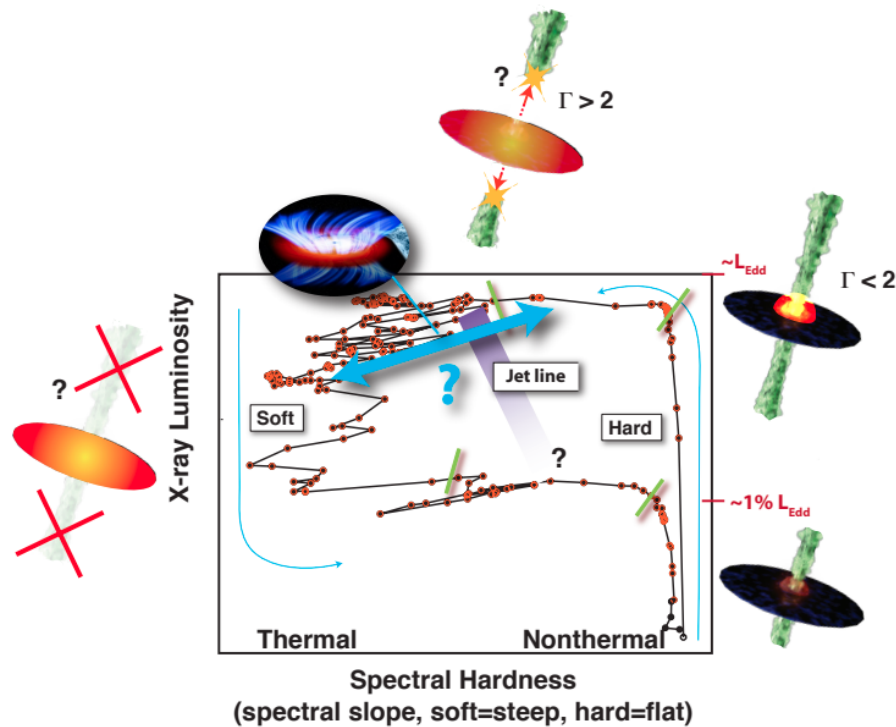
FIGURE 1.3: Different states of an XRB outburst illustrated for GX339.
Credit: Romero et al. (2017).

in the X-ray band (Zhang et al., 1997). Because of the lower mass of the compact object (compared to the AGN scenario), the dynamical timescales are much shorter. Thus, since many of the phenomena seen in quasars are accessible on the "human" timescale, these objects are known as microquasars (Mirabel and Rodríguez, 1998; Mirabel and Rodríguez, 1999).

For instance, variations in "X-ray hardness vs intensity" diagram (see, e.g., Figure 1.3) can be observed on a weekly timescale (Belloni et al., 2005). In particular, it seems that the state of a given XRB in the hardness-intensity diagram follows a clear and not random path. Therefore, for the sake of convenience, a distinction between two states (low intensity hard X-ray spectrum and high intensity soft X-ray spectrum) has been made (see, e.g., Dhawan, Mirabel, and Rodríguez 2000). This distinction is also reflected in the stability of the outflow: while stationary jets are typically observed in the low/hard state, episodic jets are observed in the high/soft state (Fender, 2001; Stirling et al., 2001).

The unification of galactic and extragalactic jets has been proposed (see, e.g., Merloni, Heinz, and di Matteo 2003), and so far it has been quite successful in linking the low power AGNs with the hard state of XRBs (Falcke, Körding, and Markoff, 2004; Markoff et al., 2008). Future observations with sufficient spatial resolution should give us a deeper insight on this interrelation.

Another category of jets launched on the small scales are the Gamma Ray Bursts (GRBs). The energy released by a GRB is of the order of $10^{51} - 10^{54}$ erg s^{-1} on a timescale of $10^{-3} - 10^{3}$ s. The first GRB events were serendipitously detected by spying satellites during the cold war (Klebesadel, Strong, and Olson, 1973) and investigated in the following years (Mazets et al., 1981; Atteia and Hurley, 1986;

Hurley et al., 1994; Meegan et al., 1995; Mészáros, 2001). Because of the large variety of curves of GRB events, the origin of GRsB is not completely clear (Piran, 2004). The energy scale suggests that the burst may be caused by internal shocks within a highly collimated relativistic ($\Gamma \sim 100$) flow.

The so-called short GRBs, i.e., the ones whose duration is less than 2 s, are most likely produced by the collision and merging of binary neutron stars and black holes. This hypothesis has been confirmed by the LIGO Scientific Collaboration and Virgo Collaboration (2017a), when a gravitational wave (LIGO Scientific Collaboration and Virgo Collaboration, 2017b) has been detected 1.7 seconds before a short GRB has been detected, from the same location, by the Fermi GRB Monitor (Goldstein et al., 2017).

Long GRBs, on the other hand, are easier to observe because of their longer afterglow ($\gtrsim$ 2 s). Most of them have been localized within galaxies with high star formation rates (Fruchter et al., 1999; P. A. Price et al., 2003; Gorosabel et al., 2005) or with core-collapse supernovae events (Woosley and Bloom, 2006; Woosley and Heger, 2006).

1.1.4 Connecting Theory and Observations

Several authors have observed and investigated the disk-jet connection, as well as the role of the magnetic field in the launching process (O'Sullivan and Gabuzda, 2009; Zamaninasab et al., 2014; Baczko et al., 2016). Alongside the observations of astrophysical jets, several theoretical models have significantly contributed toward an understanding of the physical processes involved in the launching of collimated outflows. Fully comprehensive modeling of such systems is an extremely challenging task because of the many physical mechanisms involved and the extremely wide range of spatial, energetic and temporal scales that should be taken into account.

In this regard, the employment of numerical simulations is able to ease the complexity of these interactions, which would make a purely analytical approach prohibitive. Although the numerical simulations are limited by both the scales at which the theoretical assumptions are valid and the computational resources, they represent the most accurate tool available for us to theoretically describe the physical processes behind the launching of collimated jets.

Throughout this thesis, the MagnetoHydroDynamics (MHD) approximation will be considered since the aim is to focus on the large scale launching. While more self-consistent approaches, like the Particles In Cells (PIC; Birdsall and Langdon 2004), would allow us to consider the physical processes up to the plasma skin depth scale (e.g., Chang, Spitkovsky, and Arons 2008; Sironi, Spitkovsky, and Arons 2013; Sironi and Spitkovsky 2014), they would become prohibitively expensive for describing astrophysical systems at larger scales.

1.2 Numerical Simulations of Jet launching

Jet launching mechanisms have been studied extensively in the last decades. Because of the great improvements made in terms of computational power, numerical simulations have become more affordable in order to investigate the physical mechanisms which govern the launching of a collimated outflow. The rise of the so-called

High-Resolution-Shock-Capturing (HRSC) schemes led to a number of MHD codes able to tackle the problem of jet formation.

1.2.1   Computing Aspects

Progresses in computational resources have always been followed by a deeper investigations of the numerical algorithms adopted to solve the set of MHD equations. Since the first simulations of astrophysical jets (Rayburn, 1977), several MHD codes have been developed in order to describe the behavior of both non-relativistic, see, e.g., ZEUS (Stone and Norman, 1992), FLASH (Fryxell et al., 2000), RAMSES (Fromang, Hennebelle, and Teyssier, 2006), PLUTO (Mignone, Bodo, Massaglia, et al., 2007), ATHENA (Stone, Gardiner, et al., 2008), MPI-AMRVAC (O. Porth, Xia, et al., 2014) and PENCIL (Pencil Code Collaboration et al., 2021), and (general) relativistic plasmas (following the approach of S. S. Komissarov 1999), like HARM (Gammie, J. C. McKinney, and Tóth, 2003), ECHO (Del Zanna, Zanotti, et al., 2007), ATHENA++ (White, Stone, and Gammie, 2016), BHAC (O. Porth, Olivares, et al., 2017) and H-AMR (M. Liska, Chatterjee, et al., 2019). Despite the differences between the codes, several comparisons (e.g., O. Porth, Chatterjee, et al. 2019) have shown very good agreement between them, when a high enough resolution is provided.

Several challenges have been faced by the scientific community through the years (see, e.g., the review of Martí and Müller 2015). One of the most important issues is how to increase the accuracy of a numerical scheme at almost no additional computation cost. In this regard, the development of higher order schemes has allowed us to obtain the same accuracy at a much lower resolution, as well as a higher convergence. Recent advances in the development of MHD numerical codes include high order schemes in spatial reconstruction (Borges et al., 2008; McCorquodale and Colella, 2011), including non-cartesian coordinates (Mignone, 2014), and time integration schemes (S. Gottlieb, C. Shu, and Tadmor, 2001; Isherwood, Grant, and Gottlieb, 2018). Nowadays several codes rely on 3rd order or higher (Mignone, Bodo, Massaglia, et al., 2007; D. S. Balsara, 2017; Felker and Stone, 2018) finite volume methods.

Another key challenge is the absence of unphysical magnetic monopoles. The treatment of the divergence-free condition of the magnetic field has been extensively studied through the years. Several schemes have been implemented in order to keep $\nabla \cdot \mathbf{B} = 0$ to machine accuracy, including centered (Dedner et al., 2002; Mignone, Tzeferacos, and Bodo, 2010) and staggered (Stone and Norman, 1992; D. S. Balsara and Spicer, 1999; Londrillo and del Zanna, 2004; Mignone and Del Zanna, 2021) formulations. The choice of the divergence-free algorithms can severely impact the outcome of a simulation (see, e.g., Mignone and Del Zanna 2021; Puzzoni, Mignone, and Bodo 2021).

The Riemann problem represents another essential step in the development of accurate and robust numerical methods, since exact analytical or semi-analytical approaches are not feasible because of the complexity of the equations and the huge computational cost that they would require. While the ability of capturing more intermediate waves leads to a significant increase in the accuracy of a numerical scheme, the stability and the computational time required to solve the Riemann

problem may be affected. The HLL Riemann solver (Harten, Lax, and Leer, 1983) represents the standard benchmark because of its great stability and lack of internal structure. More accurate Riemann solvers included the ability to capture a higher number of intermediate waves both in the non-relativistic (S. Li, 2005; Miyoshi and Kusano, 2005) and relativistic (Mignone and Bodo, 2006; Mignone, Ugliano, and Bodo, 2009) regimes. White, Stone, and Gammie (2016) extended such approaches to the general-relativistic MHD equations. In the last decades the extension to multidimensional Riemann solvers (D. S. Balsara, 2010), which allow for a more consistent formulation of the electric field (required in the staggered divergence-free algorithms), has been possible.

In order to perform higher resolution simulations, several approaches can be followed. In some circumstances, great disparities in both spatial and temporal scales may arise, namely some parts of the domain require a higher resolution compared to other regions. To overcome such problems, one possibility is to dynamically adapt the computational grid so that the features of interest can be adequately captured and resolved without requiring a prohibitive computational time. The Adaptive Mesh Refinement (AMR) approach has been implemented in several codes, e.g., Flash (MacNeice et al., 2000), AMR-VAC (Keppens et al., 2003), PLUTO (Mignone, Zanni, et al., 2012), BHAC (Olivares et al., 2019), Athena++ (Stone, Tomida, et al., 2020) and H-AMR (M. Liska, Chatterjee, et al., 2019). The computational speed of the H-AMR code is also enhanced by GPU acceleration.

Alongside the numerical improvements, additional physical process (e.g., magnetic diffusivity, dynamo and radiation) can be included in the MHD codes. However such additions may require a corresponding development of adequate numerical techniques. As shown in Puzzoni, Mignone, and Bodo (2021) the choice of the numerical algorithms used to model the magnetic resistivity can play a very strong impact in terms of the magnetic reconnection process and in the acceleration of non-thermal particles. On the other hand, owing to the small resistivities typical of astrophysical plasma, the Resistive Relativistic MHD (RRMHD) equations may become stiff because of the current density source term. S. S. Komissarov (2007) presented the first numerical scheme that was able to overcome the stiffness of the RRMHD equations. Two years later Palenzuela et al. (2009) proposed an implicit-explicit Runge-Kutta method, which has been extended to the relativistic mean-field dynamo term by Bucciantini and Del Zanna (2013) and Tomei et al. (2020). The implicit-explicit schemes have also been adopted by, e.g., J. C. McKinney, Tchekhovskoy, Sadowski, et al. (2014) and Melon Fuksman and Mignone (2019) in order to properly encompass the radiative opacity of the plasma flows.

Finally, in order to bridge the gap between the macroscopic scales typical of the MHD approximation and the kinetic effects relevant to the microscales, hybrid numerical frameworks have been developed. Such approaches include, e.g., hybrid MHD-Pacrticles in Cells method (Bai, Caprioli, et al., 2015; van Marle, Casse, and Marcowith, 2018; Mignone, Bodo, Vaidya, et al., 2018; Bacchini et al., 2019), sub-grid electron physics through Lagrangian particles or additional fluid tracers (Mimica et al., 2009; Ressler et al., 2015; Vaidya, Mignone, et al., 2018) or dust grains (Youdin and Johansen, 2007; Mignone, Flock, and Vaidya, 2019).

1.2.2   Jet Launching Simulations

The very first numerical simulation of an astrophysical jet was performed by Rayburn (1977), who performed PIC simulations of a 2D cylindrical jet interacting with an external medium. Despite a resolution of only 10×20 grid cell and 16 particles per cells, both the bow shock and the reverse shock (Scheuer, 1974; R. D. Blandford and Rees, 1974) were found. A few years later, Shibata and Uchida (1985) and Uchida and Shibata (1985) simulated the launching of jets in the context of non-relativistic outflows from an accretion disk for the first time. Their initial setup consisted of a sub-Keplerian thin disk surrounded by a uniform corona. The collapse of the accretion disk yielded an advected and twisted magnetic field. The magnetic pressure was then able to drive away the gas from the inner disk in the form of a collimated outflow.

The extension to Relativistic MHD (RMHD) was brought by Koide, Shibata, and Kudoh (1998) and Koide, Shibata, and Kudoh (1999), who attempted to investigate the interaction between a thin Keplerian accretion disk and a rotating black hole. Despite some numerical issues (reported in S. S. Komissarov 2001), the formation of magnetically driven jet (similar to the one recovered by Uchida and Shibata 1985) was reproduced.

In the past 30 years, the theoretical mechanisms proposed to explain the formation of astrophysical jets have been tested through a series of MHD simulations. In the context of jets from AGN, the R. D. Blandford and Znajek (1977) mechanism (BZ) has been criticized by Punsly and Coroniti (1990), who also proposed an alternative model which had strong analogies with the Penrose mechanism (Penrose and Floyd, 1971). The similarities and differences between these processes are described in S. S. Komissarov (2009). Because of the lack of an analytical solution, this debate could have been solved only through numerical simulations.

The first experiments in the context of force-free degenerated electrodynamics (which can be seen as the zero-inertia limit of the RMHD approximation, as shown by S. S. Komissarov 2002) were carried out by S. S. Komissarov (2001) and found excellent agreement with the solution found by R. D. Blandford and Znajek (1977). The same simulation was repeated by S. S. Komissarov (2004) in the context of full General Relativistic MHD (GRMHD), finding that the electromagnetic component of the MHD solutions is astonishingly close to the BZ solution even whether some matter is injected in situ. Moreover, the small inertia was in high contrast to the MHD-Penrose mechanism proposed by Penrose and Floyd (1971) and Punsly and Coroniti (1990). On the other hand, Koide, Shibata, Kudoh, and Meier (2002) and Koide (2003) claimed the efficacy of the MHD-Penrose process.

Because of the recent advances in the development of GRMHD codes, the nature of such disagreement was due to the differences in the numerical schemes. For instance, the absence of the BZ mechanism in De Villiers, J. F. Hawley, and Krolik (2003), Hirose et al. (2004), and De Villiers, J. F. Hawley, Krolik, and Hirose (2005) was caused by a non-conservative scheme in the Boyer-Lundqvist coordinates which, unlike the Kerr-Schild spacetime splitting, does not allow the inner boundaries of the computational domain to be inside the outer horizon. The skepticism toward the BZ mechanism ended with the simulations of J. C. McKinney and Gammie 2004 (see Figure 1.4), where a BZ-generated outflow was clearly identified. From this point, several studies on the launching of jets from rotating black holes
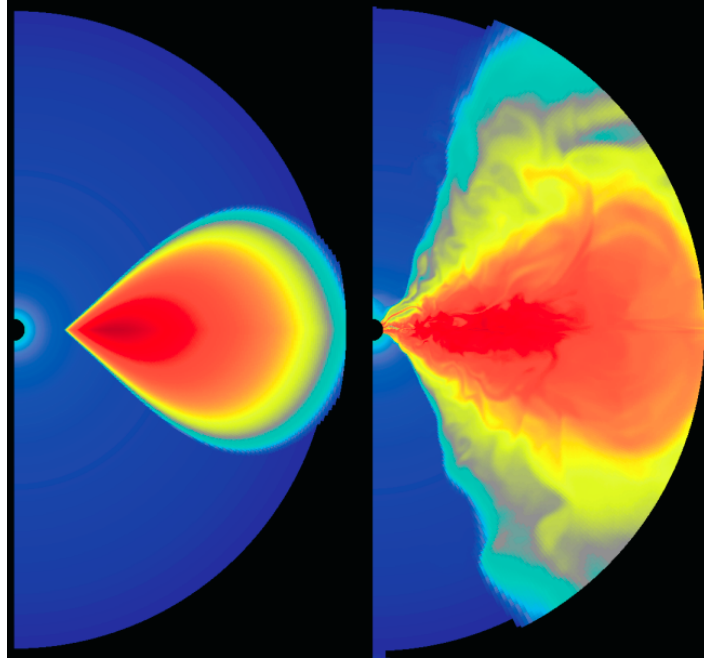
FIGURE 1.4: Initial (left) and final (right) distribution of the density (in logarithmic scale) in the fiducial model of J. C. McKinney and Gammie (2004). The density range is $[4 \cdot 10^{-7}, 1]$ for the left panel and $[4 \cdot 10^{-7}, 0.54]$ for the right panel. Credit: J. C. McKinney and Gammie (2004).

were performed in order to understand "how" (rather than "if") the magnetic flux could accumulate in the black hole magnetosphere.

The influence of the black hole spin (Gammie, Shapiro, and J. C. McKinney, 2004), current-driven instabilities (J. C. McKinney, 2006) and the strength (De Villiers, 2006) and topology (J. C. McKinney and Narayan, 2007; J. C. McKinney, Tchekhovskoy, and R. D. Blandford, 2012) of the magnetic field on the production of jets has been investigated both in 2D and in 3D (Beckwith, J. F. Hawley, and Krolik, 2008; J. C. McKinney and R. D. Blandford, 2009). A very efficient BZ outflow has been confirmed by Tchekhovskoy, Narayan, and J. C. McKinney (2011). Tchekhovskoy and J. C. McKinney (2012) studied the difference between a prograde and a retrograde rotation of the accretion disk, showing that the prograde disk has higher efficiency that increases with the disk thickness. In the last decade the coupling between radiation and fluid has been investigated by, e.g., J. C. McKinney, Tchekhovskoy, Sadowski, et al. (2014), J. C. McKinney, Dai, and Avara (2015), Sądowski, Narayan, et al. (2015), Avara, J. C. McKinney, and Reynolds (2016), Sądowski, Wielgus, et al. (2017), Yoon et al. (2020), and M. T. P. Liska et al. (2022).

At the same time, the formation of non-relativistic jets has been investigated in order to validate the R. D. Blandford and Payne (1982) mechanism (BP). The first simulations showing a collimated outflow from an accretion disk were performed by Casse and Keppens (2002) and Casse and Keppens (2004). In this context, the presence of the magnetic diffusivity (in order to characterize the turbulence, which acts on a much smaller scale than the disk resolution) was a key ingredient which allowed the matter to cross the magnetic field lines.
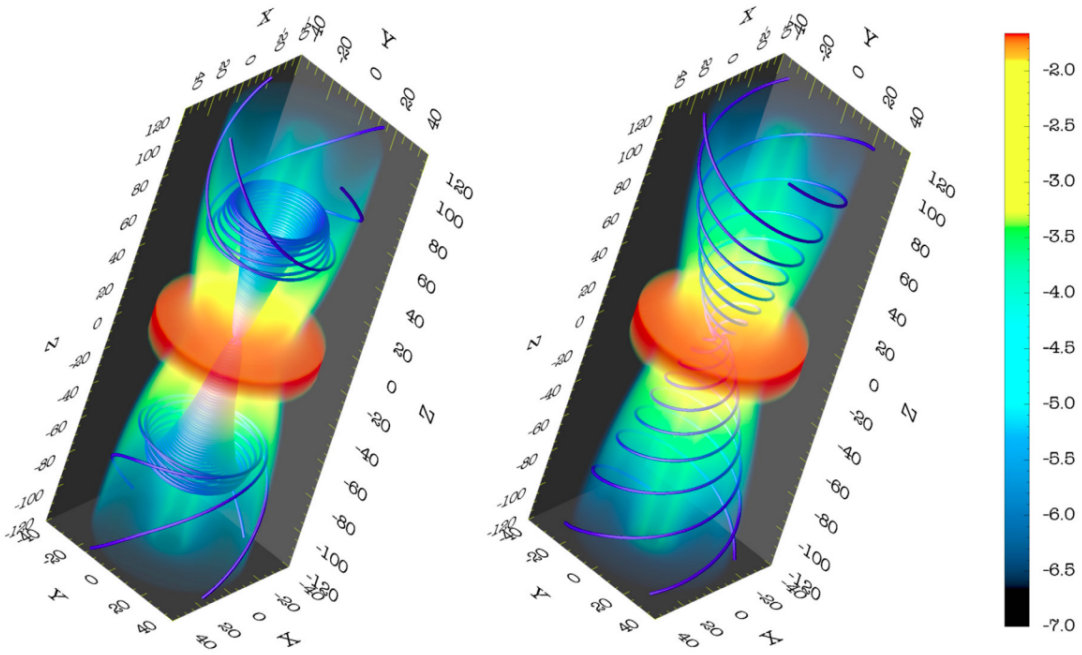
FIGURE 1.5: Influence of different diffusivity models on the evolution
of the magnetic field. Shown are the density (colormap in logarithmic
scale) and the magnetic field lines. Credit: Zanni, Ferrari, et al. (2007).

The structure (Zanni, Ferrari, et al. 2007, see Figure 1.5) and the impact of the
magnetic diffusivity has been extensively studied by several authors (see, e.g., Fendt
and Cemeljić 2002; Zanni, Ferrari, et al. 2007; Tzeferacos, Ferrari, et al. 2009; Sheikh-
nezami et al. 2012; Fendt and Sheikhnezami 2013; Stepanovs, Fendt, and Sheikhne-
zami 2014) in the context of non-relativistic jets and, later-on, by Qian, Fendt, and
Vourellis (2018), Vourellis, Fendt, et al. (2019), Ripperda, Bacchini, and Philippov
(2020), and Nathanail et al. (2022) in the context of jets from rotating black holes.
In particular, the magnetic diffusivity is a key ingredient for the magnetic reconnec-
tion process, which seems to be able to explain the non-thermal particles in astro-
physical jets, as well as the formation of black holes flares (Ripperda, M. Liska, et
al., 2022). Other non-ideal physical processes, like viscosity (Murphy, Ferreira, and
Zanni, 2010) and heating (Tzeferacos, Ferrari, et al., 2013) have also been thoroughly
investigated.

While self-similar solutions of magnetically-driven jets from accretion disks sug-
gest that jets are able to accelerate to super-Alfvénic speed only when the midplane
magnetization is close to equipartition, numerical simulations have shown that a
steady launching can be obtained considering a much wider range of the magneti-
zation (Tzeferacos, Ferrari, et al., 2009; Murphy, Ferreira, and Zanni, 2010; Sheikh-
nezami et al., 2012; Stepanovs and Fendt, 2014). The correlation between the accre-
tion disk (magnetic field and hydrodynamics) and the jet properties, such as the
jet speed, power and collimation, have been extensively studied throughout the
years encompassing different physical processes (Pudritz, Rogers, and Ouyed, 2006;
Fendt, 2006; Fendt, 2009; Tzeferacos, Ferrari, et al., 2009; Vaidya, Fendt, et al., 2011;
Stepanovs and Fendt, 2016). The stability of the jet and the midplane (a)symmetry
has been extensively studied in Fendt and Sheikhnezami (2013) (see Figure 1.6).
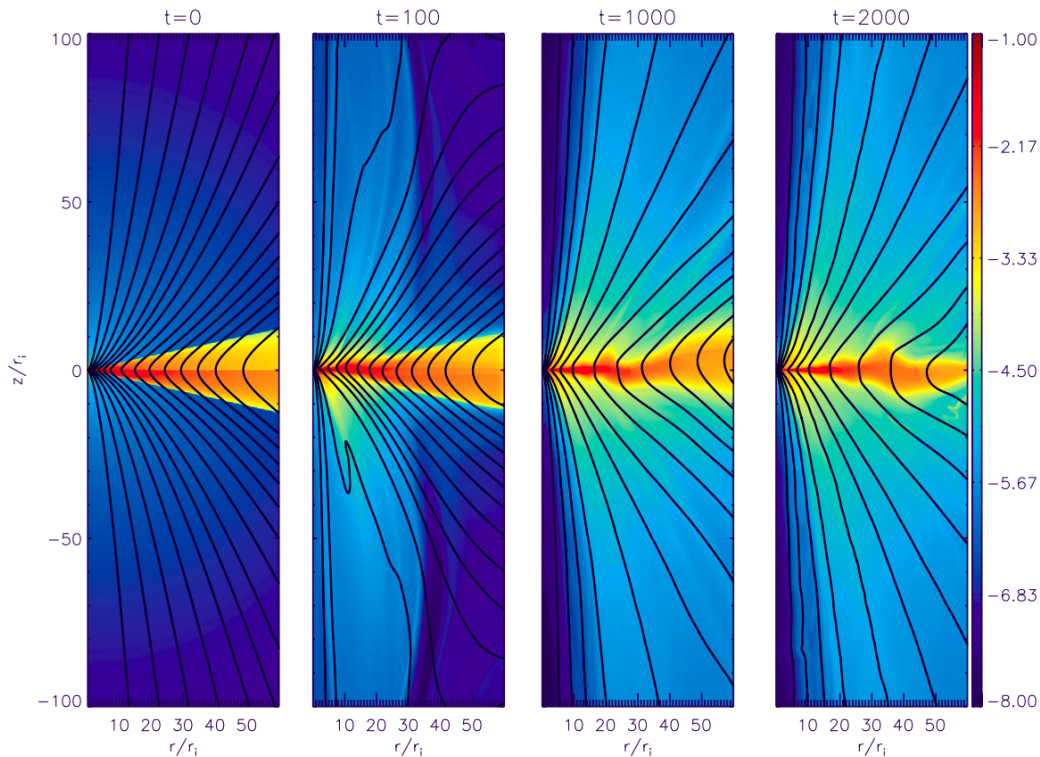
FIGURE 1.6: Time evolution of the bipolar disk-jet density (in color) with different initial thermal scale heights for the upper and lower disk hemispheres. Credit: Fendt and Sheikhnezami (2013).

1.3 Dynamo Theory

The origin of the magnetic jet-launching disk magnetic field is still an open question. Analytical models and numerical simulations have so far mostly assumed a large-scale strong initial magnetic field that allows for the launching of jets. For different central objects, several options for the magnetic field origin may be considered. For instance, in the case of a *stellar* accreting object, the magnetic field may be provided by the star itself.

Several scenarios have been conjectured (F. Shu et al., 1994; Fendt and Elstner, 1999; Fendt and Elstner, 2000; Fendt, 2003; Matt and Pudritz, 2005) in order to explain the interplay between the stellar magnetic field and the dynamics of the accretion disk. However, this scenario is not feasible for AGNs, since black holes are not able to generate a magnetic field. Another scenario is that the jet-launching magnetic field is just advected through the accretion process from the ambient medium. Still, for protostars, strong evidence for the advection of magnetic flux has not been found yet (Pudritz and T. P. Ray, 2019).

A particularly interesting scenario, which is valid for both YSOs and AGNs, is that the magnetic field can be generated and amplified by a dynamo process that is working in the accretion disk. Since the two main ingredients for a dynamo are turbulence and rotation, accretion disks are a very suited astrophysical object for the dynamo action to take place. In this thesis, we will indeed focus on the accretion disk dynamo mechanism, since it looks like a general mechanism to generate the desired magnetic flux in jet-launching accretion disks.

1.3.1   The Dynamo Process

The dynamo action in astrophysical objects is not limited only to the jet scenario. For instance, Larmor (1919) proposed, in order to explain the magnetic field in the Sun's sunspots, that small variations of the magnetic field are able to generate electric current which amplify the magnetic field itself. Although several anti-dynamo theorems emerged, restricting the applicability of the dynamo theory (e.g., Cowling 1933; Ivers and James 1984), solutions of the induction equation consisting in the amplification of the magnetic field are possible (Herzenberg, 1958; Backus, 1958; Ponomarenko, 1973).

The most successful dynamo theory is the so-called "mean-field dynamo", which assumes that the fluid bulk velocity and the magnetic field can be split into a mean value and its variations. The first mean-field dynamo theory was proposed by Parker (1955), and then developed in the following years by, e.g., Steenbeck and Krause (1966), Steenbeck and Krause (1969a), Steenbeck and Krause (1969b), Krause and Raedler (1980), and Beresnyak (2012).

The physics of cosmic dynamo action has been extensively studied in the last decades, in particular by numerical simulations (see, e.g., Brandenburg and Subramanian 2005; Rincon 2019). The existence and the implication of the dynamo action has been investigated in several types of astronomical objects, e.g., galaxies (Schultz, Elstner, and Ruediger, 1994; Moss and Shukurov, 1996; Elstner, Ruediger, and Schultz, 1996; Subramanian, 1998; Kulsrud, 1999; Schober, D. R. G. Schleicher, and R. S. Klessen, 2013; Beck, 2015), stars (Tobias, 2002; Schober, D. Schleicher, Federrath, Glover, et al., 2012; Charbonneau, 2014; Fan and Fang, 2014; Käpylä et al., 2016; Warnecke and Käpylä, 2020; Perri et al., 2021), neutron stars (Bonanno, Rezzolla, and Urpin, 2003; Franceschetti and Del Zanna, 2020) and accretion disks (Stepanovs, Fendt, and Sheikhnezami, 2014; Dyda et al., 2018; M. Liska, Tchekhovskoy, and Quataert, 2020; Tomei et al., 2020; Sharda et al., 2021; Vourellis and Fendt, 2021).

Astrophysical disk dynamos are believed to have a turbulent origin, most probably caused by the magneto-rotational instability (MRI; Steven A. Balbus and John F. Hawley 1991; J. F. Hawley and S. A. Balbus 1991). Accretion disk dynamos have been suggested already decades ago (Pudritz, 1981b; Pudritz, 1981a; Brandenburg, Nordlund, et al., 1995), and evidence of dynamo amplification in turbulent plasma is currently well established, for example also in laboratory experiments (Gailitis et al., 2000; Blackman and Ji, 2006; Monchaux et al., 2007; Tzeferacos, Rigby, A. Bott, et al., 2017; Tzeferacos, Rigby, A. F. A. Bott, et al., 2018).

1.3.2   Direct Dynamo and Mean-Field Dynamo

Because of the different physical mechanisms that operate over a very wide range of spatial, energetic and temporal scales, a comprehensive modeling of the disk-jet connection represents a very challenging task. On one hand there is the scale at which the turbulence occurs, on the other the scale on which the jet is launched and where it propagates.

On small scales, convergence studies of the MRI have been performed by a number of groups (Guan and Gammie 2009; S. W. Davis, Stone, and Pessah 2010; Shi, Krolik, and Hirose 2010; Parkin and Bicknell 2013; J. F. Hawley, Richers, et al. 2013;
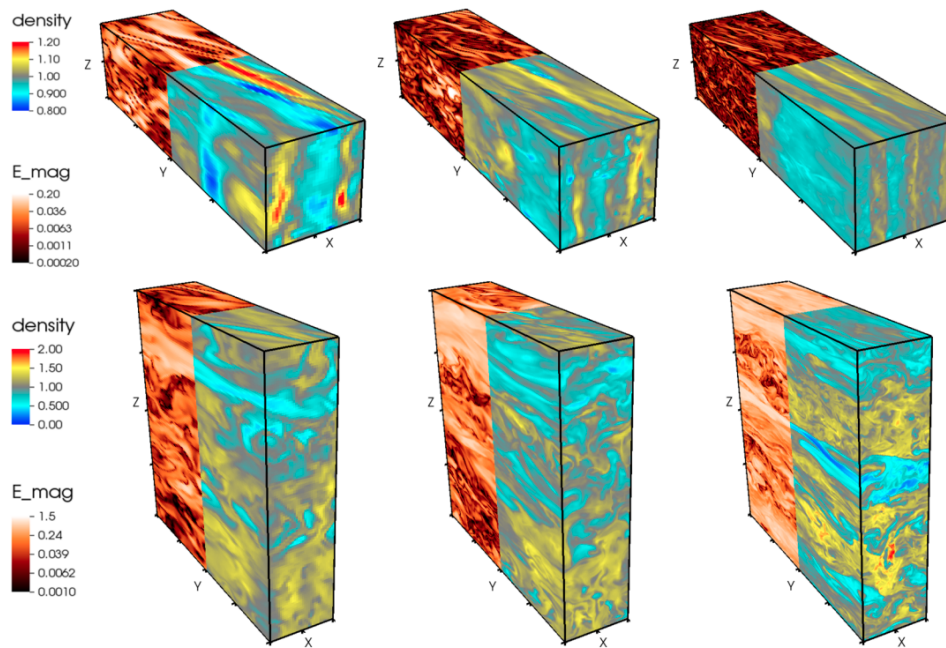
FIGURE 1.7: Resolution study of the turbulence in standard and taller boxes. Credit: Shi, Stone, and Huang (2016).

Bodo et al. 2014; Shi, Stone, and Huang 2016; Ryan et al. 2017 to name a few), showing the importance of the grid resolution (see Figure 1.7). Despite the advances in the numerical methods and computational resources (see Sorathia et al. 2012; Shiokawa et al. 2012; O. Porth, Chatterjee, et al. 2019; White, Stone, and Quataert 2019; White and Chrystal 2020 for convergence studies of large scale simulations), modeling both the turbulent and the disk-jet scales would require unrealistically high computational resources.

For all these reasons, mainly two different types of dynamo action have been investigated. On one hand we have the so-called direct simulations, which focus on the natural amplification of the magnetic field at the turbulent scales. Several studies have focused on whether the turbulence is able to generate a dynamo (Sur, Brandenburg, and Subramanian, 2008; Federrath et al., 2014; Schober, D. R. G. Schleicher, Federrath, et al., 2015; Walker and Boldyrev, 2017; Gressel and Elstner, 2020), focusing on recovering the large scale dynamo coefficient (Gressel, 2010; Gressel and Pessah, 2015; Bendre et al., 2020; Dhang et al., 2020; Gressel and Pessah, 2022) and on investigating the influence of, e.g., disk height (Hogg and Reynolds, 2018), thermal conduction (Schober, D. Schleicher, Federrath, R. Klessen, et al., 2012; Schober, D. Schleicher, Bovino, et al., 2012; Gressel, 2013), gravity (Riols and Latter, 2018) and magnetic fields (Bai and Stone, 2013; Salvesen et al., 2016).

On the other hand, there is the so-called mean-field dynamo approach that relies on modeling, through (semi-)analytical solutions, the large scale effect of the turbulent motion (see, e.g., Krause and Raedler 1980; Ruediger, Elstner, and Stepinski 1995; Campbell 1999; Rekowski, Rüdiger, and Elstner 2000; Bardou et al. 2001; Chabrier and Küker 2006) allowing us to perform numerical simulations at the scales on which accretion disks and jets evolve.

In this thesis we follow the mean-field dynamo approach, since the main focus of
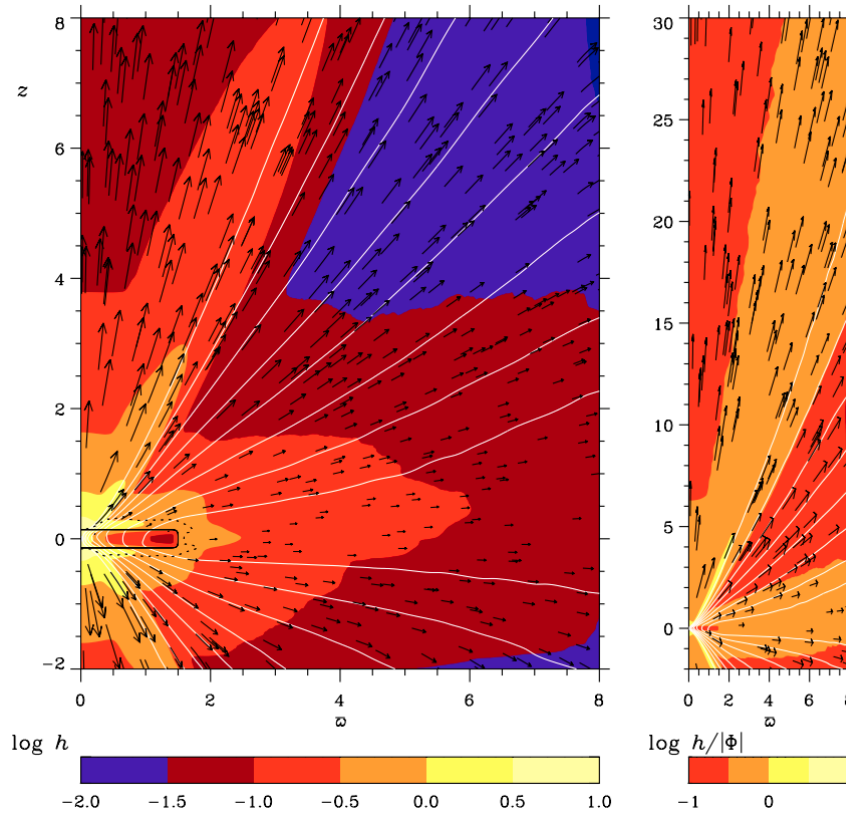
FIGURE 1.8: Velocity and poloidal magnetic field lines in the inner region of a dynamo active accretion disk. Credit: von Rekowski, Brandenburg, et al. (2003).

this work is to investigate the launching of jets. Investigations on the mean-field dynamo action in accretion disks has been done by von Rekowski, Brandenburg, et al. (2003), Stepanovs, Fendt, and Sheikhnezami (2014), and Fendt and Gaßmann (2018) (see Figure 1.8), showing that a mean-field dynamo-amplified, strong magnetic field is able to launch a jet or a disk outflow in general.

In particular, it has been shown by von Rekowski and Brandenburg (2004) and Dyda et al. (2018) that the interplay between the mean-field accretion disk dynamo and the central stellar magnetic field can lead to an outflow. Recently, the mean-field dynamo approach has also been extended to general relativistic MHD simulations in tori (Bucciantini and Del Zanna, 2013; Bugli, Del Zanna, and Bucciantini, 2014; Tomei et al., 2020; Tomei et al., 2021; Del Zanna, Tomei, et al., 2022) or in thin accretion disks (Vourellis and Fendt, 2021), showing how the dynamo is a very promising process to recover the magnetic field strength and topology required to match the observational values and the theoretical limits of the BZ launching mechanism.

1.4 Outline of the Thesis

In this thesis we address the question of how the magnetic field required for jet launching is generated and maintained by a dynamo process.

Chapter 2

is a review of the theoretical concepts used in this work. We briefly discuss the theory of non-relativistic MHD, adapted in order to include non-ideal effects like the magnetic diffusivity and the mean-field dynamo, and the theory of ideal special-relativistic MHD. Finally, we discuss the basic ideas behind the jet launching mechanisms in astrophysics.

Chapter 3

describes the numerical aspects of this work. First, we describe the PLUTO code and the implementation of the mean-field dynamo. Then we discuss the initial and boundary conditions adopted in the jet launching simulations of this thesis. Finally we discuss the general features of the dynamo and diffusivity model adopted in this thesis.

Chapter 4

compares a selected choice of Riemann solvers (HLL, HLLC, HLLD, HLLEM and GFORCE) for the relativistic MHD equations. We tested, through a rigorous set of numerical benchmarks, the accuracy, robustness and stability of the numerical algorithms described in this chapter. This chapter is based on the published work of Mattia and Mignone (2022).

Chapter 5

performs the first investigation of a non-isotropic dynamo model in the context of jet launching simulations. By adopting a toy anisotropic dynamo model, we have disentangled the effects of the single dynamo components and their role in the launching process. This chapter is based on the published work of Mattia and Fendt (2020a).

Chapter 6

presents a consistent non-isotropic accretion disk dynamo model, based on an analytical solution of the mean-field dynamo theory. By applying a more consistent model we are able to link the strength and anisotropy of both the mean-field dynamo and the magnetic diffusivity to a single parameter, the Coriolis number. This chapter is based on the published work of Mattia and Fendt (2020b).

Chapter 7

shows a quantitative study of the feedback of the magnetic field on the mean-field dynamo in the context of jet launching simulations. We also present a more consistent feedback model which incorporates the suppression of the turbulence on both the mean-field dynamo and the magnetic diffusivity. This chapter is based on a paper submitted to the Astrophysical Journal Mattia and Fendt (2022).

Chapter 8

presents and summarizes the final results of the thesis and the plans for future research.

Chapter 2

Theoretical Background

In this chapter we describe the fundamental theoretical concepts about the MHD equations and Jet launching theory that will be used in this thesis. The chapter is structured as follows. In Section 2.1 we describe the fundamental ideal MHD equations, while in Section 2.2 we extend the MHD formalism to non-ideal mean-field theory. In Section 2.3 we describe the MHD equations in the context of special relativity. Finally, in Section 2.4 we review the fundamental jet launching mechanisms.

2.1 Ideal MHD Equations

The non-relativistic MHD approximation (Bellan, 2006; Chiuderi and Velli, 2015) is based on the following assumptions:

- the plasma is charge-neutral (i.e., its characteristic lengths are longer than the Debye length);

- both ion and electrons cyclotron periods are much shorter than the plasma timescale, i.e., the time required for the plasma to undergo substantial changes;

- the plasma is collisional and a gas temperature can be defined;

- the plasma characteristic velocities (i.e., fluid, sound and Alfvén speed) are non relativistic, i.e., slow compared to the speed of light.

Under those assumptions, the set of MHD equations accounts for the conservation of mass, momentum, total energy and magnetic field. For the sake of convenience, we use physical units such that $c = 4\pi = 1$. The mass conservation is defined by the continuity equation:

$$\frac{\partial \rho}{\partial t} + \nabla \cdot (\rho \mathbf{v}) = 0, \tag{2.1}$$

where ρ and $\mathbf{v}$ are, respectively, the fluid density and velocity. The momentum is conserved through the Euler's equation (including the magnetic forces)

$$\frac{\partial \rho \mathbf{v}}{\partial t} + \nabla \cdot \left[\rho \mathbf{v v} + \left(p + \frac{\mathbf{B} \cdot \mathbf{B}}{2} \right) \mathsf{I} - \mathbf{B B} \right] + \rho \nabla \Phi_{\mathrm{g}} = 0, \tag{2.2}$$

where p is the fluid pressure, $\mathbf{B}$ is the magnetic field and ϕ_{g} is the gravitational potential. In this thesis the gravitational potential Φ_{g} is provided by a central object

mass M, i.e. $\Phi_g = -GM/R$. The conservation of total energy (i.e., thermal, kinetic, magnetic and gravitational) consists in

$$\frac{\partial e}{\partial t} + \nabla \cdot \left[\left(\frac{\rho v^2}{2} + \frac{\Gamma}{\Gamma - 1} p + \rho \Phi_g \right) \mathbf{v} + \mathbf{E} \times \mathbf{B} \right] = \Lambda_{\text{cool}}, \tag{2.3}$$

where the total energy is defined as

$$e = \frac{p}{\Gamma - 1} + \frac{\rho v^2}{2} + \frac{B^2}{2} + \rho \Phi_g, \tag{2.4}$$

assuming an ideal equation of state. The electric field (whose contribution is negligible in the momentum equation) is defined by $\mathbf{E}$, while Λ_{cool} consists in a generic cooling term.

The polytropic index is set to $\Gamma = 5/3$ in all the jet launching simulations of this thesis. Finally, the temporal evolution of the electromagnetic field is taken into account by a subset of the Maxwell's equations:

$$\begin{aligned} \nabla \cdot \mathbf{B} &= 0, \\ \nabla \times \mathbf{E} &= -\frac{\partial \mathbf{B}}{\partial t}. \end{aligned} \tag{2.5}$$

In the non-relativistic MHD approximation, the temporal variations of both electric field and electric charge are negligible. Thus, the continuity equation for the electric charge and the Gauss's law can be neglected. Moreover, the Ampere's law can be rearranged into:

$$\nabla \times \mathbf{B} = \mathbf{J}. \tag{2.6}$$

In the non-relativistic MHD approximation the electric field can be fully described by the Ohm's law. In the ideal MHD (and ideal RMHD) approximation, we get:

$$\mathbf{E} = -\mathbf{v} \times \mathbf{B}. \tag{2.7}$$

For the sake of convenience we split the MHD variables into primitive $(\rho, \mathbf{v}, p, \mathbf{B})$ and conserved variables $(\rho, \mathbf{m}, e, \mathbf{B})$, where the momentum $\mathbf{m}$ is defined as

$$\mathbf{m} = \rho \mathbf{v}. \tag{2.8}$$

In the non-relativistic regime, the conversion between primitive and conserved variables can be performed analitically.

2.2 Non-Ideal MHD Equations

In the ideal MHD approximation the plasma is supposed to be a perfect conductor. A direct consequence is the Alfvén theorem (Alfvén, 1942), which states that, in case of infinite conductivity, the magnetic field is frozen into the fluid and has to move along with it. An even stronger consequence is that, in a perfectly conducting fluid, the flux through a co-moving surface is conserved (Chiuderi and Velli, 2015).

However, microscopic interactions between charged particles and between neutral and charged particles may reflect on the larger scales as non-ideal MHD processes.

In this thesis we assume that the non-ideal processes descend from the turbulence within the accretion disk. The main idea behind the mean field theory (Moffatt, 1978; Krause and Raedler, 1980) is that both the velocity and the magnetic field can be split into mean values and fluctuation values:

$$\mathbf{B} = \overline{\mathbf{B}} + \mathbf{B}' \qquad \mathbf{v} = \overline{\mathbf{v}} + \mathbf{v}'. \tag{2.9}$$

The induction equation becomes:

$$\frac{\partial \overline{\mathbf{B}}}{\partial t} = \nabla \times (\overline{\mathbf{v} \times \mathbf{B}}). \tag{2.10}$$

By expanding Equation (2.10) we get:

$$\frac{\partial \overline{\mathbf{B}}}{\partial t} = \nabla \times (\overline{\mathbf{v}} \times \overline{\mathbf{B}} + \overline{\mathbf{v}' \times \mathbf{B}'}), \tag{2.11}$$

since $\overline{\overline{\mathbf{v}} \times \mathbf{B}'} = \overline{\mathbf{v}' \times \overline{\mathbf{B}}} = 0$. The electric field can be then defined as

$$\mathbf{E} = -\mathbf{v} \times \mathbf{B} - \overline{\mathbf{v}' \times \mathbf{B}'} = -\mathbf{v} \times \mathbf{B} - \mathcal{E}, \tag{2.12}$$

where, since we have confined all the fluctuation terms into $\mathcal{E}$, we can assume from now on $\mathbf{B} = \overline{\mathbf{B}}$ and $\mathbf{v} = \overline{\mathbf{v}}$

The solution of the induction equation depends on the explicit form of $\mathcal{E}$. The mean-field dynamo theory (Krause and Raedler, 1980) suggests that we can express $\mathcal{E}$ as a (convergent) series expansion of the mean magnetic field. By expanding $\mathcal{E}$ into its series components we obtain:

$$\mathcal{E}^i = \alpha^{ij} B_j + \eta^{ijk} \frac{\partial B_j}{\partial x^k} + \dots. \tag{2.13}$$

Thus, we can rewrite the induction equation as

$$\frac{\partial \mathbf{B}}{\partial t} = \nabla \times (\mathbf{v} \times \mathbf{B} + \alpha \cdot \mathbf{B} - \eta \cdot \mathbf{J}). \tag{2.14}$$

The system of Equations (2.1-2.3 and 2.14) can be written in the standard conservation form

$$\frac{\partial \mathcal{U}}{\partial t} + \sum_k \frac{\partial \mathcal{F}^k}{\partial x^k} = \mathcal{S}(\mathcal{U}), \tag{2.15}$$

(where $k = x, y, z$) together with the divergence-free condition of magnetic field

$$\nabla \cdot \mathbf{B} = 0. \tag{2.16}$$

The conserved variables are defined as $\mathcal{U} = (\rho, \rho\mathbf{v}, e, \mathbf{B})$. Here, for the sake of simplicity, the cooling term Λ_{cool} is set to be equal to the non-ideal (i.e. diffusive and dynamo) contribution of the electric field to the energy equation, as in Sheikhnezami et al. (2012) and Stepanovs and Fendt (2014).

2.3   Ideal Relativistic MHD Equations

In order to write the Relativistic MHD equations, we consider an ideal relativistic magnetized fluid (Lichnerowicz, 1976; Anile, 2005) in flat space-time (with Minkowski metric tensor $\eta^{\mu\nu} = \mathrm{diag}(-1, 1, 1, 1)$)) described by the conservation of mass,

$$\partial_\mu(\rho u^\mu) = 0, \tag{2.17}$$

energy-momentum,

$$\partial_\mu[(\rho h + b^2)u^\mu u^\nu - b^\mu b^\nu + p\eta^{\mu\nu}] = 0, \tag{2.18}$$

and the Maxwell dual tensor,

$$\partial_\mu(u^\mu b^\nu - u^\nu b^\mu) = 0. \tag{2.19}$$

Here we follow the standard convention that Latin indices take values for spatial components while Greek indices label space and time components. The quantities introduced in Equations (2.17)-(2.19) are, respectively, the fluid rest mass density ρ, the four-velocity u^μ, the relativistic specific enthalpy h, the covariant magnetic field b^μ and the total pressure (thermal + magnetic) $p = p_g + |b^2|/2$. Note that, as for the non-relativistic equations, the speed of light $c = 1$ and a factor $\sqrt{4\pi}$ has been reabsorbed in the definition of b^μ. The four-vector u^μ and the fluid velocity v^i are related through

$$u^\mu = \gamma\, (1, v^i), \tag{2.20}$$

where $\gamma = (1 - v^2)^{-1/2}$ is the Lorentz factor, while the relation between b^μ and the laboratory magnetic field B^i is

$$b^\mu = \gamma[\mathbf{v} \cdot \mathbf{B}, \frac{B^i}{\gamma^2} + v^i(\mathbf{v} \cdot \mathbf{B})]. \tag{2.21}$$

The square modulus of the covariant magnetic field can be written as

$$b^2 = \frac{B^2}{\gamma^2} + (\mathbf{v} \cdot \mathbf{B})^2. \tag{2.22}$$

The system of RMHD equations is closed through an appropriate equation of state. Throughout the thesis we assume an ideal gas equation of state, described by a constant $\Gamma-$law

$$h = 1 + \frac{\Gamma}{\Gamma - 1}\frac{p_g}{\rho}, \tag{2.23}$$

where Γ is the adiabatic exponent, although alternative equations, as in Mignone and Jonathan C. McKinney (2007), may be adopted.

The system of Equations (2.17)-(2.19) can be written in the conservation form described in Equation (2.15), with $\mathcal{S}(\mathscr{U}) = 0$ The conserved variables and the fluxes

along the direction k are, respectively,

$$\mathcal{U} = \begin{pmatrix} D \\ m^i \\ B^i \\ E \end{pmatrix}, \qquad \mathcal{F}^k = \begin{pmatrix} Dv^k \\ m^i v^k + p\delta^{ik} - b^i B^k/\gamma \\ v^k B^i - v^i B^k \\ m^k - Dv^k \end{pmatrix}, \qquad (2.24)$$

where the quantities D, m^i and E stand, respectively, for the laboratory mass density, the momentum density and the energy density (net of mass contribution).

In addition to the conserved variables $\mathcal{U}$, the set of primitive variables $\mathcal{V} = (\rho, v^i, B^i, p_g)$ is also routinely employed. While the conversion from primitive to conserved variables can be recovered analytically through

$$\begin{aligned} D &= \rho\gamma, \\ m^i &= (\rho h\gamma^2 + B^2)v^i - (\mathbf{v} \cdot \mathbf{B})B^i, \\ E &= \rho h\gamma^2 - p_g - \rho\gamma + \frac{B^2}{2} + \frac{v^2 B^2 - (\mathbf{v} \cdot \mathbf{B})^2}{2}, \end{aligned} \qquad (2.25)$$

primitive variables must be computed numerically from the conserved quantities (see, e.g., Del Zanna, Bucciantini, and Londrillo 2003; Noble et al. 2006; Mignone and Jonathan C. McKinney 2007). In this thesis we follow the approach of Mignone and Jonathan C. McKinney (2007).

2.4 Jet Launching Mechanisms

2.4.1 Blandford-Znajek Mechanism

If the central object is a spinning black hole, the rotational energy can be transferred into the magnetic field and escape as Poynting flux (see Figure 2.1). The theory of R. D. Blandford and Znajek (1977) assumes a force-free magnetosphere that should be in equilibrium with the spinning accreting black hole. A key ingredient of the BZ mechanism is the ergosphere (Ruiz et al., 2012), i.e., the region in which an object cannot appear stationary to an outside observer at a great distance. An accretion disk magnetic field threading the black hole horizon is also assumed.

The rotating black hole (and therefore the ergosphere) twists the magnetic field, producing an electromagnetic flux which extracts energy and angular momentum from the space–time. In the membrane paradigm of Thorne, R. H. Price, and Mac-Donald (1986), the black hole event horizon is replaced by the surface of a rotating magnetized star with finite resistivity. However, numerical simulations showed how the ergosphere is an unavoidable ingredient in order to launch a jet through the BZ mechanism (while in the membrane paradigm only the field lines that cross the horizon are rotating).
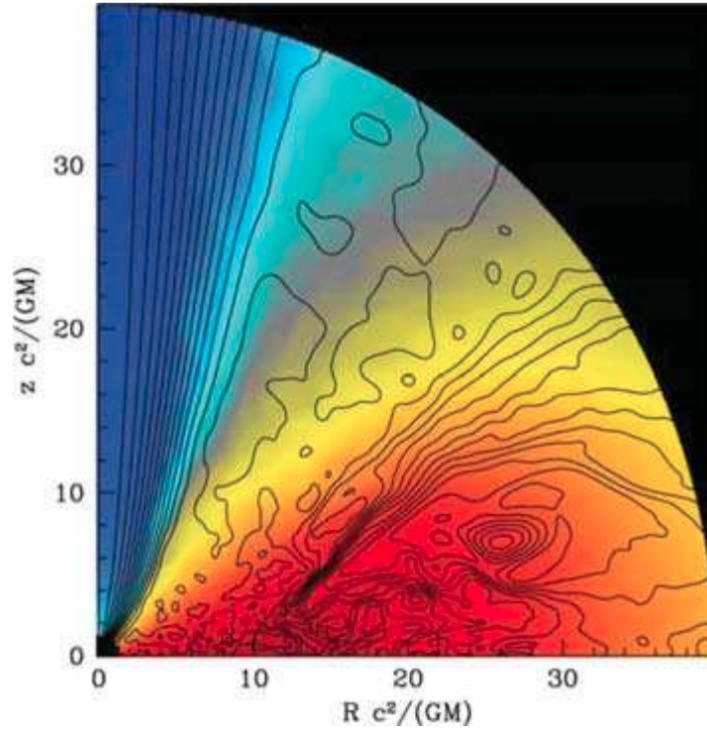
FIGURE 2.1: Example of Blandford-Znajek jet. Credit: J. C. McKinney
and Narayan (2007).

2.4.2 Blandford-Payne Mechanism

Since jets are formed not only from a black hole, the Blandford-Znajek process can-
not describe the totality of the astrophysical jets. In 1982, R. D. Blandford and Payne
(1982) proposed an alternative jet launching mechanism in which the outflow is
launched from the surface of the accretion disk.

The Blandford-Payne mechanism does not necessarily require a black hole as
accreting object. However, a thin Keplerian (e.g., the rotation of the disk scales as
$\propto R^{1/2}$, where R is the distance from the central accreting object) disk must be con-
sidered. By adopting the same approach of (R. D. Blandford, 1976) (and replacing
the speed of light with the Alfvén speed), it is possible to obtain that the magnetic
field should scale as $B \propto R^{-5/4}$. Since the disk rotates, the poloidal magnetic field
start rotating as well. The gas elements on the magnetic field lines start behaving
like beads on a rigid rotating wire. As the magnetic field (which can be seen as the
wire) gets twisted by the disk rotation, the fluid elements (the beads) that are located
at a large distance from the central object will be pushed by the magnetocentrifugal
force (a schematic display is shown on Figure 2.2) .

Considering a small volume element inside the disk, whose distance from the
central object is (r_0, z_0) in cylindrical coordinates (r, z), its potential (gravitational +
centrifugal) can be written as

$$\phi(r,z) = -\frac{GM}{r_0} \left[\frac{1}{2} \left(\frac{r}{r_0} \right)^2 + \frac{r_0}{(r^2 + z^2)^{1/2}} \right] = const., \qquad (2.26)$$

where in Figure 2.3, for the sake of simplicity, G, M and r_0 have been set to 1.
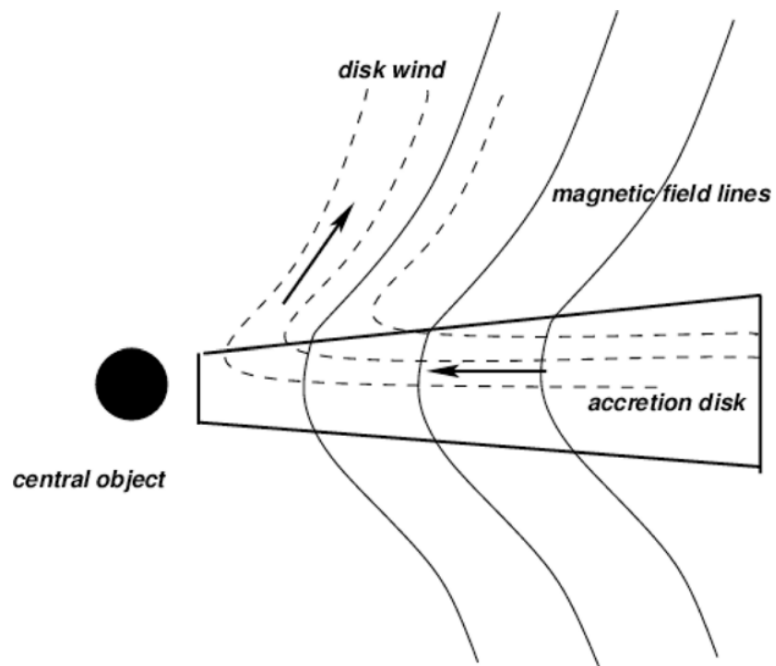
FIGURE 2.2: Schematic display of the Blandford-Payne launching mechanism. Credit: Sheikhnezami et al. (2012).
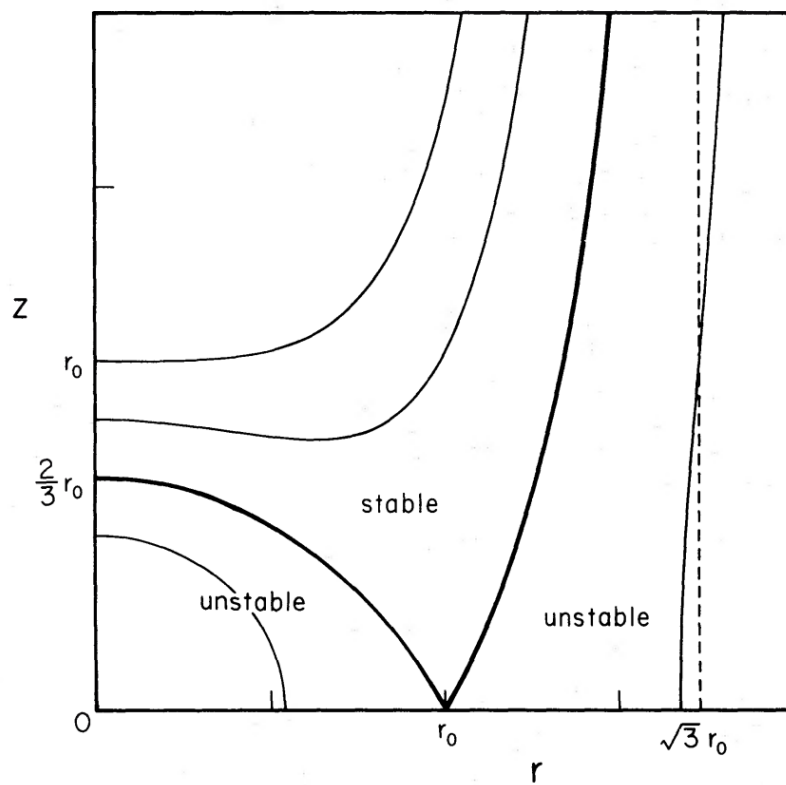
FIGURE 2.3: Isopotential surfaces of the potential ϕ (see Equation 2.26). Credit: R. D. Blandford and Payne (1982).
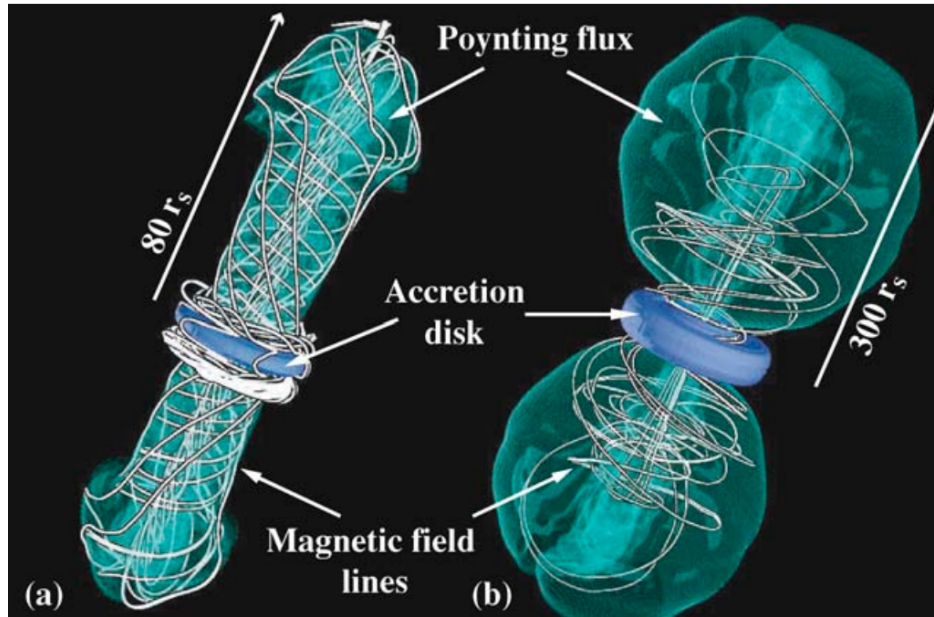
FIGURE 2.4: Examples of tower jet. Credit: Kato (2007).

The gradient of the potential expressed in Equation (2.26) determines the force acting on the volume element in case of launching from the disk surface. As shown in Figure 2.3, if the field line inclination is greater than $60°$ then the equilibrium is stable. Conversely, if the field lines have an inclination of less than $60°$ with the disk surface, the volume element will be either launched as outflow from the disk or accreted towards the central object. By including the thermal pressure effects, the maximum angle necessary to launch an outflow is $\sim 78°$ (Pelletier and Pudritz, 1992).

2.4.3   Tower Jets

The "magnetic tower" (see Figure 2.4) launching mechanism was presented first by Lynden-Bell and Boily (1994) and later by Lynden-Bell (1996), Lynden-Bell (2003), and Kato (2007). The main ingredients of this launching mechanism are an accretion disk and a poloidal disk magnetic field whose topology is looped. The footpoints of the magnetic field loops are anchored to the accretion disk surface at different radii.
Another important component is a force-free state corona surrounding the accretion disk. Because of the disk rotation, the magnetic pressure caused by the toroidal field (which is a consequence of both the rotation and the magnetic loops) is amplified and it pushes the poloidal magnetic field lines outwards until an equilibrium between the magnetic pressure and the external pressure is reached. At that point, the field lines cannot be pushed outwards any further and therefore they can expand only in the vertical direction. If the pressure becomes too large (Kato, Mineshige, and Shibata, 2004) the jet, which may still get launched, collapses into a very complex quasi-steady state. Magnetic towers have also been investigated in laboratory astrophysics experiments (see, e.g., Lebedev et al. 2005), finding good agreement with the theory of Lynden-Bell (1996).

Chapter 3

Numerical Methods

All the simulations described in this and the following chapters are performed with the PLUTO code (Mignone, Bodo, Massaglia, et al., 2007). In this chapter we describe the main structure and the numerical algorithms used in this thesis. In Section 3.1 we describe the structure of the PLUTO code and the numerical algorithms used in this thesis. In Section 3.2 we describe the implementation of the mean-field dynamo term in the PLUTO code. The numerical tests used as code verification are described in Section 3.3. Then, in Section 3.4, we describe the numerical setup used for the jet launching simulations.

3.1 The PLUTO Code

The PLUTO code (Mignone, Bodo, Massaglia, et al., 2007; Mignone, Zanni, et al., 2012; Mignone, Vaidya, et al., 2020) is a finite-volume code built on Godunov-type high resolution shock capturing schemes (Godunov, 1959). The code is designed to solve a set of partial differential equations in the form of conservation law:

$$\frac{\partial \mathscr{U}}{\partial t} = -\nabla \cdot \mathsf{F}(\mathscr{U}) + \mathcal{S}(\mathscr{U}). \tag{3.1}$$

In the finite volume formulation, volume averages are evolved in time. While the variables evolved are the conservative ones $\mathscr{U}$, the fluxes are computed from the primitive variables $\mathcal{V}$ (such as velocity or pressure). The reasons behind such choice are the following: first of all it is much more practical to compute the fluxes using the primitive variables; in addition, some physical constraints (e.g., subluminal speed or pressure positivity) can be ensured only by looking at the primitive variables.

The numerical integration of Equation (3.1) is performed in 4 steps, as shown in Figure 3.1, which consist in a reconstruct-solve-average strategy. The very first step is the conversion from conservative to primitive quantities (in order to perform the next steps more easily). Such conversion, if the the regime is relativistic and magnetized, is numerical due to the high non-linearity of the equations:

$$\mathscr{U} \to \mathcal{V}. \tag{3.2}$$

The subsequent step is the reconstruction: starting from the primitive variables defined at the center of each cell, the left and right states (which correspond to the cell faces) are computed through an interpolation routine (LeVeque et al., 1998; E. Toro, 2009):
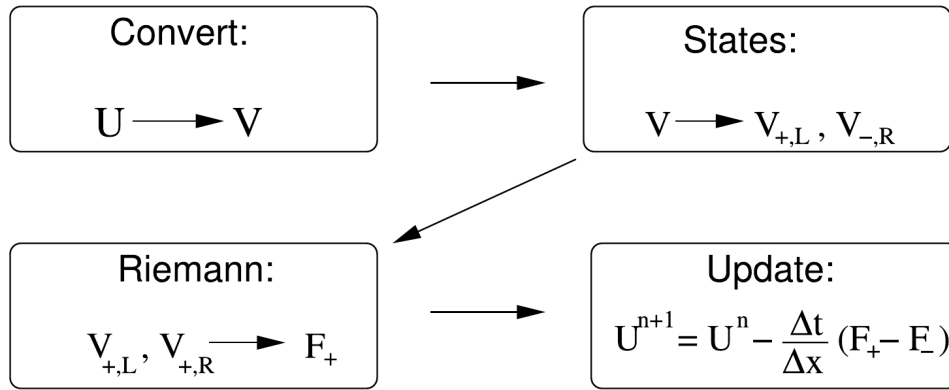
FIGURE 3.1: Structure of the PLUTO code. Credit: Mignone, Bodo, Massaglia, et al. (2007).

$$\mathcal{V}_{\pm,L/R} = \mathcal{I}(\mathcal{P},\mathcal{V}), \tag{3.3}$$

where $\mathcal{P}$ is a piecewise polynomial approximation. The reconstruction step must satisfy several constraints, e.g., monotonicity (in order to avoid spurious oscillations near discontinuities), pressure positivity and subluminal speed (in the relativistic case). In this thesis several reconstruction methods are adopted. In particular, for the investigation of jet launching we used the piecewise parabolic method (Colella and Woodward, 1984) for spherical coordinates (Mignone, 2014) and the default limiter of the PLUTO code, which corresponds to a combination of different limiters. More specifically, the monotonized central (van Leer, 1977) flux limiter is adopted for the density, the van Leer (van Leer, 1974) flux limiter is adopted for both velocity and magnetic field and the MinMod (Roe, 1986) flux limiter is adopted for the pressure. Conversely, for the investigation of numerical algorithms (i.e., Riemann solvers or the numerical benchmarks for the mean-field dynamo), a flat or linear interpolation is adopted (LeVeque et al., 1998; E. Toro, 2009) with, respectively, monotonized central and van Leer flux limiters for the linear interpolation.

Once the left and right states are computed, the code recovers the numerical fluxes by solving the Riemann problem at the zone interfaces:

$$\mathsf{F}_{\pm} = \mathsf{F}_{\pm}(\mathcal{V}_{\pm,L}, \mathcal{V}_{\pm,R}). \tag{3.4}$$

The Riemann solvers studied in the relativistic case are fully described in Chapter 4, while we have adopted two different Riemann solvers in the jet launching simulations. While in Chapters 3 (in order to test the impementation), 5 and 6 we employed a standard HLL solver (Harten, Lax, and Leer, 1983; E. Toro, 2009), in Chapter 7 we started with the HLLC Riemann solver (E. F. Toro, Spruce, and Speares, 1994; S. Li, 2005) and then switched to the HLL solver whether numerical issues have been encountered.

The last step is temporal evolution which, starting from a set of conservative quantities at a given time t, calculates the same set of variables at time $t + \delta t$, where δt is the time step:

$$\mathscr{U}^n, \mathsf{F}_\pm \to \mathscr{U}^{n+1}. \tag{3.5}$$

As for the previous steps, we employed different numerical methods depending on the context. The jet launching simulations are performed by using a 3rd-order Runge-Kutta method (S. Gottlieb, C. Shu, and Tadmor, 2001), while for the study of the Riemann solvers and the implementation of the dynamo we adopted a 1st order Euler scheme and a 2nd order Runge-Kutta scheme (S. Gottlieb, C. Shu, and Tadmor, 2001), respectively for the 1D and the 2-3D tests.

Explicit time stepping requires that any characteristic signal cannot cross more than one computational zone in a single time step. Such constraint is given by the Courant-Friedrich-Lewy (CFL, Courant, Friedrichs, and Lewy 1928) condition:

$$\Delta t = \mathrm{C}FL \cdot N_d \cdot \min\left(\frac{\Delta x_d}{|\lambda_d|}\right), \tag{3.6}$$

where λ_d and Δx_d are, respectively, the largest characteristic velocity and the grid spacing for each cell in each direction and N_d is the number of spatial dimensions. Unless otherwise stated, we set the maximum CFL number to 0.8, 0.4, and 0.25, respectively, for 1D, 2D, and 3D computations. We point out that additional limitations may come because of the parabolic diffusive term in the induction equation.

So far we have considered only the evolutionary equations. However, the absence of magnetic monopoles should be always preserved by keeping the divergence of the magnetic field to 0. The divergence-free constraint of magnetic field is controlled through the constrained transport method. In particular, in Chapter 4 we adopted the CT-Contact scheme by Gardiner and Stone (2005), while for the dynamo simulations we applied the method of upwind constrained transport UCT-HLL by Londrillo and del Zanna (2004) (with a slight modification in order to incorporate the dynamo, see the following section) to compute the electromotive force at the zone edges.

3.2   Implementation of the Dynamo

In order to reproduce the same results of Stepanovs, Fendt, and Sheikhnezami (2014) and Fendt and Gaßmann (2018), the mean-field dynamo term has been implemented in the PLUTO code (version 4.3).

3.2.1   Numerical Details

The numerical implementation of the dynamo term in PLUTO, version 4.3, is different from the one in PLUTO, version 4.0 (the version adopted in Stepanovs, Fendt, and Sheikhnezami 2014; Fendt and Gaßmann 2018). The main reason why the same term has to be implemented in a different way is the computation of the resistive flux. In PLUTO 4.0 the flux is cell-centered, and only at later steps it becomes staggered. Therefore the resistive term (which is parabolic) and the dynamo term (which is hyperbolic) can be treated in the same way. In PLUTO 4.3 the resistive term is staggered in a different part of the code and is computed through different numerical

recipes; therefore mixing the resistive (parabolic) term and the dynamo (hyperbolic) term is not possible anymore. Thus, the additional dynamo components in the flux term have been incorporated during the update of the hyperbolic terms as an additional term of the electric field in the energy and induction equations. Moreover the dynamo term has been taken into account while computing the total ElectroMotive Force (EMF), following D. S. Balsara and Spicer (1999). For the sake of simplicity we updated this part only for 2-dimensional simulations, although the extension to full 3D domain can be implemented in the same fashion. This implementation is based on an arithmetic average of the staggered dynamo term:

$$\text{EMF}_{z,\text{dyn}} = -\frac{1}{4}\left(B_{z,i,j} + B_{z,i+1,j} + B_{z,i,j+1} + B_{z,i+1,j+1}\right)\alpha_z. \tag{3.7}$$

3.2.2 Stability Analysis

Because of the exponential increase of the magnetic field, which is a natural consequence of the dynamo term, testing the validity of the implementation can be challenging. In order to understand whether a generic numerical benchmark involving the dynamo term can lead to a stable configuration, we need to perform a stability analysis of the dynamo equations for a scalar constant (in time and space) α. We start from a 1D problem:

$$\begin{cases} \partial_t B_x &= 0, \\ \partial_t B_y &= -\alpha\partial_x B_z, \\ \partial_t B_z &= \alpha\partial_x B_y. \end{cases} \tag{3.8}$$

Given a solution $\mathbf{B}_0$ which solves the dynamo equations, we assume the magnetic field to be:

$$\mathbf{B} = \mathbf{B}_0 + \mathbf{B}_1 e^{i(kx-\omega t)}, \tag{3.9}$$

where $k \in \mathbb{R}$ and $\omega \in \mathbb{C}$. Since the dynamo equations are linear and $\mathbf{B}_0$ solves Equation (3.8), we can apply the dynamo equations only to the perturbation. This means that such analysis can be applied to every configuration that solves dynamo equations. Solving the derivatives we obtain:

$$\begin{cases} \omega B_{x,1} &= 0, \\ \omega B_{y,1} &= \alpha k B_{z,1}, \\ \omega B_{z,1} &= -\alpha k B_{y,1}. \end{cases} \tag{3.10}$$

The first equation (which shows the perturbation of B_x) can be neglected. The other two equations lead to the following dispersion relation:

$$\omega^2 = -\alpha^2 k^2 \rightarrow \omega = \pm i\alpha k, \tag{3.11}$$

which is unstable. Therefore, even for 1D dynamo solution, the exponential amplification of the magnetic field is imediately triggered. In order to overcome this problem ,the resistivity term can be taken into account. The full set of dynamo + resistivity equations (2D) is:

$$\begin{cases} \partial_t B_x = \alpha \partial_y B_z - \eta \partial_{xy} B_y + \eta \partial_{yy} B_x, \\ \partial_t B_y = -\alpha \partial_x B_z + \eta \partial_{xx} B_y - \eta \partial_{xy} B_x, \\ \partial_t B_z = \alpha \partial_x B_y - \alpha \partial_y B_x + \eta \partial_{xx} B_z + \eta \partial_{yy} B_z. \end{cases} \tag{3.12}$$

Now, given $\mathbf{B}_0$ a solution of dynamo + resistivity equation, we assume the magnetic field to be:

$$\mathbf{B} = \mathbf{B}_0 + \mathbf{B}_1 e^{i(kx+hy-\omega t)}, \tag{3.13}$$

where $k, h \in \mathbb{R}$ and $\omega \in \mathbb{C}$. Since the set of equations is linear and $\mathbf{B}_0$ is a solution, we can neglect it from the equations. Solving the derivatives we obtain:

$$\begin{cases} (i\omega - \eta h^2)B_x + \eta kh B_y + ih\alpha B_z = 0, \\ \eta kh B_x + (i\omega - \eta k^2)B_y + (-ik\alpha)B_z = 0, \\ -ih\alpha B_x + ik\alpha B_y + (i\omega - \eta k^2 - \eta h^2)B_z = 0. \end{cases} \tag{3.14}$$

The determinant of such system is:

$$\Delta = -i\omega(\alpha^2(h^2 + k^2)) - (\eta(h^2 + k^2) - i\omega)^2 = 0. \tag{3.15}$$

Solving for ω:

$$\omega = -i\eta(h^2 + k^2) \pm i\alpha\sqrt{h^2 + k^2}, \tag{3.16}$$

which is unstable only under certain conditions. We can determine whether the amplification of the magnetic field occurs by looking at the ratio between dynamo (α) and resistivity (η); a stable solution is reached when:

$$\frac{\alpha}{\eta} < \sqrt{k^2 + h^2}, \tag{3.17}$$

where $2\pi/\Delta x > \sqrt{k^2 + h^2} > 2\pi/L$ is the wave-number, L is the size of the domain and Δx is the size of a grid cell. The reason why we have such inequality is that for waves smaller than one cell size or larger than the domain, no amplification can take place. The upper limit $2\pi/\Delta x$ can be reduced by a factor of $\sim 3 - 4$, but since we are looking for the highest values of the wave number we will assume from now on $\sqrt{k^2 + h^2} = 2\pi/L$. For our numerical setup the stability condition turns out to be $\alpha/\eta < \pi$. This analysis is in agreement with the standard dynamo simulations, which showed a higher amplifications of the magnetic field for higher values of α.

3.3 Test Simulations Including the Dynamo

Some analytical solutions of the dynamo equation have been tested in order to see if the implementation of the mean-field dynamo in PLUTO 4.3 is able to reproduce the expected theoretical results. In order to neglect the hydrodynamics of the system (and to consider only the evolution of the magnetic field), the density is set to $\rho = 10^{12}$ while the velocity is set to $\mathbf{v} = 0$. We also consider an isothermal plasma, i.e., $p \propto \rho$ at every time. In this way we are able to get rid of the energy equation and
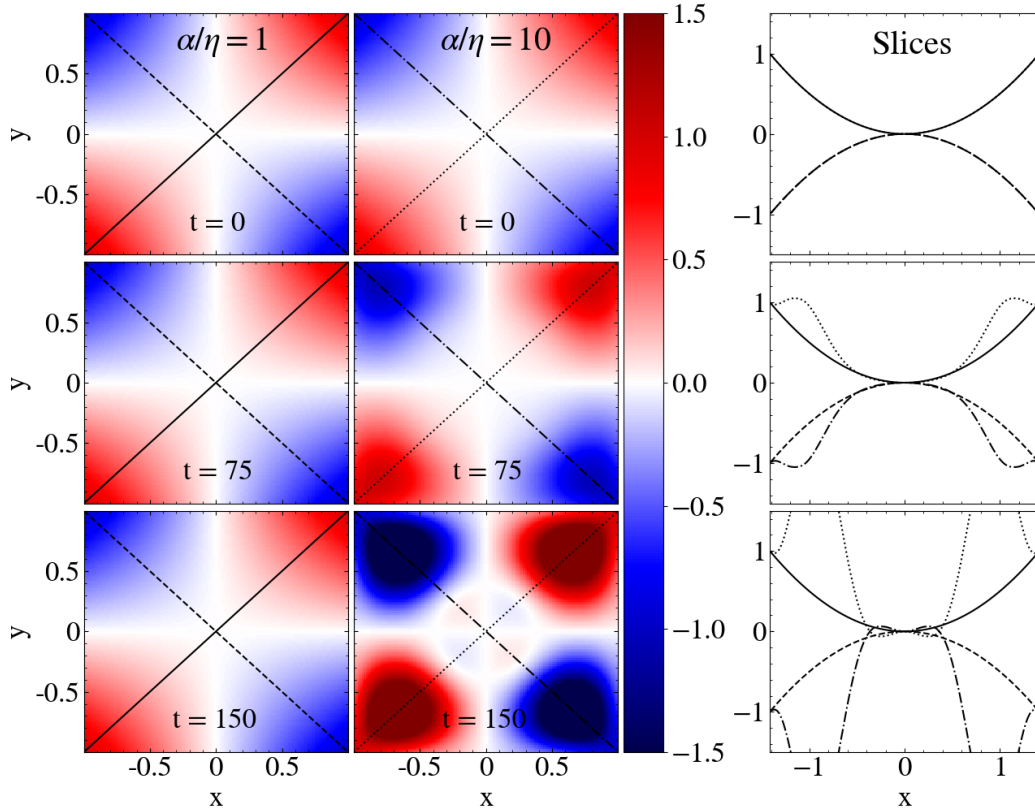
FIGURE 3.2: Evolution of the magnetic field component B_z for the linear increase benchmark. Shown on the left and middle panels are the evolution for different cases, while on the right panel are shown the 1D profiles along the two diagonals.

reduce both eventual numerical issues and computational time. The set of equations studied becomes:

$$\begin{cases} \partial_t B_x & = & \partial_y(\alpha_z B_z), \\ \partial_t B_y & = & -\partial_x(\alpha_z B_z), \\ \partial_t B_z & = & \partial_x(\alpha_y B_y) - \partial_y(\alpha_x B_x). \end{cases} \tag{3.18}$$

For all the simulations the domain is a cartesian grid $[N_x \times N_y] = [128 \times 128]$ where $x, y \in [-1, 1]$. The extension to non-cartesian grids and to higher order algorithms is automatically handled by the PLUTO code.

3.3.1   Linear Increase

The first case studied is the following:

$$\begin{cases} B_x & = & \alpha x(t+1), \\ B_y & = & -\alpha y(t+1), \\ B_z & = & xy, \end{cases} \tag{3.19}$$

where α represents the three dynamo components. The boundary conditions are determined by the analytical solution.
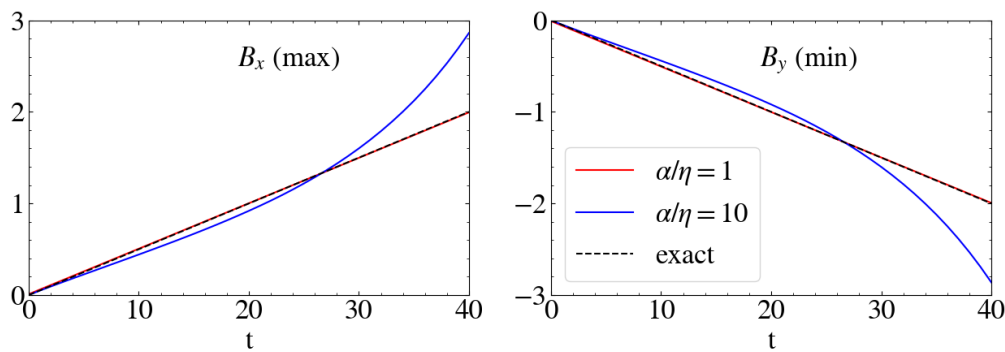
FIGURE 3.3: Comparison of the magnetic field components B_x (left panel) and B_y (right panel) between the numerical and the analytical solutions.

Two different simulations have been performed: in the first $\alpha/\eta = 10$ ($\alpha = 10^{-2}, \eta = 10^{-3}$) and therefore a strong amplification of the magnetic field should occur, while in the second $\alpha/\eta = 1$ ($\alpha = 10^{-2}, \eta = 10^{-2}$) and therefore the system should remain stable.

Results are shown in Figure 3.2 and exhibit the different behavior of the stable and unstable configurations. Up to time $t = 75$ it is possible to see how the two configurations show almost no differences. Then, around time $t = 75$, the amplification of the magnetic field in the unstable case starts to be relevant as the system evolves, in agreement with the linear analysis.

In order to check the accuracy of our implementation we have reported in Figure 3.3 a comparison between the two cases and the analytical solution at $t = 60$. The red line, which represents the case $\alpha/\eta = 1$ shows extremely good agreement, while the blue line, which represents the case $\alpha/\eta = 10$ deviates from the analytical solution. We point out that the unstable case is simply a different solution of the induction equation with an endless amplification of the magnetic field.

3.3.2 Constant Case

The second case studied is the following:

$$\begin{cases} B_x &= \cosh(x)\cos(y), \\ B_y &= -\sinh(x)\sin(y), \\ B_z &= 0. \end{cases} \tag{3.20}$$

We point out that this solution is a constant solution (no changes in time) and it has no dependence on α, therefore is suited to test the behavior of the numerical algorithms with different ratios between the mean-field dynamo and the magnetic diffusivity.

As shown in Figure 3.4, when $\alpha/\eta = 1$ (therefore below the stability critical value π), the system remains in equilibrium, while, for $\alpha/\eta = 10$ the magnetic field is exponentially amplified. Here the amplified magnetic field, around $t = 60$, starts to interfere with the boundary conditions (which are computed assuming a stable solution where no amplification of the magnetic field takes place). By applying
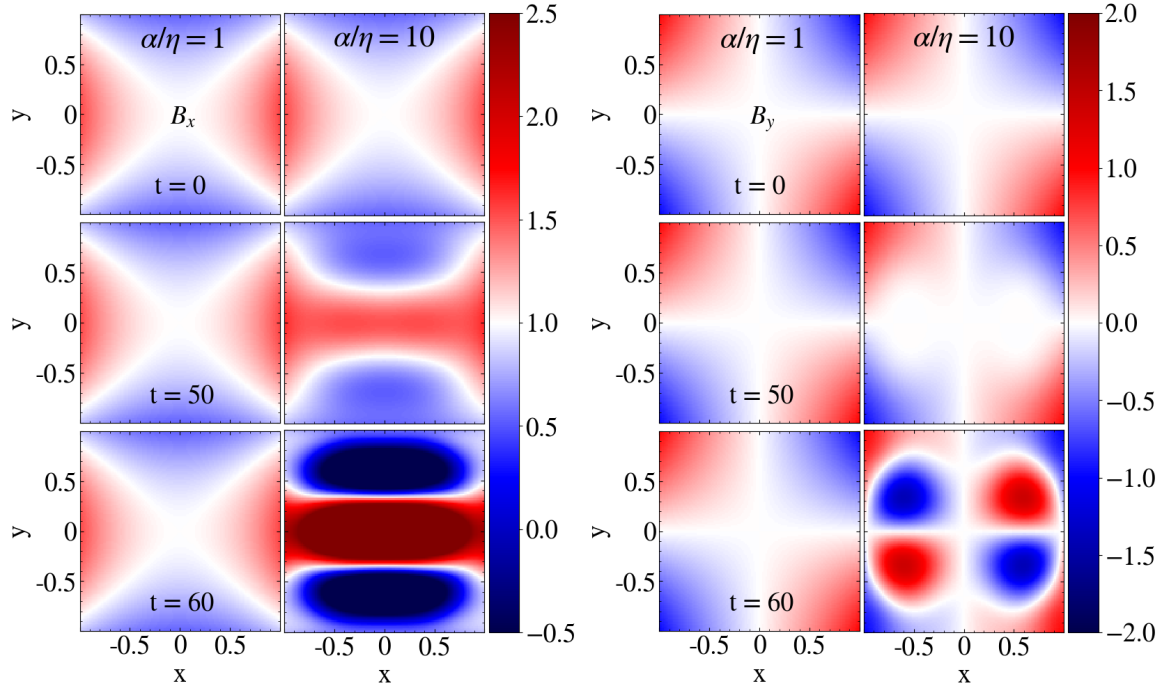
FIGURE 3.4: Temporal evolution of the components B_x (left panels) and B_y (right panels) for different cases of the constant case benchmark.

different boundary conditions for the magnetic field we would expect a different outcome in the outer domain.

3.3.3 The Impact of the Initial Conditions

Since the constant case benchmark solution does not depend on the dynamo, we have chosen it to briefly test the impact of the initial conditions (this section) and of the feedback models (Section 3.3.4). We first need to define the average magnetic energy density

$$E_{mag} = \frac{1}{2} \sum_{i,j} \frac{B_{i,j}^2}{N_x N_y} = \frac{1}{2} \sum_{i,j} \frac{\left(B_x^2 + B_y^2 + B_z^2 \right)_{i,j}}{N_x N_y}, \tag{3.21}$$

which will be used to determine if the amplification of the magnetic field occurs or not. In general we find that when the dynamo acts (i.e., the ratio α/η is above the critical value) it leads to an exponential increase of the (average) magnetic energy. For such configurations, we compute the growth rate of the magnetic energy a function of time assuming an exponential increase,

$$s = \frac{\log_{10} E_{mag}(t_2) - \log_{10} E_{mag}(t_1)}{t_2 - t_1}, \tag{3.22}$$

where for t_2 we choose the last time when $E_{mag} < 1000$ while t_1 is the first time when $E_{mag} > 10$.

TABLE 3.1: Main characteristics of the parameter runs described in Section 3.3.3.

α/η	10	10	10	10	1	1	1	1
r	0	0.1	0.2	0.4	0	0.1	0.2	0.4
Slope	0.044	0.045	0.045	0.045	0	0	0	0
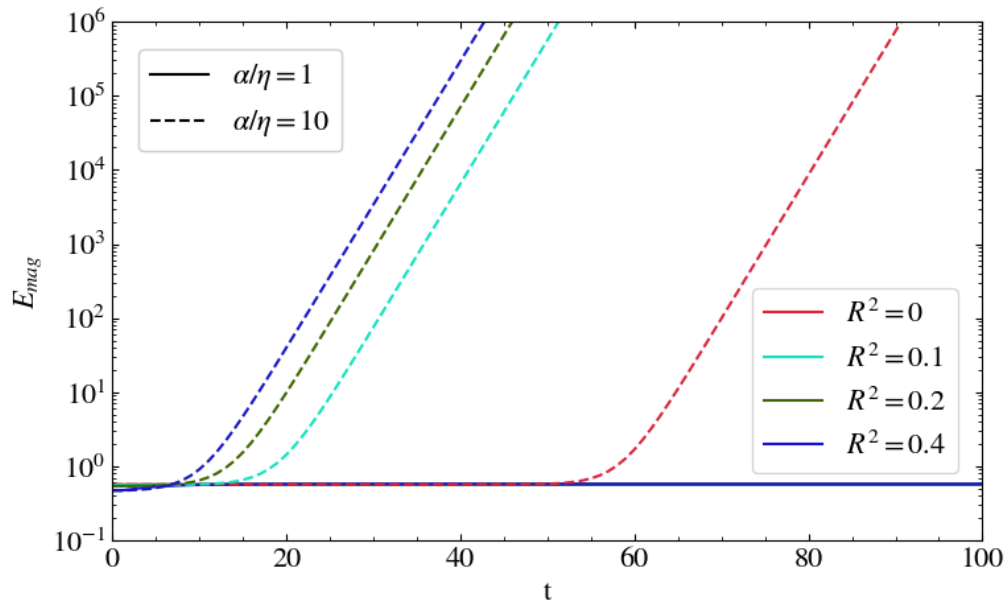
FIGURE 3.5: Evolution of the magnetic energy density of the different simulations for the constant case benchmark with different initial conditions.

The initial conditions for our parameter runs are as follows. All the quantities are set from the analytical solution described by Equation (3.20), but we have added the option to change the initial conditions in the center of the domain such that we obtain an artificial decrease of the central flux:

$$\mathbf{B}(x,y) = \mathbf{B}_{ex}\left(1 - e^{-\frac{x^2 + y^2}{r^2}}\right), \tag{3.23}$$

where $\mathbf{B}_{ex}(x,y)$ is the analytical solution Equation (3.20) and r is the radius within we decrease the flux (a "hole"). We have tested the impact of the initial conditions by changing the value of r. The different parameters are summarized in Table 3.1, while the evolution of the magnetic energy density is reported in Figure 3.5.

As expected, the cases with $\alpha/\eta = 1$ show no amplification of the magnetic field over time. Conversely, the cases for which the amplification occurs show a very similar evolution growth rate (with deviations $\sim 2\%$). Because of the different initial conditions, the amplification occurs at different times. More specifically, a

larger "hole" leads to a faster amplification of the magnetic field, i.e., the amplification starts earlier. The reason behind such difference lies in the fact that a different magnetic field distribution leads to a different amplification in the early stages of the dynamo. However, this difference is related only to the time at which the amplification starts and not to the growth rate of the magnetic energy.

3.3.4   Quenching Models

The constant case benchmark can also be used to test the role of the quenching of the dynamo term. Such study is not only necessary to investigate te feedback of the magnetic field on the dynamo (see Chapter 7) but also to test the implementation of a dynamo term which depends on the MHD variables.

The following quenching models have been implemented:

0 No quenching
$$\alpha = \alpha_0; \tag{3.24}$$

1 Sharp quenching
$$\alpha = \begin{cases} 0 & (E_{mag} > B_0), \\ \alpha_0 & (E_{mag} < B_0); \end{cases} \tag{3.25}$$

2 Standard quenching
$$\alpha = \frac{\alpha_0}{1 + \dfrac{E_{mag}}{B_0}}; \tag{3.26}$$

3 Strong diffusivity quenching
$$\eta = \begin{cases} \eta_0 & (E_{mag} < B_0), \\ \eta_0 \dfrac{E_{mag}}{B_0} & (E_{mag} > B_0); \end{cases} \tag{3.27}$$

4 Smoothed quenching
$$\alpha = \begin{cases} 0 & (E_{mag} > B_0), \\ \alpha_0 \left(1 - \dfrac{E_{mag}}{B_0}\right) & (E_{mag} < B_0), \end{cases} \tag{3.28}$$

where α_0 represents the value of α at $t = 0$.

The evolution of the magnetic energy is shown n Figure 3.6. The "sharp" quenching model stops the amplification of the magnetic field if the local magnetic energy has overcome a threshold value: the result is that the average magnetic energy tends to such upper limit. After the local cells have triggered the quenching, the diffusivity should lead to a small decrease of the magnetic field, which is brought to lower values, for which the dynamo is triggered again and so on.

The standard quenching model has been applied with two values of B_0: it is possible to notice that for the lower value of B_0 the amplification of the magnetic field is triggered earlier than the model with higher B_0. One possible reason for this feature is that the standard quenching model starts to act almost immediately in
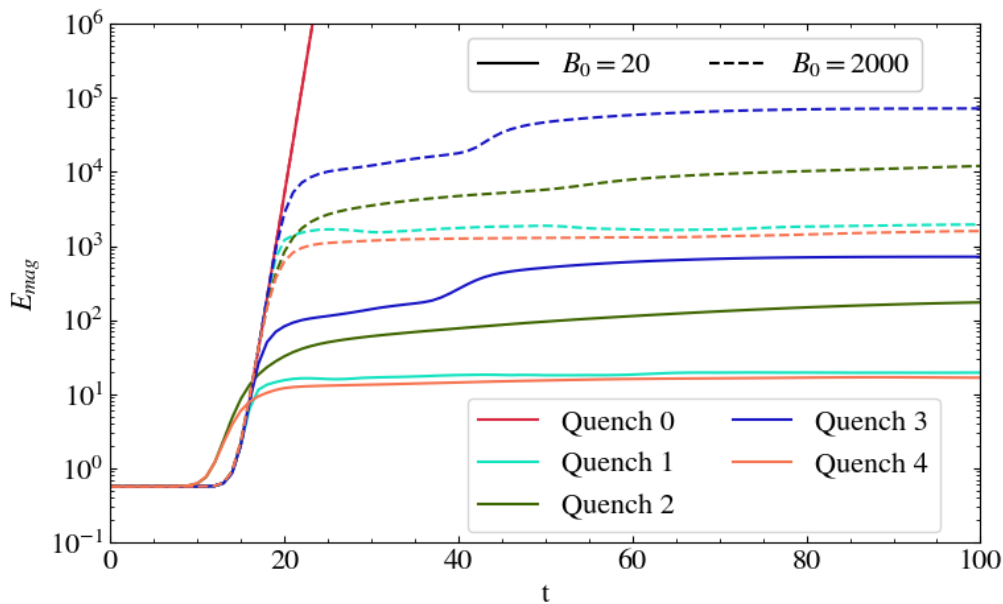
FIGURE 3.6: Evolution of the magnetic energy density of the different simulations for the constant case benchmark with different dynamo quenching methods.

some zones of the domain, leading to higher gradients in the magnetic field which increase the dynamo action and therefore the magnetic field amplification. This quenching model does not lead to a sudden suppression of the magnetic flux (obtained imposing $\alpha = 0$), so the magnetic energy has an increase (even if with much smaller growth rate) when $E_{mag} > B_0$. However, the magnetic energy starts to increase less rapidly (due to the quenching effect) until it reaches an almost constant value.

The "strong diffusivity" quenching is the one with the highest number of constraints. The lower constraint for the quenching model is due to the analytical form of the quenching: if $E_{mag} << B_0$ the diffusivity, according to this model, should drop leading to a large α/η ratio. On the other hand, a too sudden increase in the diffusivity would lead to a very rapid change in the time-step, even for a stable configuration. For this reason, unphysical high values of η should be avoided.

Finally, we notice how the smoothed quenching shows very similar features of the sharp quenching. This result is not unexpected, since both quenching models completely suppress the dynamo for high values of E_{mag}. The differences between these two quenching models lie in the feedback at lower values of the magnetic energy. While, by construction, the sharp quenching does not suppress the dynamo at lower values of E_{mag}, the smoothed quenching starts to act earlier, leading to an earlier saturation of the system.

3.3.5 Non-Isotropic Dynamo

The last numerical benchmarks concern the anisotropy of the dynamo. Here we are testing our implementation in case of a non-isotropic dynamo tensor. In order to test
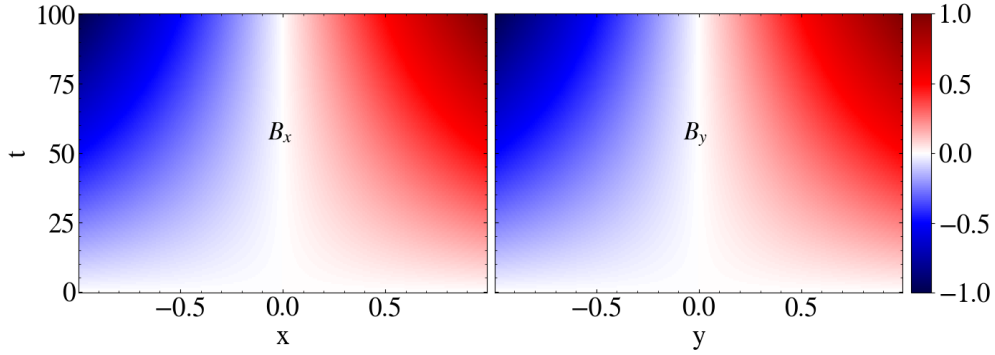
FIGURE 3.7: Evolution of the components B_x (left panel) and B_y (right panel) for the anisotropic benchmark with $\alpha_z \neq 0$.

if the single dynamo components are implemennted correctly, we have recovered three particular solutions of the dynamo equation in which two components of the dynamo tensor are set to zero. The first solution involves the component α_z:

$$\begin{cases} B_x & = & \alpha_z x t, \\ B_y & = & -\alpha_z y t, \\ B_z & = & xy. \end{cases} \tag{3.29}$$

We choose $\alpha_z = \eta = 0.01$ in order to test a stable case. We show the evolution of the components B_x and B_y in Figure 3.7. Both component of the magnetic field show great agreement with the exact solution, while the component B_z, as expected, does not change over time. The absolute average error on both components settles around 10^{-5}, confirming the validity of our implementation. The second and third tests involve the components B_x and B_y. Since the dynamo simulations in this thesis are in 2D assuming axisymmetry, we can investigate the $x-$ and $y-$components of the dynamo by rotating the domain by $90°$. The solution of the dynamo equation equation considered for this test is the following:

$$\begin{cases} \alpha_x & = & 0.01 \cdot \cos\theta_D, \\ \alpha_y & = & 0.01 \cdot \sin\theta_D, \\ B_x & = & y\cos\theta_D, \\ B_y & = & x\sin\theta_D, \\ B_z & = & \alpha_y t - \alpha_x t, \end{cases} \tag{3.30}$$

where the quantity θ_D determines which dynamo component is turned on/off. As in the previous benchmark, we set $\eta = 0.01$. We choose $\theta = 0, \pi/2$ in order to isolate the two dynamo components $\alpha_x = \alpha_y = 0.01$. The evolution of, respectively, B_x (left panel, $\theta_D = 0$) and B_y (right panel, $\theta_D = \pi/2$) is reported in Figure 3.8 and is shows perfect agreement with the analytical solution.

This series of benchmarks shows how the implementation of the dynamo allows a non-isotropic diagonal dynamo tensor.
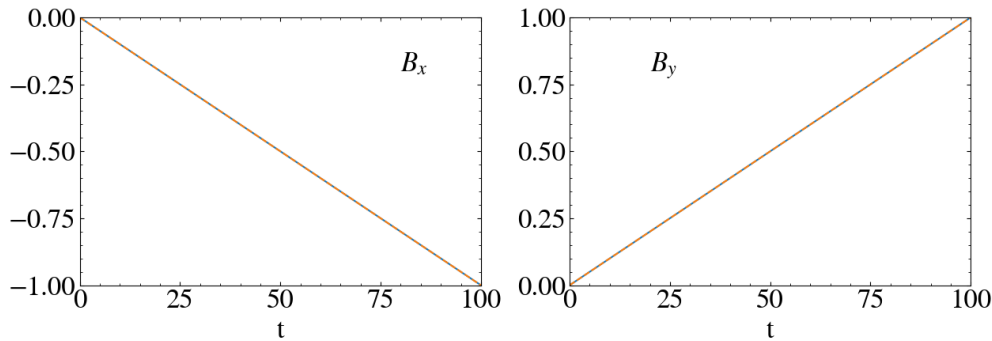
FIGURE 3.8: Evolution of the components B_x and B_y for the anisotropic benchmarks with $\alpha_z = 0$.

3.4 Numerical Setup for Jet Launching

In this section we describe the numerical setup adopted for the jet launching simulations (see Chapters 5, 6 and 7).

3.4.1 Numerical Grid and Normalization

As we solve the non-dimensional MHD equations, no intrinsic physical scales are involved. We refer to (r, z) as cylindrical coordinates and to (R, θ) as spherical coordinates. All the primitive MHD variables, i.e., ρ,$\mathbf{v}$,p,$\mathbf{B}$, as well as the length and time scales, are normalized to their value at the initial inner disk radius $R_{\rm in}$. Thus, velocities are normalized to $v_{\rm K,in}$, corresponding to the Keplerian speed at $R_{\rm in}$. As a consequence, the time unit is given in units of $t_{\rm in} = R_{\rm in}/v_{\rm K,in}$, and therefore the quantity $2\pi t_{\rm in}$ corresponds to one revolution at the inner disk radius. In the following, all times are measured in units of $t_{\rm in}$, implying that $t = 2000$ (in short) corresponds to $t = 2000\,t_{\rm in}$.

In all the jet launching simulations, the computational domain covers a radial range of $R = [1, 100]R_{\rm in}$ and an angular range of $\theta = [10^{-8}, \pi/2 - 10^{-8}] \simeq [0, \pi/2]$. A stretched grid is applied in the radial direction considering $\Delta R = R\Delta\theta$.

In Chapters 5 and 6, the domain is discretized with a number of $[N_R \times N_\theta] = [512 \times 128]$ grid cells, which allows to resolve the initial disk height $H = 0.2r$ with 16 cells. However, because of the strong interplay between the magnetic field and the dynamo in the innermost accretion disk region, we found that, in order to study the feedback of the magnetic field on the dynamo, a higher angular resolution was required to avoid potential numerical issues. For such reason, in Chapter 7 we adopted a resolution of $[N_R \times N_\theta] = [512 \times 256]$ grid cells, which gives us a resolution of 32 cells per geometrical disk height.

For the resolution study (see Appendix B) we have discretized the domain with $[N_R \times N_\theta] = [1024 \times 256]$ and $[N_R \times N_\theta] = [256 \times 64]$ grid cells, namely 32 and 8 cells per disk height, respectively.

Our scale-free simulations may be scaled to a variety of jet sources. We apply the same physical scaling as described previous works (Zanni, Ferrari, et al., 2007; Tzeferacos, Ferrari, et al., 2009; Sheikhnezami et al., 2012; Stepanovs and Fendt, 2014).

	YSO	BD	AGN	[units]
R_0	0.1	0.01	20	AU
M_0	1	0.05	10^8	$M_\odot$
ρ_0	10^{-10}	10^{-13}	10^{-12}	g cm^{-3}
v_0	94	66	6.7×10^4	km s^{-1}
B_0	15	0.5	1000	G
t_0	1.7	0.25	0.5	days
$\dot{M}_0$	3×10^{-5}	2×10^{-10}	10	$M_\odot$yr^{-1}

TABLE 3.2: Typical parameter scales for different sources, in particular Young Stellar Objects, Brown Dwarfs and Active Galactic Nuclei.

For an astrophysical scaling of our normalized quantities for typical jet systems we refer to Table 3.2.

3.4.2 Initial Conditions

The initial conditions adopted in Chapters 5, 6 and 7, are the same of the ones applied in Stepanovs, Fendt, and Sheikhnezami (2014) and in Fendt and Gaßmann (2018) (although we do not consider here the extension to the lower hemisphere).

The simulations start with a very weak initial seed magnetic field, thus with a very low disk magnetization, defined as the ratio between the magnetic pressure and the thermal pressure $\mu_{\rm in} = B_{\rm in}^2/p_{\rm in} = 10^{-5}$ measured at the disk midplane. Therefore, the initial structure of the accretion disk can be obtained as a solution of the hydrostatic equilibrium between thermal pressure gradients, gravity and centrifugal force (Zanni, Ferrari, et al., 2007; Stepanovs and Fendt, 2014), neglecting the Lorentz force (Stepanovs, Fendt, and Sheikhnezami, 2014; Fendt and Gaßmann, 2018),

$$\nabla p + \rho \nabla \Phi_{\rm g} - \frac{1}{R}\rho v_\phi^2 (\mathbf{e}_R \sin\theta + \mathbf{e}_\theta \cos\theta) = 0. \tag{3.31}$$

This equation can be solved by assuming that all the hydrodynamical variables scale as power laws of the radius R, $X = X_0 R^{\beta_X} F_X(\theta)$, where X_0 is the corresponding variable evaluated at the innermost radius (at the disk midplane), while F_X is the angular dependence. Self-similarity requires that every characteristic speed should scale as the Keplerian velocity, $\propto R^{-1/2}$. In addition we assume a polytropic gas, e.g., $p \propto \rho^\Gamma$. Combining together all these assumptions, the power law coefficients are $\beta_{u_\phi} = -1/2$, $\beta_p = -5/2$, and $\beta_\rho = -3/2$ (as in the self-similar solution of, e.g., R. D. Blandford and Payne 1982). A key parameter to describe the initial disk structure is the ratio between the isothermal sound speed and the Keplerian velocity at the disk midplane of the inner radius $\epsilon = c_{\rm s}/v_\phi |_{\theta=\pi/2}$. Following the recipes of Zanni, Ferrari, et al. (2007) for an initially thin disk, we set $\rho_0 = 1$ and $\epsilon = 0.1$. Solving for the z-component of Equation (3.31) with $\rho_{\rm in} = 1$ at the inner disk radius, we obtain

$$F_p = \left[\frac{2}{5\epsilon^2}\left(1 - \frac{1}{\sin\theta}\right) + \frac{1}{\sin\theta} \right]^{5/2}, \tag{3.32}$$

and where we have chosen $p_{\text{in}} = 0.01$. Following the polytropic relation assumed before, the disk pressure is defined by $F_\rho = F_p^{3/5}$.

Following Stepanovs and Fendt (2014) and Stepanovs, Fendt, and Sheikhnezami (2014), we use the combination of the radial and angular component of Equation (3.31) in order to compute the angular dependence of the toroidal velocity:

$$F_{v_\phi} = \frac{1 - \dfrac{5\epsilon^2}{2} \dfrac{F_P}{F_\rho}}{\sqrt{1 - \dfrac{5\epsilon^2}{2}}}. \tag{3.33}$$

If we neglect the angular dependence (given by the ratio F_p/F_ρ) we recover the expression of Zanni and Ferreira 2009; Zanni and Ferreira 2013 (without the viscous terms). However, the toroidal velocity has a very weak dependence on the angle, and therefore it is safe to assume that $F_p/F_\rho \approx 1$. Outside the disk we define a hydrostatic ($\mathbf{v} = 0$) corona,

$$\rho_{\text{c}} = \rho_{\text{c,in}} R^{1/(1-\gamma)}, \quad p_{\text{c}} = \frac{\gamma - 1}{\gamma} \rho_{\text{c,in}} R^{\gamma/(1-\gamma)}, \tag{3.34}$$

with $\rho_{\text{c,in}} = 10^{-3}\rho_{\text{in}}$. At the transition between accretion disk and corona, the disk pressure equals the coronal pressure, involving a jump in density.

As pointed by Stepanovs and Fendt (2014), we can define as geometrical disk height the region where density and toroidal velocity decrease significantly. Since through all the thesis we assume $\epsilon = 0.1$, we adopt a linear approximation $H = 2r\epsilon$ which is able to reproduce with great accuracy the relation between the thermal and the geometrical disk height.

If not stated otherwise, all the simulations are initialized with a purely radial magnetic field vanishing outside the disk, defined by the vector potential

$$\mathbf{B} = \nabla \times A\mathbf{e}_\phi = \nabla \times \left[\frac{B_{\text{p,in}}}{r} \exp\left(-8\left(z/H\right)^2\right)\right] \mathbf{e}_\phi. \tag{3.35}$$

The strength of the initial poloidal magnetic field is determined by $B_{\text{p,in}} = \sqrt{2p_0\mu_{\text{in}}}$, where $\mu_{\text{in}} = 10^{-5}$ is the initial magnetization along the disk midplane. By construction, the initial toroidal magnetic field B_ϕ is set to zero.

3.4.3 Boundary Conditions

The physical evolution is heavily determined by the choice of the boundary conditions. A "wrong" choice of the boundary conditions may easily lead to a non consistent or unphysical scenarios (see, e.g., a recent review on these issues by Boneva et al. 2021). In this thesis we adopt different boundary conditions, which are reported in Table 3.3 for the sake of clarity.

Along the rotational axis and the equatorial plane the standard symmetry conditions are applied. The inner radial boundary is divided into two different areas. One is the area that is suited for disk accretion located at $\theta > \theta_c$, the other is the coronal area at $\theta < \theta_c$. We choose $\theta_c = \pi/2 - \arctan(2\epsilon) \approx \pi/2 - 2\epsilon$ in Chapters 5 and 6,

TABLE 3.3: Boundary conditions. Symmetric and anti-symmetric boundary conditions are marked by "Sym" and "Anti", respectively.
.

	Inner Disk	Inner Corona	Outer Disk	Outer Corona	Axis	Equator
ρ	$\propto R^{-3/2}$	$\propto R^{-3/2}$	$\propto R^{-3/2}$	$\propto R^{-3/2}$	Sym	Sym
p	$\propto R^{-5/2}$	$\propto R^{-5/2}$	$\propto R^{-5/2}$	$\propto R^{-5/2}$	Sym	Sym
v_R	$\propto R^{-1/2} \leq 0$	0.2 (Ch. 5, 6) 0.1 (Ch. 7)	Outflow ≤ 0	Outflow ≥ 0	Sym	Sym
v_θ	0	0	Outflow	Outflow	Anti	Anti
v_ϕ	$\propto R^{-1/2}$	$\propto R^{-1/2}$	Outflow	Outflow	Anti	Sym
B_R	Slope	Slope (Ch. 5, 6) Flux (Ch. 7)	$\nabla \cdot \mathbf{B} = 0$	$\nabla \cdot \mathbf{B} = 0$	Sym	Anti
B_θ	Slope	Slope (Ch. 5, 6) Flux (Ch. 7)	$\propto R^{-1}$	$\propto R^{-1}$	Anti	Sym
B_ϕ	$\propto R^{-1}$	0	$\propto R^{-1}$	$\propto R^{-1}$	Anti	Anti

while in Chapter 7 we adopt the prescription $\theta_c = \pi/2 - \arctan(3\epsilon) \approx \pi/2 - 3\epsilon$. The extent of the inner disk boundary in Chapter 7 is somewhat broader than the initial disk height. The reason is that the disk, especially in case of strong accretion, may slightly inflate, but all material delivered by disk accretion must be able to be absorbed by the boundary.

The boundary conditions along the inner radial boundary are essential for stabilizing the corona against collapse to the central object. While $v_\theta = 0$ along the inner disk boundary, the radial velocity follows a power law, $v_R = v_{R_{\rm in}} R^{-1/2} \leq 0$, where the inequality is imposed in order to enforce the boundary behaving as a "sink". Along the coronal area, we prescribe a constant inflow velocity into the domain $v_{\rm p}$ (in units of the Keplerian speed at $R_{\rm in}$) in the radial direction, that could be interpreted astrophysically as a stellar wind. We choose $v_{\rm p} = v_R = 0.2$ for Chapters 5 and 6, while we adopt a lower value, $v_{\rm p} = v_R = 0.1$ in Chapter 7 in order to allow for a more stable evolution between the disk and the coronal boundary.

From previous jet formation simulations (e.g., Ouyed and Pudritz 1997; Fendt and Gaßmann 2018) we expect the terminal jet speed to reach the Keplerian velocity at the inner disk. For v_ϕ we prescribe a power law across the inner boundary (for both the inner disk and coronal boundary)

$$v_\phi = v_\phi\big|_{R_{\rm in}} R^{-1/2}, \tag{3.36}$$

where $R_{\rm in}$ is the inner radius of the domain. Along the inner boundary we prescribe $B_\phi = 0$ toward the coronal region, while we adopt a power-law $\propto R^{-1}$ for the boundary area toward the inner disk.

The boundary conditions for the poloidal magnetic field obey the divergence-free condition. The method of constrained transport requires to define only the θ-component of the magnetic field along the boundary, while the radial component is recovered from the Maxwell equations. At the outer boundaries both B_ϕ and B_θ follow a power law

$$B_{\phi,\theta} = B_{\phi,\theta}\big|_{\rm out} R^{-1}, \tag{3.37}$$

where R_{out} is the outer radius of the domain. The radial component of the magnetic field B_R is recovered using the solenoidality condition. This is compatible with a constant gradient condition. For the B_ϕ this implies in particular the conservation of the electric current across the boundary.

Along the inner radial disk boundary, we prescribe the poloidal magnetic field inclination, choosing an angle

$$\varphi = 70° \left[1 + \exp\left(-\frac{\theta - 45°}{15°}\right)\right]^{-1}, \qquad (3.38)$$

where φ is the angle of the magnetic field with respect to the disk surface. Note that here again we solve for the divergence-free condition of the magnetic field, recovering the solution with the inclination prescribed.

The boundary conditions for the poloidal magnetic field at the inner coronal region differ among the different chapters.

The boundary condition adopted in Chapters 5 and 6 is the same of Stepanovs and Fendt (2014), i.e., at the inner coronal boundaries the inclination of the magnetic field is fixed by Equation (3.38). As a consequence, the advection of magnetic field from the inner disk towards the axis is not suppressed. The advection of flux towards the axis has some impact for the structure of this innermost area, but does not change the structure and the evolution of the surrounding disk jet, which is our major focus. Moreover, the advection of magnetic flux towards the axis is a more physical boundary condition.

In Chapter 7 we fix the poloidal magnetic field at the coronal boundary by requiring the conservation of magnetic flux. This inner boundary condition was found to be less prone to numerical instabilities.

Across the inner disk and the outer boundaries (disk and coronal), both the density and the pressure are extrapolated by a power law,

$$\rho = \rho\big|_{R_{\text{in}}, R_{\text{out}}} R^{-3/2} \qquad P = P\big|_{R_{\text{in}}, R_{\text{out}}} R^{-5/2}. \qquad (3.39)$$

The density at the inner coronal boundary corresponds to a hydrostatic corona:

$$\rho_{r_{\text{in}}, \text{cor}} = \rho_{R_{\text{in}}, \theta=\pi/2}(t) \cdot \rho_{\text{c,in}}. \qquad (3.40)$$

Along the outer boundaries, the three velocity components follow the standard PLUTO outflow (zero gradient) conditions. In addition, we still prescribe v_R to be non-positive in the disk region and non-negative in the coronal region.

3.4.4 The Dynamo Model

For a thin disk, the non-diagonal components of the mean-field dynamo tensor are negligible. In our approach we consider the explicit form of the dynamo terms following Ruediger, Elstner, and Stepinski (1995) and Rekowski, Rüdiger, and Elstner (2000),

$$\alpha = (\alpha_R, \alpha_\theta, \alpha_\phi) = -[\bar{\alpha}_0 \circ \bar{q}_\alpha] c_s F_\alpha(z), \qquad (3.41)$$

where the symbol $\circ$ corresponds to the element-wise product of two vectors, and with the adiabatic sound speed c_s at the disk midplane. The vector $\bar{\alpha}_0$ (whose explicit form will be described in the next chapters) determines the strength of the dynamo tensor, and $F_\alpha(z)$ describes the vertical profile of the alpha-effect (Bardou et al., 2001):

$$F_\alpha(z) = \begin{cases} \sin\left(\pi\dfrac{z}{H}\right) & z \leq H, \\ 0 & z > H. \end{cases} \tag{3.42}$$

Naturally, we also need to assume a sufficiently high disk ionization. The vector $\bar{q}_\alpha$ is a generic dynamo-quenching function. In Chapters 5 and 6 we adopt the diffusive quenching model of Stepanovs, Fendt, and Sheikhnezami (2014), therefore we set $\bar{q}_\alpha = (1,1,1)$, while the quenching models adopted in Chapter 7 are described in Section 7.1.

Note that Ruediger, Elstner, and Stepinski (1995) have applied a slightly different profile, namely a linear function $F_\alpha(z) = z/H$ in the disk. We prefer the approach of Bardou et al. (2001) that effectively avoids the discontinuity at the disk surface and is thus better suited for a simulation that includes also the disk corona.

As in Stepanovs, Fendt, and Sheikhnezami, 2014, we choose a radial dependence of the dynamo $\alpha \propto R^{-1/2}$, since this profile follows also the sound speed. Note, however, that compared to Stepanovs, Fendt, and Sheikhnezami (2014), in the present setup the radial profile of the dynamo is not necessarily constant in time. As the sound speed is included in the dynamo tensor, along with the disk sound speed, also the dynamo tensor is updated every time step. This variation has only a minor impact on the overall evolution of the system. However, it represents a more consistent approach and is furthermore in agreement with the analytical models of mean-field dynamo theory (Ruediger and Kichatinov, 1993; Ruediger, Elstner, and Stepinski, 1995).

3.4.5   The Diffusivity Model

The magnetic diffusivity tensor is assumed to have a diagonal structure:

$$\eta = (\eta_R q_{\eta R}, \eta_\theta q_{\eta\theta}, \eta_\phi q_{\eta\phi}). \tag{3.43}$$

The vector $\bar{q}_\eta = (q_{\eta R}, q_{\eta\theta}, q_{\eta\phi})$ is a generic eta-quenching function. If not stated otherwise, we set $\bar{q}_\eta = (1,1,1)$. The diffusivity profile is anisotropic, following

$$\eta_R = \eta_\theta = \eta_\phi \frac{\eta_{0,R}}{\eta_{0,\phi}}. \tag{3.44}$$

(Ferreira and Pelletier, 1995). The explicit form of $\bar{\eta}_0 = (\eta_{0,R}, \eta_{0,\theta}, \eta_{0,\phi})$ will be describe in the later chapters.

As in Stepanovs, Fendt, and Sheikhnezami (2014), we adopt an α-prescription:

$$\eta_\phi = \alpha_{\mathrm{ss}} c_s H F_\eta(z), \tag{3.45}$$

where c_s is the adiabatic sound speed at the disk midplane, H denotes the geometrical disk height, and $F_\eta(z)$ describes the vertical profile of the magnetic diffusivity. Again we define a profile function,

$$
F_\eta(z) = \begin{cases} 1 & z \leq H, \\ \exp\left[-2\left(\dfrac{z-H}{H}\right)^2\right] & z > H, \end{cases}
\tag{3.46}
$$

that confines the diffusivity within the disk region.

The quantity α_{ss} represents the dimensionless parameter measuring the strength of the turbulence (Shakura and Sunyaev, 1973). Implicitly, the magnetic diffusivity is assumed to do have a turbulent nature, most likely caused by the MRI (Steven A. Balbus and John F. Hawley, 1991). Note that the magnetic diffusivity, or resistivity, respectively, is motivated here as caused by the disk turbulence, thus much stronger than the microscopic value. In the literature of jet launching simulations (see, e.g., Jacquemin-Ide, Ferreira, and Lesur 2019) without a mean-field dynamo, the magnetic diffusivity is usually computed as

$$
\overline{\eta} = \overline{\eta}_0 v_A H F_\eta(z),
\tag{3.47}
$$

where the two model approaches described above coincide if

$$
\alpha_{ss} = \eta_{0,\phi} \sqrt{\frac{2\mu|_{\pi/2}}{\Gamma \mu_0}},
\tag{3.48}
$$

where Γ is the polytropic index and μ_0 is the magnetization computed at the disk midplane. Through all this thesis we set $\mu_0 = 0.01$. This model approach is, however, not used in this thesis. One reason is that we want to avoid the accretion instability to occur (Campbell, 2009). Moreover, the magneto-rotational instability can be triggered by both the poloidal and the toroidal field (Fromang, 2013).

In Chapters 5 and 6 the feedback between the magnetization and the magnetic diffusivity is chosen stronger than $\alpha_{ss} \propto \sqrt{\mu}$ (see Stepanovs and Fendt 2014). Note that we already have a feedback loop on the magnetic diffusivity, as the growth of the magnetic field is naturally related to the mean-field dynamo. We therefore apply the so-called *strong diffusivity* model (Stepanovs and Fendt, 2014; Stepanovs, Fendt, and Sheikhnezami, 2014),

$$
\alpha_{ss} = \eta_{0,\phi} \sqrt{\frac{2}{\gamma}} \left(\frac{\mu_D}{\mu_0}\right)^2.
\tag{3.49}
$$

Since the initial magnetic field does not intersect the disk midplane, for the quantity μ_D we calculate the ratio between the *average* total magnetic field (vertically averaged at a certain radius) in the disk and the gas pressure at the disk midplane (Stepanovs, Fendt, and Sheikhnezami, 2014). As demonstrated in Stepanovs and Fendt (2014), this approach allows to perform a more stable evolution of the disk-jet structure over long simulation time (Stepanovs, Fendt, and Sheikhnezami, 2014; Fendt and Gaßmann, 2018).

In Chapter 7 we take a step forward and try to connect the non-dynamo simulations (e.g., Zanni, Ferrari, et al. 2007; Sheikhnezami et al. 2012) to the mean-field dynamo simulations. Therefore the diffusivity model is defined by

$$\alpha_{\rm ss} = \eta_{0,\phi} \sqrt{\frac{2\mu_D}{\Gamma\mu_0}}. \tag{3.50}$$

3.4.6 Control Volumes and Fluxes

Here we define how we integrate global quantities that are used throughout the thesis. The accretion rate is calculated by integrating the net radial mass flux through the disk, defined by an opening angle $\theta_S \equiv \arctan(2H/r)$,

$$\dot{M}_{\rm acc}(R) = 2\pi R \int_{\pi/2}^{\pi/2-\theta_S} \rho v_R R d\theta, \tag{3.51}$$

while the ejection rate is calculated by integrating the outflow in vertical direction (through the disk surface),

$$\dot{M}_{\rm eje}(R;\theta_S) = \int_{R_{\rm in}}^{R} \rho v_\theta(\tilde{R}) 2\pi \tilde{R} d\tilde{R}, \tag{3.52}$$

respectively. The magnetic disk energy (poloidal or toroidal) is integrated from a radius of choice R to the outer radius $R_{\rm out}$, and from the disk midplane to the disk surface, defined by θ_S. We thus consider the disk magnetic energy outside R for our considerations,

$$E_{\rm mag} = \int_{R}^{R_{\rm out}} \int_{\pi/2-\theta_S}^{\pi/2} \frac{1}{2} B^2 \sin(|\theta|) 2\pi R^2 d\theta dR. \tag{3.53}$$

The so-called *disk magnetic field* (and also the *disk magnetization*) is simply calculated as the average value of the magnetic field, at each radius, within the initial disk defined by $\theta_i \equiv \arctan(H/r)$,

$$B_{\rm disk}(R) = \frac{1}{\theta_i} \int_{\pi/2-\theta_i}^{\pi/2} B(R,\theta) d\theta, \tag{3.54}$$

while the so-called *disk diffusivity* is the average value of the diffusivity at a certain radius within the initial accretion disk,

$$\eta_{\rm disk}(R,t) = \frac{1}{\theta_i} \int_{\pi/2-\theta_i}^{\pi/2} \eta(R,\theta) d\theta. \tag{3.55}$$

On the other hand, the *poloidal disk magnetization* is calculated by integrating the poloidal magnitization from the inner radius $R_{\rm in}$ to the outer radius $R_{\rm out}$ and from the disk midplane to the disk surface $\theta_i \equiv \arctan(H/r)$ and dividing it by the disk area.

3.4.7   Dynamo Number and Turbulence Parameter

MHD simulations, in particular those which consider a mean-field dynamo, may apply a wide range of parameters. Consequently, it may be difficult to compare a set of different numerical simulations. For this reason, dimensionless parameters which do not have a strict dependence on the initial parameter space play a key role in order to understand the physical evolution. In the context of the mean-field dynamo simulations the dynamo number $\mathcal{D}$ plays the essential role when it comes to understand the efficiency of the dynamo process,

$$\mathcal{D} = \frac{\alpha_\phi \Omega H^3}{\eta_{\phi,\mathrm{D}}^2}. \tag{3.56}$$

High dynamo numbers imply the possibility of an efficient dynamo process, low numbers vice versa. The critical dynamo number, separating the two regimes, depends on the details of the model setup (see, e.g., Stepinski and Levy 1988; Stepinski and Levy 1990; Torkelsson and Brandenburg 1994) and has to be found by applying a series of parameter runs. For example, Brandenburg and Subramanian (2005) found a critical dynamo number $\mathcal{D} \lesssim 10$, below which the magnetic field cannot be amplified. By connecting galactic dynamo simulations with accretion disk simulations, Boneva et al. (2021) found $\mathcal{D} \lesssim 7$.

The dynamo number is a combination of the azimuthal magnetic Reynolds number $\mathcal{R}_\eta = |\Omega| H^2 / \eta_{\phi,\mathrm{D}}$ and the magnetic Reynolds number $\mathcal{R}_\alpha = \alpha_\phi H / \eta_{\phi,\mathrm{D}}$, the latter including the shear $d\Omega/dr$ of the system and the turbulent α-effect. The size of the system is denoted by H, here represented by the disk height. By construction, the dynamo components vanish at $z = H$. We therefore compute the quantity α_ϕ at $z = H/2$.

As demonstrated by Stepanovs, Fendt, and Sheikhnezami (2014), both the disk orbital velocity and the sound speed at the disk midplane undergo some little variation during the temporal evolution of the system. Therefore, for an almost constant diffusivity profile with radius, $\mathcal{D}$ would scale almost linearly with the radius. We note that this is a rough estimate - as the disk diffusivity does not follow a constant radial profile, even in quasi-steady state.

The dynamo number also depends on α_{ss},

$$\mathcal{D} \propto \alpha_{\mathrm{ss}}^{-2}, \tag{3.57}$$

as pointed by (Stepanovs, Fendt, and Sheikhnezami, 2014; Fendt and Gaßmann, 2018). The dependence of the Dynamo number on the disk magnetization is strictly related with the diffusivity and dynamo model.

Another key parameter in disk simulations as well as in jet launching simulations is the turbulence parameter α_{ss}, which parametrizes the strength of disk turbulence, respectively the disk turbulent viscosity (Shakura and Sunyaev, 1973). On one hand, it represents a direct link between the disk magnetization and the disk diffusivity (see Equations 3.48 and 3.49), on the other hand it can be recovered both from observations and direct simulations. As pointed by King, Pringle, and Livio (2007), observational evidences show that a range $0.1 < \alpha_{\mathrm{ss}} < 0.4$ is required to provide a good description of the behaviour of fully ionized, thin accretion discs.

Nevertheless, numerical simulations of direct turbulence recover values which are an order of magnitude below the observational values.

Chapter 4

Riemann Solvers for Relativistic MHD

The contents of this chapter are adapted from Mattia and Mignone (2022), published in the *Monthly Notices of the Royal Astronomical Society*. All the simulations (excluding the 3D blast wave), the figures and most of the scientific discussion and interpretation presented in this chapter were done by the author of the thesis.

In this chapter we compare a particular selection of approximate solutions of the Riemann problem in the context of ideal relativistic magnetohydrodynamics, whose equations are described in Section 2.3. In particular, we focus on Riemann solvers not requiring a full eigenvector structure. Such solvers recover the solution of the Riemann problem by solving a simplified or reduced set of jump conditions, whose level of complexity depends on the intermediate modes that are included. Five different approaches - namely the HLL, HLLC, HLLD, HLLEM and GFORCE schemes - are compared in terms of accuracy and robustness against one- and multi-dimensional standard numerical benchmarks. In particular, we demonstrate that - for weak or moderate magnetizations - the HLLD Riemann solver yields the most accurate results, followed by HLLC solver(s). The GFORCE approach provides a valid alternative to the HLL solver being less dissipative and equally robust for strongly magnetized environments. Finally, our tests show that the HLLEM Riemann solver is not cost-effective in improving the accuracy of the solution and reducing the numerical dissipation.

The chapter is organized as follows. In Section 4.1 we briefly describe the different numerical methods. In Section 4.2 we show a set of numerical benchmarks in order to assess the computational speed, robustness and accuracy of the Riemann solvers mentioned above. Finally, in Section4.3 we summarize our findings.

4.1 Non-linear Approximate Riemann Solvers

Over the last decades, several approximate solutions to the Riemann problem have been developed in the context of relativistic MHD. Roe's type Riemann solvers (S. S. Komissarov 1999; D. S. Balsara 2001; Koldoba, Kuznetsov, and Ustyugova 2002) are based on the exact linearization of the equations and require the full characteristic decomposition. Unfortunately, as pointed in Einfeldt et al. (1991) and S. S. Komissarov (1999), linear solvers may not satisfy the entropy condition through strong rarefactions. In RMHD, a state of art of the Roe-type Riemann solvers has been developed by Antón et al. (2010) (and earlier by Koldoba, Kuznetsov, and Ustyugova, 2002), which have provided the (quite lengthy) analytical expressions for both right
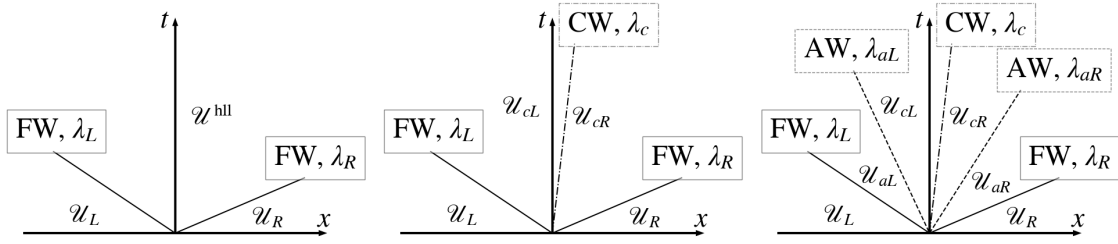
FIGURE 4.1: Riemann fan structure for the HLL, HLLC and HLLD approaches, respectively.

and left eigenvectors. Albeit the linearized approach of Roe is capable of accounting for all the seven waves present in the solution, we shall not consider it here because of its heavy numerical cost. For this reason we prefer to focus on incomplete Riemann solvers, which do not include in their structure the full set of waves.

4.1.1 HLL

A second family of (approximate) Riemann solvers (of which the HLL solver can be considered the progenitor) dates back to the original work of Harten, Lax, and Leer, 1983. The HLL Riemann solver has become extremely popular because of its ease of implementation, reduced computational cost and robustness (see, e.g. Gammie, J. C. McKinney, and Tóth, 2003; Del Zanna, Zanotti, et al., 2007; Beckwith and Stone, 2011; White, Stone, and Gammie, 2016, in the context of Special and General relativistic MHD).

The HLL Riemann solver for the equations of gas-dynamics (Del Zanna and Bucciantini, 2002; Del Zanna, Bucciantini, and Londrillo, 2003), approximates the internal structure of the Riemann fan with a single state U^{hll} bounded by two outermost fast magnetotosonic waves (leftmost panel in Figure 4.1). This single state is required to satisfy the jump conditions across each of the two waves

$$
\begin{aligned}
\lambda_L(\mathscr{U}_L - \mathscr{U}^{\text{hll}}) &= \mathscr{F}_L - \mathscr{F}^{\text{hll}}, \\
\lambda_R(\mathscr{U}_R - \mathscr{U}^{\text{hll}}) &= \mathscr{F}_R - \mathscr{F}^{\text{hll}}.
\end{aligned}
\tag{4.1}
$$

As such, the HLL approach avoids the full characteristic decomposition of the equations since only an estimate to the two outermost fast waves λ_L and λ_R is needed.

Equations (4.1) yield a total of 14 equations in the 14 unknowns given by the components of $\mathscr{U}^{\text{hll}}$ and $\mathscr{F}^{\text{hll}}$ (note that $\mathscr{F}^{\text{hll}} \neq \mathscr{F}^x(\mathscr{U}^{\text{hll}})$). The solution is readily found as

$$
\mathscr{U}^{\text{hll}} = \frac{\lambda_R \mathscr{U}_R - \lambda_L \mathscr{U}_L + \mathscr{F}_L - \mathscr{F}_R}{\lambda_R - \lambda_L},
\tag{4.2}
$$

and

$$
\mathscr{F}^{\text{hll}} = \frac{\lambda_R \mathscr{F}_L - \lambda_L \mathscr{F}_R + \lambda_R \lambda_L (\mathscr{U}_R - \mathscr{U}_L)}{\lambda_R - \lambda_L},
\tag{4.3}
$$

where $\mathscr{F}_s = \mathscr{F}^x(\mathscr{U}_s)$, for $s = L, R$. Equation (4.2) is also known as the integral representation of the Riemann fan (E. Toro, 2009).

The outermost wave speeds λ_L and λ_R represent an upper bound to the actual wave speeds and can be estimated using the initial left and right input states see, e.g Mignone and Bodo, 2006.

The actual numerical flux is finally computed as follows:

$$
\hat{\mathcal{F}} = \begin{cases} \mathcal{F}_L & \text{if} \quad \lambda_L \geq 0, \\ \mathcal{F}^{\text{hll}} & \text{if} \quad \lambda_L \leq 0 \leq \lambda_R, \\ \mathcal{F}_R & \text{if} \quad \lambda_R \leq 0. \end{cases} \tag{4.4}
$$

The HLL scheme approximates only two out of the seven waves by collapsing the full structure of the Riemann fan into a single average state. Because of this, this solver is simple to implement, cost-effective and requires only a guess to the outermost fast speed without any particular knowledge of the solution. On the other hand, the solver has large numerical dissipation and has pushed the quest for more accurate approaches.

4.1.2 HLLC

An extension of the HLL scheme, able to restore the contact wave, was developed originally by E. F. Toro, Spruce, and Speares (1994) for the Euler equation. The so-called HLLC (where 'C' stands for Contact) formulation, was later extended to RMHD by (Mignone and Bodo, 2006; Honkkila and Janhunen, 2007). In both Mignone and Bodo (2006) and Honkkila and Janhunen (2007) the solution method differs depending on whether the normal component of the magnetic field vanishes or not. A solution to this problem was brought by Kim and D. S. Balsara (2014) and then improved in D. S. Balsara and Kim (2016), who developed a HLLC solver which retrieves naturally the hydrodynamical limit when the magnetic field tends to zero.

The solver attempts to restore the intermediate contact wave thus leading to a two-state representation of the internal Riemann fan structure:

$$
\mathcal{U}(x,t) = \begin{cases} \mathcal{U}_L & \text{if} \quad \lambda_L \geq x/t, \\ \mathcal{U}_L^* & \text{if} \quad \lambda_L \leq x/t \leq \lambda^*, \\ \mathcal{U}_R^* & \text{if} \quad \lambda^* \leq x/t \leq \lambda_R, \\ \mathcal{U}_R & \text{if} \quad \lambda_R \leq x/t, \end{cases} \tag{4.5}
$$

where λ^* is now the velocity of the middle contact wave, see also the middle panel in Figure 4.1. Likewise, the corresponding numerical fluxes at the interface evaluates as:

$$
\hat{\mathcal{F}}(0,t) = \begin{cases} \mathcal{F}_L & \text{if} \quad \lambda_L \geq 0, \\ \mathcal{F}_L^* & \text{if} \quad \lambda_L \leq 0 \leq \lambda^*, \\ \mathcal{F}_R^* & \text{if} \quad \lambda^* \leq 0 \leq \lambda_R, \\ \mathcal{F}_R & \text{if} \quad \lambda_R \leq 0. \end{cases} \tag{4.6}
$$

Intermediate states and fluxes must satisfy the Rankine-Hugoniot jump conditions:

$$
\begin{aligned}
\lambda_L(\mathcal{U}_L^* - \mathcal{U}_L) &= \mathcal{F}_L^* - \mathcal{F}_L, \\
\lambda^*(\mathcal{U}_R^* - \mathcal{U}_L^*) &= \mathcal{F}_R^* - \mathcal{F}_L^*, \\
\lambda_R(\mathcal{U}_R - \mathcal{U}_R^*) &= \mathcal{F}_R - \mathcal{F}_R^*.
\end{aligned}
\tag{4.7}
$$

Adding together the previous equations yields the consistency condition

$$
\frac{(\lambda^* - \lambda_L)\mathcal{U}_L^* + (\lambda_R - \lambda^*)\mathcal{U}_R^*}{\lambda_R - \lambda_L} = \mathcal{U}^{\mathrm{hll}},
\tag{4.8}
$$

or, upon dividing by the corresponding λ, the equivalent condition on the fluxes:

$$
\frac{\mathcal{F}_L^* \lambda_R(\lambda^* - \lambda_L) + \mathcal{F}_R^* \lambda_L(\lambda_R - \lambda^*)}{\lambda_R - \lambda_R} = \lambda^* \mathcal{F}^{\mathrm{hll}}.
\tag{4.9}
$$

In general one can not take $\mathcal{F}^* = \mathcal{F}(\mathcal{U}^*)$ since fewer waves in the Riemann fan are accounted for. For this reason we can look at Equations. (4.7) as providing, in principle, $3 \times 7 = 21$ relations across three waves and a consistent solution can therefore be sought by introducing 21 unknowns. However, if the speed of the contact mode is chosen to coincide with the fluid normal velocity, the continuity equation across the middle wave is trivially satisfied and the number of equations reduces to 20 (10 per state). This allows states ($\mathcal{U}_{L/R}^*$) and fluxes ($\mathcal{F}_{L/R}^*$) in the star region to be expressed in terms of the 20 unknowns

$$
\left(D, v_x, v_y, v_z, m_y, m_z, B_y, B_z, p, E\right)_{L/R}^*,
\tag{4.10}
$$

with the condition $\lambda^* = v_{x,L}^* = v_{x,R}^*$. The normal component of the momentum is not considered an independent quantity since it can be expressed through a combination of the previous unknowns as

$$
m_x^* = (E' + p)^* v_x^* - (\mathbf{v} \cdot \mathbf{B})^* B_x,
\tag{4.11}
$$

where $E' = E + D$, which holds both for the left or the right state in the *star* region. Note also that B_x enters as a constant parameter in the solution process.

The HLLC solvers of Mignone and Bodo, 2006; Honkkila and Janhunen, 2007; Kim and D. S. Balsara, 2014 are based on this formalism although they require different conditions to be satisfied across the middle contact wave. In this thesis we describe and compare the original approach of Mignone and Bodo, 2006 and the more recent improvement by Kim and D. S. Balsara, 2014.

In the approach of Mignone and Bodo (2006) (henceforth HLLC-MB), the solution of the Riemann problem differs depending on whether the normal magnetic field vanishes or not. When $B_x \neq 0$, the following conditions across the contact discontinuity are assumed:

$$
\begin{aligned}
v_{x,L}^* = v_{x,R}^* \quad & v_{y,L}^* = v_{y,R}^* \quad v_{z,L}^* = v_{z,R}, \\
p_L^* = p_R^* \quad & B_{y,L}^* = B_{y,R}^* \quad B_{z,L}^* = B_{z,R}^*.
\end{aligned}
\tag{4.12}
$$

The solution of the Riemann problem can then be divided into the following steps:

(i) By virtue of their continuity, the transverse components of **B** are given by the HLL single state

$$B_y^* = B_y^{\text{hll}} \quad B_z^* = B_z^{\text{hll}} .\tag{4.13}$$

(ii) The normal component of the velocity is recovered from the negative branch of the quadratic equation

$$a\,(v_x^*)^2 + b v_x^* + c = 0 ,\tag{4.14}$$

with coefficients

$$\begin{aligned}
a &= \mathcal{F}_E^{\text{hll}} + \mathcal{F}_D^{\text{hll}} - \mathbf{B}_\perp^{\text{hll}} \cdot \mathcal{F}_{\mathbf{B}_\perp}^{\text{hll}} , \\
b &= -\left(\mathcal{F}_{m^x}^{\text{hll}} + E'^{\text{hll}}\right) + |\mathbf{B}_\perp^{\text{hll}}|^2 + |\mathcal{F}_{\mathbf{B}_\perp}^{\text{hll}}|^2 , \\
c &= m_x^{\text{hll}} - \mathbf{B}_\perp^{\text{hll}} \cdot \mathcal{F}_{\mathbf{B}_\perp}^{\text{hll}} ,
\end{aligned}\tag{4.15}$$

where $E' = E + D$, $\mathbf{B}_\perp^{\text{hll}} = (0, B_y^{\text{hll}}, B_z^{\text{hll}})$ and $\mathcal{F}_{\mathbf{B}_\perp}^{\text{hll}} = (0, \mathcal{F}_{B_y}^{\text{hll}}, \mathcal{F}_{B_z}^{\text{hll}})$.

(iii) Compute the transverse components of the velocity from

$$B_x v_y^* = B_y^* v_x^* - \mathcal{F}_{B_y}^{\text{hll}} \qquad B_x v_z^* = B_z^* v_x^* - \mathcal{F}_{B_z}^{\text{hll}} .\tag{4.16}$$

Here the L/R subscripts have been removed because of (4.12).

(iv) Recover the total pressure p^* from

$$[\mathcal{F}_E^{\text{hll}} + \mathcal{F}_D^{\text{hll}} - B_x^*(\mathbf{v}^* \cdot \mathbf{B}^*)]v_x^* - \left(\frac{B_x^*}{\gamma^*}\right)^2 + p^* - \mathcal{F}_{m^x}^{\text{hll}} = 0 ,\tag{4.17}$$

where $\mathbf{v}^* = (v_x^*, v_y^*, v_z^*)$ and $\mathbf{B}^* = (B_x, B_y^*, B_z^*)$.

(v) Compute the remaining conserved hydrodynamical variables across the contact discontinuity:

$$\begin{aligned}
D^* &= \frac{\lambda - v_x}{\lambda - v_x^*} D, \\
E^* &= \frac{\lambda E - \mathcal{F}_E + p^* v_x^* - (\mathbf{v}^* \cdot \mathbf{B}^*)B_x^*}{\lambda - v_x^*}, \\
m_x^* &= (E'^* + p^*)v_x^* - (\mathbf{v}^* \cdot \mathbf{B})B_x^*, \\
m_t^* &= \frac{-B_x^*\left[(B_t^*/(\gamma^*)^2) + (\mathbf{v}^* \cdot \mathbf{B}^*)v_t^*\right] + \lambda m_t - \mathcal{F}_{m_t}}{\lambda - v_x^*}.
\end{aligned}\tag{4.18}$$

where $t = y, z$ denotes a generic transverse component and, for the sake of clarity, we have omitted the suffix (L/R).

(vi) Derive the corresponding fluxes from the Rankine-Hugoniot conditions of E-
quation (4.7).

While this approach is fully consistent with the integral average of the solution
across the Riemann problem (Equation 4.8), a major drawback is that transverse
components of velocity and momentum remain bounded, as $B_x \rightarrow 0$, only for
strictly 2D configurations ($v_z = B_z = 0$) while this may not hold in a general 3D
vector orientations, as originally noted by Mignone and Bodo, 2006. In these situ-
ations (i.e., $\mathbf{v}^* \cdot \mathbf{v}^* \geq 1$) we replace the HLLC flux with the the HLL flux (Equation
4.4).

The limit $B_x = 0$ corresponds to a degenerate situation where slow and Alfvén
waves propagate at the same speed of the entropy wave. In this case, not only the
density, but also the transverse components of the velocity and magnetic field can
experience jumps. As a consequence, only the normal component of the velocity
(v_x^*) and the total pressure (p^*) are assumed to be continuous. The previous steps
are then modified as follows:

(i) Find the normal velocity using Equation (4.14) but with coefficients

$$
\begin{aligned}
a &= \mathcal{F}_E^{\text{hll}} + \mathcal{F}_D^{\text{hll}}, \\
b &= -\mathcal{F}_{m^x}^{\text{hll}} + E'^{\text{hll}}, \\
c &= m_x^{\text{hll}},
\end{aligned}
\tag{4.19}
$$

where F_E^{hll}, F_D^{hll} and $F_{m_x}^{\text{hll}}$ are the energy, density and x-momentum component
of the HLL flux (Equation 4.3).

(ii) Derive the total pressure from

$$
p^* = \mathcal{F}_{m_x}^{\text{hll}} - (\mathcal{F}_E^{\text{hll}} + \mathcal{F}_D^{\text{hll}})v_x^*.
\tag{4.20}
$$

(iii) Compute the conserved values across the contact discontinuity from

$$
\begin{aligned}
D^* &= \frac{\lambda - v_x}{\lambda - v_x^*}D, \\
E^* &= \frac{\lambda E - \mathcal{F}_E + p^* v_x^*}{\lambda - v_x^*}, \\
m_x^* &= (E'^* + p^*)v_x^*, \\
m_t^* &= \frac{\lambda - v_x}{\lambda - v_x^*}m_t, \\
B_t^* &= \frac{\lambda - v_x}{\lambda - v_x^*}B_t,
\end{aligned}
\tag{4.21}
$$

where, again, $t = y, z$ label a generic transverse component and we have omit-
ted the suffix (L/R) for the clarity of exposition.

(iv) Derive the corresponding fluxes from the Rankine-Hugoniot conditions of E-
quation (4.7).

Notice that, in case of vanishing magnetic field, the latter approach (the one where $B_x = 0$) reduces to the relativistic hydro HLLC solver in Mignone and Bodo (2005).

The approach of Kim and D. S. Balsara, 2014 (henceforth HLLC-KB, later corrected in the Appendix B of D. S. Balsara and Kim, 2016) presents an improved version of the HLLC solver aimed at resolving the limitations of the previous approach. For the sake of completeness, we revise here the fundamental steps in order to elucidate some potentially ambiguous aspects in the original formulation. In particular, Equation (4.12) is replaced with the weaker requirement

$$
\begin{aligned}
v_{x,L}^* = v_{x,R}^* \quad v_{y,L}^* \neq v_{y,R}^* \quad v_{z,L}^* \neq v_{z,R'}^* \\
p_L^* = p_R^* \qquad B_{y,L}^* = B_{y,R}^* \quad B_{z,L}^* = B_{z,R'}^*
\end{aligned}
\tag{4.22}
$$

that is, the transverse components of velocity are discontinuous across the middle wave while normal velocity, magnetic fields and total pressure are still continuous.

As for the previous HLLC solver, the continuity of B_y and B_z leads to the unique choice

$$
B_y^* = B_y^{\mathrm{hll}} \qquad B_z^* = B_z^{\mathrm{hll}}.
\tag{4.23}
$$

By suitable algebraic manipulations, we rewrite the jump condition of the transverse momenta across the outermost waves as

$$
\begin{aligned}
\Big[\mathbf{v}_t^* (m_x - E'\lambda) - p^* \mathbf{v}_t^* \lambda + \mathbf{B}_t^* (\mathbf{v}^* \cdot \mathbf{B}^*)(\lambda - v_x^*) + \\
+ B_x \frac{\mathbf{b}_t}{\gamma} - B_x \mathbf{B}_t^* [1 - (\mathbf{v}^*)^2] + \mathbf{m}_t (\lambda - v_x) \Big]_S = 0 \,,
\end{aligned}
\tag{4.24}
$$

where, e.g., $\mathbf{v}_t^* = (0, v_y^*, v_z^*)$ denotes the transverse velocity vector (the same holds for $\mathbf{B}_t^*$ and $\mathbf{b}_t^*$) while, here and in what follows, $S = L$ ($S = R$) implies that the expression applies to the left (right) state. Equation (4.24) yields indeed a total of 4 equations.

Likewise, it is possible to derive a pair of equations across the left and right waves involving the normal velocity and total pressure:

$$
\begin{aligned}
\Big[(1 - \lambda v_x^*) p^* - B_x^2 [1 - (\mathbf{v}^*)^2] + B_x (\mathbf{v}^* \cdot \mathbf{B}^*)(\lambda - v_x^*) + \\
+ (m_x - \lambda E') v_x^* - m_x v_x + B_x \frac{b_x}{\gamma} + p + \lambda m_x \Big]_S = 0 \,.
\end{aligned}
\tag{4.25}
$$

Equations (4.24) and (4.25) provide a closed system of 6 equations in the 6 unknown $Q = (\mathbf{v}_{t,L}^*, \mathbf{v}_{t,R}^*, v_x^*, p^*)$, and, due to its nonlinearity, has to be solved numerically. As pointed in Kim and D. S. Balsara (2014), the solution of the full set would make the HLLC solution too expensive. For this reason, the three sets of equations - corresponding, respectively to Equation (4.24) (for the transverse velocities) for $S = L$ and $S = R$, and Equation (4.25) for the normal velocity and total pressure - are solved as three 2×2 subsystems via multidimensional Newton-Raphson algorithm. In particular, referring to the left hand sides of Equation (4.24) as, respectively, $G_{y,R}$

and $G_{z,R}$, the corrections to the transverse velocities $(\delta v_{y,R}, \delta v_{z,R})$ are recovered as

$$
\begin{pmatrix} \delta v_y^* \\ \delta v_z^* \end{pmatrix}_S = - \begin{pmatrix} a_{11} & a_{12} \\ a_{21} & a_{22} \end{pmatrix}^{-1} \begin{pmatrix} G_y \\ G_z \end{pmatrix}_S , \tag{4.26}
$$

where the matrix a is the Jacobian matrix, with elements:

$$
\begin{aligned}
a_{11} &= \left[m_x - \lambda E' - p^* \lambda + (B_y^*)^2 (\lambda - v_x^*) + 2 B_x B_y^* v_y^* \right]_S , \\
a_{12} &= \left[B_y^* B_z^* (\lambda - v_x^*) + 2 B_x B_y^* v_z^* \right]_S , \\
a_{21} &= \left[B_y^* B_z^* (\lambda - v_x^*) + 2 B_x B_y^* v_y^* \right]_S , \\
a_{22} &= \left[m_x - \lambda E' - p^* \lambda + (B_z^*)^2 (\lambda - v_x^*) + 2 B_x B_z^* v_y^* \right]_S .
\end{aligned} \tag{4.27}
$$

Pressure and normal velocity in this subsystem are kept at the previous iteration level and updated as new values become available during the iteration cycle.

Simultaneously, we solve the 2×2 subsystem given by Equations (4.25) for the left and right states. Denoting with H_L and H_R the left-hand side of Equation (4.25), respectively for the left and right state, we get

$$
\begin{pmatrix} \delta v_x^* \\ \delta p^* \end{pmatrix} = - \begin{pmatrix} b_{11} & b_{12} \\ b_{21} & b_{22} \end{pmatrix}^{-1} \begin{pmatrix} H_R \\ H_L \end{pmatrix} , \tag{4.28}
$$

where the elements of the Jacobian matrix are

$$
\begin{aligned}
b_{11} &= \left[-\lambda p^* + B_x^2 (\lambda + v_x^*) - (\mathbf{v}^* \cdot \mathbf{B}^*) B_x + m_x + \lambda E' \right]_R , \\
b_{12} &= 1 - \lambda_R v_x^* , \\
b_{21} &= \left[-\lambda p^* + B_x^2 (\lambda + v_x^*) - (\mathbf{v}^* \cdot \mathbf{B}^*) B_x + m_x + \lambda E' \right]_L , \\
b_{22} &= 1 - \lambda_L v_x^* .
\end{aligned} \tag{4.29}
$$

As for the previous 2×2 subsystem, the transverse velocities are one iteration late and are taken from Equation (4.24).

Finally, the initial guess to start the Newton-Raphson algorithm is provided by the primitive variables in the HLL state. The iterative cycle $Q^{*,n+1} = Q^{*,n} + \delta Q$, where n is the iterations number, proceeds until convergence of all the variables is reached (we require an absolute accuracy of 10^{-7}).

Once the intermediate velocities and total pressure are recovered, the intermediate conserved quantities are computed from

$$
\begin{aligned}
D^* &= \frac{\lambda - v_x}{\lambda - v_x^*} D , \\
E^* &= \frac{\lambda E - \mathcal{F}_E + p^* v_x^* - (\mathbf{v}^* \cdot \mathbf{B}^*) B_x^*}{\lambda - v_x^*} , \\
\mathbf{m}^* &= (E^* + p^* + D^*) \mathbf{v}^* - (\mathbf{v}^* \cdot \mathbf{B}^*) \mathbf{B}^* .
\end{aligned} \tag{4.30}
$$

The numerical fluxes are then computed from the jump conditions of Equation (4.7).

When one or more variables fail to converge within 20 iterations, we switch to the simpler HLL method (this has shown, in our experience, to greatly improve the range of applicability of the solver).

We point out, however, that this formulation does not satisfy the state consistency condition given by Equation (4.8), nor the flux condition (4.9). The reason for this incongruity stems from the assumed continuity of B^* across the middle wave while keeping a jump in the transverse velocities. As one can immediately verify, in fact, the two assumptions are not compatible with the Rankine-Hugoniot jump conditions for the transverse components of magnetic field across the contact mode, e.g.,

$$\lambda^* \left(B^*_{y,R} - B^*_{y,L} \right) \neq v^*_x \left(B^*_{y,R} - B^*_{y,L} \right) - B_x \left(v^*_{y,R} - v^*_{y,L} \right) , \tag{4.31}$$

which trivially follows from Equation (4.22) together with the assumption $\lambda^* \equiv v^*_x$. As a matter of fact, this inconsistency extends also to the momentum and energy jump conditions across the middle wave.

4.1.3 HLLD

A further step was made by Mignone, Ugliano, and Bodo (2009) who developed a HLL-type Riemann solver able to preserve both contact discontinuities and Alfvén waves by extending the classical solver of Miyoshi and Kusano (2005) to relativistic MHD. Despite it complexity, the HLLD (here 'D' stands for Discontinuities) is able to reduce drastically the numerical dissipation at the cost of solving a nonlinear equation through an iterative scheme.

Here, the Riemann fan is approximated by introducing five waves: two outermost fast shocks, two rotational discontinuities and a contact surface in the middle (slow waves are not considered). Since the normal velocity is no longer constant across the rotational waves, the solver is more elaborate than its classical counterpart. Still, proper closure is obtained by solving a non-linear scalar equation in the total pressure variable which, for the chosen configuration, has to be constant over the whole Riemann fan. Hereafter we summarize the procedure and refer the reader to Mignone, Ugliano, and Bodo, 2009 for the details of the derivation.

The system of jump conditions is written in terms of the 8 unknonws $D, v_x, v_y, v_z,$ B_y, B_z, w, p to express states and fluxes:

$$\mathscr{U}_S = \left(D, w\gamma^2 v_k - b_0 b_k, w\gamma^2 - p - b_0 b_0, B_k \right) ,$$
$$\mathcal{F}_S = \left(D v_x, w\gamma^2 v_x v_k - b_k b_x + p\delta_{ik}, w\gamma^2 v_x - b_0 b_x, B_k v_x - B_x v_k \right) , \tag{4.32}$$

where $S = L, aL, cL, cR, aR, R$ labels one of the possible 6 states (see the third panel in Figure 4.1) while $k = x, y, z$ is the subscript for the spatial component. If λ_S separates state S from state S' (clockwise), state and fluxes must satisfy the jump conditions

$$(\lambda \mathscr{U} - \mathcal{F})_S = (\lambda \mathscr{U} - \mathcal{F})_{S'} . \tag{4.33}$$

We begin from the states immediately behind the outermost fast waves. Dropping the indices aL or aR in the unknowns and using λ to denote either λ_L or λ_R, the following expressions for the velocities in the region aL and aR can be derived:

$$v_x = \frac{B_x\left(AB_x + \lambda C\right) - \left(A + G\right)\left(p + R_{m_x}\right)}{X}, \tag{4.34}$$

$$\mathbf{v}_t = \frac{Q\mathbf{R}_{m_t} + \mathbf{R}_{B_t}\left[C + B^x\left(\lambda R_{m_x} - R_E\right)\right]}{X}, \tag{4.35}$$

where $\mathbf{v}^t = (0, v_y, v_z)$, while the different R_Q's denote the components of the array $R = (\lambda \mathscr{U} - \mathcal{F})_S$ corresponding to variable Q, with $S = L, R$ for the left or right fast magnetosonic wave, respectively. The remaining quantities are defined as

$$
\begin{aligned}
A &= R_{m_x} - \lambda R_E + p\left(1 - \lambda^2\right), \\
G &= \mathbf{R}_{B_t} \cdot \mathbf{R}_{B_t}, \\
C &= \mathbf{R}_{m_y} \cdot \mathbf{R}_{B_z}, \\
Q &= -A - G + (B^x)^2\left(1 - \lambda^2\right), \\
X &= B_x\left(A\lambda B_x + C\right) - \left(A + G\right)\left(\lambda p + R_E\right).
\end{aligned}
\tag{4.36}
$$

Having defined the three components of velocity through Equations (4.34)-(4.35), one immediately obtains the transverse magnetic field, total enthalpy, density and energy from the jump conditions across the fast waves:

$$\mathbf{B}_t = \frac{\mathbf{R}_{B_t} - B_x\mathbf{v}_t}{\lambda - v_x}, \quad w = p + \frac{R_E - \mathbf{v} \cdot \mathbf{R}_m}{\lambda - v_x}, \tag{4.37}$$

$$D = \frac{R_D}{\lambda - v_x}, \quad E = \frac{R_E + pv_x - (\mathbf{v} \cdot \mathbf{B})B_x}{\lambda - v_x}, \tag{4.38}$$

while the momentum components follow from $m_k = (E + p)v_k - (\mathbf{v} \cdot \mathbf{B})B_k$

At the Alfvén waves, we take advantage of the fact that the expressions

$$K^k_{cL} = K^k_{aL} = \left[\frac{R_{m_k} + p\delta_{kx} - R_{B_k}S_x\sqrt{w}}{\lambda p + R_E - B_xS_x\sqrt{w}}\right]_L, \tag{4.39}$$

$$K^k_{cR} = K^k_{aR} = \left[\frac{R_{m_k} + p\delta_{kx} + R_{B_k}S_x\sqrt{w}}{\lambda p + R_E + B_xS_x\sqrt{w}}\right]_R, \tag{4.40}$$

are invariant, respectively, across λ_{aL} and λ_{aR} (Anile and Pennisi, 1987) and that $K^x_{aL} = \lambda_{aL}$, $K^x_{aR} = \lambda_{aR}$. In the previous expressions $S_x = \text{sign}(B_x)$ and the R's are the components of Equation 4.33 (with $S = L, R$) computed at the outermost waves using either $\lambda = \lambda_L$ or $\lambda = \lambda_R$.

Finally, we impose continuity of the normal velocity across the tangential discontinuity, $v_{x,cL} - v_{x,cR} = 0$, yielding

$$\left(K^x_{aR} - K^x_{aL}\right) = B^x\left[\frac{1 - \mathbf{K}^2_R}{S_x\sqrt{w_R} - \mathbf{K}_R \cdot \mathbf{B}_c} + \frac{1 - \mathbf{K}^2_L}{S_x\sqrt{w_L} + \mathbf{K}_L \cdot \mathbf{B}_c}\right], \tag{4.41}$$

where $\mathbf{B}_c = \mathbf{B}_{cL} = \mathbf{B}_{cR}$ is the magnetic field in proximity of the contact wave, obtained from the consistency condition between the innermost waves

$$\mathbf{B}_c = \frac{[\mathbf{B}(\lambda - v_x) + B_x \mathbf{v}]_{aR}}{\lambda_{aR} - \lambda_{aL}} - \frac{[\mathbf{B}(\lambda - v_x) + B_x \mathbf{v}]_{aL}}{\lambda_{aR} - \lambda_{aL}}. \qquad (4.42)$$

Equation (4.41) is a nonlinear equation in the total pressure p and has to be solved by means of a standard root-finder method. Once p has been found with sufficient accuracy, the velocities across the tangential discontinuity can be found by inverting the relation that holds between K^k and the velocity v_k. The final result is

$$v_k = K^k - \frac{B_k(1 - \mathbf{K}^2)}{\pm S_x \sqrt{w} - \mathbf{K} \cdot \mathbf{B}}, \qquad (4.43)$$

for $k = x, y, z$. Finally, density, energy and momentum are recovered from the jump conditions across λ_{aL} and λ_{aR} similarly to what done after Equation (4.38).

Once the solution has been found we compute the final interface flux through

$$\hat{\mathcal{F}} = \begin{cases} \mathcal{F}_L & \text{if} \quad 0 < \lambda_L \\ \mathcal{F}_{aL} & \text{if} \quad \lambda_L < 0 < \lambda_{aL}, \\ \mathcal{F}_{aL} + \lambda_{aL}(\mathscr{U}_{cL} - \mathscr{U}_{aL}) & \text{if} \quad \lambda_{aL} < 0 < \lambda_c, \\ \mathcal{F}_{aR} + \lambda_{aR}(\mathscr{U}_{cR} - \mathscr{U}_{aR}) & \text{if} \quad \lambda_c < 0 < \lambda_{aR}, \\ \mathcal{F}_{aR} & \text{if} \quad \lambda_{aR} < 0 < \lambda_R, \\ \mathcal{F}_R & \text{if} \quad \lambda_R < 0, \end{cases} \qquad (4.44)$$

where

$$\begin{aligned} \mathcal{F}_{aL} &= \mathcal{F}_L + \lambda_L (\mathscr{U}_{aL} - \mathscr{U}_L), \\ \mathcal{F}_{aR} &= \mathcal{F}_R + \lambda_R (\mathscr{U}_{aR} - \mathscr{U}_R), \end{aligned} \qquad (4.45)$$

follow from the jump conditions across the fast waves. Note that Equation (4.44) corrects the original Eq. [16] reported in Mignone, Ugliano, and Bodo, 2009 which contains an erroneous speed λ_c in the third and fourth cases.

Although Equation (4.41) may have, in some circumstances, more than one root, the rationale for choosing the physically relevant solution is based on positivity of density and on preserving the correct eigenvalue order, i.e., $\lambda_{aL} > \lambda_L$, $v_{x,cL} > \lambda_{aL}$ for the left state and $\lambda_{aR} < \lambda_R$, $v_{x,cR} < \lambda_{aR}$ for the right state. When one or more of these conditions cannot be met, we revert to the simpler HLL solver.

4.1.4 HLLEM

Other approaches have also been attempted as well to restore the intermediate missing waves in the solution of the Riemann problem. Following the approach of Einfeldt et al. (1991), Dumbser and D. S. Balsara (2016) have proposed a solution to the Riemann problem based on the HLLEM (called also HLLI in some papers) formulation which restores selected anti-diffusive flux terms on top of the HLL structure, in order to capture selected intermediate waves.

The solution of the Riemann problem can be written as three possible states

$$
\mathscr{U}(0, t) = \begin{cases} \mathscr{U}_L & if \ \lambda_L \geq 0, \\ \mathscr{U}^{\text{hll}} - \mathscr{U}^{\text{hllem}} & if \ \lambda_L \leq 0 \leq \lambda_R, \\ \mathscr{U}_R & if \ \lambda_R \leq 0, \end{cases} \tag{4.46}
$$

as in the HLL formulation. The intermediate state, for the sake of clarity, has been split into the HLL component and an antidiffusive term

$$
\mathscr{U}^{\text{hllem}} = \sum_m \mathbf{R}_*^m(\mathscr{U}_*) \delta_*^m(\mathscr{U}_*) \mathbf{L}_*^m(\mathscr{U}_*) \frac{\lambda_R + \lambda_L}{\lambda_R - \lambda_L} (\mathscr{U}_R - \mathscr{U}_L), \tag{4.47}
$$

where m indicates the $m-$th intermediate eigenvalue. The vectors $\mathbf{R}_*$ and $\mathbf{L}_*$ are the right and left eigenvectors of the RMHD equations, where the subscript $*$ means that they are computed from the average of the conserved variables, while the matrix δ_* is computed as follows:

$$
\delta_*^m(\mathscr{U}) = 1 - \frac{\lambda_{m,*} - |\lambda_{m,*}|}{2\lambda_L} - \frac{\lambda_{m,*} + |\lambda_{m,*}|}{2\lambda_R}. \tag{4.48}
$$

The corresponding numerical fluxes are:

$$
\hat{\mathcal{F}} = \begin{cases} \mathcal{F}_L & if \ \lambda_L \geq 0, \\ \mathcal{F}^{\text{hll}} - \mathcal{F}^{\text{hllem}} & if \ \lambda_L \leq 0 \leq \lambda_R, \ , \\ \mathcal{F}_R & if \ \lambda_R \leq 0, \end{cases} \tag{4.49}
$$

where $\mathcal{F}^{\text{HLLEM}}$ is the antidiffusive term

$$
\mathcal{F}^{\text{hllem}} = \left(\frac{\lambda_R \lambda_L}{\lambda_R - \lambda_L} \right) \sum_m \delta_*^m \mathbf{R}_*^m \left[\mathbf{L}_*^m \cdot (\mathscr{U}_R - \mathscr{U}_L) \right]. \tag{4.50}
$$

Clearly, such solver becomes complete if all of the intermediate waves are considered, although, as pointed by D. S. Balsara and Kim (2016) and Punsly, D. Balsara, et al. (2016), the eigenvectors for the fast and slow magnetosonic waves are very expensive to evaluate computationally. Therefore we consider, as in Punsly, D. Balsara, et al. (2016), the 5-wave HLLEM formulation, which captures only contact discontinuities and Alfvén waves, with eigenvalues, respectively,

$$
\lambda_e = v^x \qquad \lambda_{a,\pm} = \frac{b^x \pm \sqrt{w_T} u^i}{b^0 \pm \sqrt{w_T} \gamma}, \tag{4.51}
$$

where $w_T = \rho h + b^2$ is the total enthalpy.

Finally we note that we provided a slightly modified strategy from Antón et al. (2010) to recover the left and right eigenvectors corresponding to the contact and Alfvén waves. This is shown in detail in Appendix C.

4.1.5 GFORCE

The generalized FORCE flux (E. F. Toro and Titarev, 2006) is a generalization of the First ORder CEntred (FORCE) scheme and it consists of a convex average of the Lax-Wendroff ($\mathcal{F}^{LW}$) and Lax-Friedrichs ($\mathcal{F}^{LF}$) fluxes:

$$\mathcal{F} = \omega_g \mathcal{F}^{LW} + (1 - \omega_g)\mathcal{F}^{LF}. \tag{4.52}$$

where $\omega_g \in [0,1]$. Here the Lax Wendroff flux is computed as $\mathcal{F}^{LW} = \mathcal{F}(\mathscr{U}^{LW})$, where $\mathcal{F}$ is given by Equation (2.24), and

$$\mathscr{U}^{LW} = \frac{\mathscr{U}_R + \mathscr{U}_L}{2} - \frac{\tau}{2}(\mathcal{F}_R - \mathcal{F}_L), \tag{4.53}$$

while the Lax-Friedrichs flux is defined by

$$\mathcal{F}^{LF} = \frac{\mathcal{F}_R + \mathcal{F}_L}{2} - \frac{1}{2\tau}(\mathscr{U}_R - \mathscr{U}_L). \tag{4.54}$$

In the original formulation by E. F. Toro and Titarev (2006), the variable τ (which has the dimensions of inverse velocity) is set to be $\tau = \Delta t/\Delta x$. However, we choose to follow the formulation of Mignone and Del Zanna (2021), where τ is the inverse of the local maximum signal velocity:

$$\tau = [\max(|\lambda_L|, |\lambda_R|)]^{-1}. \tag{4.55}$$

The parameter ω_g can be tuned according to stability and monotonicity criteria, as thoroughly explained in E. F. Toro and Titarev (2006) and E. Toro (2009). While $\omega_g = 0$ reduces the scheme to the simple Lax-Fridrichs solver, the choice $\omega_g = 1/2$ yields the FORCE flux which is precisely the arithmetic mean between the Lax-Friedrichs and Lax-Wendroff fluxes. This scheme has reduced dissipation when compared to the LF solver and it corresponds to a monotone scheme with the maximum region of monotonicity, without resorting to wave propagation information. Larger values of ω_g are also possible without violating the monotonicity region by choosing

$$\omega_g = \frac{1}{1 + c_g}, \tag{4.56}$$

where $c_g \in [0,1]$ is the Courant number. Equation (4.56) will be used dy default unless otherwise stated.

4.2 Numerical Benchmarks

4.2.1 Isolated Contact and Rotational Waves

We begin our benchmark section by testing the solvers ability in capturing isolated contact and rotational waves, as shown in Mignone, Ugliano, and Bodo, 2009. The initial conditions together with the final time and number of points are listed in the 1st and 2nd row in Table 4.1.

TABLE 4.1: Initial conditions for left and right states (column 2-9) and adiabatic index (col 10) for the 1D test problems. Here "CW" and "RW" refer to the isolated contact and rotational wave, while "ST1"-"ST4" corresponds to the different shock tubes.

Case		ρ	p	v_x	v_y	v_z	B_x	B_y	B_z	Γ_{eos}
CW	L	10.0	1.0	0.0	0.7	0.2	5.0	1.0	0.5	5/3
	R	1.0	1.0	0.0	0.7	0.2	5.0	1.0	0.5	
RW	L	1.0	1.0	0.4	-0.3	0.5	2.4	1.0	-1.6	5/3
	R	1.0	1.0	0.37724	-0.48239	0.42419	2.4	-0.1	-2.17821	
ST1	L	1.0	1.0	0.0	0.0	0.0	0.5	1.0	0.0	2.0
	R	0.125	0.1	0.0	0.0	0.0	0.5	-1.0	0.0	
ST2	L	1.08	0.95	0.4	0.3	0.2	2.0	0.3	0.3	5/3
	R	1.0	1.0	-0.45	-0.2	0.2	2.0	-0.7	0.5	
ST3	L	1.0	0.1	0.999	0.0	0.0	10.0	7.0	7.0	5/3
	R	1.0	0.1	-0.999	0.0	0.0	10.0	-7.0	7.0	
ST4	L	1.0	5.0	0.0	0.3	0.4	1.0	6.0	2.0	5/3
	R	0.9	5.3	0.0	0.0	0.0	1.0	5.0	2.0	
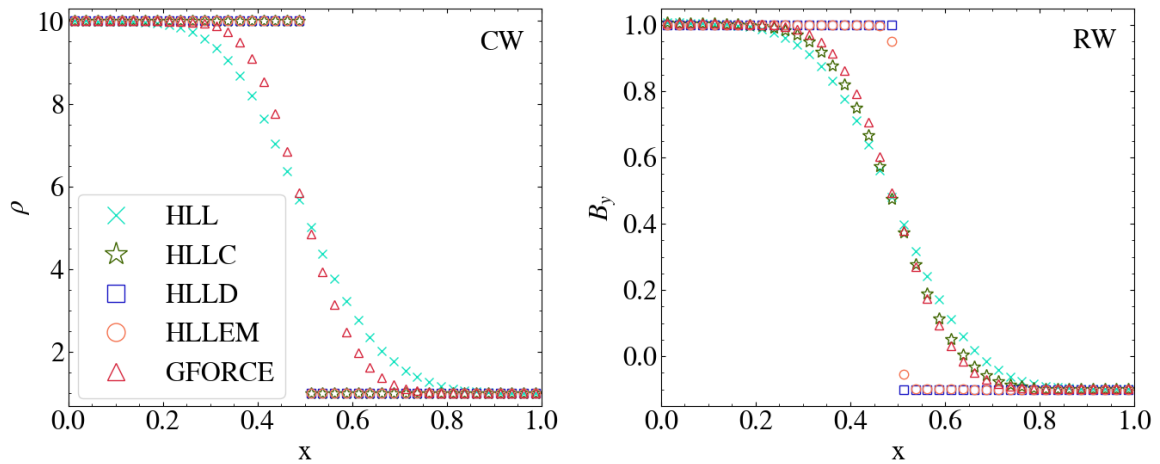
FIGURE 4.2: Left panel: density profile at $t = 1$ for a single contact wave. Right panel: y-component of magnetic field at $t = 1$ in the case of an isolated rotational discontinuity. Different solvers are labeled in the legend.
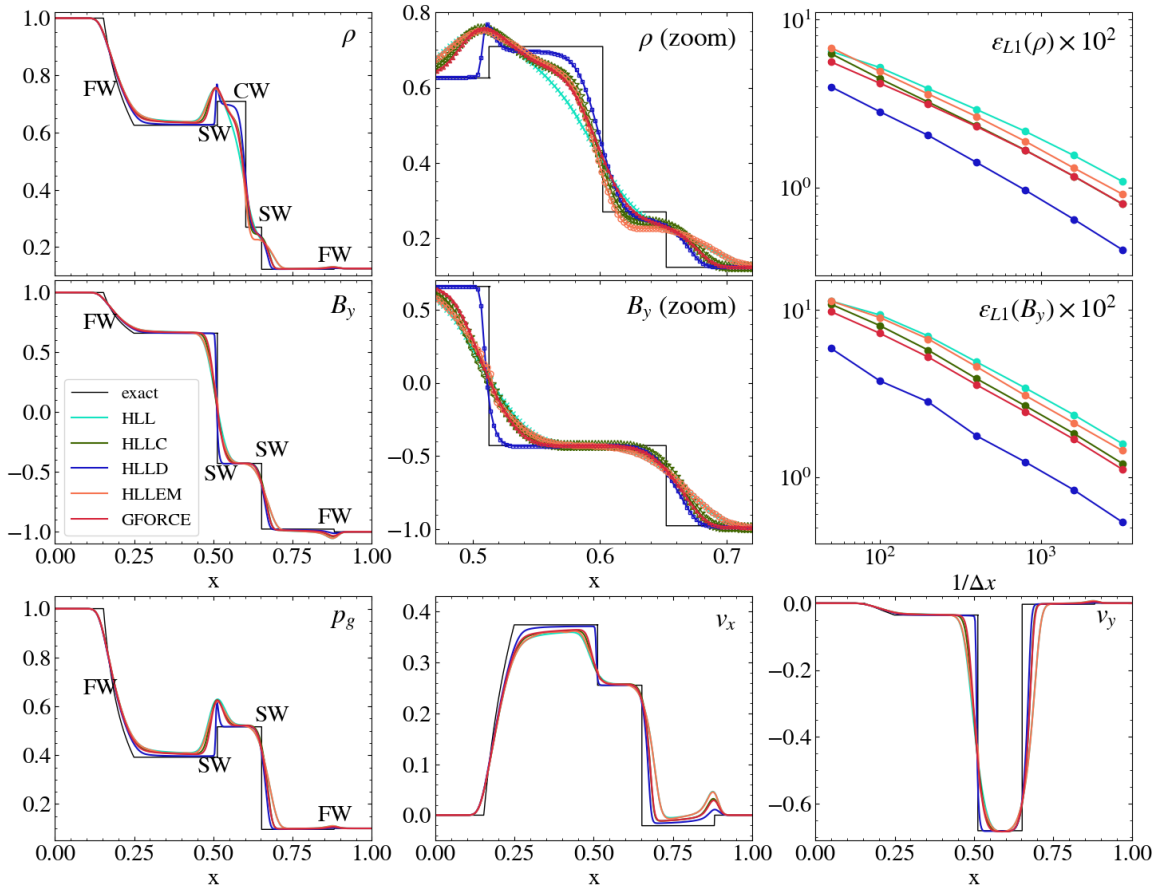
FIGURE 4.3: Numerical results for the 1$^{\text{st}}$ shock tube (ST1) at $t = 0.4$ with 400 grid zones and different Riemann solvers. Top panels (left to right): density profile, closeup view across the contact mode and $L1$-norm errors. Middle panels: same as before but for the y-component of magnetic field. Bottom panels: gas pressure, x- and y-components of velocity.

In the case of an isolated contact wave, the left panel in Figure 4.2 shows that the numerical solutions recovered HLLD, HLLC and HLLEM solvers resolve the contact mode exactly, while HLL and GFORCE spread the discontinuity over several zones, although the latter performs noticeably better than the former (~ 22 vs. ~ 16 cells, respectively).

For a single rotational wave, only the HLLEM and HLLD solver catch the correct behavior as can be inferred from the right panel of Figure 4.2 showing the profile of B_y. On the contrary, results obtained with the other solvers (i.e., HLL, HLLC and GFORCE) present significant amount of numerical diffusion by spreading the initial jump over ~ 10 computational zones. No difference has been found between HLLC-MB and HLLC-KB.

4.2.2 Shock Tube 1

This test, performed previously by D. S. Balsara, 2001; Mignone and Bodo, 2006; Mignone, Ugliano, and Bodo, 2009; Antón et al., 2010, contains only co-planar vectors on either side of the discontinuity and thus no rotational wave can form in the solution. The approximate structure of the Riemann fan is shown in Figure 4.3 at $t = 0.4$ for various solvers. HLLD performs the best, by showing enhanced resolution and better accuracy in proximity of all waves: at the fast rarefaction tail (FW, $x \approx 0.25$), the compound wave (SW, $x \approx 0.5$), the contact mode (CW, $x \approx 0.6$), the right-facing slow shock (SW, $x \approx 0.65$) and the fast shock (FW, $x \approx 0.9$). A zoomed view across the contact wave (top central panel), reveals that also HLLC, HLLEM and GFORCE capture equally well this mode while relatively poor resolution is observed at the slow shock (central panel, closeup view on B_y), where the HLLEM solver shows a slightly worse performance than the HLLC and GFORCE Riemann solvers. This is also confirmed from the $L1$-norm error of density and y-component of magnetic field (rightmost top and middle panels), indicating that the HLLD has considerable smaller errors, followed by GFORCE, HLLC and, close-by, by HLLEM and HLL.

This result should not be surprising, since the characteristic information restored in the HLLEM solver is based on a linearization process and can cope specifically only with those waves it was initially intended to resolve (contact and rotational waves in our implementation). On the contrary, HLLC and HLLD solvers stem from a nonlinear approximation to the Riemann fan, in conformity with the integral representation of the Riemann fan where, for mathematically consistency, fewer conditions are imposed on the internal wave structure. This leads to a set of jump conditions where flow variables can experience jumps not necessarily corresponding to the specific wave (e.g., contact or Alfvén) they were originally designed for.

4.2.3 Shock Tube 2

This test, also considered in D. S. Balsara, 2001; Mignone, Ugliano, and Bodo, 2009; Antón et al., 2010; Beckwith and Stone, 2011, features a non-planar Riemann problem leading to a change in orientation of the transverse magnetic field across the Riemann fan. The emerging wave pattern consists of a contact wave (CW at $x \approx 0.475$) separating a left-going fast shock (FW, $x \approx 0.13$), Alfvén wave (AW, $x \approx 0.185$) and slow rarefaction (SW, $x \approx 0.19$) from a slow shock (SW, $x \approx 0.7$), Alfvén wave (AW, $x \approx 0.725$) and fast shock (FW, $x \approx 0.88$) heading to the right.

Results, at $t = 0.55$ are shown in Figure 4.4. Now the differences between the chosen Riemann solvers are less pronounced. Such alikeness is reflected in the $L1$-norm errors in the right panels, where HLLD, GFORCE and HLLC show similar accuracy, while the HLLEM and HLL solvers exhibit somewhat larger errors.

The contact mode is well resolved by all solvers (although with spurious undershoots, see the top central panel), exception made for HLL and GFORCE which are not designed to minimize the diffusion across the contact wave. As for the previous test, we again note that GFORCE spreads the contact wave over fewer zones when compared to HLL.

The slow modes, which are not designed to be resolved by any of such solvers (see the central panels of the 2$^{\text{nd}}$ and 3$^{\text{rd}}$ rows), are better captured by the solvers
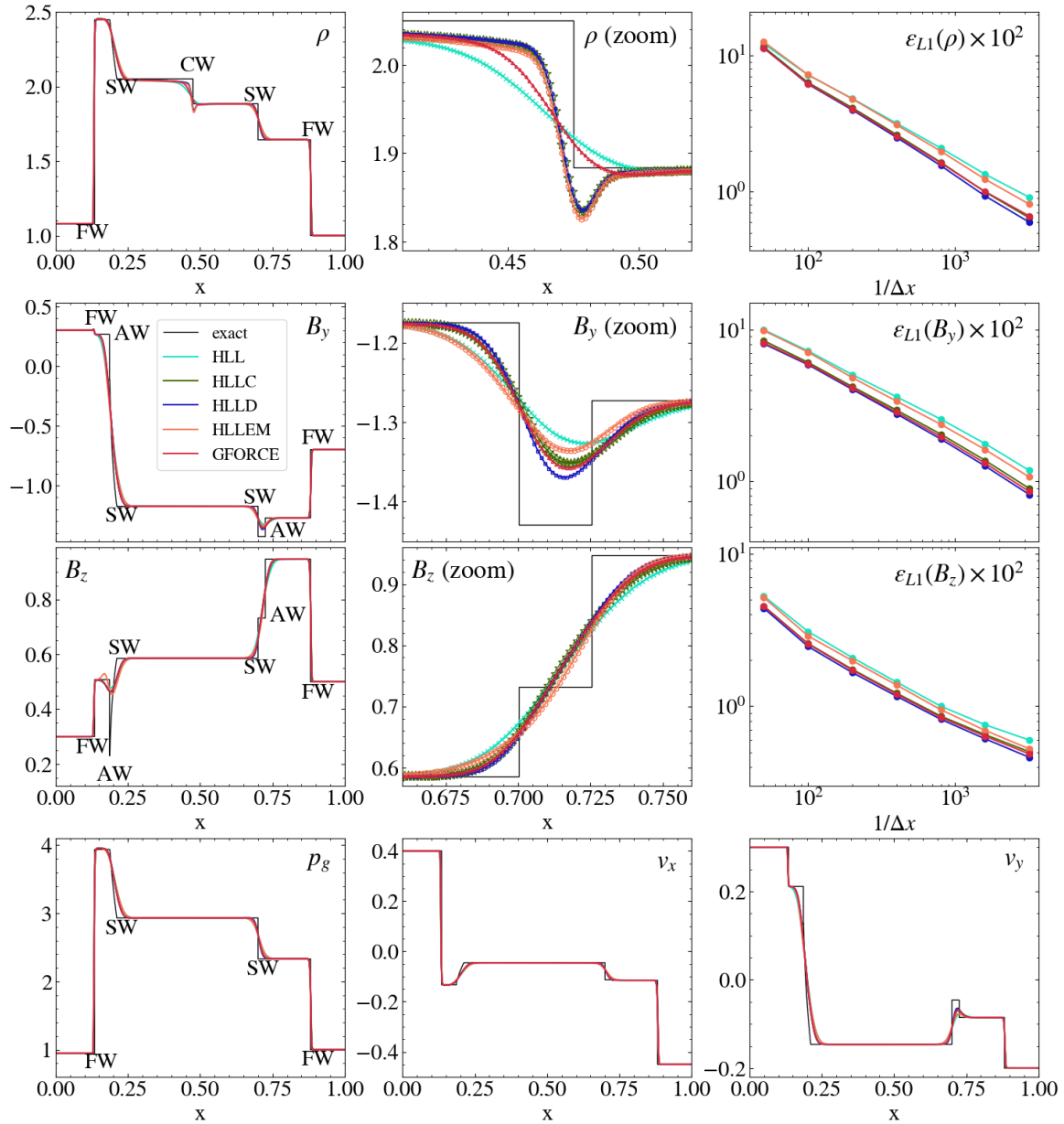
FIGURE 4.4: Results for the 2nd shock tube (ST2) at $t = 0.55$ using a 1st-order scheme with 800 grid zones. Top row (left to right): density profile, closeup view across the contact wave and $L1$-norm errors. Second (third) row: y- (z-) component of magnetic field, closeup view across the slow and Alfvén wave and $L1$-norm errors. Bottom row: profiles for gas pressure, x- and y-velocity components.
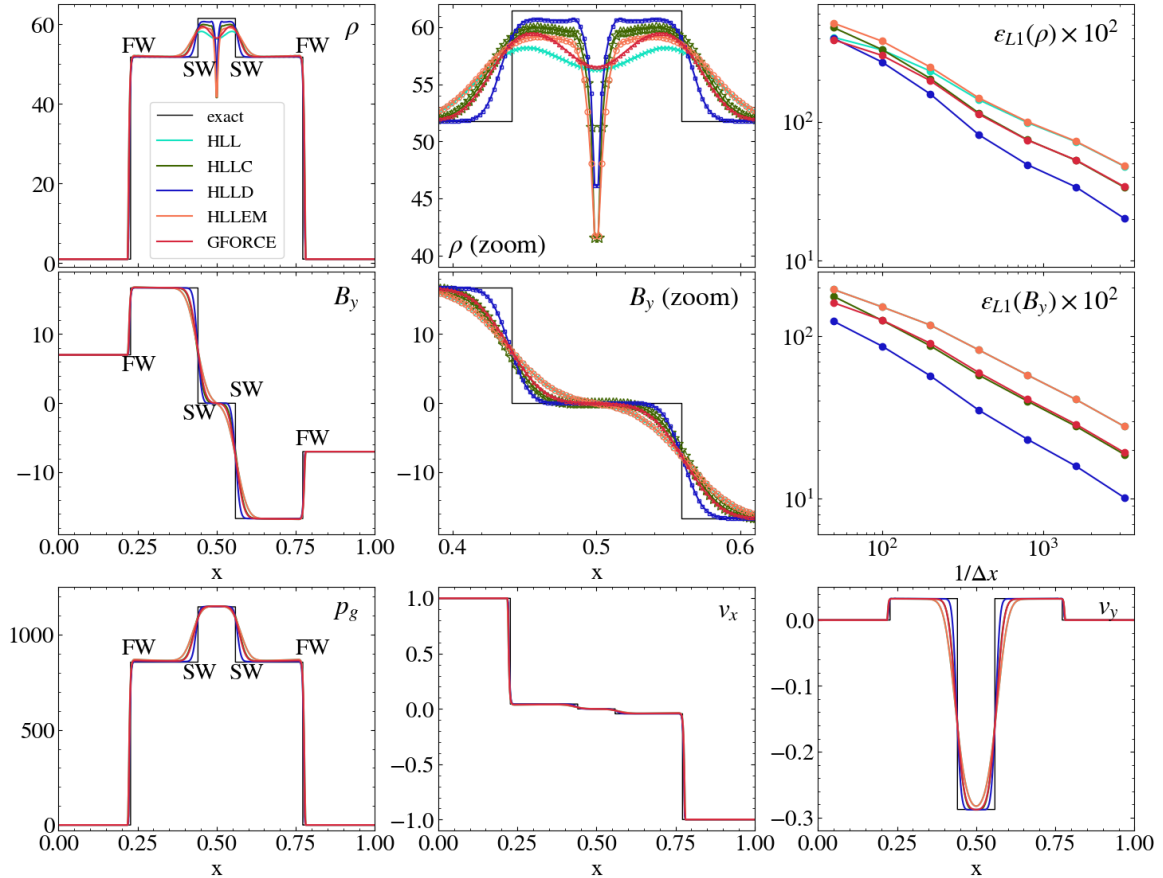
FIGURE 4.5: Same as Figure 4.3 but for the $3^{\rm rd}$ shock tube (ST3).

HLLD, GFORCE and HLLC, while the HLLEM and the HLL solvers behave in the same way. Since the slow and the Alfvén modes are very close to each other, the accuracy of the HLLEM solver results strongly reduced despite its ability to capture the rotational discontinuities. Furthermore, the HLLEM shows a non-physical overshoot behind the left Alfvén wave (see left panel of the 3-rd row), which vanishes at higher resolution.

The previous considerations are verified more quantitatively by the three error plots in the rightmost panels, again confirming that the HLLD Riemann solver yields the most accurate results followed, in decreasing order of accuracy, by the solvers GFORCE, HLLC, HLLEM and HLL. Note that, as in the previous test, while the GFORCE and the HLLC solvers have the same level of accuracy in the density, the GFORCE performs slightly better when looking at other variables because of the reduce dissipation along the slow modes.

4.2.4 Shock Tube 3

The initial conditions for this test problem, given in Table 4.1, sets the stage for two oppositely colliding relativistic streams. This test problem has been previously considered also by D. S. Balsara, 2001; Mignone and Bodo, 2006; Mignone, Ugliano, and Bodo, 2009; Antón et al., 2010.

The impact generates two strong relativistic fast shocks ($x \approx 0.23$, $x \approx 0.77$) heading outwards in opposite directions about the impact point at $x = 0.5$, see Figure 4.5. Behind, two slow shocks (SW, $x \approx 0.44$ and $x \approx 0.56$) delimit a high-pressure and constant density region. Similarly to ST1, this is a co-planar problem and no rotational mode can develop in the solution. No contact wave is formed either. Because of the absence of contact and Alfvén waves, the HLLEM and the HLL solvers are not distinguishable in every variable (but the density).

We notice that the GFORCE solver suffers from negative values of gas density and pressure caused by the strong gradients of the fast shocks. In order to overcome such issue, we switched to the FORCE flux ($\omega_g = 1/2$) which still yields reduced numerical diffusion when compared to the HLL solver.

The spurious density dip at the initial collision point ($x = 0.5$) is a symptom of the "wall heating" phenomenon occurs (Noh, 1987; Donat and Marquina, 1996). Because of the larger numerical diffusion, the HLL and the FORCE solvers are less prone to such pathology (the error respect to the analytical solution at $x = 0.5$ is, respectively, $\sim 8.4\%$ and $\sim 7.9\%$). On the other hand, HLLD, HLLC and HLLEM feature a deeper "hole" in the rest-mass density (the numerical undershoot is, respectively, $\sim 25\%$, $\sim 32.3\%$ and $\sim 32\%$). As a consequence, as shown in the top right panel, the HLL and the HLLD solvers shows a similar accuracy in the density at low resolution. As the number of grid cells increases, this density undershoot is progressively confined to a smaller fraction of the computation domain, leading to a better accuracy in the HLLD solver. This feature is not found in other variables, where the HLLD solver performs significantly better than the other solvers. From the error plots, we evince that the FORCE solver performs better than the HLLEM and HLL solver with errors comparable to the HLLC-MB.

4.2.5 Shock Tube 4

The initial discontinuity of ST4, which corresponds to the "Generic Alfvén test" of Giacomazzo and Rezzolla (2006), leads to solution consisting of 7 waves: a fast rarefaction ($x \approx 0.04$), a rotational wave ($x \approx 0.44$), a left-going slow shock ($x \approx 0.46$), a contact discontinuity ($x \approx 0.52$), a right-going slow shock ($x \approx 0.57$), a rotational wave ($x \approx 0.58$) and a fast shock ($x \approx 0.97$).

Results, plotted in Figure 4.6, demonstrate that the HLLD is able to reach better accuracy than all the other solvers, as in the previous tests. Looking at the left-going slow and rotational modes (B_y profile in the central column, 2nd row), we observe that the HLLD solver is the only one able to resolve both modes, while all the other solvers are unable to capture them.

Again, we remark that HLLC and GFORCE solvers give comparable results. In particular, the HLLC solver provides a better resolution only at the contact wave (giving better results for the density error), while fast, slow and Alfvén modes are resolved with comparable accuracy.

Since the Alfvén mode is very prominent in the $z-$components of the magnetic field (central panel, 3rd row), the HLLEM is able to reach a higher precision, comparable to the HLLD solver. In addition, the HLLEM and the HLLD solvers are the only able to capture the right-going slow and Alfvén modes (visible from the y-component of **B**, central panel, 2nd row). Still, the HLLEM solver presents some
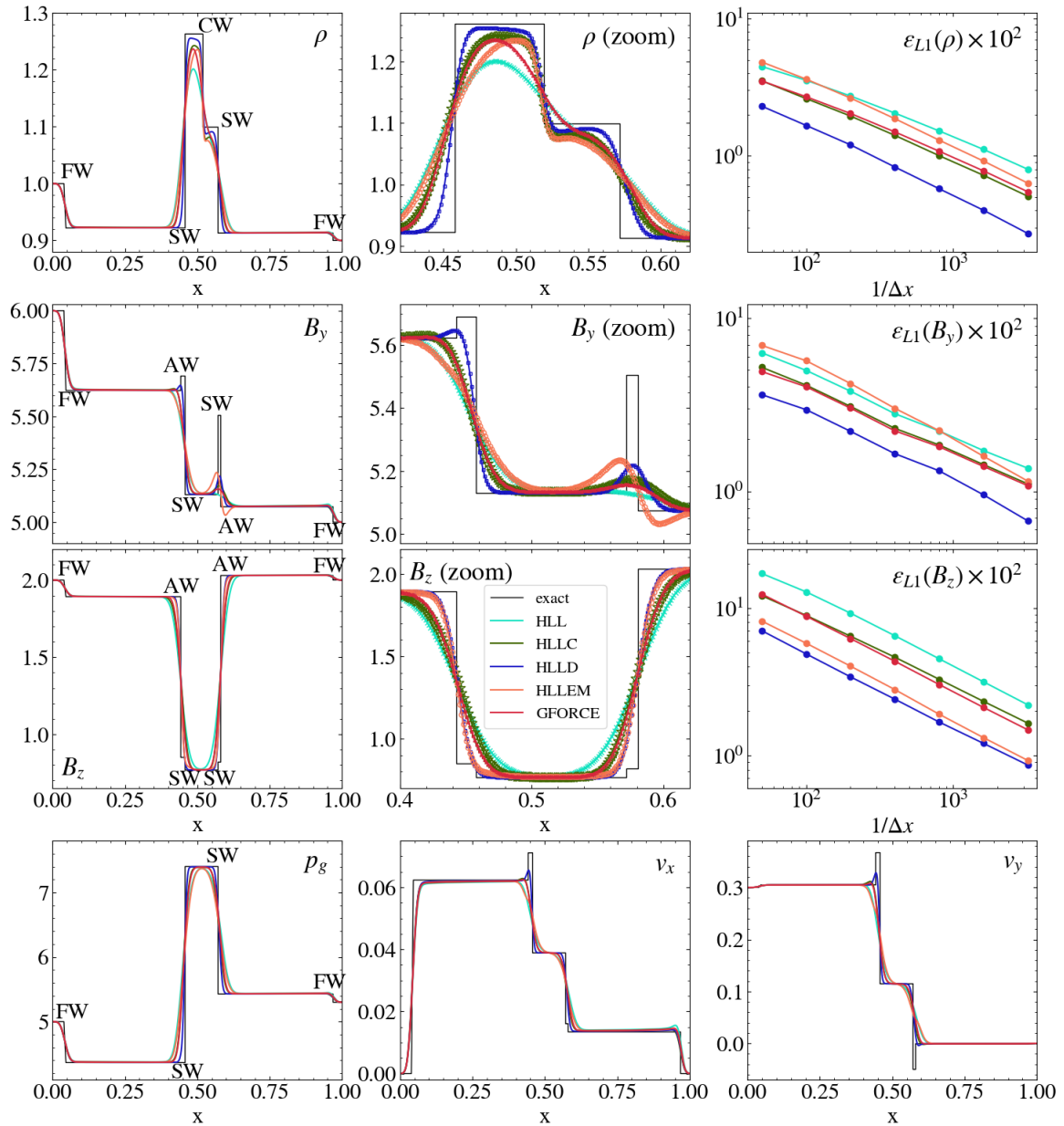
FIGURE 4.6: Same of 4.4 but for the 4th shock tube (ST4).
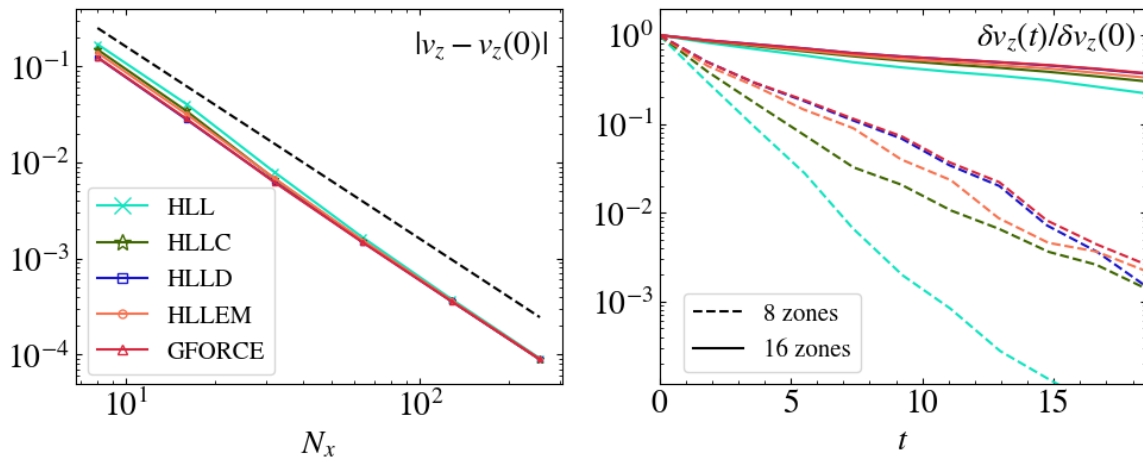
FIGURE 4.7: Left panel: L_1-norm error for v_z in the circularly polarized Alfvén test problem after one period $T = 1/\sqrt{2}v_A \approx 1.851$ and different Riemann solvers (see the legend). Right panel: amplitude decay as a function of time using, respectively, 8 (dashed lines) and 16 (solid lines) zones per wavelength.

unphysical undershoots in the y-component of the magnetic field, which (contrary to the expectation) severely affects the error. Such issue lowers at larger resolutions (see the error plots in the right panel, 2$^{\text{nd}}$ column). The other solvers show some barely visible structure (HLLC and GFORCE) or just a single blended wave (HLL solver).

4.2.6 Circularly Polarized Alfvén Waves

Next, we consider the propagation of large amplitude, circularly polarized (CP) Alfvén waves on a two-dimensional unit square domain, as in Del Zanna, Zanotti, et al., 2007. The initial condition consists of a region of uniform density and pressure ($\rho = p = 1$) while magnetic field and velocity, for a wave front propagating along the x' direction, are given by

$$\mathbf{B}' = B_0 \left(1, \eta \cos\phi\, \eta \sin\phi\right) \quad \mathbf{v}' = -v_A \left(0, \frac{B'_y}{B_0}, \frac{B'_z}{B_0}\right), \qquad (4.57)$$

where $\phi = k'x'$ is the wave phase, k' is the wavenumber. In Equation (4.57) $B_0 = 1$ is the (constant) magnetic field component in the direction of propagation, $\eta = 1$ is the amplitude and the Alfvén velocity v_A is computed from

$$v_A^2 = \frac{2\alpha}{1 + \sqrt{1 - 4\eta^2\alpha^2}} \qquad \alpha = \frac{B_0^2}{w_g + B_0^2(1 + \eta^2)}, \qquad (4.58)$$

and $w_g = \rho + \Gamma p/(\Gamma - 1)$. This yields $v_A \approx 0.382$ for our parameter choice (we use $\Gamma = 4/3$). The previous conditions provide an exact wave solution of the RMHD equations provided $\phi \to \phi - \omega t$, where $\omega = k'v_A$ is the angular frequency and are thus valid for arbitrary amplitude η.

We perform the test on a 2D Cartesian domain $x \in [0, L_x]$, $y \in [0, L_y]$ with $L_x = L_y = 1$ and rotate the coordinate system by an angle α around the z-axis, so that vectors are rotated according to

$$
\mathbf{q} = \mathsf{R}\,\mathbf{q}' \qquad\qquad \mathsf{R} = \begin{pmatrix} \cos\alpha & -\sin\alpha & 0 \\ \sin\alpha & \cos\alpha & 0 \\ 0 & 0 & 1 \end{pmatrix}, \qquad (4.59)
$$

where $\mathbf{q}$ is a generic vector in the rotated (computational) frame while $\mathbf{q}'$ is the corresponding vector in the 1D (unrotated) frame. The wave vector components are chosen so that exactly one wavelength fits along the domain sizes, $\mathbf{k} = (2\pi/L_x)\hat{e}_x + (2\pi/L_y)\hat{e}_y$ (note that ϕ is invariant under rotations). Computations are performed with $N_x \times N_x$ grid zones using a Courant number $C_a = 0.4$.

In the left panel of Figure 4.7 we measure, as a function of the resolution N_x, the accuracy of the selected Riemann solvers by computing, after one period $T = 1/(\sqrt{2}v_A)$, the L_1 norm errors of the vertical component of velocity v_z. Second-order accuracy is obtained with all solvers, although HLL has a slightly large errors at small resolutions.

In the right panel of Figure 4.7 we compare the dissipative properties of the different solvers by measuring the decay of the wave amplitude, defined as $\delta v^z = \max(v^z) - \min(v^z)$ (normalized to its initial value) up to ten revolutions, using 8 and 16 zones per wavelength, respectively. Overall, the HLLD and GFORCE Riemann solvers yield the smallest dissipation, followed by HLLEM and HLLC and lastly by HLL. At low resolution, the wave amplitudes decrease approximately by $\sim 10^{-3}$ of the nominal value (for the first four solvers) while to $\sim 10^{-5}$ for the HLL solver. By increasing the resolution to 16 zones, differences are less pronounced and wave amplitudes drop to ~ 0.37 (HLLD and GFORCE), ~ 0.33 (HLLEM), ~ 0.30 (HLLC) and ~ 0.22 (HLL).

We point out that the smoothness of the solution allowed the GFORCE scheme to be run with ω defined as in Equation (4.56) with $c_g = 0.4$. Smaller values of ω (higher values of c_g) bias the scheme towards a more diffusive behavior. In the limit $\omega \to 1/2$ one retrieves the FORCE scheme which yields results comparable with the HLLC solver for this problem.

4.2.7   Blast Waves

Cylindrical and spherical explosions in Cartesian coordinates challenge the robustness of the method and its response to different kinds of degeneracies.

Among the several variants of this problem discussed in the literature (see, for instance, Del Zanna, Bucciantini, and Londrillo, 2003; Mignone and Bodo, 2006; Del Zanna, Zanotti, et al., 2007; Beckwith and Stone, 2011; Martí, 2015; D. S. Balsara and Kim, 2016, and reference therein) here we consider the configuration given by Beckwith and Stone, 2011. In the (original) 2D version of the problem, the computational domain is defined by the square $x, y \in [-6, 6]$ initially filled with a uniform ($\rho = 10^{-4}$, $p = 5 \cdot 10^{-3}$) and static ($\mathbf{v} = 0$) medium. In 3D, the domain becomes a cube with $z \in [-6, 6]$. A high-pressure region is set up inside the region $r < 0.8$
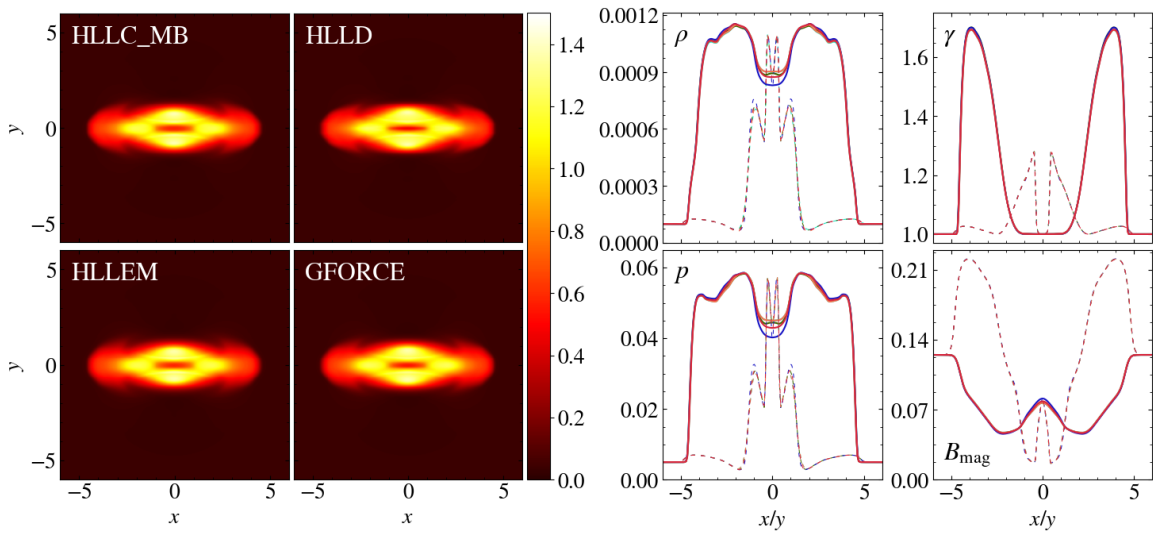
FIGURE 4.8: Results for the 2D blast wave problem at $t = 4$, for $B_0 = 0.5$ and $\phi = 0°$. In the left half we show Coloured maps of the plasma $\beta = 2p/B^2$ (left) for different Riemann solvers while in the right half we present 1D profiles along the x-axis (solid line) and y-axis (dotted lines). Color convention is the same adopted for previous tests in this chapter.
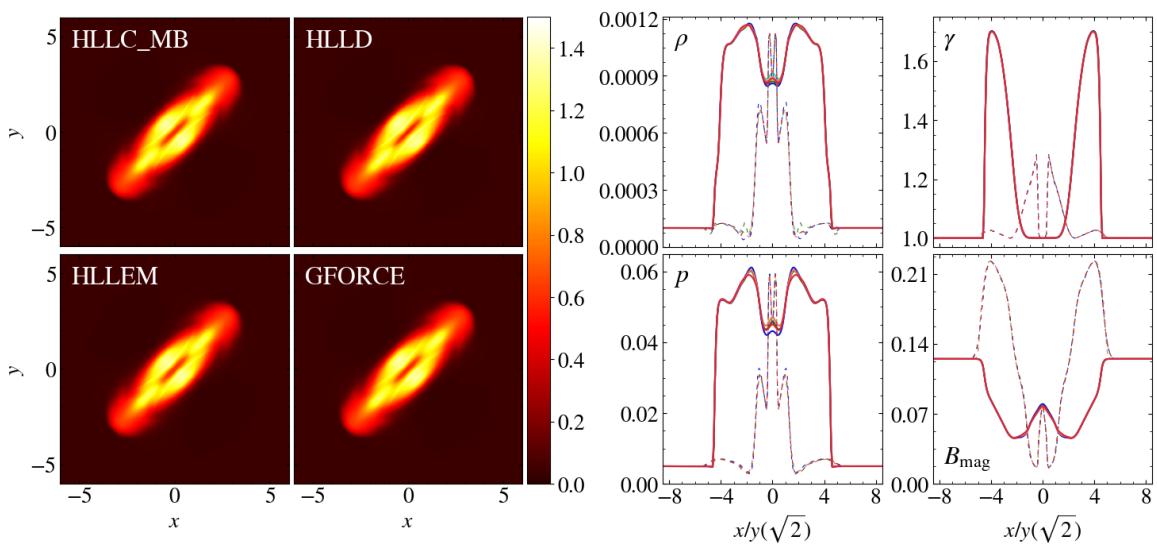
FIGURE 4.9: Same as Figure 4.8 but for the inclined case ($\phi = 45°$).
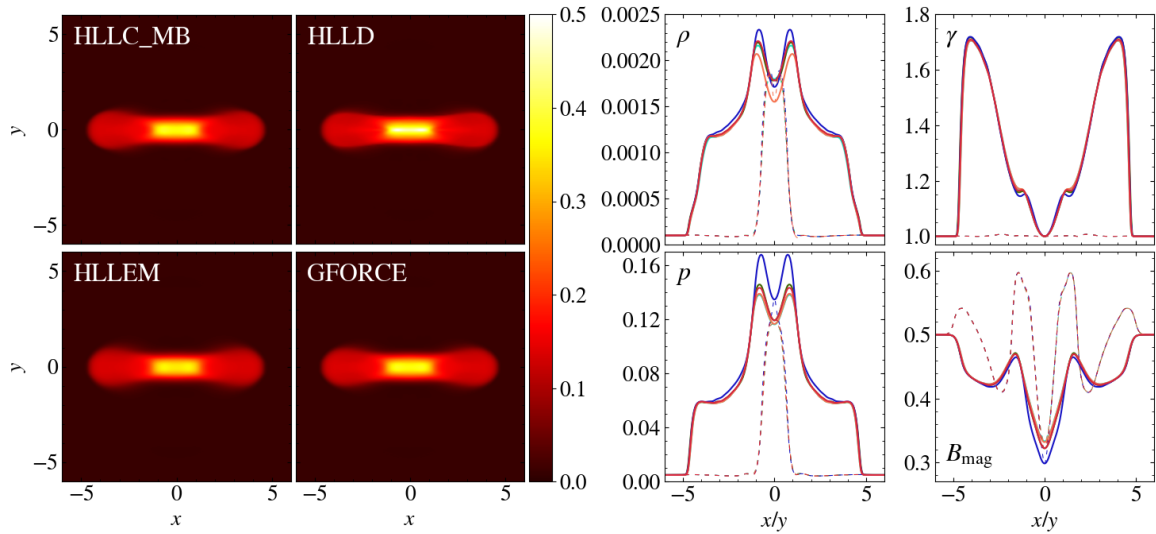
FIGURE 4.10: Same as Figure 4.8 but for the 3D case and strong magnetization $B_0 = 1$. Coloured maps are shown in the xz plane while 1D profiles are taken along the x-axis and y-axis.
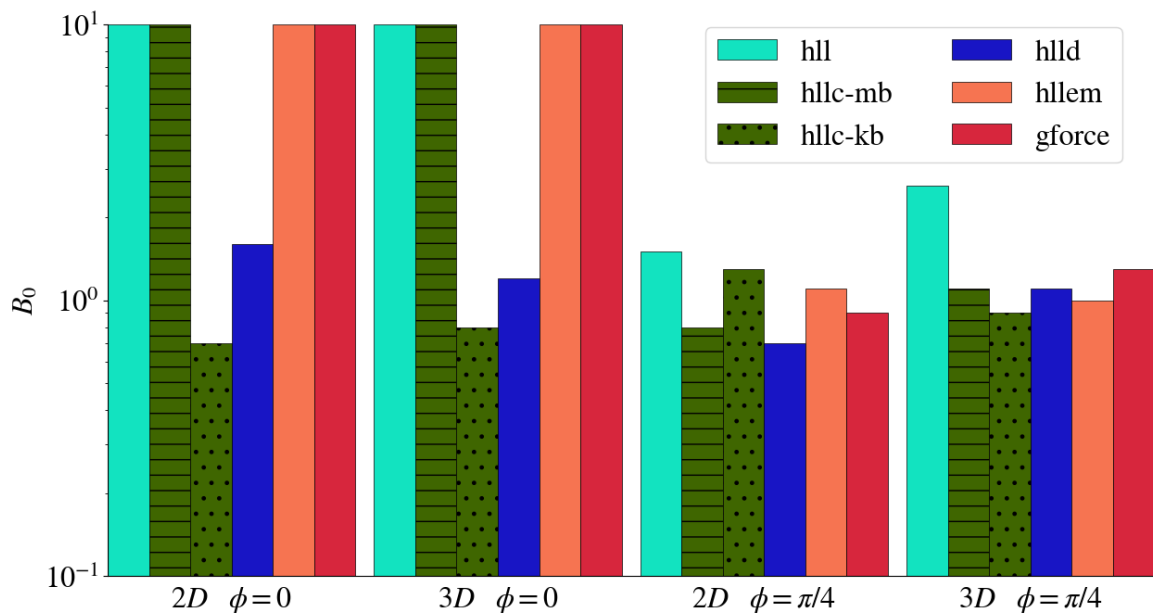
FIGURE 4.11: Permitted magnetization values for the blast wave problem. From left to right the four histograms (2D and 3D with $\phi = 0$, 2D and 3D with $\phi = \pi/4$) cover the values of B_0 (in the range $[0, 10]$) for which numerical integration succeeded. Each color bar corresponds to a different Riemann solver. The minmod limiter has been used.

having $\rho = 10^{-2}$, $p = 1$, where r is the cylindrical (in 2D) or spherical (in 3D) radius. The computational domain is threaded with a uniform magnetic field

$$\mathbf{B} = B_0 \left[\sin\theta \left(\cos\phi \hat{e}_x + \sin\phi \hat{e}_y \right) + \cos\theta \hat{e}_z \right], \tag{4.60}$$

where θ and ϕ are the polar and azimuthal angles, respectively (we set $\theta = \pi/2$). The grid resolution is fixed to 200^2 grid zones in 2D and 192^3 in 3D and computations are carried out until $t = 4$ using the ideal EoS with $\Gamma = 4/3$.

We begin by showing, in Figure 4.8 and 4.9, the results of 2D computations using, respectively, $\phi = 0$ (grid aligned) and $\phi = \pi/4$ (oblique case) and moderate magnetization $B_0 = 0.5$. The left and right halves of the figures include, respectively, a coloured map of the plasma $\beta = 2p_g/B^2$ (left half) and 1D-profiles along the x- and y-axis (in the aligned case) or along the two diagonals (in the oblique case). The explosion is delimited by an outer fast forward shock and the presence of a magnetic field makes the propagation anisotropic by compressing the gas in the direction parallel to the field. In the perpendicular direction the outer fast shock becomes magnetically dominated with very weak compression. Results between different solvers are very similar and the salient features of the solution are confirmed also in the oblique case.

In 3D and for stronger magnetization ($B_0 = 1$), differences are slightly more emphasized around the center where less diffusive solvers such as HLLD and GFORCE yield larger density and pressure peaks and smaller magnetic energies, see Figure 4.10. We point out that the HLLD solver and the two flavours of HLLC could not successfully complete the 3D case with $B_0 = 1$ without enabling the corresponding "failsafe" switches to HLL (see the discussion in Sections 4.1.2 and 4.1.3).

It should be clear by now that the stability of the computations crucially depends on the chosen solver. Figure 4.11 reports the allowed range of magnetization values (above which computation breaks down) for different Riemann solvers using different inclinations in the $x - y$ plane ($\phi = 0$ and $\phi = 45°$) in 2D as well as in 3D. The histograms have been obtained by increasing B_0 in steps of 0.1 in the range $[0, 10]$ for each computations. Overall, larger magnetizations are attained for grid-aligned configurations ($\phi = 0$) in both 2D and 3D while the oblique cases appear to be more stringent in terms of stability. In the former case, HLL, HLLEM and GFORCE (with $\omega = 1/2$) yield the most robust results. In the oblique cases, however, the maximum permitted values decrease to values of order unity. The HLLC-MB solver seems to be more robust than the KB version for grid-aligned configurations while it becomes comparable for $\phi = \pi/4$. We point out that the limits have been obtained by quitting the computation at the first failure of the conservative to primitive inversion scheme. Larger values may be possible by applying corrections to energy and/or momentum (see, e.g., the work of Mignone and Bodo, 2006; Beckwith and Stone, 2011; Martí, 2015).

The CPU time required by the different Riemann solvers on this particular test were found to be $t_{hll} : t_{hllc-MB} : t_{gforce} : t_{hllc-KB} : t_{hlld} : t_{hllem} = 1 : 1.07 : 1.43 : 1.47 : 1.72 : 2.43$ (the CPU time for the HLLC solvers is computed in the case with $B_0 = 0.1$).

4.2.8   Kelvin-Helmoltz Instability

As a final test we choose the 2D Kelvin-Helmholtz instability (KHI) using the configuration of Beckwith and Stone (2011). The initial shear velocity is given by

$$v^x = \text{sign}(y) v_{\text{sh}} \tanh \left[\frac{2y - \text{sign}(y)}{2a} \right] , \qquad (4.61)$$

where $a = 0.01$ represents the thickness of the shear layer and $v_{\text{sh}} = 0.5$. The shear layer is perturbed by a non-zero y-component of the velocity:

$$v^y = \text{sign}(y) A_0 v_{\text{sh}} \sin(2\pi x) \exp \left[- \left(\frac{2y - \text{sign}(y)}{2\sigma} \right)^2 \right] , \qquad (4.62)$$

where $A_0 = 0.1$ is the amplitude of the perturbation and $\sigma = 0.1$ is the perturbation length-scale. We set an uniform initial pressure $p = 1.0$ and employ the ideal EoS with adiabatic exponent $\Gamma = 4/3$, while the magnetic field is non-zero only in the x-direction $\mathbf{B} = (10^{-3}, 0, 0)$. Finally, the density distribution is set as:

$$\rho = \frac{1}{2}(\rho_l + \rho_h) + \frac{1}{2}(\rho_h - \rho_l)\frac{v^x}{v_{\text{sh}}} , \qquad (4.63)$$

with $\rho_h = 1.0$ and $\rho_l = 0.01$. The Cartesian domain has extension of $x \in [-0.5, 0.5]$, $y \in [-1.0, 1.0]$ with periodic boundary conditions applied in all directions. We use a nominal resolution of 512×1024 grid zones and evolve the system until $t = 3$. Lower resolutions (128×256 and 256×512) have been employed for convergence purposes.

Our results confirm and extend those obtained by Beckwith and Stone (2011), namely, that the choice of the Riemann solver plays a crucial role in its ability to capture the turbulence at smaller scales leads to an increase in the effective resolution. The density maps shown in Figure 4.12 show, in fact, that only the HLLC and HLLD solvers are able to capture small scale structure (i.e., the secondary vortexes at $t = 3$) while, on the contrary, the remaining solvers (HLL, GFORCE and HLLEM) disclose a lesser amount of substructure and a larger amount of numerical diffusion, even at very high resolution (not shown here).

The same setup has been tested also employing the HLL Riemann solver and a higher order scheme (in particular, a parabolic reconstruction and a 3$^{\text{rd}}$-order time integration Runge-Kutta scheme have been adopted). As shown in the bottom right panel of Figure 4.12, the secondary vortexes are not developing. Interestingly, the differences between the HLL and the HLLEM solver are almost negligible regardless of the resolution, even though the HLLEM solver is designed to preserve the contact wave.

In order to explain this apparently unexpected behavior, we first observe that this problem is i) only weakly magnetized ($\beta \sim 10^5$) and ii) strictly two-dimensional (no z component is present). These conditions imply that slow waves become almost degenerate on the contact mode, while Alfvén waves are not present in the solution. Thus only 3 (out of 5) waves can be accounted for by the HLLEM solver: two outermost acoustic waves and the middle contact mode describing a density jump.
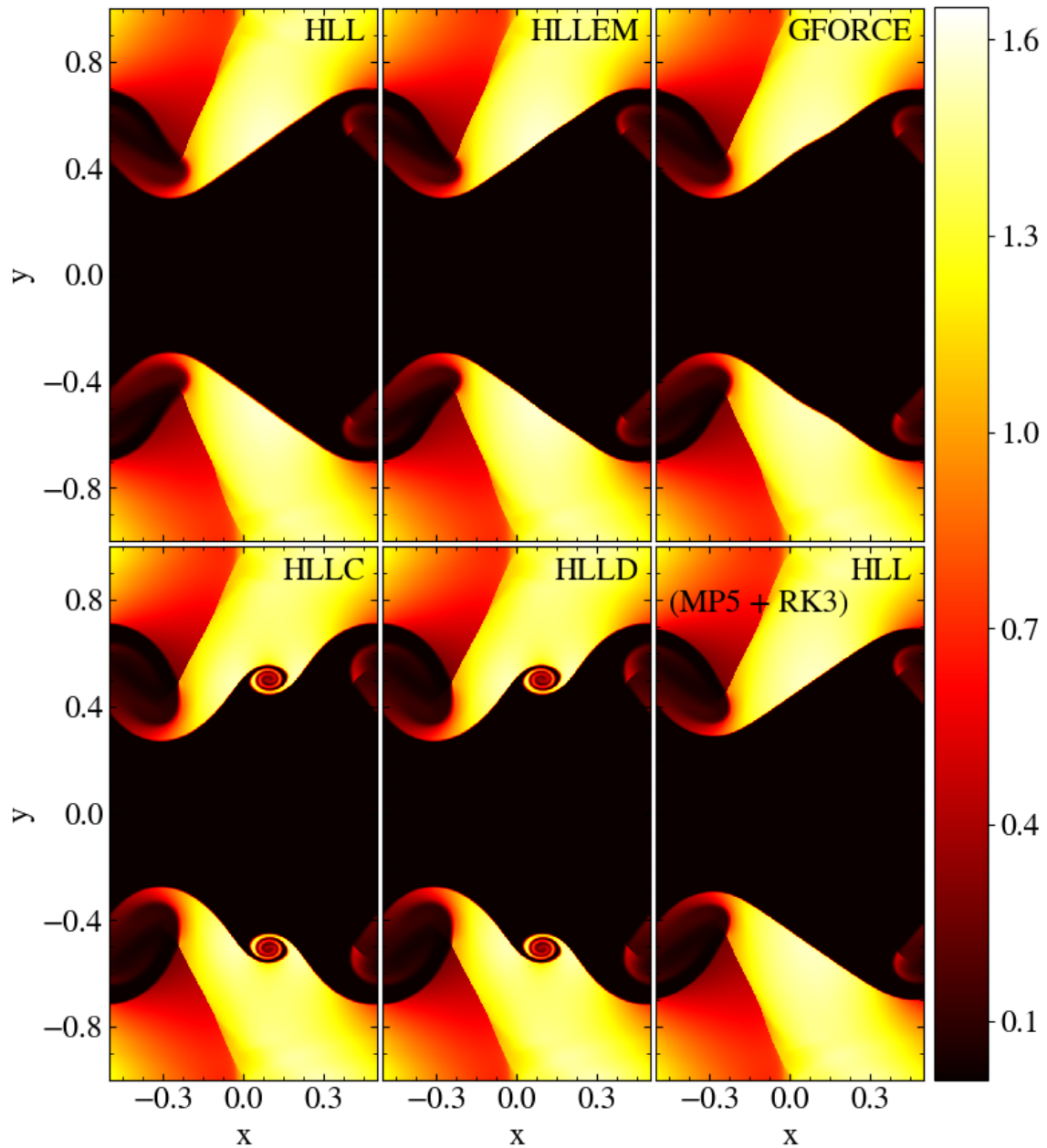
FIGURE 4.12: Density distribution of the Kelvin-Helmoltz instability test problem at $t = 3$ with different Riemann solvers. All the runs have been performed with 512×1024 grid cells.
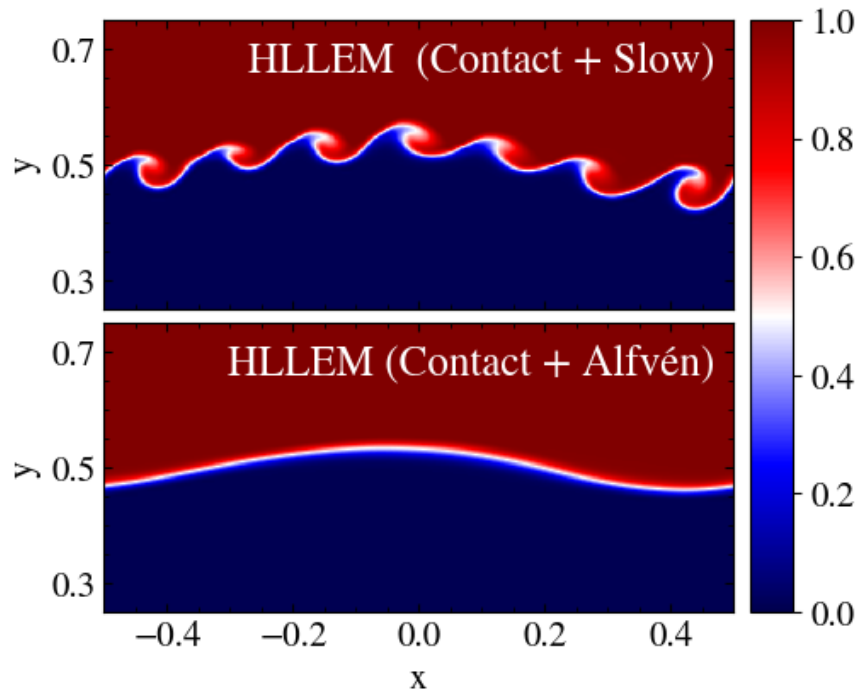
FIGURE 4.13: Density maps for the KHI instability at $t = 1.5$ in the non-relativistic case using the 5-waves HLLEM solver including contact + slow waves (top panel) and including contact + Alfvén waves (bototm panel).

When $B_x \to 0$, however, the middle wave is best identified as a tangential discontinuity, carrying jumps in the transverse vector components as well. These variations are crucial in the vortex formation process but they cannot be described and are thus smoothed out by the HLLEM solver. On the contrary, both HLLC and HLLD solvers are able to capture the discontinuities in the transverse components of the velocity, even if none of them is specifically designed to fully capture slow waves. Both solvers, in fact, are able to "detect" a transverse velocity jump[1] since this is inherently part of the nonlinear solution process.

In order to prove our statement, we now show that restoration of the slow modes in the HLLEM Riemann solver is decisive in resolving small-scale structure. We demonstrate this by performing the same computation in the non-relativistic regime (MHD), since this sensibly reduces the required computational time (as shown in Antón et al. 2010). Two sets of solvers have been considered: in the first case (top panel in Figure 4.13) the HLLEM solver is designed to capture contact and slow modes, while in the second case (bottom panel of the same figure), the HLLEM solver resolves contact and Alfvén waves. A comparison between the two panels in Figure 4.13 clearly reveals that the former is able to resolve multiple secondary vortices across the shear layer while the latter completely smooths them out.

We also provide in Figure 4.14 a measure of the instability growth rate through the volume-integrated transverse velocity squared, $\langle |v_y|^2 \rangle$ at different resolutions . While the HLLC and the HLLD solvers converge almost immediately, the GFORCE,

---

[1]For HLLC-MB, this statement holds in the $B_x \to 0$ limit.
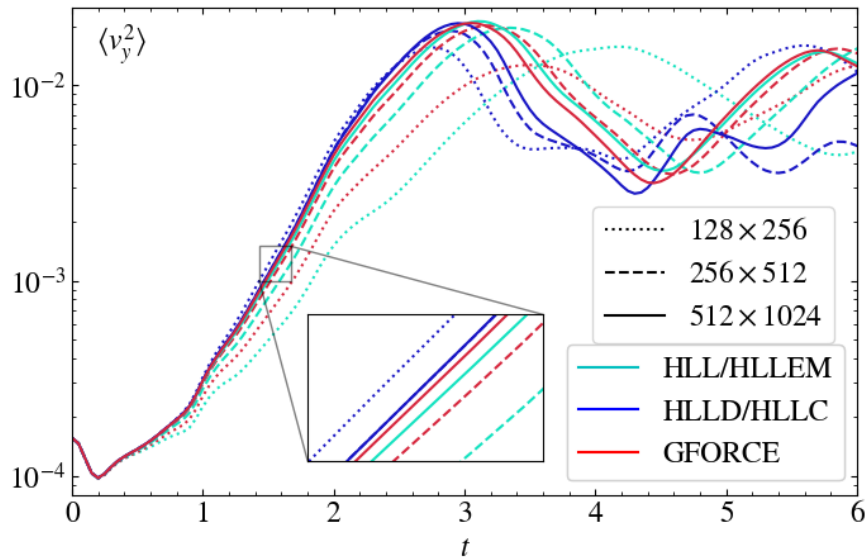
FIGURE 4.14: Growth rate, defined as $\langle |v_y|^2 \rangle$ computed using different solvers at different resolutions. Since HLL and HLLEM show the same growth rate, they have been represented by a single line. We applied the same strategy also for the HLLC/HLLD solvers.

HLL and HLLEM solvers achieve complete convergence only at larger resolutions. In spite of this, the GFORCE scheme approach the nominal growth rate at a somewhat faster rate when compare to HLL or HLLEM.

4.3 Summary

A comparison between several non-linear approximate Riemann solvers, namely, HLL, HLLC, HLLD, HLLEM and GFORCE, has been presented through a series of 1, 2 and 3D numerical tests, in order to assess their efficiency, stability and robustness. Our conclusions, can be summarized as follows:

1) Owing to its ability to approximate the Riemann fan structure by including rotational and contact discontinuities, the HLLD solver of Mignone, Ugliano, and Bodo (2009) is able to achieve the best results in terms of accuracy. Despite being more computationally expensive than more diffusive Riemann solvers, its ability to converge at lower resolution allows comparable accuracies to be achieved with a reduced number of grid cells (e.g., 256×512 vs 512×1024 required by HLL, see the the Kelvin-Helmoltz instability problem). On the other hand, because of its complex and iterative character, this solver may not be a robust option for strong magnetizations.

2) While the HLL Riemann solver showed great performances in terms of stability and computational efficiency, its inability of resolving any internal wave of the Riemann fan lead to a very diffusive behavior in all of the presented tests.

3) The HLLC Riemann solver showed dissipation properties intermediate between the HLLD and the HLL formulation. Since several approaches have been developed through the years, the approaches of Mignone and Bodo (2006) and of

D. S. Balsara and Kim (2016) have been compared. The former formulation (HLLC-MB) showed a better performance in terms of computational efficiency, since it does not require any iterative cycle. On the contrary, the second approach (HLLC-KB) involves the solution of couples systems of nonlinear equations and it is thus more computational intensive. In addition we found that the HLLC-KB solver is not fully consistent with the integral form of the conservation law, failing to satisfy some jump condition across the contact mode.

4) The GFORCE Riemann solver shows accuracy comparable (or slightly inferior) to the HLLC approach. Its increased stability properties, which are intermediate between the HLL and the HLLD approach, makes it a valid robust alternative when the HLLD Riemann solver becomes brittle. The solver is non-iterative and it requires one additional conversion from conservative to primitive variables slowing down the flux computation by approximately 50% when compared to the HLL solver. In the presence of strong shock and/or magnetizations, the GFORCE should be reduced, in our experience, to the FORCE flux by tuning the parameter $\omega_g = 1/2$ for safety purposes.

5) The HLLEM formulation, despite its ability of resolving the contact and rotational discontinuities, has often shown poor accuracy and numerical dissipation comparable to the HLL formulation. Better performances can be obtained when Alfvén waves are predominant, although not superior than the HLLD formulation. Since its intermediate eigenstructure is built on top of the HLL solver, its stability properties are better than other less diffusive Riemann solvers. On the other hand, its large computational cost (related to the computation of left and right eigenvectors) does not make it - in our opinion - an efficient and valid alternative in the context of relativistic MHD, although its performance may improve for those systems where conserved eigenvectors are easier to compute (e.g., non relativistic MHD equations).

Chapter 5

A Non-Isotropic Dynamo and Diffusivity Toy Model

The contents of this chapter are adapted from Mattia and Fendt (2020a), published in *The Astrophysical Journal*. All the simulations, the figures and most of the scientific discussion and interpretation presented in this chapter were done by the author of the thesis.

In this chapter we present the first non-ideal MHD simulations of jet launching including a non-scalar accretion disk mean-field $\alpha^2\Omega$-dynamo. By applying selected non-isotropic dynamo tensors, we are able to disentangle the effects of the single dynamo components into the amplification of the poloidal magnetic field and the formation of anti-aligned magnetic loops within the accretion disk. We find that such loops trigger the formation of dynamo inefficient zones, which are characterized by a weak magnetization. We also present correlations between the strength of the disk toy dynamo coefficients and the dynamical parameters of the jet that is launched.

This chapter is structured as follows. In Section 5.1 we briefly describe the numerical scheme and setup. In Section 5.2 we investigate the effect of a non-scalar dynamo on the magnetic field. In Section 5.3 we focus on the impact on the disk-jet connection. In Section 5.4 we discuss the impact of a non-radial initial magnetic field. Lastly, we summarize the key findings in Section 5.5.

5.1 Numerical Details

5.1.1 The Diffusivity Model

As shown in Section 3.4.5, we consider a diagonal structure for the magnetic diffusivity with no quenching. We apply the *strong diffusivity* model of (Stepanovs and Fendt, 2014; Stepanovs, Fendt, and Sheikhnezami, 2014), where the turbulence parameter α_{ss} has a quadratic dependence on the disk magnetization (see Equation 3.49). The role of the diffusivity has been widely discussed in the literature (Zanni, Ferrari, et al., 2007; Sheikhnezami et al., 2012). For the initial strength and anisotropy of the magnetic diffusivity we assume

$$\overline{\eta}_0 = \left(\frac{1}{2}, \frac{1}{2}, 1\right)\eta_0,$$

(5.1)

TABLE 5.1: Simulations with the dynamo coefficients $\overline{\alpha}_0 = (\phi, \psi, \chi)\alpha_0$. The magnetic diffusivity distribution is the same with $\eta_0 = 0.165$. The run time of the simulations t_F is in units of 10^3.

run ID	ϕ	ψ	χ	t_F	Comment
Scalar	1.0	1.0	1.0	30	as Stepanovs, Fendt, and Sheikhnezami (2014)
phi_A	1.0	1.0	2.0	10	strong amplification
phi_B	1.0	1.0	0.5	10	weak amplification
phi_C	1.0	1.0	0.1	10	very weak amplification
R_A	2.0	1.0	1.0	10	magnetic loops at $R \simeq 40$
R_B	0.75	1.0	1.0	10	magnetic loops at $R \simeq 20$
th_A	1.0	5.0	1.0	10	multiple loops in $R \in [15, 80]$
th_B	1.0	0.1	1.0	4	magnetic loops at $R \simeq 15$

where $\eta_0 = 0.165$ recovers the reference values of Stepanovs, Fendt, and Sheikhnezami (2014). Because of the diffusivity model adopted, the dependence of the disk magnetization on the dynamo number becomes:

$$\mathcal{D} \propto \alpha_{ss}^{-2} \propto \mu_{disk}^{-4}, \tag{5.2}$$

as in Stepanovs, Fendt, and Sheikhnezami (2014) and Fendt and Gaßmann (2018). We note that we do not put any lower bounds on the turbulence level α_{ss}. This may effect, via the dynamo-alpha α_0, the critical dynamo number, above which we expect an effective magnetic field amplification.

5.1.2 The Dynamo Model

Our aim is to generalize the dynamo models applied previously (von Rekowski, Brandenburg, et al., 2003; Stepanovs, Fendt, and Sheikhnezami, 2014; Fendt and Gaßmann, 2018). These works applied a scalar (thus isotropic) α coefficient.

Here we apply the anisotropy of the dynamo, assuming that the coefficients $\overline{\alpha}_0$ are not necessarily the same (Ruediger, Elstner, and Stepinski, 1995).

In order to have a direct comparison with the simulations of Fendt and Gaßmann (2018), we set the dynamo tensor components as

$$\overline{\alpha}_0 = (\phi, \psi, \chi)\alpha_0, \tag{5.3}$$

with $\alpha_0 = 0.775$. Setting $\psi = \phi = \chi = 1$, we recover the reference simulation of Fendt and Gaßmann (2018)[1]. The strength of the dynamo coefficients (ϕ, ψ, χ) are summarized in Table 5.1. From this set of simulation runs, we will consider a sample of eight exemplary runs in order to disentangle the influence of the different components of the alpha tensor on the magnetic field structure and the disk and jet evolution.

---

[1]Note that α_{ss} as well as the dynamo tensor (now also considering sound speed) are now differently defined. Thus, the coefficients α_0 and η_0 are not defined in the same way.
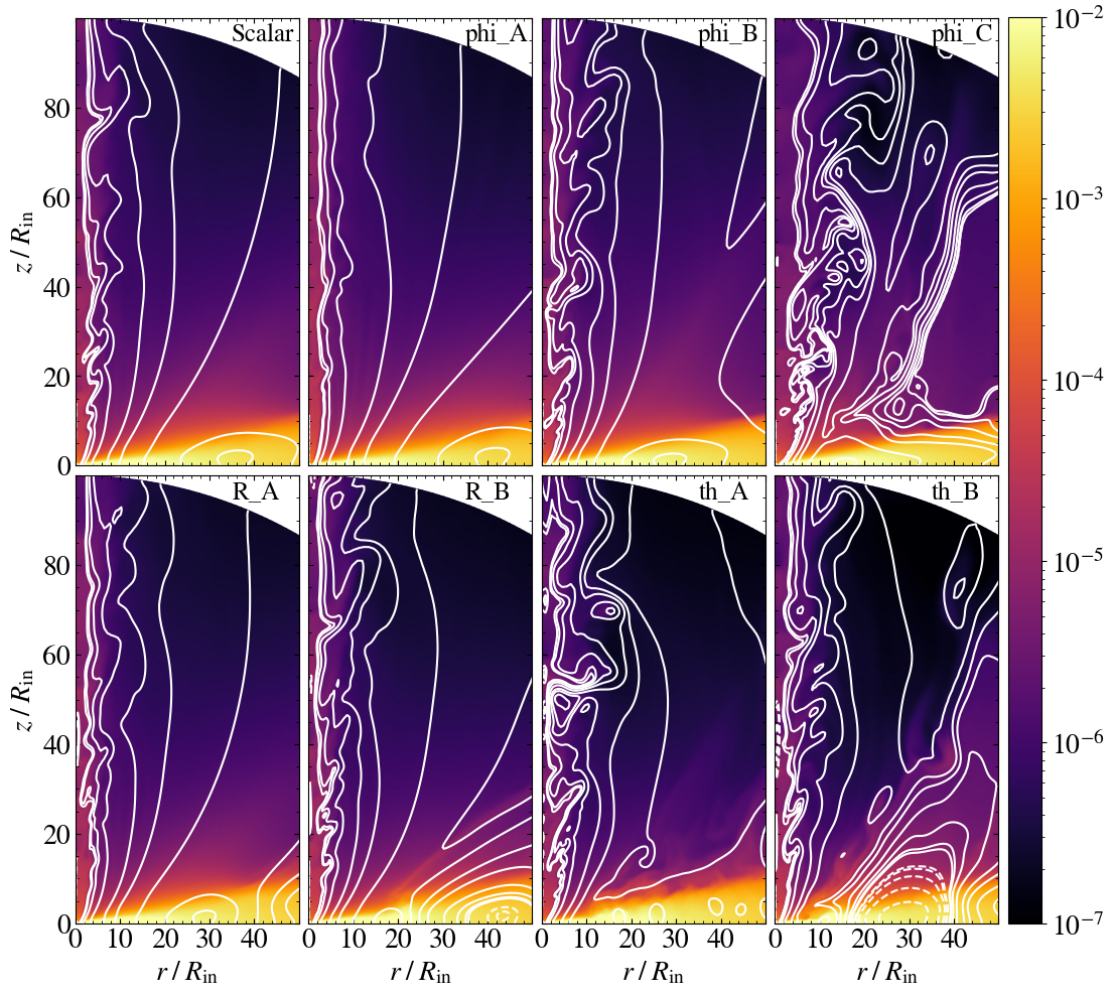
FIGURE 5.1: Magnetohydrodynamic evolution of the toy model dynamo simulations (see Table 5.1 at $t = 4000$. Shown is the density distribution (color) and magnetic field lines (white lines). The poloidal magnetic is field is represented by the contour lines of the vector potential A_ϕ. The dashed lines indicate a negative polarity of the poloidal magnetic field.

As previously shown (Stepanovs, Fendt, and Sheikhnezami, 2014), the strong diffusivity model is able to suitably quench the dynamo action, preventing an endless amplification of the magnetic field. For this reason we do not apply any direct quenching on the dynamo ($q_{\alpha R} = q_{\alpha \theta} = q_{\alpha \phi} = 1$).

5.2 Evolution of the Magnetic Field

Figure 5.1 shows for the different parameter runs the density distribution of the disk-jet structure, together with the magnetic field geometry (as contour lines of the vector potential). We point out that in all cases but simulation *th_B* (which is described more in detail in Section 5.4), the initial magnetic field has the radial structure as described in Section 3.4.2.

Overall, we see that in all simulation runs the magnetic field in the inner region close to the rotation axis that has been generated by dynamo action shows a large scale open geometry. Together with a substantial strength, this magnetic field structure is able to eject disk material in to an outflow with a high degree of collimation. On the other hand, we also see that the very field structure depends on the choice of the dynamo tensor, thus the strength of the tensor components. The choice of different coefficients (ϕ, ψ, χ) in our toy dynamo model leads to a different magnetic field configuration.

5.2.1 A Super-Critical Poloidal Dynamo

The induction equation tells us that the dynamo action governed by α_ϕ is the only way to increase the poloidal magnetic field up to the strength that is required for jet launching. Even for $\alpha_\phi = 0$ the toroidal magnetic field is still amplified through the Ω effect and also the α_R dynamo component. However, the dynamo does not lead to a substantial amplification of the poloidal magnetic field. Therefore the latter cannot increase and stays confined within the disk. Neither the strength nor the launching angle can be reached that is required to produce a Blandford-Payne outflow.

On the other hand, as a consequence of the quenching model applied, the magnetic diffusivity still increases as the toroidal magnetic field grows. As a consequence, the poloidal magnetic field still evolves, even if the field is not enhanced by the dynamo action. Note, however, that even if $\chi > 0$, if α_ϕ is under a critical strength α_{crit}, the dynamo action for the poloidal field is still negligible.

When comparing the time scales for diffusion and dynamo action for different strength for α_ϕ (see Fendt and Gaßmann 2018), we find a critical value of $\alpha_{\text{crit}} \simeq 0.003$, corresponding to $\chi \simeq 0.03$.

Because of the diffusivity model applied in these simulations, we find that the dynamo number is not an unambiguous measure for the initial critical dynamo action, as the disk diffusivity does not only depend on the *poloidal* magnetic field (that is not amplified as the dynamo α_ϕ is sub-critical), but also on the *toroidal* magnetic field (that remains amplified by the dynamo α_R and by the Ω effect). Moreover, as shown in Stepinski and Levy (1988), Stepinski and Levy (1990), and Torkelsson and Brandenburg (1994), the initial critical dynamo number depends on several factors, e.g., the number of grid cells or the magnetic field configuration. Nevertheless, the dynamo number still remains a key parameter in order to understand the evolution and saturation of the dynamo action (see Sect. 3.4.7).

For $\alpha_\phi < \alpha_{\text{crit}}$, the poloidal magnetic field increases only by less than one order of magnitude in the outer disk before time $t = 3000$, while the inner disk region is not at all magnetically amplified. For $\alpha_\phi > \alpha_{\text{crit}}$, the dynamo effect substantially amplifies the poloidal magnetic field, as shown in Figure 5.2, changing both its strength and geometry which subsequently may lead to an disk outflow of material similar to Stepanovs, Fendt, and Sheikhnezami (2014). All the cases that we investigated and that are listed in Table 5.1 satisfy the condition $\alpha_\phi > \alpha_{\text{crit}}$.
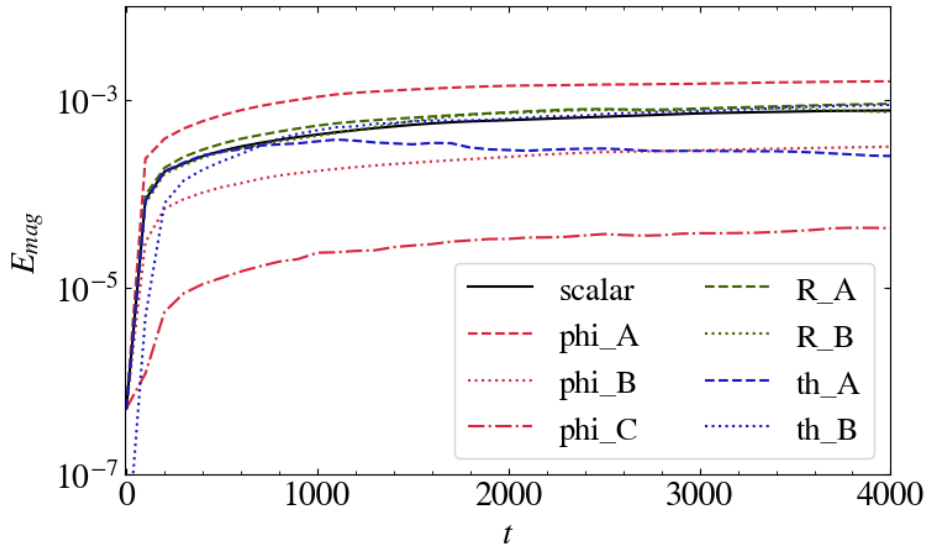
FIGURE 5.2: Temporal evolution of the disk poloidal magnetic energy integrated from radius $R = 10$ to the end of the domain, $R_{\text{out}} = 100$.

5.2.2 Induction of Multiple Magnetic Loops

Dynamo action triggered by the ϕ-component of the alpha tensor leads to a topological magnetic field structure such that the magnetic field loops generated in the inner disk region open up and drive a collimated outflow (see also Figure 5.1, but also Stepanovs, Fendt, and Sheikhnezami 2014; Fendt and Gaßmann 2018). Outside this inner jet launching region, magnetic loops are continuously formed. This loop structure, that is basically corresponding to a reversal in the radial field B_R, is diffusing outwards due to the radial magnetic field pressure gradient of the inner disk. Such loops do not correspond to a reversal in the toroidal field and since they are diffused away, their impact on the jet dynamics is negligible.

In case of dynamo action that is substantially an-isotropic (as our cases *R_A*, *R_B* and *th_A*), we observe an essentially different evolution of the magnetic field topology. That is, for $\phi < 0.8$ or $\phi > 1.5$, *a second magnetic loop* is formed that is *anti-aligned* to the loop structure induced further in. These loops, characterized by a reversal in the toroidal field, are substantially different from the ones described previously, and play a significant role in the evolution of the magnetic field and of the disk-jet system (see our discussion below). We point out that the anti-aligned magnetic loops can be formed also when considering a scalar dynamo tensor, when the scalar $\alpha_0 < 0.6$ (Fendt and Gaßmann, 2018).

As shown in Section 5.2.1, the coupling between the toroidal magnetic field and the dynamo tensor component α_ϕ is the main mechanism responsible for generation of the poloidal field. For $0.8 < \phi < 1.5$, the toroidal magnetic field, being amplified by the Ω-effect from the radial weak seed field, shows a monotonous behavior (after being amplified). As the system evolves, the poloidal field is amplified over the whole accretion disk.

By looking at the spatial and temporal numerical derivatives of the toroidal field, we find that because of the highly anisotropic character of α_R, some "dynamo-inefficient zones" are formed. These are areas of vanishing poloidal field strength,
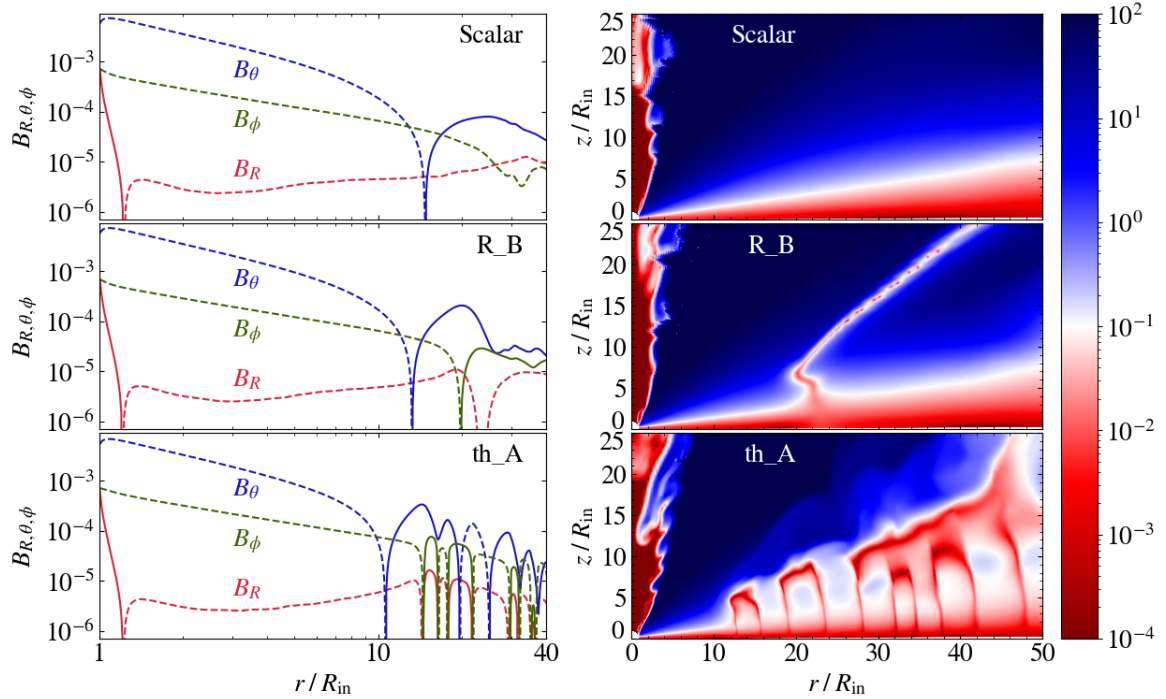
FIGURE 5.3: Presence and absence of dynamo-inefficient zones in the disk for different dynamo prescriptions, *Scalar* (top panels, *R_B* (middle panels), and *th_A* (bottom panels), respectively. The left column shows the three magnetic field components close to the disk mid-plane at time $t = 1000$, where the solid lines represent positive values of the magnetic field and the dashed lines represent negative values of the magnetic field. The right column shows the disk magnetization at time $t = 4000$.

but, in addition, in such zones also the toroidal magnetic field cannot be amplified. The number and the location of these zones, where the dynamo is not efficient, depends on the strength of the three dynamo components and not exclusively by α_R.

Furthermore, for $\alpha_\theta > 3$, we find that the toroidal field shows multiple dynamo-inefficient zones. On the other hand, the dynamo-inefficient zones of case *th_A* remain confined in the accretion disk.

This is illustrated in the right panels of Figure 5.3 where we show the disk magnetization at the same evolutionary time, $t = 4000$. The difference between between the three simulation runs *Sc*, *R_B*, and *th_A* is clearly visible.

For the case of the scalar dynamo the local disk magnetization is only weakly dependent on the radius. It is relatively low along the mid-plane and increases towards the disk surface. This is understandable as the disk gas pressure decreases with altitude while the poloidal field remains rather constant vertically.

For simulation run R_B, for which $\alpha_R = 0.75$, we see that a dynamo-inefficient zone has developed around radius $R \simeq 23$. Typically, these zones seem to be anchored at the disk mid-plane. As they are balanced by a low magnetic pressure, they vertically extend while preserving the total pressure equilibrium.

For simulation run *th_A*, for which $\phi = 1$ and $\psi = 5$, we find multiple dynamo-inefficient zones along the accretion disk. Note that due to their proximity, these zones are able to connect – and reconnect.

Because the coupling between the toroidal field and the α_ϕ-component of the dynamo tensor is the only way to dynamo-amplify the radial field component, the radial field that is amplified from the toroidal has also different polarities.

Since we have physical resistivity included, the magnetic field is able to reconnect and to change its topology within the accretion disk. In particular, instead of one magnetic loop that is visible (see Figure 5.3, middle left panel), now more magnetic loops arise (see Figure 5.3, bottom left panel). On the other hand, the reversal of the toroidal field is associated with a maximum in the tensor component α_θ, which undergoes a reversal at smaller radii (bottom left panel of Figure 5.3).

Compared to the results of Fendt and Gaßmann (2018), here we find that the re-configuration of the magnetic field structure does impact the jet evolution on a weaker level. We believe that this is mainly due to the mid-plane boundary condition, that is absent in Fendt and Gaßmann (2018). In particular, here we enforce symmetry between upper and lower hemisphere that can be violated in a bipolar setup. However, the reversal of the toroidal and radial field components that directly define the disk magnetization still play a key role in the disk-jet evolution. We note that the disk magnetization is the main ingredient of the diffusivity model for the resistive disk evolution.

Since the dynamo-inefficient zones correspond to zones of low diffusivity, as a result the accretion process can be affected. In fact, accretion can be suppressed across such zones, leading to under-dense and over-dense regions (compared to the simulations without multiple loops). We find that these under-dense/over-dense regions are strongly related to the existence of a vertical field. We experienced numerical issues when under-dense zones are located too close to the inner boundary, for example unphysical values of the fluid density or the fluid pressure.

Here we need to comment briefly on the "dead zones" that has been proposed for protoplanetary disks. Although the dynamo-inefficient zones we detect in our simulations may look similar to these dead zones, the physical processes involved are not the same. Dead zones in protoplanetary disks have been proposed by Gammie (1996) on the basis of a lack of coupling between matter and magnetic field due to an insufficient degree of ionization. This lack of coupling would not allow the MRI to operate, and, as a consequence, also accretion unlikely to happen, since the lack of angular momentum exchange. As a result, a layered accretion is expected on a theoretical basis, which could indeed be realized in numerical simulations (T. P. Fleming, Stone, and J. F. Hawley, 2000; T. Fleming and Stone, 2003). Also, resistivity was found to play an essential role in suppressing the MRI (see, e.g., Sano et al. 2000; Fromang, Terquem, and S. A. Balbus 2002; Flock, Henning, and Klahr 2012). Dead zones in protoplanetary disk are also thought to be responsible to create transition disks (Pinilla et al., 2016).

It is interesting to note that for both the protoplanetary dead zones and for our dynamo-inefficient zones the resistivity plays a leading role. However, for the first approach it is the resistive de-coupling which suppresses the MRI (and would subsequently suppress the dynamo action of the MRI), while for our models the dynamo-inefficient zone is formed as result of a minimum of the magnetic diffusivity.

Finally we note that the dynamo-efficient zones are basically resulting from the feedback of the magnetic field on the magnetic diffusivity. Therefore a change in the

quenching model – from the diffusive quenching to the standard quenching – can affect the exact location and width of the dynamo-inefficient zones.

5.2.3 Amplification of the Magnetic Field

All our parameter runs apply a super critical dynamo $\alpha_\phi > \alpha_{\text{crit}}$ (Table 5.1). The resulting magnetic field strength and geometry supports a collimated outflow. In Figure 5.2 we show the time evolution for the disk poloidal magnetic energy, integrated from $R = 10$. For a comparison the case of an isotropic dynamo is shown.

The three different dynamo tensor components play a different role in the amplification of the poloidal magnetic field. The ϕ-component of the dynamo is the main ingredient that amplifies the poloidal magnetic field in the disk, while the R and θ-components determine the formation of the dynamo-inefficient zones, that, subsequently, also determines the poloidal magnetic field structure.

The $\phi-$component of the dynamo tensor essentially influences already the very early stages of the disk-jet evolution – a higher strength of α_ϕ leads to a faster and stronger amplification, as we can see by comparing the "*phi*"-simulations to the isotropic model in Figure 5.2.

The other dynamo components (α_R and α_θ) become important only once the poloidal field has been amplified to substantial strength, and through the presence (or absence) of the dynamo-inefficient zones. In particular, where a dynamo-inefficient zone is built up in the *inner* disk, it triggers the temporal evolution of the system already on short timescales ($\simeq 100$ after its formation). A dynamo-inefficient zone located further out plays a minor role during the early phase of the disk evolution.

We emphasize that the evolution of the disk magnetic field is strictly correlated with the existence of dynamo-inefficient zones, since these features lead to the formation of multiple anti-aligned magnetic loops in the disk (see Figure 5.1 and Section 5.2.2). A higher strength of the dynamo tensor component α_R leads to an – on average – higher amplification of the toroidal field. However, once the dynamo is quenched by magnetic diffusivity, the magnetic field strength decreases to the magnitude that we recovered in the isotropic dynamo simulation. Therefore, we interpret that the effect of a higher α_R is a more rapid amplification of the poloidal field. On the other hand, a lower α_R leads to a slower toroidal (and therefore poloidal) field amplification.

We find a different behavior when a dynamo-inefficient zone (only one) is forming which extends beyond the accretion disk surface. As discussed in Section 5.2.2, the reversal of the toroidal field corresponds to a spatially stationary point in the $\theta-$component of the magnetic field. As a result, the poloidal magnetic energy is higher than for the isotropic dynamo model, simply because in the dynamo-inefficient regions of the disk the vertical field component becomes stronger.

On the other hand, this increase in the vertical component of the magnetic field is partially suppressed in the presence of multiple magnetic zones, compared to the case of an isotropic dynamo tensor. Our understanding of this effect is that the existence of quite a number of field reversals (that effectively decrease of the local magnetic energy), more than compensates the induction of a vertical field component (that would lead to a decrease of the local magnetic energy).
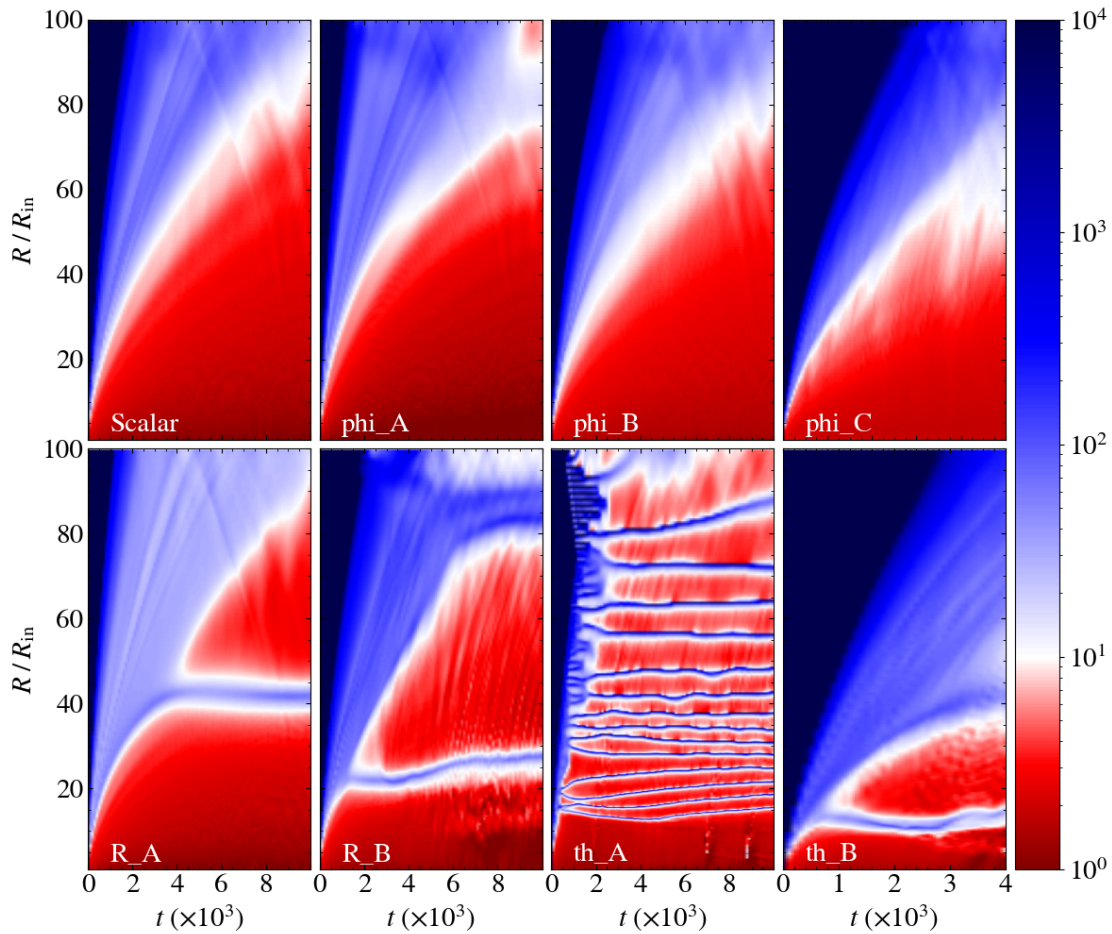
FIGURE 5.4: Dynamo number for selected simulation runs. Note the presentation of this figure as a $t - R$ diagram, displaying the strength dynamo number along the disk (vertically, in $R-$direction) as a function of time (horizontal axis).

5.2.4 The Dynamo Number

The dynamo number is usually quoted as a measure for dynamo activity. Only dynamos with a super-critical dynamo number evolve rapidly and work efficiently against magnetic diffusivity, and finally lead to a strong, saturated poloidal magnetic field. The dynamo number can therefore tell us when and where the growth of the magnetic field reaches saturation. In Figure 5.4 we compare the dynamo number as function of time and radius for different cases.

We first show the dynamo number for different strength of the tensor component α_ϕ (top panel). We see that as χ decreases, the amplification of the poloidal field is weaker and also slower, as also indicated by Figure 5.2. These differences in the magnetic field evolution are reflected on the dynamo number. In the time evolution of the dynamo number for all simulations we can clearly distinguish three evolutionary stages[2].

---

[2]Here, we point out that, as opposed to the simulations described in the lower panel of Figure 5.4, the top panel is marked by the absence of the multiple magnetic loops described in Section 5.2.2. For this reason the three evolutionary stages we prefer to define considering both time and space.

We may first define an (i) initial phase (indicated in blue) during which the dynamo number is almost infinite, simply because the diffusivity is still low (as implied by the quenching triggered by the magnetic diffusivity). Then comes a (ii) dynamo phase (indicated in white) that is characterized by a strong competition between dynamo action and diffusive quenching. During this phase we recognize magnetic loops being present, surviving from the early stages ($t \lesssim 500$ in the inner disk region) of dynamo evolution. In a subsequent (iii) final phase (indicated in red), these magnetic loops have been washed out or have been broken-up, respectively, and a quasi-steady state of the dynamo evolution is reached. The time scale when the final phase is reached depends of the radius (thus on the dynamical time scale that is defined by the disk rotation at this radius). In the inner radii the final stage is reached around $t \lesssim 500$, while in the outer disk regions is reached only at $t \gtrsim 5000$. In this final phase, dynamo action and diffusive quenching are fully balanced.

Note that in the inner disk region the second dynamo phase is missing because of the rapid evolution of the dynamo. Here, the magnetic energy reaches the saturation level already very early, with a timescale of the first two phases being much smaller.

Considering now the effect of different levels of dynamo an-isotropy we find the following results. For larger χ we do not find a second phase at larger radii since the magnetic field is amplified on a shorter timescale. In addition to that, for larger χ the first phase has a shorter lifetime at every radius.

Looking at the innermost parts of the accretion disk, a larger χ leads to an overall smaller dynamo number at the stage of quasi-steady state. This is a consequence of the quadratic dependence on the disk diffusivity (see Equation 3.49) that balances, respectively quenches the mean-field dynamo effect. For the latest evolutionary stages we notice that, although this happens at different times, for each choice of χ, the simulation reaches its steady stage also at a larger radius. This is an indicator of a faster evolution of the magnetic field for larger χ.

Note that the dynamo number can also be used as a tracer to identify the dynamo-inefficient zones. As the latter correspond to a minimum in the magnetic diffusivity, here the dynamo number will have a sudden growth. On the other hand, the dynamo-inefficient zones are not only zones where the toroidal magnetic field has a minimum, but they also zones where the toroidal field cannot be amplified. For such reason, the general application of the dynamo number as a measure of dynamo activity can be misleading, since its sudden growth (in correspondence of the field reversal) does not necessarily lead to a further magnetic field amplification.

This is shown in Figure 5.4, where we display in the bottom panels the dynamo number for the simulation runs that result in the generation of dynamo-inefficient zones. In contrast, the upper panels show simulations that do not lead to dynamo-inefficient zones. The figure nicely demonstrates a similar evolution of these simulation up to radii where the dynamo-inefficient zones have established when a quasi-steady state is reached.

Interestingly, the dynamo-inefficient zones – representing a minimum in the toroidal and in the radial magnetic field component, do not directly affect the dynamo activity further out. Outside the field reversal zone a saturation of the magnetic field can be reached. This is in particular visible when comparing the two right panels (runs *phi_C* and *th_B*).

Looking at the dynamo number in more detail, we understand why case *R_A* and case *Scalar* (isotropic dynamo) are almost not distinguishable (Figure 5.2, left). The dynamo-inefficient zone that is present in the case *R_A* appears only at later stages of the evolution, as it is located at about $R \simeq 40$ while the magnetic field in the ambient parts of the disk is amplified only on a longer timescale. In contrary, the dynamo-inefficient zone of *R_B* is formed already earlier at $t \simeq 1000$, and therefore a different evolution of the poloidal disk magnetic field takes place, and also on a shorter timescale. The time evolution of cases *th_A* and *th_B* will be discussed below (see Section 5.4).

5.3 Dynamics of Accretion-Ejection

So far we have investigated mainly the evolution of the magnetic field structure that is generated by the accretion disk dynamo, applying different model assumptions for the dynamo tensor. Obviously, the difference in the field structure - difference in strength and geometry - will have strong impact on the dynamics of the accretion disk and the disk wind or jet. In this section we want to discuss the dynamical evolution of the accretion-ejection structure and compare the results for different dynamo models.

5.3.1 Accretion and Ejection Rate

As pointed in the previous sections, the dynamo tensor components that amplify the toroidal field (α_R and α_θ) work on longer timescales than the ϕ-component of the dynamo tensor (which amplifies the poloidal magnetic field). Also, a larger dynamo component α_ϕ leads to a higher magnetic diffusivity. In turn, this leads to a higher accretion rate, as shown in the left panel of Figure 5.5, since the disk diffusivity enables to replenish the disk matter that is lost from the inner disk (by accretion or ejection) from the outer disk regions.

On the other hand, the ejection rate only weakly depends on the strength of the ϕ-dynamo, especially in the early stages of the evolution, ($t \simeq 100$), as shown in the right panel of Figure 5.5. While the inner regions reach a quasi-steady state for $t \gtrsim 500$, the ejection rate decreases until it reaches a quasi-constant level. This magnitude is higher for larger χ, mostly because of the enhanced accretion rate.

We find that the ratio between the ejection and the accretion rate is higher for lower χ. This can be understood as follows. A higher strength of α_ϕ leads effectively to a stronger and faster amplification of the magnetic field. A larger χ, which is itself a consequence of applying an anisotropic dynamo tensor, leads to a stronger disk magnetization[3]. Because of the diffusive quenching we apply, a higher disk magnetization implies a higher disk magnetic diffusivity, which in turn supports higher accretion rates.

For example, Figure 5.5 shows that for $\chi = 2.0$ about $< 50\%$ with of the accretion mass flux becomes ejected. For $\chi < 0.5$ all the matter accreted becomes

---

[3]Note that the disk gas pressure, in absence of dynamo-inefficient zones, is subjected to only very small changes during the temporal evolution of the accretion disk.
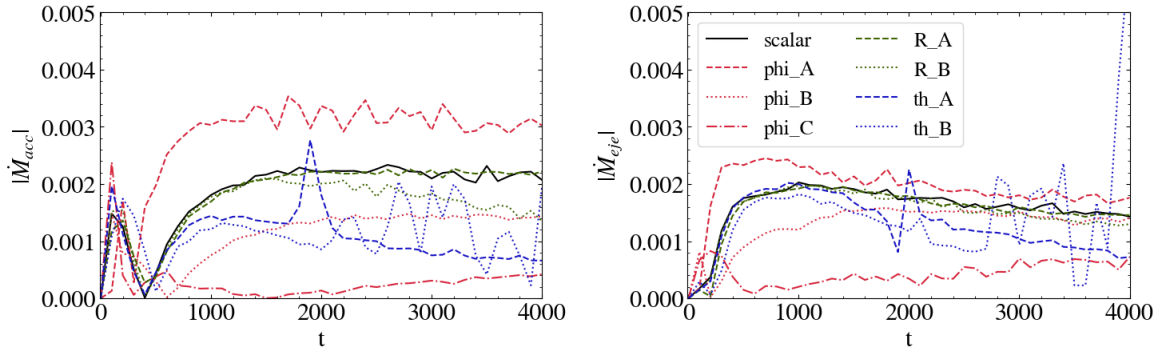
FIGURE 5.5: Temporal evolution of the accretion (left panel) and ejection (right panel) rates. The accretion rate is computed at fixed radius $R = 7$, while the ejection rate is computed along the disk surface from $R = 1$ to $R = 7$. See Sect. 3.4.6 for a definition of the control volume.

ejected into the jet structure. This result is in nice agreement with resistive non-dynamo launching simulations (Zanni, Ferrari, et al., 2007; Sheikhnezami et al., 2012), which showed a correlation between the disk magnetic diffusivity and the ejection-accretion rate ratio.

Once the poloidal field has become dynamo-amplified, the R and θ-components of the dynamo tensor can play a major role in the magnetic field evolution and, thus, also in the dynamics of accretion-ejection as they potentially induce dynamo-inefficient zones in the disk. For simulations for which NO dynamo-inefficient zones emerge, differences in the toroidal magnetic field do not really impact on the poloidal field components, even on longer time scales.

On the other hand we find that a toroidal field reversal and the subsequent formation of multiple anti-aligned loops (and the correspondent dynamo-inefficient zones) in the disk leads to a decrease in the accretion rate. The reason is the diffusive quenching we apply. At the locations where the toroidal field vanishes in the disk, also the magnetic diffusivity has a minimum (because of the low disk magnetization, see Equation 3.49). A low diffusivity lowers the accretion efficiency.

We point out that the increase in the poloidal magnetic energy shown in Figure 5.2 is a value integrated over a control volume. Therefore, even if the overall magnetic energy is high, the formation of zones of low magnetic diffusivity leads to a decrease in the overall accretion rate. As a consequence, the disk mass that is lost by accretion and ejection cannot be efficiently replenished, therefore the accretion rate decreases with time. Also the ejection rate is affected, but at later times. The most immediate consequence of the lower accretion rate is the formation of under-dense and over-dense zones in the accretion disk.

The radial distance of a dynamo-inefficient zone from the inner disk radius is strictly correlated with the timescale at which we observe a decrease in the accretion rate. This is the case for example for simulations R_B and R_A (see Figure 5.5, left). While in the former case the dynamo-inefficient zone leads to a decrease in the accretion rate already at time $t \simeq 2000$, the latter case shows no difference to the simulation applying an isotropic dynamo tensor until time $t \simeq 4000$. Note that the dynamo-inefficient zone is formed only at $t \simeq 4000$, and, therefore, can impact the accretion and ejection rates only on a longer time scale (see Figure 5.4).

5.3.2 Jet Speed and Collimation

An immediate consequence of a variation in the dynamo tensor components is the jet kinematics. As pointed by Stepanovs and Fendt (2016), a higher poloidal disk magnetization will leads to a stronger jet, for example in terms of mass flux and velocity. We know from simulations applying a scalar dynamo model (Fendt and Gaßmann, 2018) that the terminal jet speed is correlated with the strength of α_0; in particular, a stronger dynamo leads to a faster jet. Note that these properties – jet speed, mass flux, or collimation – are global properties and thus accessible in principle by observations, different from the intrinsic local conditions in the disk such as turbulence and dynamo action.

As for the evolution of the magnetic field, the three components of the dynamo tensor have a different impact also for the jet kinematics. When considering different magnitudes of the dynamo-χ, from our simulations we find an correlation similar to the one discovered in Stepanovs and Fendt (2016). That is the fact that a stronger $\phi-$component of the dynamo results in a stronger amplification of the poloidal magnetic field. As a direct consequence, since the midplane pressure shows only a very weak dependence on the dynamo model, a larger χ leads to a higher poloidal disk magnetization (see Figure 5.6). Consequently, with a higher disk magnetization more magnetic energy is available to accelerate the outflow.

We show the terminal jet speed, here computed as the maximum speed at $R = 100$, as function of the magnetization in Figure 5.6. This figure indicates a very clear trend, as proposed by Stepanovs and Fendt (2016). In addition, it demonstrates again the gain in magnetization for different parameters for the dynamo parameter. We find that the maximum jet speed reaches the Keplerian velocity at the inner disk radius However, the maximum speed decreases for smaller χ. This is shown also in Figure 5.7 where we compare the distribution of the jet poloidal velocity for different simulation runs.

The two other dynamo tensor components affect the evolution of the disk magnetization in term of generation (or not generating) magnetic loops and/or dynamo-inefficient zones. Since minima in the magnetic field strength do only have a very minor impact on the overall disk poloidal magnetic energy (and therefore on the disk poloidal magnetization, see Figure 5.2), a difference in ϕ does not necessarily lead to a different jet. The main reason why the jet dynamics is not substantially changed, at least in the early stages of the jet formation and propagation, is that the magnetic field structure remains very similar in the innermost disk regions (see Figure 5.3). This is actually the field structure that is responsible for launching the strongest - and also collimated - jet component.

On the other hand, the dynamo-inefficient zones lead to a different disk mass distribution (see Figure 5.5), which naturally affects the evolution of the whole disk-jet system. In particular, we observe a more turbulent configuration of the poloidal magnetic field (see Figure 5.7), which leads to the ejection of a slower and less massive jet (i.e., with smaller ejection rate, as shown in the bottom panel of Figure 5.5). The latter has been proposed already by Fendt (2006).

Another observable is the jet collimation as an imprint of the overall jet dynamics. There are several options how to best define jet collimation For example, in Fendt (2006), Pudritz, Rogers, and Ouyed (2006), and Sheikhnezami et al. (2012) the degree of collimation has been computed as the ratio of the (normalized) mass fluxes
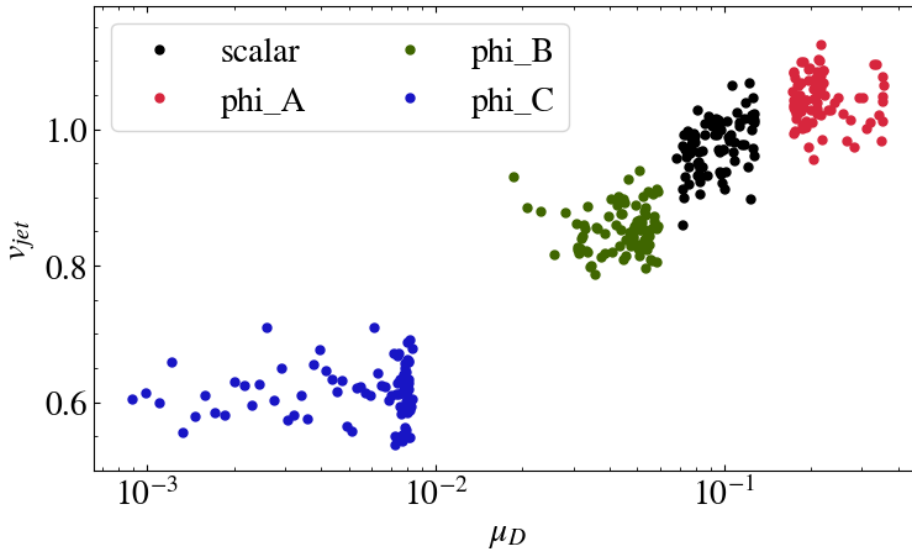
FIGURE 5.6: Jet speed vs disk magnetization. Shown is the maximum jet velocity versus the disk magnetization calculated from the poloidal magnetic field. Note that the disk magnetization is solely resolution from the dynamo component ζ and does not depend from a further quenching parameter.

in the axial and in the lateral direction, respectively. Another option is the pure opening angle. Here we choose a different way to measure the jet collimation quantitatively, taking advantage of the spherical coordinates we applied. More specifically, we compute the opening angle of the jet flow for which the jet has its maximum velocity (or mass flux). Comparing the angle obtained for different (spherical) radii we obtain a gradual change that in particular demonstrates the *process of collimation*.

What we find from our dynamo simulations is essentially that the jet degree of collimation shows only a weak dependence on the strength of the dynamo component α_ϕ. This is maybe expected as we know that collimation depends on the profile of the disk magnetic field rather than its strength (Fendt, 2006; Pudritz, Rogers, and Ouyed, 2006). Therefore, no significant differences are found in the jet collimation for a substantially isotropic dynamo, while an anisotropic dynamo in general leads to a lower degree of jet collimation (see Figure 5.7, left).

Another feature that impacts the degree of jet collimation is the presence of magnetic islands, respectively magnetized vortices. This loops severely disturb of the accretion-ejection structure, enhance the turbulence in the outflow flow, and also affect the efficiency of mass ejection.

The toroidal magnetic field, which plays a leading role in the jet collimation, is affected by α_R and α_θ. In particular, the existence of zones where the mean-field dynamo does not work efficiently, leads to a more turbulent configuration of both the poloidal and toroidal magnetic field (see Figure 5.7, right). Note, however, that jets also self-generate a substantial toroidal field that usually supports collimation (R. D. Blandford and Payne, 1982). Here, the turbulent injection and the turbulent field structure hinder a regular jet toroidal field. Thus, a weak or non-isotropic dynamo will produce a less collimated jet (see again Figure 5.7, right). To summarize,
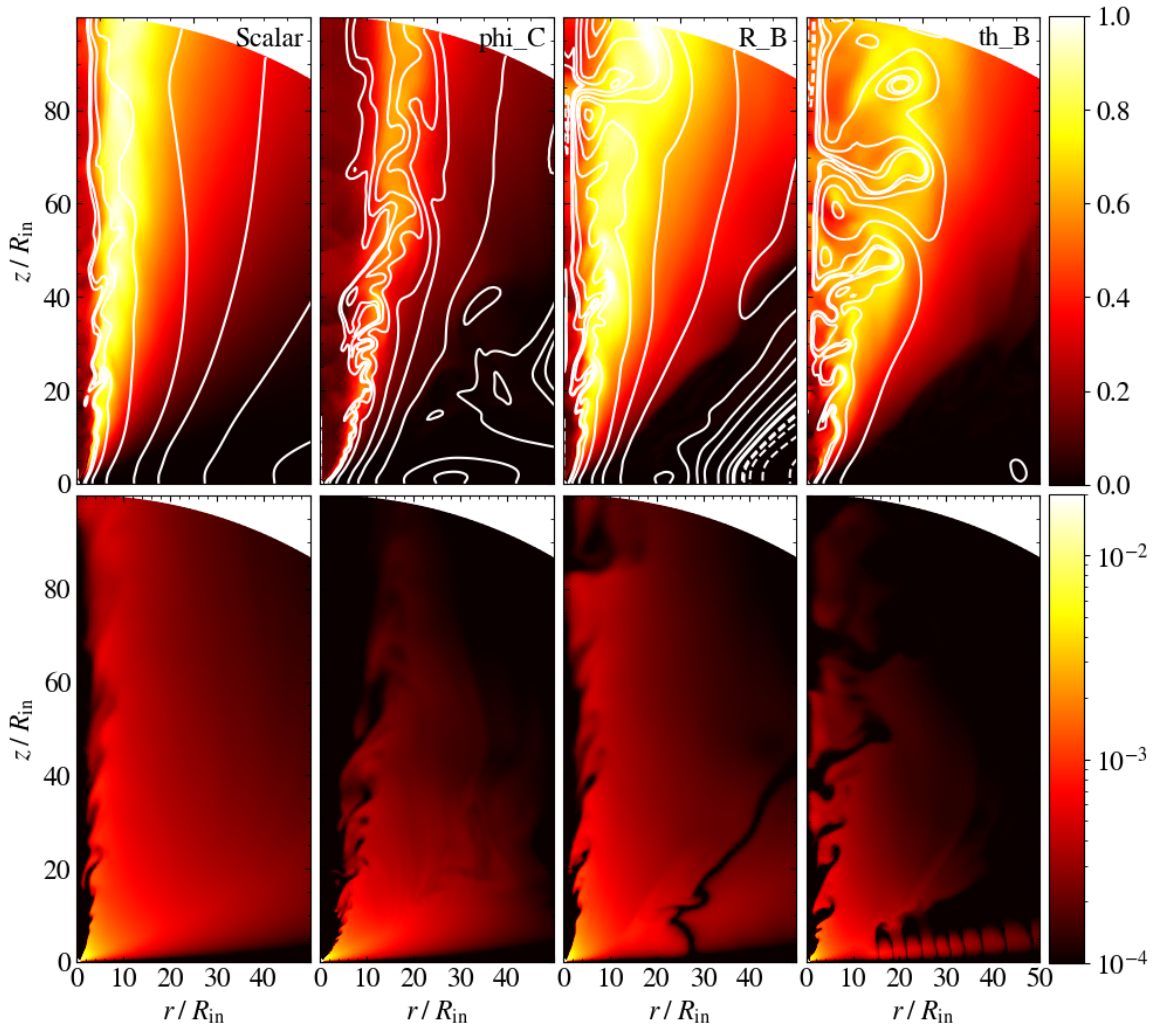
FIGURE 5.7: Comparison of parameter runs at $t = 10000$. Shown is the distributions of the poloidal velocity (top), overlaid with contour lines of the vector potential (following poloidal field lines)(top), and toroidal magnetic field strength (bottom).

the dynamo-inefficient zones lead to a more turbulent evolution of both the magnetic field and the hydrodynamical quantities, resulting in a more turbulent and less collimated jet structure.

5.4 Early Evolution

Since the target of this toy model is to investigate the effects of the different dynamo components on the launching process, we now discuss the impact of the tensor component α_θ in more detail. This mostly relates to the very initial evolution of the simulation.

A first result is that for $0 < \psi < 3$ the evolution of the disk-jet system shows no difference when compared with a scalar dynamo. A likely explanation we find come directly from the choice of the initial configuration of the magnetic field in combination with the induction equation. Since the seed field is purely radial, there

is no B_θ-component that can be coupled by a dynamo process. Therefore, in the initial evolutionary states no contribution can be provided from α_θ. As the system evolves, the diffusive quenching takes place quite rapidly, leading to a quasi-steady state. Eventually, the dynamo effects are counterbalanced by magnetic diffusivity and the component α_θ plays a minor role, just because they are weak and had no time to evolve.

However, when increasing α_θ, as for simulation run *th_A*, its dynamo effect on the temporal evolution becomes stronger. The most important difference to the scalar dynamo simulations is the formation of multiple dynamo-inefficient zones within the accretion disk. As the magnetic field can be amplified only between the dynamo-inefficient zones, this further leads to multiple regions in the disk where the magnetic diffusivity does not grow (see Figure 5.4).

The reason why the early temporal evolution is mostly dominated by the other two dynamo components, essentially depends on the initial magnetic field configuration. On one hand this might look unphysical, as the long-term dynamo amplification of the magnetic field should not depend on its initial structure. On the other hand, a weak field seed must be present in order to initialize a mean-field dynamo effect.

Essentially, a toroidal initial magnetic field leads to the same results (see also Stepanovs, Fendt, and Sheikhnezami 2014). Similar to the case of a radial initial field, the component α_θ is not involved in the initial temporal evolution of the B_ϕ, and therefore is able to play a role only when the magnetic field has already saturated. Thus, the field evolution generated from a purely toroidal initial field leads to results similar to those obtained from a radial seed field.

This is in contrast to simulations starting from a vertical seed field. We find a strong impact on the evolution of the system because of the strong shear between the rotating disk and the non-rotating (at $t = 0$) corona (Fendt and Gaßmann, 2018). In addition, this is amplified by the α_θ dynamo effect of the magnetic field.

This can be nicely seen by our simulation *th_B* applying a vertical seed magnetic field that is derived from a constant vector potential $A_\phi = 10^{-5}$ and is applying an anisotropic dynamo with $\psi = 0.1$. Here, the vertical initial field is able to affect, through the mean-field dynamo, the magnetic field evolution and amplification. A dynamo-inefficient zone is formed around $R \simeq 15$. A collimated outflow is launched, although the overall jet structure shows less collimation compared to the simulation with isotropic dynamo (with radial initial field).

5.5   Summary

Extending the previous works on mean-field dynamo-driven jets (Stepanovs, Fendt, and Sheikhnezami, 2014; Fendt and Gaßmann, 2018), here we have essentially investigated the effects of a *non-scalar* dynamo tensor. We have applied various (ad-hoc) choices for the dynamo tensor components.

In particular we have obtained the following results:

1) We have disentangled different effects of the dynamo tensor components concerning the magnetic field amplification and geometry. We find that the strength of the amplification is predominantly related to the dynamo component α_ϕ. The stability of the disk and the launching process can be affected by re-connection events.

The field geometry that is favouring re-connection is mainly governed by the dynamo components α_R and α_θ.

2) We find that the component α_ϕ is strongly correlated to the amplification of the poloidal magnetic field, such that a stronger α_ϕ results in a more magnetized disk, which then launches a faster, more massive and more collimated jet. In contrast, the amplification of the poloidal field depends substantially on the existence of dynamo-inefficient zones, which, subsequently, affect the overall jet-disk evolution, thus accretion and ejection.

3) We find that not only a stronger dynamo component α_θ but also a radial component α_R defined by $\phi < 0.8 \vee \phi > 1.5$, respectively, leads to the formation of dynamo-inefficient zones. The formation of the dynamo-inefficient zones can also be triggered by a vertical component of the initial magnetic field, even for a weak dynamo component α_θ. A strong α_θ component triggers the formation of the dynamo-inefficient zoned predominantly in the inner disk region. Those loops in general lead to a different evolution of the disk dynamics, since these zones are dynamo-inefficient and prevent accretion of material from the outer regions of the accretion disk to the inner disk that looses mass by accretion and ejection.

4) We have investigated how the action of the three different dynamo components affect the jet structure, respectively. We find the strength of the magnetic field has a minor influence on the jet speed and mass, however the field geometry, in particular the disk magnetic field profile matters a lot. For lower α_ϕ or in presence of dynamo-inefficient zones within the accretion disk, the magnetic field follows a different configuration (with more large-scale magnetic compared a more turbulent structure), which immediately affects the jet structure and collimation.

5) We have disentangled a clear correlation between the anisotropy of the dynamo tensor and the large-scale motion of the jet. In particular, dynamos working with a larger α_ϕ produce a magnetic field that is able to drive faster jets. The reason is that these dynamos lead to a stronger disk magnetization, thus provide more magnetic energy for launching. This result nicely couples to correlations between the disk magnetization and various parameters of the jet dynamics as found by Stepanovs and Fendt (2016).

6) We have investigated the formation of co-called *dynamo-inefficient zones* within the accretion disk and their effect on the disk-jet connection. In particular, such zones are related to a toroidal field reversal with zero derivative, which leads to the formation of multiple loops in the disk. As a consequence, the poloidal magnetic field (in both the disk and the jet) follows a more turbulent evolution, forming, e.g., reconnecting magnetic loops, which affects the overall jet launching, the jet mass loading and, subsequently the jet propagation. These zones result from certain conditions for the dynamo action, i.e., certain combinations of the dynamo tensor components.

Chapter 6

A Consistent Non-Isotropic Dynamo Tensor for Thin Disks

The contents of this chapter are adapted from Mattia and Fendt (2020b), published in *The Astrophysical Journal*. All the simulations, the figures and most of the scientific discussion and interpretation presented in this chapter were done by the author of the thesis.

In this chapter we continue our work from Chapter 5 considering a non-scalar accretion disk mean-field $\alpha^2\Omega$-dynamo in the context of large scale disk-jet simulations. We now investigate a disk dynamo that follows analytical solutions of mean-field dynamo theory, essentially based only on a single parameter, the Coriolis number. We thereby confirm the anisotropy of the dynamo tensor acting in accretion disks, allowing to relate both the resistivity and mean-field dynamo to the disk turbulence. Our new model recovers previous simulations applying a purely radial initial field, while allowing for a more stable evolution for seed fields with a vertical component. We also present correlations between the strength of the disk dynamo coefficients and the dynamical parameters of the jet that is launched, and discuss their implication for observed jet quantities.

The chapter is structured as follows. In Section 6.1 we describe the explicit form of accretion disk dynamo tensor and magnetic diffusivity. In Section 6.2 we describe our reference simulation, showing how this new dynamo model is able to recover the previous results with a reduced number of parameters. We then perform a parameter run in Section 6.3, showing the dependence of the launching process on the Coriolis number. Our findings are summarized in Section 6.4.

6.1 Numerical Details

In Chapter 5 we have considered an an-isotropic mean-field dynamo tensor as a toy model for a realistic accretion disk dynamo. In this chapter we put this on more physical grounds, considering a dynamo tensor that follows from analytical dynamo theory. In particular, we now model the magnetic diffusivity $\overline{\eta}$ and the mean-field dynamo $\overline{\alpha}_{\mathrm{dyn}}$ by applying the mean-field theory of Ruediger, Elstner, and Stepinski, 1995; Bardou et al., 2001. Here, the strength and distribution of the tensor components of both diffusivity and dynamo are constrained by the mean-field theory of turbulence.
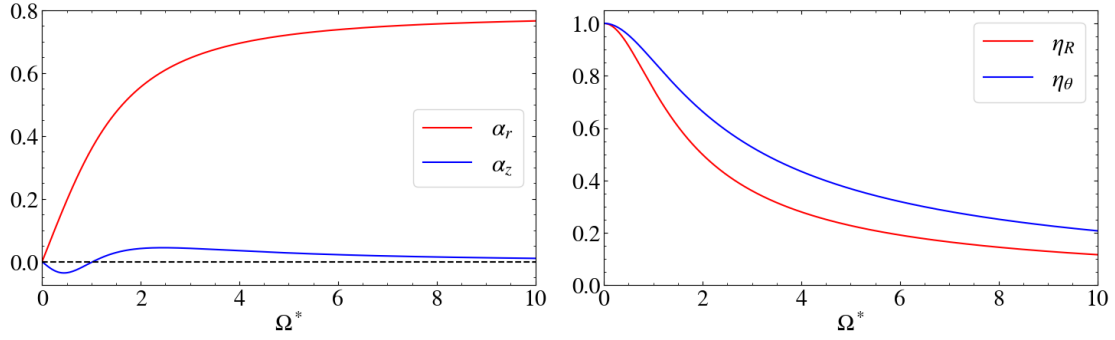
FIGURE 6.1: Diagonal components of the dynamo tensor (left), α_r and α_z, and the magnetic diffusivity tensor (right), η_R and η_ϕ, for different Coriolis numbers Ω^*.

The basic assumptions made are that the accretion disk is sufficiently ionized and that the effects of rotation on turbulence can be described by the Coriolis number

$$\Omega^* = 2\Omega\tau_c, \tag{6.1}$$

where Ω is the frequency of revolution and τ_c is the turbulence correlation time, which can be recovered only by direct simulations (see, e.g., Gressel 2010; Nauman and Blackman 2015; Gressel and Pessah 2015; Gressel and Pessah 2022).

The exact connection between the local shearing box simulations and the large-scale mean-field dynamo is still unclear, since the values found by the local approach ($\Omega^* \simeq 0.4$) are $\simeq 10$ smaller than the ones required in order to recover the amplitude of the mean-field dynamo. For this reason we will present a parameter study of Ω^* in Section 6.3. Future multi-scale dynamo simulations are hoped to solve this problem.

6.1.1   The Dynamo Tensor

An essential assumption for the α-tensor is that we are considering a *thin disk*. In this case, the non-diagonal components of the dynamo tensor are negligible (Bardou et al., 2001). The explicit form of the dynamo term we consider is described by Equation (3.41). The strength of the respective components of α tensor in cylindrical coordinates is

$$\begin{cases} \alpha_{0,r} &= \dfrac{1}{2\Omega^{*3}}\left(\Omega^2 + 6 - \dfrac{6 + 3\Omega^{*2} - \Omega^{*4}}{\Omega^*}\arctan\Omega^*\right), \\[2ex] \alpha_{0,z} &= \dfrac{1}{2\Omega^{*3}}\left(-\dfrac{10\Omega^{*2} + 12}{1 + \Omega^{*2}} + \dfrac{2\Omega^{*2} + 12}{\Omega^*}\arctan\Omega^*\right), \\[2ex] \alpha_{0,\phi} &= \alpha_r. \end{cases} \tag{6.2}$$

(Ruediger, Elstner, and Stepinski, 1995). These component are plotted in the left panel of Figure 6.1. We notice that for larger Ω^* the horizontal component α_r overcomes the vertical component α_z. Moreover, the vertical component changes sign around $\Omega^* \simeq 1.0$.

Since the tensors for the alpha dynamo of Ruediger, Elstner, and Stepinski (1995) is given in cylindrical coordinates (see Equation 6.2), we have transformed all tensor components to the spherical coordinate system we apply for all the simulations discussed here. So, once the cylindrical components of the dynamo vector are computed, they are rotated in order to recover the components also in the spherical coordinates.

For the quenching of the dynamo effect we apply the model of Chapter 5. This basically involves quenching by diffusivity, through the strong feedback of the disk magnetization on the magnetic diffusivity.

6.1.2 The Magnetic Diffusivity

The magnetic diffusivity tensor follows the same general structure as the dynamo tensor (diagonal, and therefore treated as a vector). For the time evolution of the diffusivity, we again adopt the model described in Eqs. (3.44) and (3.45). However, the quantity $\overline{\eta}_0$ which determines the strength and the anisotropy of the diffusivity tensor, is computed following Ruediger, Elstner, and Stepinski (1995),

$$
\begin{cases}
\eta_{0,R} &= \dfrac{3}{4\Omega^{*2}} \left[1 + \left(\dfrac{\Omega^{*2} - 1}{\Omega^*} \right) \arctan \Omega^* \right], \\[2ex]
\eta_{0,\theta} &= \eta_{0,R}, \\[2ex]
\eta_{0,\phi} &= \dfrac{3}{2\Omega^{*2}} \left[-1 + \left(\dfrac{\Omega^{*2} + 1}{\Omega^*} \right) \arctan \Omega^* \right].
\end{cases}
\tag{6.3}
$$

We note that, contrary to the dynamo prescription, the magnetic diffusivity is computed directly in spherical coordinates. The reason is the way the $\eta_\parallel$ and $\eta_\perp$ are computed in Ruediger, Elstner, and Stepinski (1995). The latter can be directly transformed in spherical coordinates, while the dynamo is computed in cylindrical coordinates. However, in the thin disk approximation (which is the case of this thesis), the spherical and cylindrical components show only little differences.

The right panel of Figure 6.1 shows the different components of the magnetic diffusivity as a function of the Coriolis number Ω^*. If the turbulence is weak, $\Omega^* < 1$, the magnetic diffusivity is basically isotropic (Ruediger, Elstner, and Stepinski, 1995). For strong turbulence, the diffusivity becomes highly anisotropic. Overall, the turbulence has a major impact on both the dynamo action and the diffusivity. We point out that the ratio between η_ϕ and η_R in the limit of fast rotation and high turbulence ($\Omega^* \simeq 10$) is comparable with the one used previously (Stepanovs and Fendt, 2014; Stepanovs, Fendt, and Sheikhnezami, 2014).

6.2 A Reference Simulation

The main aim of this chapter is to investigate jet launching by a mean-field dynamo based on a *physical* model of dynamo theory (Ruediger, Elstner, and Stepinski, 1995). In our new approach, the parameter which governs both the mean-field dynamo and the magnetic diffusivity is the Coriolis parameter Ω^*. We will discuss below
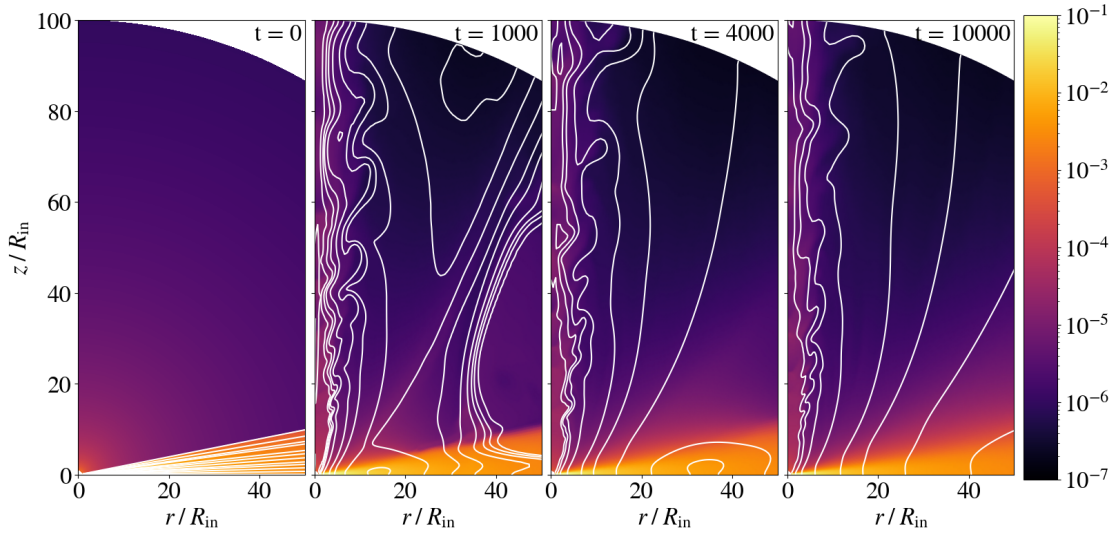
FIGURE 6.2: Time evolution of the disk-jet structure of the reference dynamo simulation with $\Omega^* = 10$. Shown are simulation steps at $t = [0, 1000, 4000, 10000]$ on a subset of the full numerical grid ($r < 50$, $z < 100$). We display the mass density (colors, in log scale), superimposed by contours of the vector potential, respectively magnetic flux surfaces.

simulations applying different Coriolis numbers in the range $\Omega^* \in [0, 10]$, therefore changing the strength of the dynamo and the diffusivity.

For a reference simulation we have chosen a Coriolis number of $\Omega^* = 10$, while the other parameters (see above) are taken from Fendt and Gaßmann (2018). Our reference simulation is mainly used to provide a link to the toy models discussed above and that prescribe certain combinations of the dynamo tensor. With the present section we therefore also link the toy model to the physical theory of Ruediger, Elstner, and Stepinski (1995)

A Coriolis number $\Omega^* = 10$ may be considered as high (Gressel, 2010; Gressel and Pessah, 2015), this magnitude has commonly been used for example of studies of a direct dynamo (Ruediger, Elstner, and Stepinski, 1995; Rekowski, Rüdiger, and Elstner, 2000) in order to describe rotating disks for which turbulence has a major effect on the mean-field dynamo.

The run time of our reference simulation (denoted as *OM10* from now on) is $t_\text{F} = 10000$, corresponding to $\simeq 1500$ inner disk rotations. This time is needed to reach a quasi-steady state across the majority of the domain. As for Stepanovs, Fendt, and Sheikhnezami (2014), this time is not dictated by numerical issues, but chosen in order to save CPU time, as the configuration of the accretion-ejection system does not really change afterwards.

In Figure 6.2 we show the temporal evolution of the reference simulation. Again the initial setup consists in a weak radial magnetic field confined within the accretion disk. While the poloidal magnetic field is (if absent, i.e., B_θ) generated and amplified only through a dynamo effect, the toroidal magnetic field is generated by the differential disk rotation and then amplified through the mean-field dynamo. As discussed in Chapter 5, the dynamo component α_ϕ provides the only mechanism that is able to amplify the poloidal magnetic field from the toroidal magnetic field.
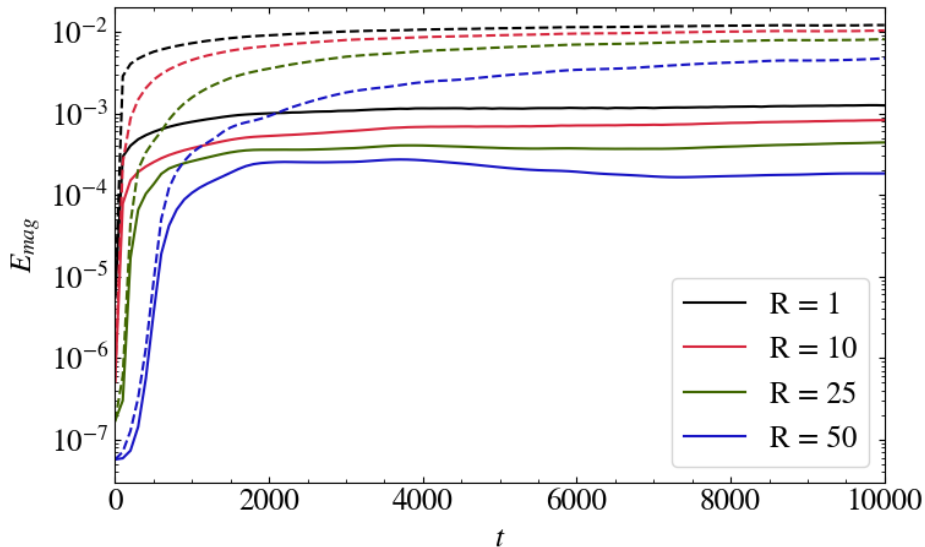
FIGURE 6.3: Time evolution of the disk magnetic energy for different integration domains for the reference simulation. Solid lines show the poloidal magnetic energy, while dashed lines show the total magnetic energy (poloidal + toroidal). The radii that are labeled denote the lower integration boundary, while the upper integration boundary is at the end of the domain, $R = 100$.

Essentially, the reference model evolves very similar to the scalar model of Chapter 5, we hardly detect any differences. The magnetic field is most rapidly amplified in the innermost disk region $t \lesssim 500$. As a consequence, super-Alfvénic and super-fast (in the outer domain we reach $v_{\text{jet}} \simeq 1.5 v_{\text{A}}$, where v_{A})is the Alfvén speed) outflows emerge from this part of the accretion disk, very similar to our toy model and to the literature (Stepanovs, Fendt, and Sheikhnezami, 2014; Fendt and Gaßmann, 2018), while in the outer regions the magnetic field is amplified on a longer timestcale ($t \lesssim 5000$).

Also the inclination of the dynamo-generated magnetic field is favorable for the Blandford-Payne magneto-centrifugal acceleration mechanism (R. D. Blandford and Payne, 1982; Pelletier and Pudritz, 1992), just as in the scalar dynamo simulations. The jet is ejected from the inner radii of the accretion disk, $R \lesssim 10$. Its opening angle decreases as it moves away from the disk - thus, the jet becomes collimated. Because the disk is magnetically diffusive, the magnetic field structure is able to re-arrange, leading to a loop structure in the disk without dynamo-inefficient zones. This loop structure is swept outward during the long term temporal evolution for $t \gtrsim 5000$.

In Figure 6.3 we again display the evolution of the disk poloidal and toroidal magnetic energy as a main signature of the mean-field dynamo, however here derived from a physical model of the dynamo tensor. The field amplification works on a very short timescales - naturally for a dynamo effect, with the dynamo working much faster in the inner part of the disk.

After a rapid amplification, the magnetic energy slightly decreases over time. This is caused by the new model for the dynamo tensor, which now depends on the mid-plane adiabatic sound speed, and therefore is not constant in time. Although
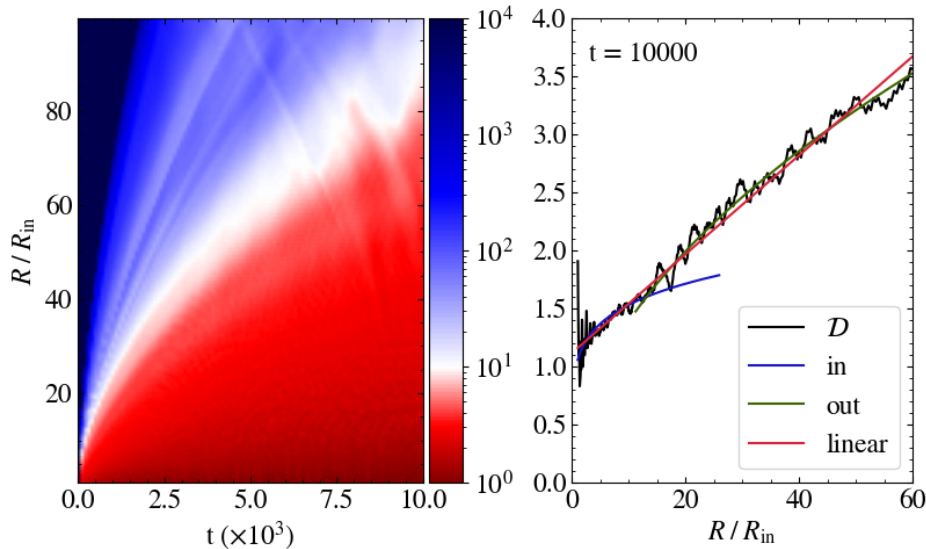
FIGURE 6.4: Dynamo number $\mathcal{D}$ as function of time and radius for the reference simulation. The left panel shows the evolution of the dynamo number for all radii. The right panel shows the dynamo number at $t = 10000$ within an area of steady state. The lines denote the dynamo number D (black), and the power law approximations (dashed, see text).

the sound speed shows no significant change through the temporal evolution, it decreases with time due to the mass loss from the disk by accretion and ejection. We find this behaviour in both scalar and vector dynamo simulations as a consequence of the decrease in the dynamo efficiency (sound speed) together with the high diffusivity (diffusive quenching).

As for the toy model, we have considered the dynamo number $\mathcal{D}$ as a key parameter to determine the stability and the evolution of the system (see Figure 6.4). In the inner disk region the diffusive quenching acts on a very rapid timescale, saturating the magnetic field and decreasing the dynamo number critically below 10 in the very early stages of the evolution. As we move further out in radius, the mean-field dynamo leads to a slower and weaker field amplification. The disk magnetization and, thus, the critical dynamo number, defined as the magnitude of the dynamo number at which the disk has reached a stable configuration is reached on a longer timescale. We find that the critical dynamo number is $\mathcal{D} \simeq 10$, which is similar to the magnitude[1] found in the literature (see, e.g., Brandenburg and Subramanian 2005).

In quasi steady state, the local dynamo number grows with radius (see Figure 6.4, right panel). Interestingly, we may fit this dependence with a broken power law. Thus, after saturation, we may divide the domain of dynamo action into two parts. We find an inner part with $R \in [1, 20]$ that is best reproduced with a power law exponent $\simeq 0.25$, while for the outer part for $R > 20$ a square root dependence is the best fit.

---

[1]The critical dynamo number represents the threshold for the onset of non-linear dynamo action. As it depends on the physical setup of the problem it is not straight forward to compare these number for different model setups.

TABLE 6.1: Simulations applying the tensor model for the dynamo coefficients. The sole dynamo parameter is now the Coriolis number Ω^*. The run time of the simulations is t_F in units of 1000.

run ID	Ω^*	t_F	Comment
OM01	0.1	10	no jet collimation
OM04	0.4	10	dynamo-inefficient zones present
OM1	1.0	10	dynamo-inefficient zones present
OM5	5.0	10	dynamo-inefficient zones absent
OM10	10.0	10	reference simulation

As a physical reason for the broken power law we have disentangled the evolution of the disk diffusivity, in particular the dependence on the magnetization provided by α_{ss} (see Equation 3.49). In the inner region, a power-law approximation of the disk magnetization suggests a power index of -0.07 (blue dashed dotted line), while in the outer region a power index of -0.17 is preferred (green dashed dotted line).

Physically, this indicates that the accretion disk is pressure dominated, although very close to a magnetization constant in radius. For this reason, a linear approximation (red dashed line) also provides a reasonable fit good - without the need to separate the steady state disk regions into two parts. Essentially, even if a linear approximation is more simple, the split into two power laws is (i) more accurate, and can also be (ii) related to the disk physics.

6.3 A Parameter Survey

In order to understand in more detail how the magnetic field evolution is correlated with a different dynamo tensor, we have performed simulation runs applying a different Coriolis number Ω^* ranging within $[0, 10]$, see Tab. 6.1. We stress again that the Coriolis number compares effects of rotation to those of turbulence, with turbulence being responsible to amplify a poloidal field while rotation amplifying the toroidal field.

We first have a look at the dynamo coefficients and diffusivity coefficients (see Figure 6.1). We see that the α_z-component of the dynamo tensor changes sign and is vanishing at $\Omega^* \simeq 1$. However, this component of the dynamo tensor becomes effectively relevant only for low Coriolis numbers. This is the limit of low rotation. In the limit $\Omega^* \to 0$ all the dynamo components tend to vanish, and the magnetic diffusivity becomes isotropic.

6.3.1 Amplification of the Magnetic Field

As for the toy dynamo model, the primary effect of the mean-field dynamo is the amplification of the disk magnetic field. We first compare the magnetic field amplification for different Coriolis numbers (see Figure 6.5). Since the dynamo component α_ϕ depends monotonously on the Coriolis number (see Equation 6.2), one would expect a higher Ω^* to result a stronger magnetic field. However, the critical dynamo
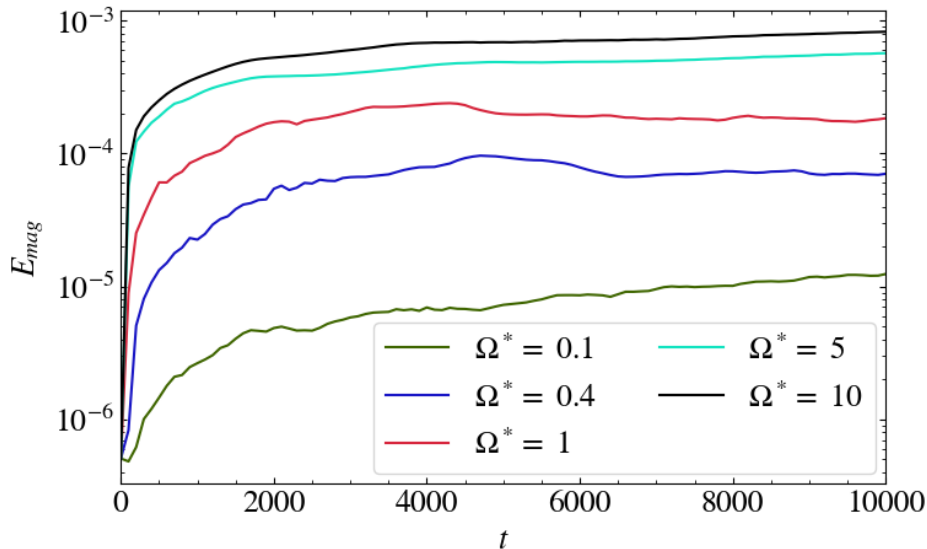
FIGURE 6.5: Evolution of the magnetic field for different Coriolis numbers $\Omega^* \in [0, 10]$. We show the poloidal magnetic energy integrated from $R = 10$ as a function of time.

number discussed in Chapter 5 is not applicable anymore, since the Coriolis number has also a strong effect on the disk diffusivity.

What we find is that for $\Omega^* \lesssim 0.15$ the dynamo-amplification of the magnetic is sufficiently efficient in order to generate a collimated outflow, corresponding to a maximum (absolute) value of $\alpha_{\text{crit}} \simeq 0.005$. Note that this value $\simeq 10$ times larger than the one recovered by Fendt and Gaßmann (2018) and almost twice as large as the value that we recovered for our toy model above.

This discrepancy is related to the model for the magnetic diffusivity, which is now self-consistently determined by the Coriolis numbers, similar to the dynamo-alpha. In fact, for the critical strength of the dynamo, now also the diffusivity level is higher than in Fendt and Gaßmann (2018) and and also higher than for the toy model discussed above. For $\Omega^* \simeq 0.1$, thus slightly below its critical magnitude, the dynamo process is also able to amplify the poloidal field, however, we do not find collimated outflows from the resulting magnetic field configuration.

We note that a correlation between the profile of disk magnetization and jet collimation has been proposed already by Fendt (2006), such that a high degree of collimation requires a flat magnetization profile, thus a sufficient magnetization also for larger disk radii. This is what we seem to observe in our dynamo simulations, since the magnetization of case *OM01* is lower for larger radii.

We therefore disentangle the following correlations. A higher Ω^* implies a large dynamo efficiency α_ϕ that leads to a larger disk magnetization (stronger field, as the disk gas pressure remains similar), which finally supports jet collimation. For $\alpha_\phi \gtrsim \alpha_{\text{crit}} \simeq 0.005$ the poloidal magnetic field is amplified to different magnitudes and also on different timescales. Naturally, a stronger dynamo term, as shown in Chapter 5, leads to a stronger amplification of the poloidal magnetic field on a faster timescale. In particular we see that the poloidal magnetic energy increases rapidly before $t = 500$, and after a strong amplification, the saturation state is reached on a later timescale.
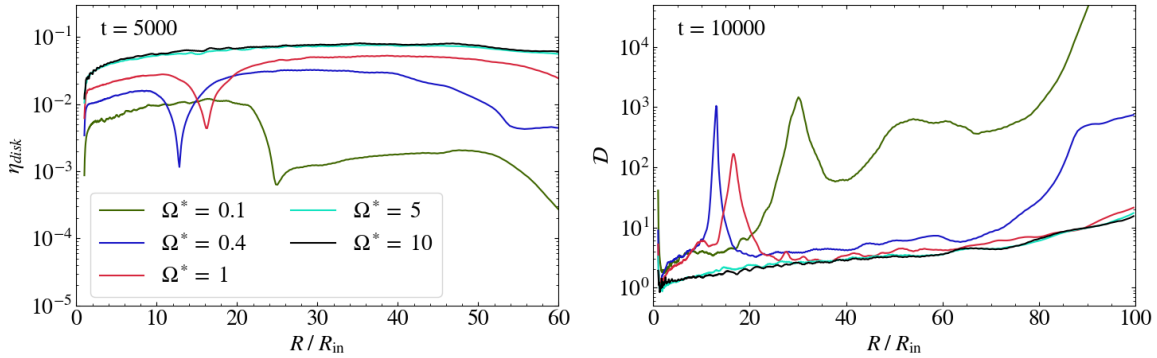
FIGURE 6.6: We show the disk diffusivity η at $t = 5000$ (left panel) and the dynamo number $\mathcal{D}$ at $t = 10000$ (right panel) as a function of radius along the disk for different Coriolis numbers $\Omega^* \in [0, 10]$.

Since a weaker dynamo can amplify the poloidal magnetic field only to lower strength, the poloidal disk magnetic energy does not increase immediately in the case of $\Omega^* \simeq 0.1$. This is simply due to the evolution of the magnetic diffusivity, which follows a faster timescale than the dynamo-α_ϕ. However, since the toroidal field is amplified from the initial field by the Ω-effect, the poloidal field is eventually amplified as well.

6.3.2 Magnetic Diffusivity and Dynamo Number

We now investigate how the magnetic diffusivity and the dynamo number evolve with respect to our main simulation parameter, the Coriolis number. In Figure 6.6 (left panel) we show the disk magnetic diffusivity profile for different Coriolis numbers at $t = 5000$. We may identify three different evolutionary characteristics.

For (i) high Coriolis numbers, $\Omega^* \gtrsim 3$, the diffusivity profile is very similar to the one for the reference simulation with $\Omega^* = 10$. The diffusivity profile remains somewhat constant for $10^{-2} < \eta < 10^{-1}$. Here, the magnetic field amplification leads to an increase of diffusivity quite rapidly (diffusive quenching) and a steady state is reached soon at $t \lesssim 500$ in the inner disk region.

For (ii) lower Coriolis number dynamo-inefficient zones are formed (one or even more) within the accretion disk, due to the low α_R. These dynamo-inefficient zones are clearly visible in Figure 6.6 as zones where the magnetic disk diffusivity sharply decreases. This behavior can be seen for simulations applying $0.4 < \Omega^* < 1.0$.

For (iii) even lower Coriolis numbers, e.g., for $\Omega^* = 0.1$, the magnetic field amplification remains low. Therefore, in addition to the emerging magnetic loops, the dynamo in outer regions of the disk is not able to amplify the magnetic field. Again, as discussed above, because of the weak magnetic field, magnetic diffusivity remains low as well. Still, the inner disk has a substantial magnetic field and also a high diffusivity.

In order to understand if and where the amplification of the magnetic field is saturating, we have a look at the dynamo number at $t = 10000$ (Figure 6.6, right panel). For larger Ω^*, e.g., $\Omega^* \gtrsim 3$, the magnetic field (both poloidal and toroidal) has been amplified in all areas of the accretion disk at this time (but not in the dynamo-inefficient zones). As we know, the actual amplification of the magnetic field plays

a key role in the diffusive quenching model (see Equation 3.49). Therefore, for the Coriolis numbers considered, the dynamo number, which directly depends on the magnetic diffusivity, falls under a critical magnitude for dynamo action.

This does not apply for the dynamo-inefficient zones. Although these zones are characterized by a large dynamo number, they are not correlated with the amplification of the magnetic field. With a lower Coriolis number, the magnetic field amplification occurs on longer timescales, especially for the outer disk. For this reason, besides the dynamo-inefficient zones, the dynamo number remains over its critical magnitude also in the outer disk regions, for which just more time would be required in order to reach a magnetic field saturation. Moreover, for $\Omega^* \lesssim 0.1$, the dynamo number is not a good measure for the mean-field dynamo, since it is not connected anymore to the process of field amplification.

6.3.3   Dependence on the Initial Seed Field

Mean-field dynamo action is expected to be independent on the initial seed field, due to the exponential growth by the dynamo amplification. However, we discovered that second-order effect of the initial evolution may affect also the long term evolution of the system.

In Chapter 5 we have discussed the impact of the dynamo component α_θ in the toy model. We had found that when applying a vertical *initial* magnetic field, the scalar dynamo model may lead to a non-physical hydrodynamical evolution, mainly caused by low density zones forming in the proximity of the inner radial boundary. The origin of these numerical issues seems to be due to the formation of dynamo-inefficient zones in the very inner part of the accretion disk. Since for the toy model there are no *a priori* constraints on the dynamo tensor components, we also have tested the effects of an initial vertical seed field with a reduced strength of α_θ ($\psi = 0.1$), just in order to avoid the formation of the dynamo-inefficient zones in the inner disk.

In the analytical model of Ruediger, Elstner, and Stepinski (1995) the anisotropy of the tensor component α_θ is introduced naturally on physical grounds and it does not require any additional constraint. We have performed a simulation with $\Omega^* = 10$ and a vertical initial magnetic field (applying a vector potential $A_\phi = 10^{-5}$). Indeed, the results are comparable with the simulations run th_B of Chapter 5 (see Figure 6.7).

Here the component α_θ is suppressed, as directly inferred from analytical dynamo theory, and no ad-hoc assumption of anisotropy is required. Therefore, the effects of shear between the rotating disk and the steady-state corona are not amplified by the dynamo as they were in the scalar dynamo model.

As demonstrated in Chapter 5, the amplification of the poloidal disk magnetic field occurs on different time scales depending on the distance from the central object. Although during early stages the field amplification looks to the case of an initially radial initial field (see, e.g., Figure 6.3 for a comparison), at $t = 4000$ the poloidal magnetic energy that is dynamo-amplified is comparable.

The saturation of the magnetic field amplification towards the same magnitude is evidence for the ongoing action of the mean-field dynamo, which is able to generate a magnetic field regardless of the initial magnetic field configuration. The fact that
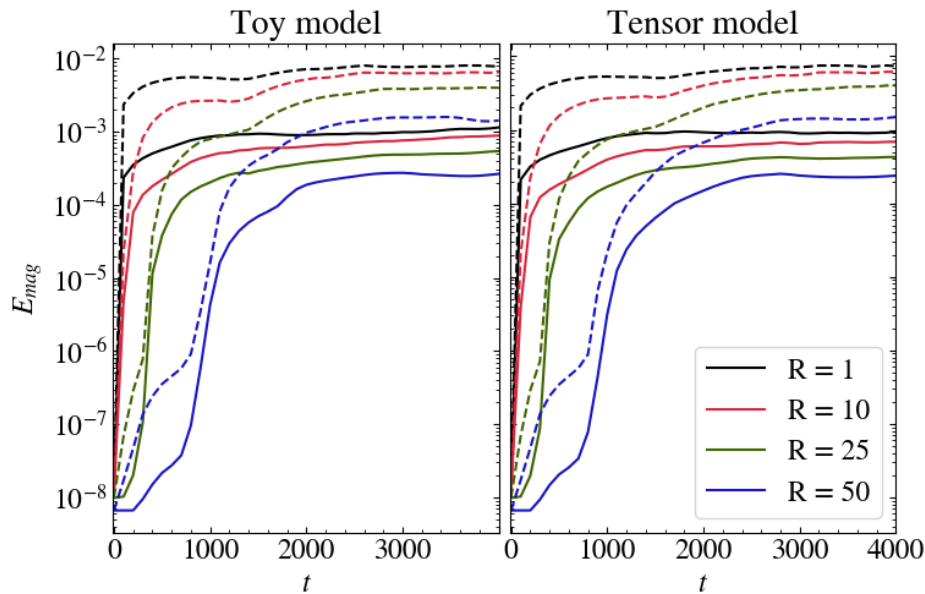
FIGURE 6.7: Time evolution of the disk magnetic energy for simulations applying a vertical seed field. The radii that are labeled denote the lower integration boundary, while the upper integration boundary is at the end of the domain, $R = 100$. Solid lines denote the poloidal magnetic energy, while dashed lines show the total magnetic energy (poloidal + toroidal).

the two panels of Figure 6.7 are basically indistinguishable from Figure 6.3 indicates how much the component α_θ is overestimated in the scalar dynamo model when non-radial initial magnetic field is present. This is a clear advantage of the tensor model, since it allows to suppress the different dynamo components without adding additional constraints.

A substantial difference between simulations applying an initially radial or vertical initial field, respectively, is the formation of dynamo-inefficient zones even for $\Omega^* = 10$. This implies that anti-aligned magnetic loops can form also in case of a high Coriolis number.

Overall, the evolution of dynamo-inefficient zones can also depend on the dynamo quenching model and the diffusivity model.

6.3.4 Accretion and Ejection

A difference in the magnetic field structure plays a key role in the dynamics of the accretion disk and the outflow. This holds for the toy model for the dynamo tensor as well as for the physical model for the tensor components. In this section we want to discuss the dynamical evolution of the accretion-ejection structure for the model of Ruediger, Elstner, and Stepinski (1995) and compare the results for different Coriolis numbers Ω^*.

In fact, as a first general result we do not significant differences between the scalar toy model and the reference simulation *OM10*. This nice agreement validates the model approach described in Chapter 5 in the context of jet launching large scale simulations.
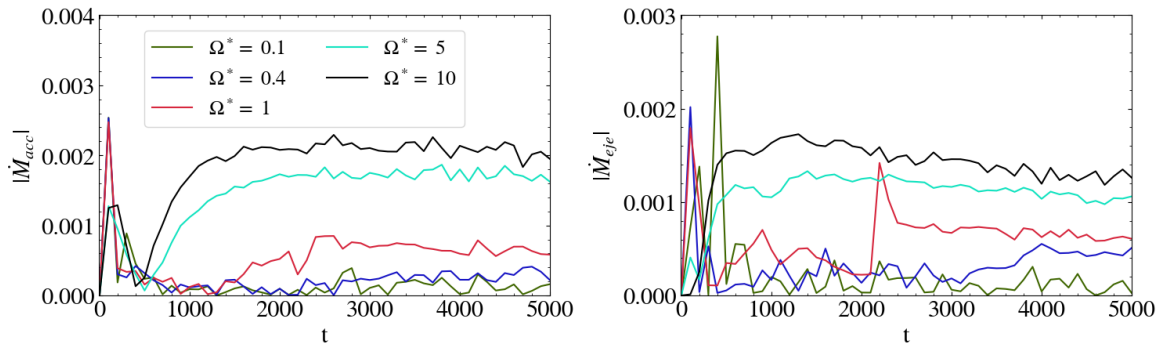
FIGURE 6.8: Evolution of the accretion (left panel) and ejection (right panel) rates for different Coriolis numbers $\Omega^* \in [0, 10]$. The accretion rate is computed at $R = 7$, while the ejection rate is computed along the disk surface between $R = 1$ and $R = 7$ (see 3.4.6 for a definition of the control volume).

We now compare further simulation runs. We first consider the accretion and ejection rates in Figure 6.8. The accretion rate increases with the Coriolis number, meaning it increases as well with the strength of the mean-field dynamo. This is because a stronger field amplification, implying a higher disk magnetization, leads to a higher diffusivity and therefore facilitates accretion. In addition, a stronger magnetic field is also more efficient in angular momentum removal. When dynamo-inefficient zones are present (see Figure 6.6), they effectively enhance the difference between accretion and ejection rates as we have discussed already in Chapter 5.

The ejection rate, increases with the Coriolis number, similar to the accretion rate. In general, the ejection-accretion ratio is higher for a lower dynamo efficiency, in agreement with previous simulations (Stepanovs, Fendt, and Sheikhnezami, 2014) and with the toy dynamo model, as it depends on the dynamo components α_ϕ and α_R.

We also notice a slow decrease over time in the ejection rates, which we understand are due to subtle changes in the disk dynamics. Such variations could be triggered by the disk mass loss, which in turn effects the dynamo tensor components, as they are parameterized by the sound speed at the disk mid-plane.

Before reaching the quasi-steady state, the accretion-ejection rate, defined as $\dot{M}_{\mathrm{eje}}/\dot{M}_{\mathrm{acc}}$ (see 3.4.6), may exceed unity[2]. The reason of such a high ejection efficiency in early evolutionary stages is due to the time scales of the processes involved. In fact, accretion requires more time to establish and to saturate, while ejection operates on a faster timescale.

A reason why there evolves a more turbulent state of the accretion disk, is the magnitude of α_R, which changes as well with the Coriolis number. As shown before, for a lower strength of Ω^* magnetic loops are formed in the disk, implying a more turbulent evolution. A peculiar case is when $\alpha_\phi < \alpha_{\mathrm{crit}}$ (e.g., for *OM01*). Here, the magnetic field is amplified, but not to a sufficient strength in order to collimate the jet. In this case the accretion rate – correlated to the magnetic diffusivity – is almost negligible, however, we still find some slight ejection in the form of un-collimated disk winds.

---

[2]This is impossible in steady-state, as the disk mass will be dispersed rapidly
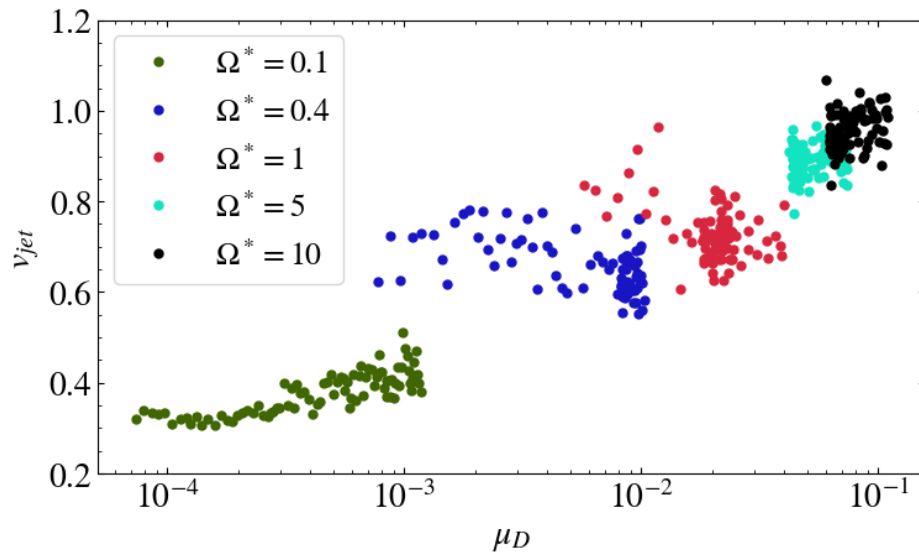
FIGURE 6.9: Jet speed vs disk magnetization. Shown is the maximum jet velocity versus the disk magnetization calculated from the poloidal magnetic field for different Coriolis numbers $\Omega^* \in [0, 10]$.
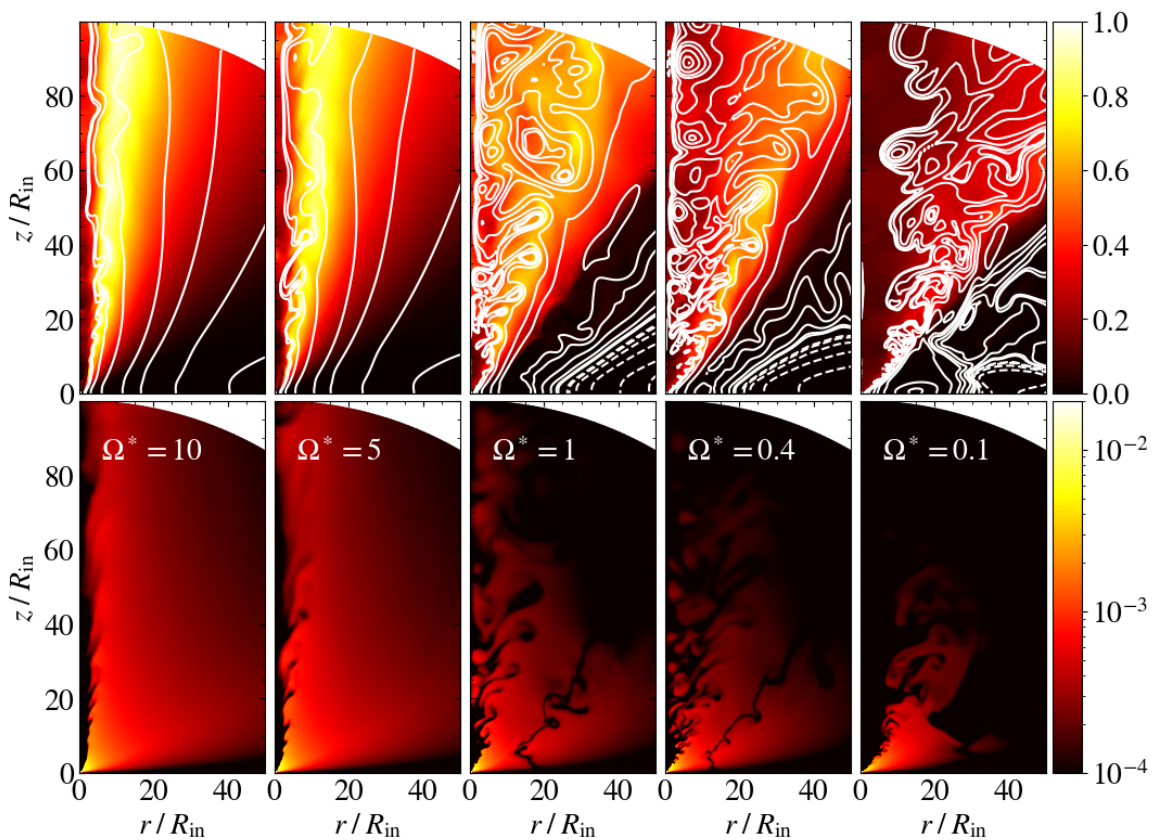
FIGURE 6.10: Comparison of parameter runs at $t = 10000$. Shown is the distributions of the poloidal velocity (top), overlaid with contour lines of the vector potential (following poloidal field lines)(top), and toroidal magnetic field strength (bottom) for different values of the Coriolis number Ω^*.

The differences in the mass loading and in the magnetic field reflect on the jet speed and kinematics. As for the toy model, we expect the jet speed increase with the magnetization, which is strictly correlated with the Coriolis number Ω^*.

The correlation between poloidal disk magnetization and jet speed is shown in Figure 6.9. The increasing in the jet speed as a function of the disk magnetization shows a nice agreement with Stepanovs and Fendt (2016) and with the toy model. We find that for $\Omega^* \gtrsim 1$ the jet speed reaches the Keplerian velocity at the inner disk radius, which is a well-know result for jet formation simulations (see, e.g., Ouyed and Pudritz 1997; Krasnopolsky, Z. Li, and R. Blandford 1999), and decreases for lower values of the Coriolis number.

Another observable is the jet collimation, which shows the impact of the disk dynamo on the jet dynamics. Using the same definition of collimation used in Chapter 5, we see from Figure 6.10 how the Coriolis number (and therefore the dynamo tensor) affects the jet collimation. As shown in Section 6.3.2, it is possible to find three different outcomes. For high Coriolis number ($\Omega^* \gtrsim 3$), we find a highly collimated jet. For $\Omega^* \lesssim 3$ the evolution is characterized by the formation of dynamo inefficient zones, which play a key role in the jet speed and collimation. The structure of the poloidal magnetic field is more turbulent, which implies a less collimated jet. In addition, a lower value of the Coriolis number means also a weaker α_ϕ component, which leads to a weaker disk magnetization (see Figure 6.9) and therefore, in agreement with Fendt (2006), a less collimated jet. Below the critical Coriolis number ($\Omega^* < 0.15$) the amplification of the poloidal field does not occur, and therefore the outflow is not collimated. We also see that the toroidal field is not able to expand through the domain, and it remains confined in the inner regions of our domain. This results are a combination of the two main results found in Chapter 5, i.e., the strength of the component α_ϕ and the formation of the dynamo inefficient zones.

Here we may close the loop to the observed jet quantities. Overall we find that magnetic fields generated by a disk dynamo can well launch outflows and accelerate and collimate them into jets. In particular this holds for a anisotropic dynamo of a thin disk, which can produce a disk magnetization that is able to eject strong jets.

However, we also find that in other that than *thin* accretion disks the dynamo is influenced also by other tensor components. Those lead to more unstable, more structured, but slower outflows, which may potentially not survive on the observed spatial scales. We find a variation in the jet speed between 0.3 and 1.1 the Keplerian speed at the inner disk orbit.

We propose that the variety of observed jet structures thus may reflect the underlying variation of accretion disks, both coupled by the disk-dynamo generated magnetic field.

6.4 Summary

Extending our approach from Chapter 5 where we applied (ad-hoc) choices for the dynamo tensor components, here we consider an analytical model of turbulent dynamo theory (Ruediger, Elstner, and Stepinski, 1995) that incorporates both the magnetic diffusivity and the turbulent dynamo term, connecting their module and anisotropy by only one parameter, the Coriolis number Ω^*.

In particular we have obtained the following results:

1) The prime advantage of the tensor dynamo model is the reduced number of the parameter space, in combination with the physically more consistent approach for the dynamo. Both the dynamo and the diffusivity tensor can be fully recovered from one single parameter – the Coriolis number Ω^*. Another significant advantage of the tensor model is the physical constraint for the different dynamo components. Applying a non-radial seed magnetic field, the tensor model naturally suppresses the dynamo action by the component α_θ, which plays a key role in presence of a non-radial initial magnetic field.

2) Our new approach confirms the previous results of dynamo simulations, as they are included in the new modeling as a limiting case (e.g., Stepanovs, Fendt, and Sheikhnezami 2014; Fendt and Gaßmann 2018). Essentially, the tensor dynamo model shows very good agreement with previous studies and the toy model described in Chapter 5, recovering very similar results, thereby approving the approach of the toy model. Looking at different Coriolis numbers, we can distinguish between high values ($\Omega^* \gtrsim 3$), where the disk shows no dynamo-inefficient zones, a low $\Omega^* \lesssim 3$, where the evolution of the disk is affected by the formation of one or more dynamo-inefficient zones. For even lower $\Omega^* \lesssim 0.15$ dynamo-inefficient zones form and the disk magnetization does not saturate at large radii – both effects affect the jet collimation on the simulation time scales considered.

3) We have studied the evolution of the launching process and and also the properties of the ejected jet flow the for different Coriolis numbers Ω^* that affect the dynamo process. We find that a higher Ω^* leads to a stronger amplification of the magnetic field. This results is in agreement with previous (scalar) mean-field dynamo simulations, but is now put on a more physical ground as it is connected to a more physical disk dynamo model.

4) We have further extended the correlation found by Stepanovs and Fendt (2016) and in Chapter 5 between the accretion disk magnetization and the jet speed, linking the former quantity to the mean-field dynamo. In particular we have found that higher values of the Coriolis number Ω^* lead to a stronger magnetization within the accretion disk and therefore to a faster jet. If the Coriolis number (and therefore the dynamo) is not strong enough to amplify the poloidal magnetic field, we find an uncollimated outflow in form of slow disk wind.

5) We have investigated the formation of the so-called *dynamo-inefficient zones* for different values of the Coriolis number and their effect on the disk-jet connection. We find that for small Coriolis numbers $\Omega^* \lesssim 3$, dynamo-inefficient zones are formed in the accretion disk.

6) We have investigated the detailed physical interaction of the dynamo with the field structure by applying a vertical seed magnetic field following the initial evolution of the field amplification by the dynamo tensor component α_θ, which is naturally overestimated in the scalar dynamo model (for disk dynamos). Essentially, we find that a non-isotropic dynamo leads to more stable evolution of the disk-jet system, since the component α_θ (leading to a magnetic field sub-structure) is naturally suppressed without any additional constraints.

7) We emphasize the astrophysical relevance of our findings. Firstly, dynamo generated magnetic fields can well launch outflows and accelerate and collimate them into jets. This holds in particular for a turbulent, anisotropic disk dynamo,

which can produce strong jets. Secondly, other than thin accretion disks are influenced also by other dynamo tensor components that lead to more unstable, more structured, but slower outflows, which may potentially not survive on the observed spatial scales. We find a variation in the jet speed between 0.3 and 1.1 the Keplerian speed at the inner disk orbit. Thirdly, the observed variety of jet structures thus may reflect the underlying variety of accretion disks, that is coupled to the outflows via the disk-dynamo generated magnetic field.

Chapter 7

The Feedback of the Magnetic Field on the Dynamo and Diffusivity

The contents of this chapter are based on a paper submitted to the Astrophysical Journal by Giancarlo Mattia and Christian Fendt, titled: Jets from Accretion Disk Dynamos: Consistent Quenching Modes for Dynamo and Resistivity (Mattia and Fendt, 2022). All the simulations, the figures and most of the scientific discussion and interpretation presented in this chapter were done by the author of the thesis.

In this chapter we address the question of how the magnetic field required for jet launching is generated and maintained by a dynamo process by investigating how the feedback of the generated magnetic field on the mean-field dynamo affects the disk and jet properties. We find that a different dynamo feedback models lead to a saturation of the magnetic field at a different vales of the disk magnetization. Despite such differences, we find that the dynamo feedback models do not alter the overall jet properties discovered in the purely resistive simulations. We then investigate a consistent feedback model of the turbulence which includes a feedback of the magnetic field on the magnetic diffusivity. Our modeling considers a more consistent approach for mean-field dynamo modeling simulations, as the magnetic quenching of turbulence should be considered for both, a turbulent dynamo and turbulent magnetic diffusivity. We find that, after the dynamo has amplified the magnetic field, the Blandford-Payne mechanism takes place efficiently, leading to slow highly collimated jets. We also find strong periods of unsteady knot ejection and flaring in case of low Coriolis numbers. In particular, flux ropes are built up and advected towards the inner disk thereby cutting off of the inner disk wind, leading to magnetic field reversals, reconnection and the emergence of intermittent flares.

The chapter is structured as follows. In Section 7.1 we describe the dynamo and diffusivity models adopted, focusing on the feedback of the magnetic field on the dynamo and diffusivity tensors. In Section 7.2 we compare the disk and jet properties for different dynamo feedback models and different Coriolis number. Then, in Section 7.3 we investigate our reference simulation with our novel consistent feedback model. Finally, in Section 7.4 we study the influence f the Coriolis number and our consistent feedback model on the launching process.

7.1 The Dynamo and Diffusivity Models

As we have shown in Chapter 6, the non-isotropic disk dynamo model of Ruediger, Elstner, and Stepinski (1995) proved to have some considerable advantages, e.g., the reduced number of parameters required to describe the dynamo tensor and the greater stability (compared to a scalar dynamo model) when the initial magnetic field has a non-zero vertical component. Therefore, in this chapter, we apply the dynamo tensor derived by Ruediger and Kichatinov (1993) and Ruediger, Elstner, and Stepinski (1995) within the thin disk approximation, thus with negligible non-diagonal components (see Equation 3.41). In order to investigate the effect of strong and weak dynamos, we select three values of the Coriolis number. With $\Omega^* = 10$ we investigate the strong dynamo regime, while $\Omega^* = 5$ refers to the moderate dynamo regime, and $\Omega^* = 1$ is the weak dynamo regime. For comparison, all of our simulations are performed in all these three regimes.

As in the previous chapters, the diffusivity model adopted in this chapter is described by Equation (3.45). However, in order to prevent unphysically high values of the diffusivity, we choose to adopt, if not specified otherwise, the standard diffusivity model described by Stepanovs and Fendt (2014) (see Equation 3.48). For the strength and the anisotropy of the diffusivity tensor we follow Kitchatinov, Pipin, and Ruediger (1994), Ruediger, Elstner, and Stepinski (1995), and Rekowski, Rüdiger, and Elstner (2000) (see Equation 6.3). Quite different models for the anisotropic diffusivity have been employed in the last decades (see, e.g., Casse and Ferreira 2000; Ferreira and Casse 2013). In our approach, the strength of anisotropy is not an independent quantity, but depends directly on the Coriolis number.

The dynamo action can be understood as a macroscopic effect of the local magneto-rotational instability, which results in an additional hyperbolic term in the induction equation. As the presence of a strong large-scale magnetic field is able to suppress the MRI, the same will happen to the dynamo process in the accretion disk as soon as the dynamo-amplified magnetic field becomes strong enough. Dynamo action will then be quenched.

7.1.1 Diffusive Dynamo Quenching

The Diffusive Dynamo Quenching (DDQ) has been proposed by Stepanovs and Fendt (2014) in the context of jet launching simulations from resistive accretion disk and by Stepanovs, Fendt, and Sheikhnezami (2014) in order to saturate the dynamo amplification of the magnetic field. With this approach, no direct quenching on the dynamo or the magnetic diffusivity is applied.

Instead, the infinite exponential increase of the magnetic field is prevented by a strong increase in the magnetic diffusivity. In contrast to the "standard" diffusivity models (e.g., Casse and Keppens 2002; Zanni, Ferrari, et al. 2007) applied in non-ideal simulations of jet launching regions, the quantity α_{ss} is defined as follows,

$$\alpha_{ss} = \eta_{0_\phi} \sqrt{\frac{2}{\Gamma}} \left(\frac{\mu_D}{\mu_0} \right)^2. \tag{7.1}$$

The main advantage with this choice of quenching mode is that it avoids the accretion instability (Campbell, 2009), which may suppress the jet launching process and, in addition, is prone to numerical issues. On the other hand, the strong dependence of α_{ss} on the magnetization may lead to un-physically high values of the magnetic diffusivity.

7.1.2 Standard Dynamo Quenching

So far there is no general consensus about how to calculate the critical magnetization value for the quenching. Since the turbulence that is causing the turbulent dynamo effect is supposed to be a consequence of the MRI, the saturation of the dynamo action should most probably depend on the relative magnetic field strength at the disk mid-plane.

Moreover, a quenching based on the disk magnetization (see Vourellis and Fendt 2021) is in agreement with the fact that the MRI is excited by both the poloidal and the toroidal magnetic field[1]. Thus, we start with the most simple approach for an isotropic quenching model (henceforth Standard Dynamo Quenching, SDQ) (Ivanova and Ruzmaikin, 1977; Brandenburg and Subramanian, 2005; Moss, Sokoloff, and Suleimanov, 2016) that is basically depending depending on the disk magnetization,

$$q_\alpha = \frac{1}{1 + \mu_D / \mu_0}. \tag{7.2}$$

We point out that such a global - thus non-local - quenching prescription is not easy to fully parallelize in the code. As investigated by Vourellis and Fendt (2021), a weak parallelization in the $\theta-$direction (i.e., a parallelization with only a few number of cores in the $\theta-$direction) overcomes this problem with only little additional computational costs. For a local quenching (using the local magnetization value on the grid cell, see Stepanovs, Fendt, and Sheikhnezami 2014; Tomei et al. 2020), that is straightforward to parallelize, the main idea of turbulence generation in the disk mid-plane in combination with the generation of a large scale magnetic flux gets somehow lost. Also, the dynamo process itself becomes in-stable when every grid cell applies a different strength of the dynamo - again a conflict with the aim of generating a large-scale magnetic flux.

7.1.3 Non-Isotropic Dynamo Quenching

As for the strength of the mean field dynamo, also the feedback of the magnetic field on the dynamo cannot always be approximated with a single scalar function. Thus, similar to the definition of an an-isotropic dynamo tensor, the quenching of the dynamo effect is also tensorial, thus acting in different strength on the dynamo tensorial components.

Here, we consider a non-isotropic feedback model (henceforth Non-isotropic Dynamo Quenching, NDQ) that follows from an analytical study of turbulence (Ruediger and Kichatinov, 1993), which has elaborated different quenching functions for

---

[1]Note that in case of hemispheric symmetry, the B_ϕ vanishes along the midplane by definition.
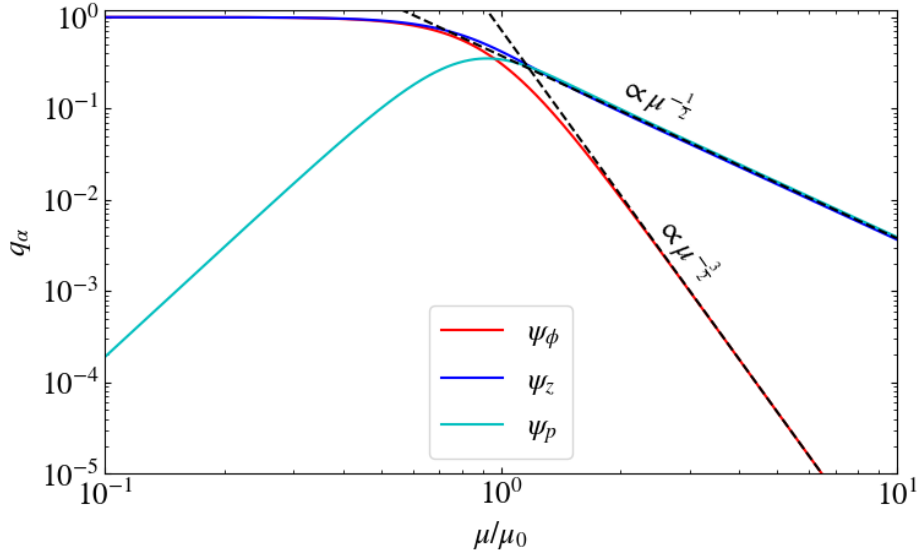
FIGURE 7.1: The quenching model of Ruediger and Kichatinov (1993) for the the different dynamo components as a function of the disk magnetization.

different components of the $\alpha-$tensor. It does not only depend on the strength but also on the orientation of the dynamo-amplified magnetic field.

For our purpose, the suppression of the mean-field dynamo is first computed in cylindrical coordinates (Ruediger and Kichatinov, 1993) and then converted to spherical coordinates,

$$
\begin{aligned}
q_{\alpha_r} &= \psi_\phi + \frac{15}{8}\frac{B_{z,D}^2}{B_D^2}\psi_p, \\
q_{\alpha_z} &= \psi_z - \frac{15}{16}\frac{B_{z,D}^2}{B_D^2}\psi_p, \\
q_{\alpha_\phi} &= \psi_\phi,
\end{aligned}
\tag{7.3}
$$

where we have defined

$$
\begin{aligned}
\psi_p &= \frac{1}{4\beta^4}\left[\beta^2 - 5 + \frac{2\beta^2}{3(1+\beta^2)}\right. \\
&\quad + \left.\frac{4\beta^4(3\beta^2-1)}{3(1+\beta^2)^3} + \frac{5+\beta^4}{\beta}\arctan\beta\right], \\
\psi_z &= \frac{15}{64\beta^4}\left[\beta^2 - 3 + \frac{8\beta^4}{3(1+\beta^2)^2}\right. \\
&\quad + \left.\frac{3+\beta^4}{\beta}\arctan\beta\right], \\
\psi_\phi &= \frac{15}{32\beta^4}\left[1 - \frac{4\beta^2}{3(1+\beta^2)^2} - \frac{1-\beta^2}{\beta}\arctan\beta\right].
\end{aligned}
\tag{7.4}
$$

The quenching parameter β is defined as $\beta = \sqrt{\mu_D/\mu_0}$.
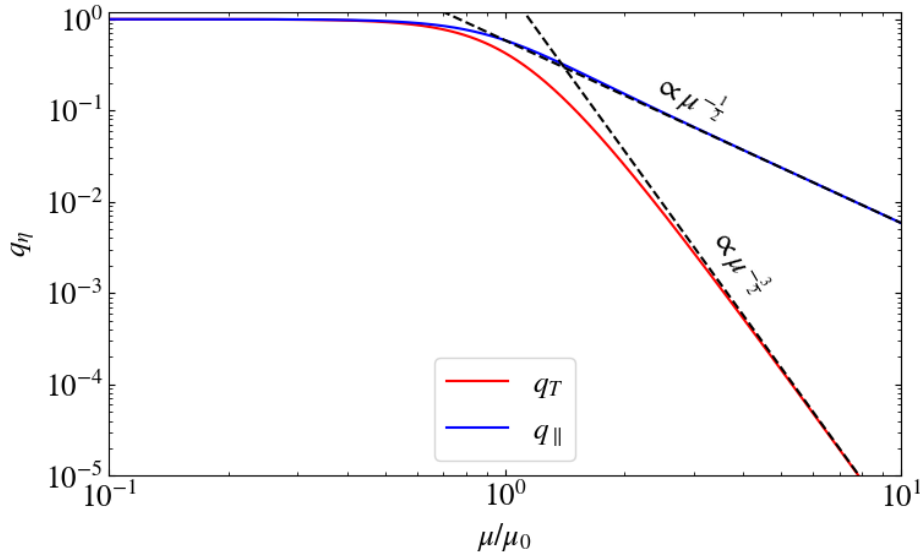
FIGURE 7.2: The quenching model of Kitchatinov, Pipin, and Ruediger (1994) and Rüdiger et al. (1994) the $\eta-$diffusivity as function of the disk magnetization.

Essentially, the quenching depends on the disk magnetization as $\propto \mu^{-3/2}$ for the radial and toroidal component, while follows $\propto \mu^{-1/2}$ for the θ-component (see Figure 7.1). Therefore, we can expect a more sudden and rapid saturation of the magnetic field at even lower magnetization. We point out that $0 \leq q_{\alpha_z} \leq 1$, regardless of the values of μ_D or $B_{z,D}$.

7.1.4 A Consistent Quenching Mode for Diffusivity

So far in this section we have considered different dynamo feedback modes, meaning how to realize the physical effect of quenching the dynamo activity by a strong magnetic field. Here, we want to go one step further towards a self-consistent modeling of mean-field dynamos. That is to consider the back-reaction of the magnetic field on the magnetic diffusivity. Because of their common origin - the turbulence of the disk material - both the quenching of the mean-field dynamo and the magnetic diffusivity should be treated in the same way. A strong global magnetic field suppresses the turbulence and, thus, both the turbulent dynamo effect and and the turbulent magnetic diffusivity.

Here we put this on more physical grounds, considering a quenching model that follows from analytical mean-field theory and that incorporates effects on both the mean-field dynamo and the magnetic diffusivity, following the prescriptions of Kitchatinov, Pipin, and Ruediger (1994) and Rüdiger et al. (1994) (henceforth Consistent Turbulence Quenching, CTQ).

For the feedback of the magnetic field on the dynamo - the dynamo quenching - we follow Ruediger and Kichatinov (1993), as described in Section 7.1.3. As in Section 3.4.5 the an-isotropic components of the magnetic diffusivity can be computed directly in spherical coordinates.

Here we apply the quenching model following Kitchatinov, Pipin, and Ruediger (1994) and Rüdiger et al. (1994),

$$\eta = (\eta_R q_{\eta_R}, \eta_\theta q_{\eta_\theta}, \eta_\phi q_{\eta_\phi}), \tag{7.5}$$

with

$$
\begin{aligned}
q_{\eta_R} &= \frac{3}{2\beta^2}\left[-\frac{1}{1+\beta^2} + \frac{1}{\beta}\arctan\beta\right], \\
q_{\eta_\theta} &= q_{\eta_R}, \\
q_{\eta_\phi} &= \frac{3}{8\beta^2}\left[\frac{\beta^2-1}{\beta^2+1} + \frac{\beta^2+1}{\beta}\arctan\beta\right].
\end{aligned}
\tag{7.6}
$$

We point out that the dependence of magnetic diffusivity on the disk magnetization is also determined by the disk turbulence parameter α_{ss}. Here, we model this applying $\alpha_{ss} \propto \sqrt{\mu_D}$ (as in Equation 3.48).

Mean-field dynamo models applying a diffusivity quenching (as in Rüdiger et al. 1994) have been applied in the context of galactic dynamos (Schultz, Elstner, and Ruediger, 1994; Elstner, Ruediger, and Schultz, 1996), although the quenching model was never coupled with a non-isotropic diffusivity. Here, because of the rapid disk rotation and the strong magnetization needed for jet launching, we have included both an-isotropic effects. In the limits of slow rotation and weak magnetization, the diffusivity tensor becomes isotropic. When either a rapid disk rotation or a strong magnetization becomes relevant, the isotropy of the diffusivity tensor is broken (see Figure 7.2). This is the first time, that such modeling with a higher degree of more self-consistency, has been applied in the context of jet launching simulations from accretion disks.

7.2 Dynamo Feedback Models

Quenching the dynamo tensor prevents an infinite field amplification. Different quenching methods lead to a different saturation of the magnetic field. As mentioned above, quenching of the turbulent dynamo is a physical consequence of the process that produces turbulence. Ideally, quenching models are derived from first principles of turbulent plasmas.

Very general correlations have been found between the accretion disk magnetization and the jet speed or the jet collimation (Fendt, 2006; Pudritz, Rogers, and Ouyed, 2006; Stepanovs and Fendt, 2016), demonstrating that a high disk magnetization is tightly correlated with a high jet velocity.

These correlations can be extended, then linking the strength of the dynamo with the jet speed, as a stronger dynamo implies a stronger field amplification (as shown in Fendt and Gaßmann 2018 and in Chapters 5 and 6). For this reason, we do investigate the interplay between the amplified magnetic field and the dynamo, and how it affects the jet launching process.

In Figure 7.3 we show the density distribution of the disk-jet structure, together with the magnetic field geometry, for different feedback models (from top to bottom, respectively, the diffusive quenching, the standard quenching and the non-isotropic quenching) and different Coriolis numbers (from left to right, respectively, $\Omega^* =$
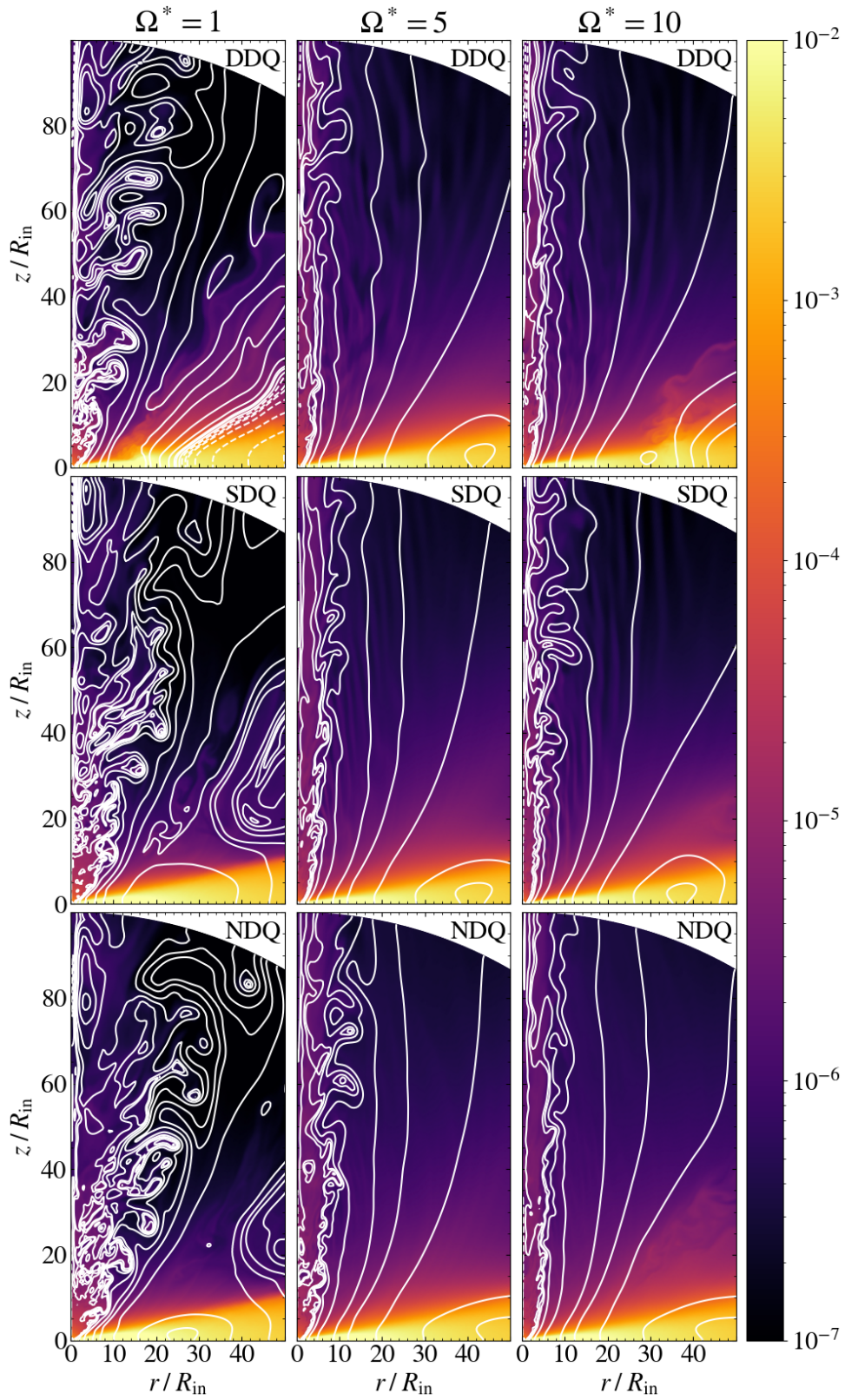
FIGURE 7.3: Density and magnetic field lines at $t = 10000$ for different dynamo feedback models and Coriolis numbers.

1, 5, 10). Overall, we see that the magnetic field, near the rotation axis, the magnetic field amplified by the dynamo, has evolved into a large-scale open geometry. The magnetic field structure, together with its amplification, leads to a highly collimated outflow.

However, for lower Coriolis numbers we notice a more turbulent outflow from the inner disk region. Such a magnetic field distribution suggests that the outflow is driven by the toroidal magnetic pressure gradient rather than by magneto-centrifugal forces. These simulations show a major magnetic loop, whose distance from the inner disk depends on the Coriolis number and on the feedback model. In addition, another loop may emerge, then indicating the presence of a dynamo inefficient zone.

7.2.1   Magnetic Field Amplification

The primary effect of the dynamo tensor is the amplification of the magnetic field. However, below a critical value of the Coriolis number, even in presence of a dynamo effect, the magnetic field is not amplified or is only weakly amplified. As a direct consequence, for example a fast and collimated outflow cannot be launched.

We identify a critical value for the Coriolis number as the one where the dynamo timescale is longer than diffusion timescale (Dyda et al., 2018; Fendt and Gaßmann, 2018),

$$\tau_\alpha = \frac{H}{\alpha_\phi} > \frac{H^2}{\eta_\phi} = \tau_\eta. \tag{7.7}$$

Note that quenching methods may act in quite a different way, as the initial strength of diffusivity for the diffusive quenching is $\sim 2 - 3$ orders of magnitudes weaker than the one from the standard quenching. This difference strongly reflects on the existence of a critical Coriolis number.

When applying the diffusive quenching method in Chapter 6, we have recovered a critical value of the Coriolis number $\Omega_C^* \simeq 0.15$. On the other hand, when applying the standard quenching method, or the non-isotropic quenching methods we have developed, a critical value of the Coriolis number (in order to determine whether the initial dynamo can amplify the magnetic field) $\Omega_C^* \simeq 2$ is found.

This difference can be seen in Figure 7.4, where we show the time evolution of the poloidal magnetic energy from radius $R = 10$ to the end of the domain ($R_{\text{out}} = 100$), while applying a Coriolis number of $\Omega^* = 1$ (dotted lines). As expected, the poloidal magnetic energy of the diffusive quenching method, which is shown in Figure 7.4, is amplified stronger and more rapidly than for the cases of the other quenching models.

Moreover, the field amplification is preceded by a short decrease. The reason behind this is that, at $t = 0$, the diffusive timescale is shorter than the dynamo timescale. Thus, the magnetic field is diffused away, leading to a decrease in the magnetization and, therefore, of the magnetic diffusivity. Once the magnetic diffusivity has decreased, the dynamo timescale becomes again shorter than the diffusive time scale.

When the Coriolis number is higher than its critical value, the amplification of the magnetic field occurs instantly. Thus, when the magnetic field increases, also the
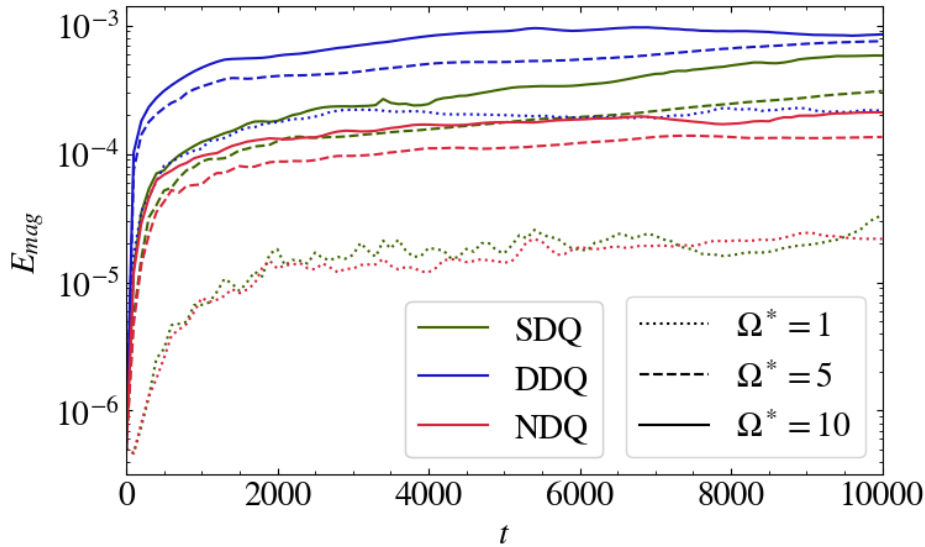
FIGURE 7.4: Evolution of the poloidal magnetic field disk energy from $R = 10$ to $R = 100$ for different feedback models and Coriolis numbers.

dynamo quenching increases, suppressing the dynamo action and lowering the amplification of the magnetic field. In order to disentangle the impact of the quenching methods we applied Coriolis numbers of $\Omega^* = 5$ and $\Omega^* = 10$. We find that the field amplification is faster and also stronger when the diffusive quenching model is applied (see Figure 7.4).

We notice that the magnetic energy that originates from dynamo action by employing the diffusive quenching method and a Coriolis number $\Omega^* = 1$ is approximately the same of the one obtained by the standard quenching method and $\Omega^* = 10$ until $t = 3000$. Since the diffusive dynamo quenching model does not involve a suppression of the dynamo tensor, the magnetic field saturates as soon as the diffusivity is strong enough to counterbalance the dynamo effect. On the other hand, the standard quenching method features both an increase of the magnetic diffusivity and a decrease of the dynamo. Thus, the same Coriolis number will lead to a different strength of the disk poloidal field depending on the feedback model.

However, as shown in Figure 7.5, the presence or the absence of the dynamo inefficient zones from the early stages (as shown in Chapter 5) plays a key role in the jet structure and evolution. We find that a low Coriolis number leads to the formation of dynamo inefficient zones regardless of the quenching model, in agreement with Chapter 6. On the other hand, we also find that dynamo inefficient zones are present for large Ω^*, which we did not find in our previous works. The formation of these zones may be connected with the increase of refinement that is coupled with the HLLC Riemann solver we now apply, which together provides a better resolution of the disk substructures (probably smeared out by the more diffusive HLL solver).

Finally, the results obtained by applying the non-isotropic dynamo quenching model show no difference from the stand dynamo quenching model for low Coriolis number. However, for higher Coriolis numbers, the different suppression of the dynamo in the non-isotropic dynamo quenching model ($\alpha_\phi \propto \mu_D^{-3/2}$, while $\alpha_\phi \propto \mu_D^{-1}$ in
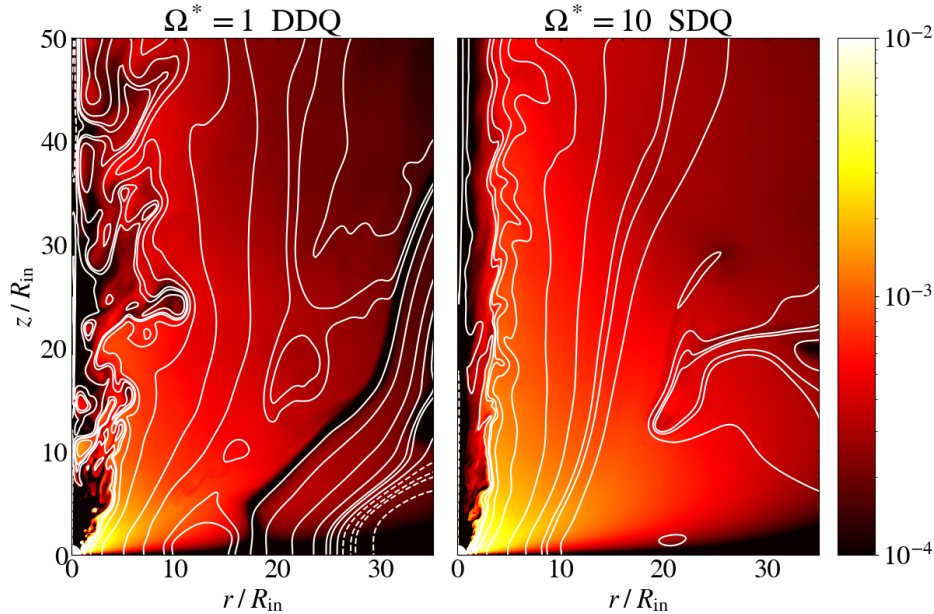
FIGURE 7.5: Snapshot of the toroidal magnetic field at $t = 3000$ for the diffusive dynamo quenching case and $\Omega^* = 1$ (left panel) and for the standard dynamo quenching case and $\Omega^* = 10$ (right panel).

the standard dynamo quenching model) leads to a different saturation of the magnetic field. More specifically, we find that the magnetic field, in the non-isotropic dynamo quenching model, is saturated towards a lower disk magnetization than the one obtained by the standard dynamo quenching model.

7.2.2 Dynamo Number and Turbulence Parameter

The dynamo number is traditionally used to indicate the strength and efficiency of dynamo activity. A high dynamo number indicates an efficient dynamo, thus leading to strong field amplification. Vice versa, a low dynamo number indicates that that dynamo cannot act efficiently anymore, and the magnetic field generated has reached its saturation value - either established by a strong magnetic diffusivity, thus by diffusive quenching (diffusive dynamo quenching), or by suppressing the dynamo activity itself, thus by direct quenching of the dynamo-alpha (standard dynamo quenching, non-isotropic dynamo quenching). The critical dynamo number (see Section 3.4.7) differentiates the two regimes.

Our simulations, as shown in Figure 7.6, confirm earlier predictions of Brandenburg and Subramanian (2005) and Boneva et al. (2021), that is that (i) field amplification does not occur for $\mathcal{D} \lesssim 10$, while (ii) amplification occurs when the dynamo number supersedes its critical value since the magnetic diffusivity decreases.

Moreover, we find that the critical value of the dynamo number does not depend on the feedback model applied or the Coriolis number that is given. This suggests, essentially, that the amplification and the saturation of the magnetic field is a very general property of the mean-field dynamo approach, and does not depend on certain modeling details. Note, that the exact value of the critical dynamo number can be influenced by the numerical resolution applied and the numerical algorithms
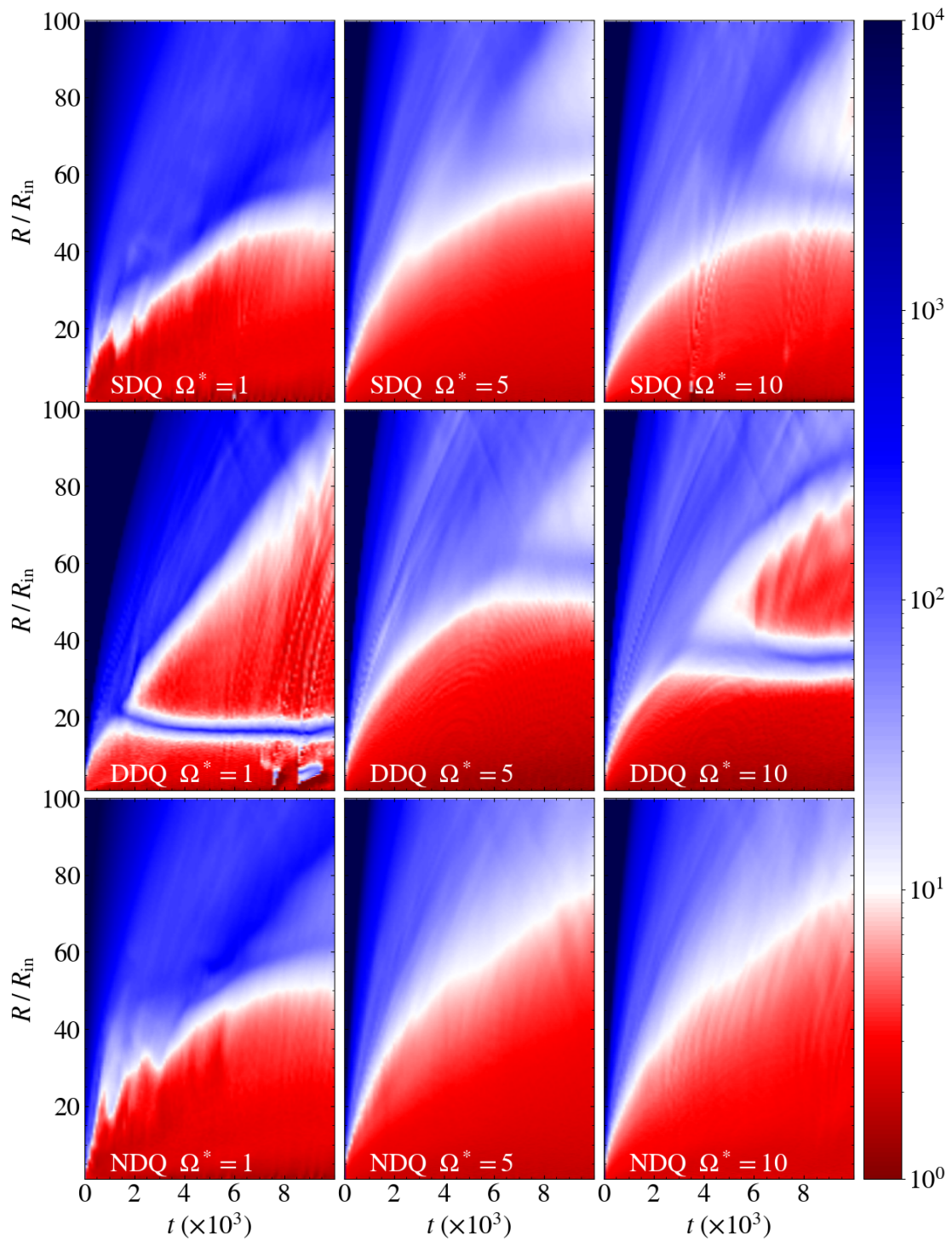
FIGURE 7.6: Dynamo number as functions of time and radius for different Coriolis numbers and feedback models.
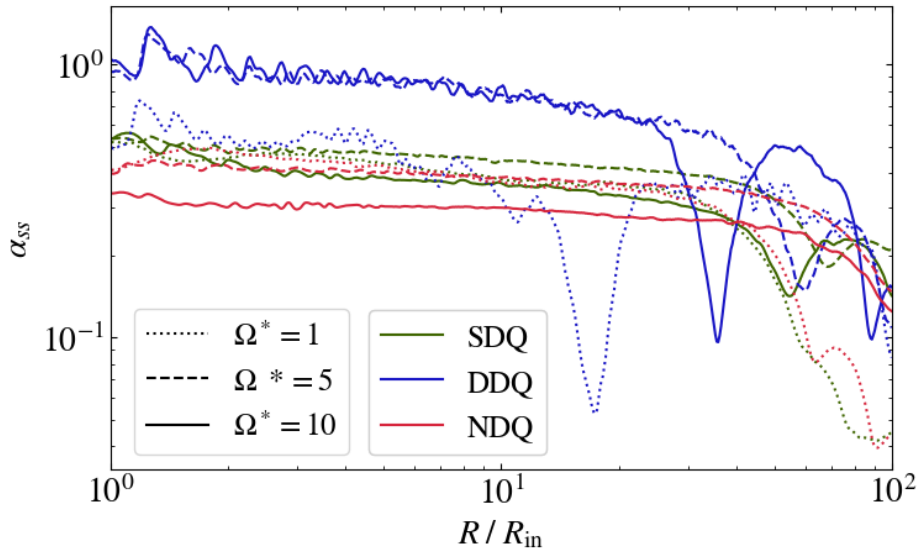
FIGURE 7.7: Turbulence parameter α_{ss} for different values of the Coriolis number and different feedback models at time $t = 10000$ as function of radius.

adopted (see, e.g., Stepinski and Levy 1988; Stepinski and Levy 1990; Torkelsson and Brandenburg 1994).

The main difference between the quenching models we apply, is the absence of dynamo inefficient zones for low values of the Coriolis number and the feedback models which imply a suppression of the dynamo. A possible explanation is that a magnetic field reversal can be maintained only if the dynamo does not vanish. If the magnetic field is not constantly amplified by the mean-field dynamo (because of the quenching), the field reversal zones are able to reconnect and be diffused away. This is not possible if the dynamo is not suppressed. However, since the standard dynamo quenching model and the non-isotropic dynamo quenching model lead to a suppression of the dynamo (and not in the diffusivity), the dynamo inefficient zones are more likely to be suppressed. We also point out that the presence of dynamo-inefficient zones, which are not strictly related to the component α_ϕ, is still possible. In this regard, the dynamo number may require a different definition considering all the tensorial components of the dynamo.

On the other hand, the turbulence parameter α_{ss} (Shakura and Sunyaev, 1973) does not depend on the dynamo tensor, but only on the magnetic diffusivity. Therefore it can be applied as a useful tool in order to understand the evolution of the magnetic diffusivity once the magnetic field amplification took place. As we can see from Figure 7.7, the standard dynamo quenching (and also the non-isotropic dynamo quenching) model and the diffusive dynamo quenching model show several differences with regard of how the turbulence parameter depends on the Coriolis number once the magnetic field is saturated. In particular, we find that the results applying the diffusive dynamo quenching model show a unique dependence on the Coriolis number.

As pointed out in the previous section, for the diffusive dynamo quenching
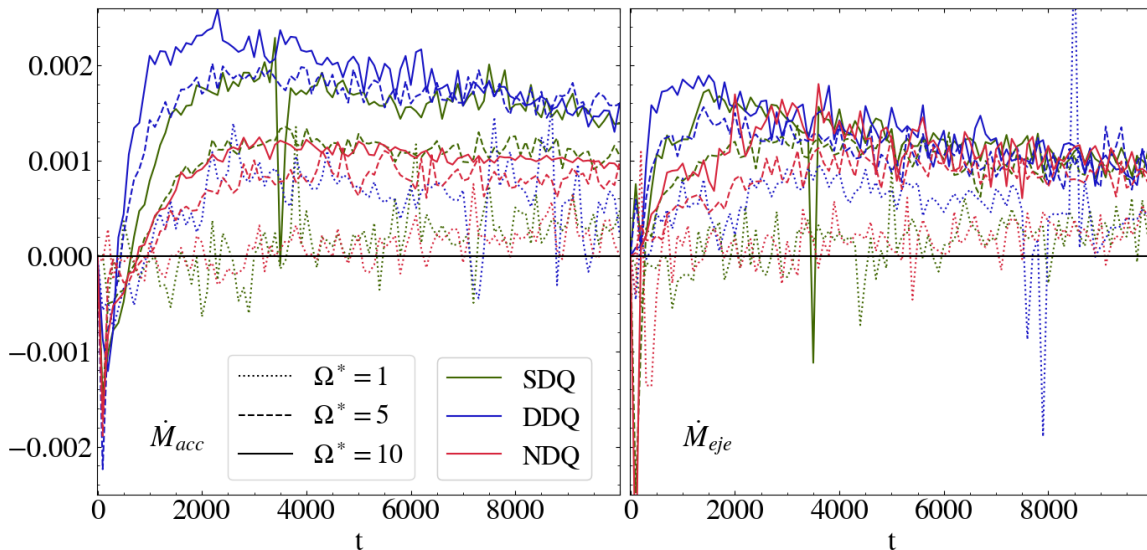
FIGURE 7.8: Accretion (left panel) and ejection (right panel) rates at
$R = 7$ for different COriolis numbers and feedback models.

model, the magnetic diffusion is the only process that is able to saturate the mean-field dynamo. Because of the different amplification of the magnetic field for different Coriolis numbers, different in both the strength of the magnetic field and the timescale of amplification, the disk magnetization saturates to different levels (see Figure 7.4). Because of the strong, i.e., quadratic, dependence of the diffusivity η on the disk magnetization μ, in the diffusive dynamo quenching model this dependence is reflected in the fact that also the α_{ss} is found to depend on μ.

7.2.3 Accretion and Ejection

The different saturation levels for the magnetic field strength play a key role in the hydrodynamical evolution of the accretion disk and the subsequent jet launching process. This is demonstrated in Figure 7.8 showing the accretion and the ejection rate of the launching area. The accretion rate is computed by integrating the net radial mass flux through the disk at $R = 7$ (as in Equation 3.51). Similarly, the ejection rate is computed by integrating between R_{in} and $R = 7$ along the disk surface, as in Equation 3.52. The interrelation between the accretion rate and the Coriolis number confirms, regardless of the feedback mode, previous results obtained by Fendt and Gaßmann (2018). In particular, we find that a stronger dynamo leads to a stronger accretion rate. We investigated the impact of the magnetic field topology on the accretion process (i.e., the presence or absence of dynamo inefficient zones) in detail previously.

This influence is also confirmed by comparing the standard dynamo quenching model for $\Omega^* = 10$ with the diffusive dynamo quenching model for $\Omega^* = 1$. Here, despite a similar amplification of the poloidal magnetic field (see Figure 7.4), the presence, respectively the absence of dynamo inefficient zones, plays a key role in the accretion of material.

On the other hand, the mass ejection, acting on much shorter timescales, shows less pronounced differences for the variety of quenching methods or the different
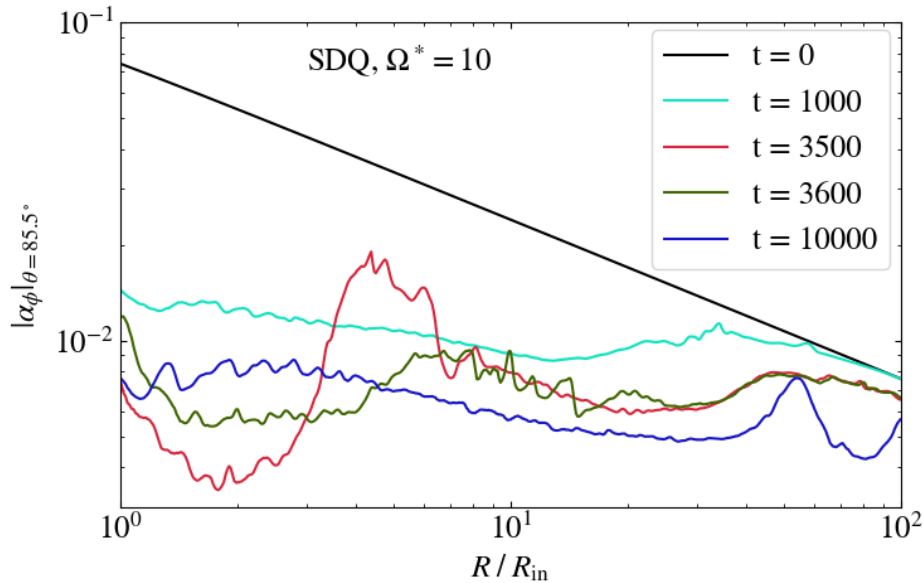
FIGURE 7.9: Temporal evolution of the dynamo at each radius for the $\Omega^* = 10$ and standard dynamo quenching model simulation.

values of the Coriolis number. However, we observe that lower Ω^* generally lead to a higher ejection-to-accretion ratio, which is in good agreement with the findings of Chapter 6. In case of a strong dynamo, all quenching models show that $< 50\%$ of the accreted material is ejected. This is in good agreement with previous resistive jet launching simulations that do not consider dynamo action, but start from a prescribed large-scale magnetic field (see, e.g., Zanni, Ferrari, et al. 2007; Sheikhnezami et al. 2012). For lower Coriolis numbers, accretion requires more time to be established because of the slower amplification of the magnetic field. For this reason, during certain periods of time, the ejection-accretion rate (defined as $\dot{M}_{eje}/\dot{M}_{acc}$) may actually exceed unity. This may imply that disk areas of very low mass or density may be present for some time until these areas are replenished from the mass reservoir at larger disk radii.

We observe a particularly interesting period at time ≈ 3500 for the standard quenching model (STQ) with high Coriolis number $\Omega^* = 10$. A sudden drop in the accretion and, consequently, in the ejection rate appears. When looking at the strength of the mean-field dynamo $\phi-$component as a function of radius, we notice that at $t = 3500$ it becomes significantly stronger than immediately before or after. We find that the reason behind this sudden change is a small decrease in the toroidal magnetic field strength, which seems amplifies the dynamo (see Figure 7.9). This is due to the quenching prescription: A low magnetic field strength triggers a lower magnetic diffusivity, which, in turn, curbs the accretion process, because it implies a lower diffusivity. Once the magnetic field is amplified again by the dynamo, the system goes back to a more stable configuration.

7.2.4 Jet Properties

All our models considering feedback by quenching lead to a quasi-steady, saturated state. Therefore, the essential jet properties found by simulations that do not invoke

a dynamo process (see, e.g., Tzeferacos, Ferrari, et al. 2009; Murphy, Ferreira, and Zanni 2010; Stepanovs and Fendt 2016), should, qualitatively, not depend by the method for the dynamo feedback.

In Chapter 6 we discovered a unique numerical correlation between the Coriolis number Ω^* (and therefore the dynamo strength) and the asymptotic jet speed. In this chapter, we now make a further step in this regard and investigate this interrelation for different feedback models. For this purpose, we select certain magnetic flux surfaces (thus contours of the vector potential, respectively poloidal magnetic field lines), and compute the disk magnetization and the poloidal velocity of the corresponding outflow along that surface. We do this for a series of evolutionary steps, starting from $t = 700$, i.e., the time when a jetted outflow is already formed and has reached the outer boundary, until the final time step of each simulation. The results are shown in Figure 7.10, where the two panels present, respectively, the values obtained for radii $1.5 < R < 5$ and $5 < R < 10$.

As we can see, the radial distance makes a difference concerning the smoothness of the interrelation. For radii $5 < R < 10$ the interrelation looks very well defined , while for smaller radii this correlation is partially broken. At small radii we notice the presence of vertical 'columns', i.e., zones with similar magnetization that exhibit a variety in jet speed. This is mainly due to the time evolution of these parameters: both the disk magnetization as well as the jet speed may vary in time for the same radial distance, during the same simulation.

More physically, the reason behind such variations in jet speed lies in the fact that, especially in the inner disk regions, the magnetic field is strongly coupled with the matter. As a result, internal shocks and magnetic field reconnection may affect the outflow significantly. Moreover, the opening angle of the magnetic field (which are quite variable in the inner region) leads to substantial changes in the jet dynamics even considering the same disk magnetization. This is a result of the magneto-centrifugal acceleration involved.

On the other hand, at larger radii the system has reached saturation towards a steady state, leading to a more narrow interrelation. At even larger radii, $R > 10$, the low magnetization and the slow rotation lead to a weak disk magnetization and, therefore, to a slower outflow speed. We point out that at these large radii, the disk has accomplished only few revolutions, and the whole inflow-outflow structure has not yet settled into a quasi-steady state.

However, as a key result, despite showing differences in both the disk magnetization and the jet speed, the different feedback models we have examined show in general a unique trend. They all follow a very similar relation between the two quantities, suggesting that this relation jet speed versus disk magnetization does not depend on the dynamo process, the diffusivity model, or the quenching method. It simply confirms the general relation between these leading inflow-outflow parameters that have been discovered previously (Stepanovs and Fendt, 2016) and recovered in Chapter 6.

Still, the feedback of the magnetic field on the dynamo action plays a key role for the saturated disk magnetization. This holds in particular, because of the more efficient suppression of the dynamo, the non-isotropic dynamo quenching model reaches the saturation of the magnetic field already at a lower magnetization levels, about one order of magnitude below.
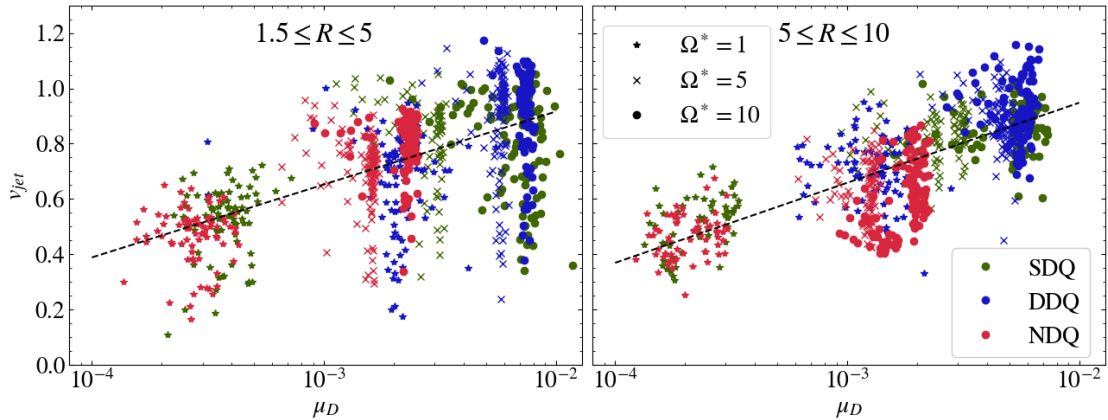
FIGURE 7.10: Relation between disk magnetization and jet speed for different feedback models and different values of the Coriolis number. The dashed line represent the extrapolated relation for the three feedback models.
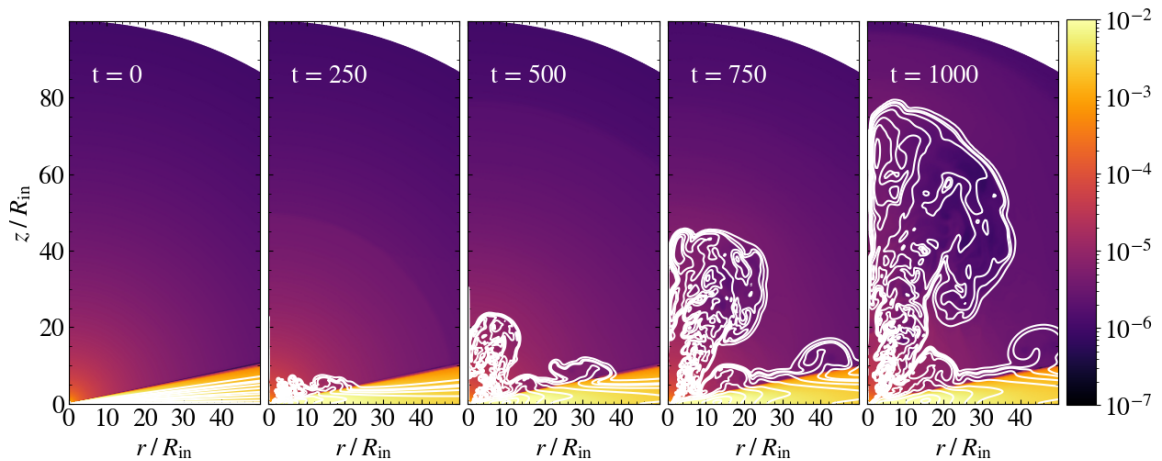
FIGURE 7.11: Mass density (colors) and magnetic field lines of the reference simulation ($\Omega^* = 1$, CTQ feedback mode) at times $t = 0, 250, 500, 750, 1000$.

7.3 Consistent Turbulence Quenching: Reference Simulation

In order to investigate the effects of the feedback of the magnetic field on the diffusivity, we have chosen to focus on the case $\Omega^* = 1$ as a reference simulation.

In Figure 7.11, we show the time evolution of the density and poloidal magnetic field of this simulation. We see that the saturation of the magnetic field occurs on a short timescale, i.e., already until $t = 1000$, corresponding to $\simeq 50$ revolutions of the inner disk. At this point in time, the magnetic energy is amplified by an order of magnitude, while the magnetic field lines are already opened up to a radius $R = 70$ in the outflow region.

Because of the combination of the α and the Ω effect – mean-field dynamo and the differential rotation – the toroidal magnetic field is amplified faster than the
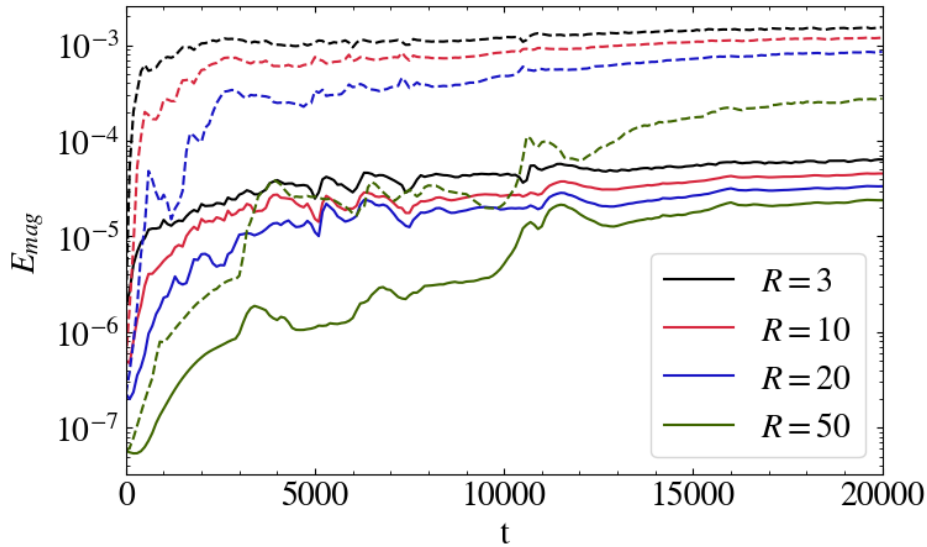
FIGURE 7.12: Evolution of the poloidal magnetic field disk energy for different disk portions. Solid lines show the poloidal magnetic energy, while dashed lines show the total magnetic energy (poloidal + toroidal). The radii that are labeled denote the lower integration boundary, while the upper integration boundary is at the end of the domain, $R = 100$.

poloidal field. Note that our initial condition is that of a purely radial field. However, as in Fendt and Gaßmann (2018), we point out that the dynamo-amplified magnetic field should not depend on the initial conditions.

The formation of a magnetic loops (rooted at foot points of different radius in the accretion disk) strongly indicates, that, at least in the early evolutionary stages, the launching mechanism for this initial outflow is that of a tower-jet, thus a magnetic pressure driven-outflow (Lynden-Bell and Boily 1994; Lynden-Bell 1996). This is further supported by the inclination of the magnetic field towards the disk surface, as being not favorable for a magneto-centrifugal driving of the outflow. As the system evolves, the magnetic loops diffuse outwards, more and more poloidal field lines break up and the magnetic field geometry reaches the inclination required for a Blandford-Payne-like outflow. The system evolves further until a quasi-steady state is reached. At this point, the system consists of a highly magnetized accretion disk and a super-Alfvénic disk wind, which evolves into a high-speed outflow. The Alfvén surface is located at ≈ 5 thermal disk scale heights above the disk surface.

7.3.1 Amplification of the Magnetic Field

The amplification of the poloidal magnetic energy within the accretion disk is shown in Figure 7.12. The amplification of the magnetic field is stronger in the innermost accretion disk regions, because of the combined effect of the ω and the $\alpha-$effects, in agreement with Fendt and Gaßmann (2018)

The poloidal magnetic energy is amplified by about 2 orders of magnitude and occurs, mostly, within $t = 3000$. By comparing the red line of Figure 7.12 with the dotted green line of Figure 7.4, we notice that the feedback on the diffusivity has a
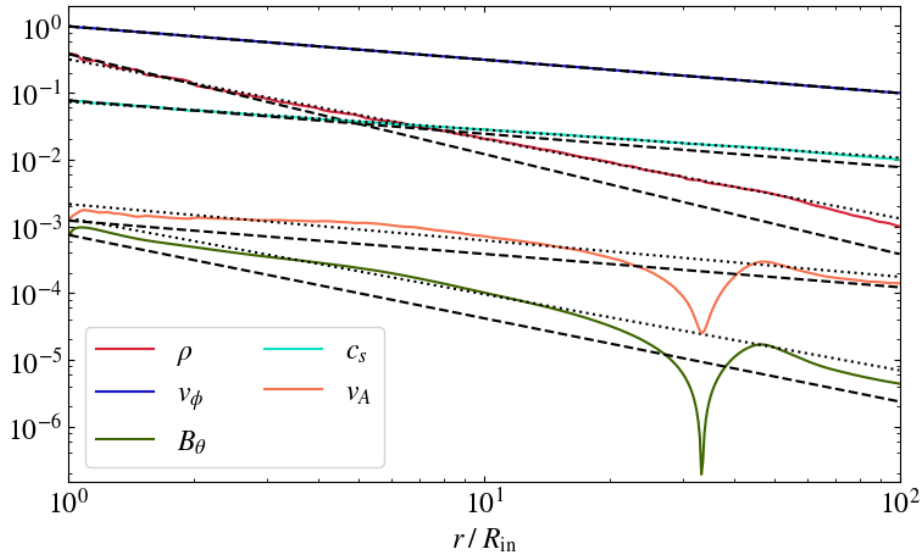
FIGURE 7.13: Mid-plane quantities at $t = 50000$ for the reference simu-
lation. The solid lines represent the radial dependence of some selected
MHD quantities at the disk mid-plane, while the dotted and dashed
lines represent, respectively, their corresponding power-law approxi-
mation and their solution assuming self-similarity. On the y-axis are
the corresponding variables, normalized in code units.

very minor impact on the disk poloidal magnetic field until $t \sim 4000$. However, the
oscillations in the magnetic energy at $t \sim 5000$, $t \sim 6000$, $t \sim 8000$ and $t \sim 12000$ are
a consequence of this novel diffusivity feedback model (see Section 7.3.3).

We observe a different evolution compared to our previous models without feed-
back on diffusivity. The magnetic energy does not undergo any intermittent de-
crease before the magnetic field reaches a quasi-steady state. We think that this
difference can be explained by a combination of effects that rely on the chosen feed-
back model. At first, the quenching of the dynamo leads to a lower disk magnetic
diffusivity, just because of the lower magnetization level at which the magnetic field
saturates. Then, because of the lower magnetic diffusivity, the disk mass loss is less
compared to a diffusive quenching model (where the dynamo tensor is not explicit
suppressed), therefore the sound speed (which affects both dynamo and the diffu-
sivity) shows no decrease. Moreover, the magnetic diffusivity is suppressed to an
even lower level, just because of the feedback model (quenching of turbulent mag-
netic diffusivity).

At $t \simeq 20000$ the magnetic field has saturated out to a radius $R \lesssim 50$. The field
still continues to be amplified in the outer disk region, as this part of the disk has
performed so far only few rotations and is not yet in dynamic equilibrium. Also,
since the $\alpha-$effect is less efficient here, it takes more time to saturate the dynamo.
Nevertheless, the evolution of the outer disk can weakly affect the disk evolution,
most likely by triggering episodic ejections (see Section 7.3.3).

7.3.2 Disk Structure

Because of the magnetic field amplification and the evolution the magnetic field structure due to dynamo activity, also the disk structure evolves through time. This is partly due to the change of forces acting on the disk material, but also due to the change of angular momentum balance and the subsequent re-distribution of disk material.

At time $t = 50000$ the magnetic field has saturated in most parts of the disk (of the size we investigate). We may therefore investigate the disk structure structure by looking at the profiles of its mid-plane quantities. In Figure 7.13 we display the radial profile of some leading MHD quantities measured at the disk midplane and compare them with an idealized radial self-similar solution of the steady-state MHD equations. We also compare with the power law approximation for each quantity.

We see that the disk kinematics remains unaffected by the dynamo action as the disk rotation remains Keplerian, i.e., $\beta_{v_\phi} = -1/2$. The density profile power-law index changes, however, from $\beta_\rho = -3/2$ to $\beta_\rho = -5/4$, as the mass is mostly accreted from the inner disk, and the whole disk looses only very little mass.

We find that both the sound speed and the Alfvén speed show very small deviations from the self-similar solution. The power-law indexes obtained are, respectively, $\beta_{c_s} \approx -4/9$ and $\beta_{v_A} \approx -5/9$. The radial dependence of the magnetization that is obviously strongly affected by dynamo action, can be recovered by computing the ratio of the Alfvén speed vs sound speed, which corresponds to computing the difference in the respective power-law indexes,

$$\beta_\mu = \beta_{v_A} - \beta_{c_S} = -\frac{1}{9}. \tag{7.8}$$

We find a very good agreement with the results obtained by Stepanovs and Fendt (2014) and Stepanovs, Fendt, and Sheikhnezami (2014), suggesting that the properties of the saturated state do not depend (or depend only weakly) on the quenching model for dynamo action and diffusivity.

7.3.3 Intermittent Ejection

As pointed before 7.3.2, also the system that undergoes consistent feedback concerning the dynamo action and magnetic diffusivity evolves to a quasi-steady state. However, we discover an interesting, intermittent feature. Between $t = 4000$ and $t = 12000$ the magnetic energy features substantial oscillations, especially in the inner disk region (see Figure 7.12). We now want investigate the origin of such processes and the consequences on the disk and jet structures. When the quenching models of Sections 7.1.1-7.1.3 are adopted, the feedback applies only to the mean-field dynamo, finally leading to a saturation of the magnetic field. Note, however, that even if the dynamo is quenched, for a low diffusivity it can lead to a re-amplification of the magnetic field. This is what is happening if the diffusivity follows a consistent quenching model.
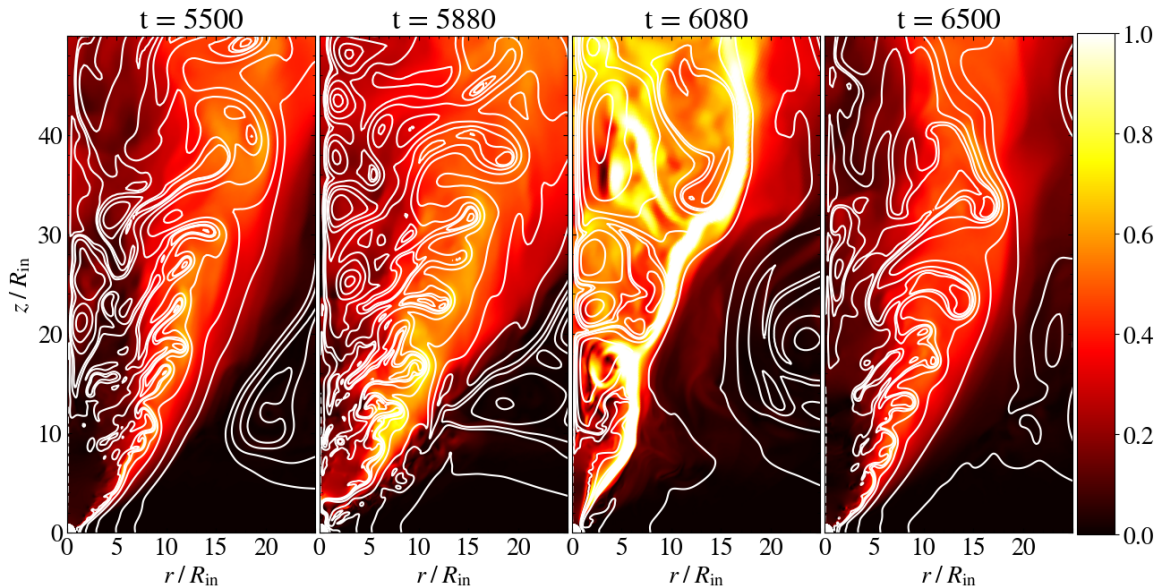
FIGURE 7.14: Time evolution of the intermittent ejection for the reference simulation ($\Omega^* = 1$, CTQ feedback model). From left to right, snapshot of the poloidal velocity (colors), superimposed with magnetic field lines, are shown at times $t = 5500, 5880, 6080, 6500$.

We point out that the amplification process of the magnetic field depends not only on the strength of the dynamo and the diffusivity tensors, but also on the radial and angular dependence of the tensor components. This is an essential property of the non-linear quenching models. The dependence of the magnetic field amplification on the radial and angular profiles for dynamo and diffusivity holds, in particular, when the magnetic field shows a reversal within the accretion disk. Under such circumstances, the magnetic diffusivity is sufficiently high in order to trigger reconnection processes, but, on the other hand, not strong enough to saturate the magnetic field amplification. As a result, flux ropes and current sheets are more prone to be formed in the accretion disk, before they are lifted above the disk surface, similar to what have been described in Yuan et al. (2009).

These flux ropes are able to reconnect above the disk surface in the disk corona, since the given magnetic diffusivity profile. Note that also the polarity of the toroidal field is opposite to the one of the launching region of the accretion disk. As a consequence, these flux ropes, after undergoing magnetic reconnection, are advected towards the accreting object and are able to disrupt the jet launching.

These features are highly interesting and may have essential relevance for jet launching conditions, such that this intermittent behavior may be related to the generation of jet knots. The understanding of the physical processes behind the flaring activity not straightforward as they result from the local resistive MHD evolution.

Our understanding is as follows. The magnetic field geometry emerging from the dynamo activity and the subsequent opening of flux loops leads to field reversals. While the field structure in these areas are prone to reconnection, the low field strength over there also implies a lack of magnetic pressure support. Further, since the reconnection area is not rooted in the disk via the magnetic field (no lever arm), it is only slowly rotating. In combination - lack of pressure support and centrifugal

forces - gravity wins and leads to a collapse of this area towards the central object, thereby cutting off the inner disk wind.

Lateron, because of the opposite polarity, the magnetic field in the inner disk decreases, leading to a restoration of the dynamo. Then the magnetic field is re-amplified, leading to a strong ejection and acceleration of the disk matter. As the field is amplified, the quenching on the mean-field dynamo saturates the magnetic field, which goes back to both strength and topology that it had before this episodic fast ejection.

The time period between to consecutive flares increases after each flare, since the reconnection process occurs further and further from the launching region. (the first flare appears at $t = 5000$, the second at $t = 6000$, the third at $t = 7500$ and the last at $t = 10000$). We expect less reconnecting plasma and thus less variability in the jet once the disk has reached a saturated state.

7.4 A Parameter Study

In order to investigate the similarities and the differences between the consistent turbulence quenching and the dynamo quenching methods, we have performed simulation runs applying different Coriolis numbers Ω^*.

The results are shown in Figure 7.15. In the left panel we see the time evolution of the poloidal disk magnetic energy, that is essentially the dynamo-generated field amplification by the α-effect. We notice that for a higher Coriolis number, the differences between the non-isotropic dynamo quenching model and the consistent turbulence quenching model are only little. This finding is interesting as it may sound counter-intuitive - wouldn't one expect that a stronger magnetization is leading to a stronger quenching on the magnetic diffusivity, and therefore to more differences with the model without the consistent quenching?

However, note that a stronger dynamo implies also a stronger feedback on the dynamo (as shown in Section 7.1). Because of the feedback (quenching) on the diffusivity, in combination the $\alpha-$ and the $\Omega-$effect lead to a stronger amplification of the toroidal magnetic field[2]. Since the dominating launching mechanism at the early evolutionary stages of jet launching is the toroidal pressure-dominated launching (tower jet), the quenching on the dynamo *and* the diffusivity is mainly triggered by the *toroidal* field.

As a result, the quenching of the diffusivity plays a minor role in the amplification and saturation of the poloidal field. Therefore, despite the quenching of magnetic diffusivity, which would be thought to lead to a higher dynamo number, we find that these numbers are almost identical as shown in Figure 7.15 (right panel) for the case $\Omega^* = 10$ at $t = 10000$. This is consistent with the usual understanding that the dynamo number is a useful tool in order to characterize the onset of field amplification for a dynamo (in the disk).

On the other hand, although working in the accretion disk, the quenching on the diffusivity plays a key role also for the jet dynamics. The interrelation between the disk magnetization and the jet speed for the new quenching setup shows substantial differences from those by applying only a quenching on the dynamo (see Figure

---

[2]which occurs on a timescale shorter than the amplification of the poloidal field
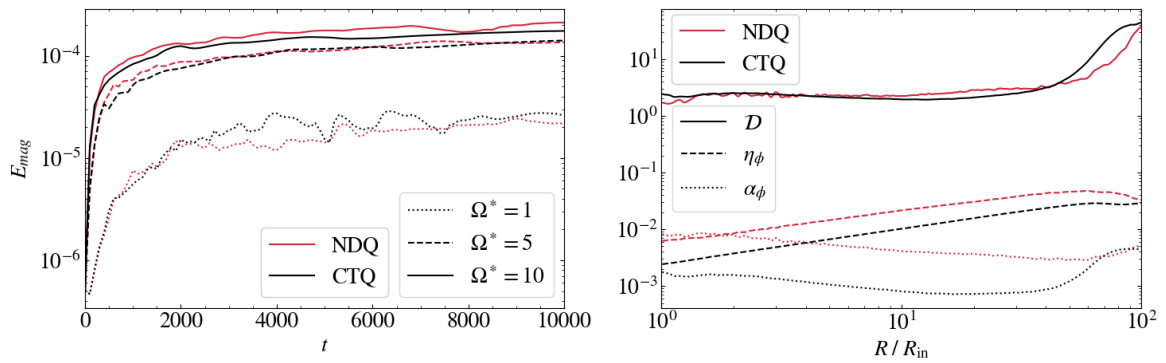
FIGURE 7.15: Magnetic field evolution for different quenching models, in particular with and without the quenching on the turbulent diffusivity. In the left panel is shown the Time evolution of the disk poloidal magnetic energy. In the right panel only the cases with $\Omega^* = 10$ are considered. Shown are the respective radial profiles for dynamo numbers, the ϕ components of magnetic diffusivity at midplane, and he mean-field dynamo α at half disk-height , all at $t = 10000$.
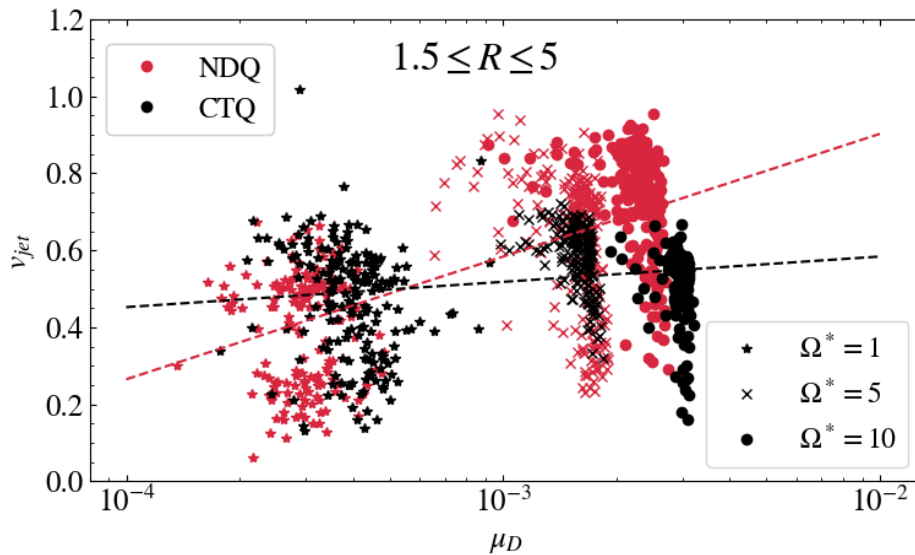
FIGURE 7.16: Jet speed vs disk magnetization for the NDQ and CTQ model. The dashed lines represent the extrapolated fit for the corresponding feedback model.
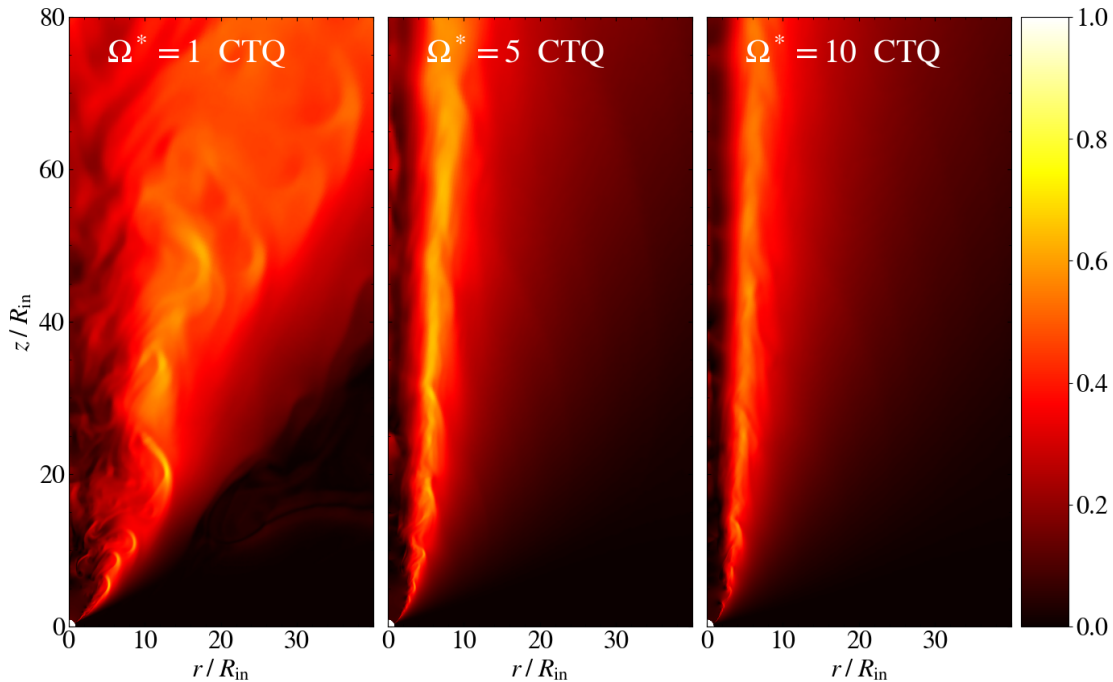
FIGURE 7.17: Jet speed at $t = 10000$ for the CTQ feedback model and different values of the Coriolis number.

7.16). While we find a clear correlation between the disk magnetization and the jet speed in Section 7.2.4 above, the simulations with the consistent feedback thus the quenching of diffusivity show almost no correlation between these two quantities. In contrast, the simulations with the consistent turbulence quenching and high Coriolis number show an outflow with an extremely high degree of collimation (see Figure 7.17).

We recognize that at $t = 10000$ the magnetic loops, which are the main driver for the magnetic tower at initial evolutionary stages, are diffused outwards, and the outflow that is launched form the inner disk is now driven by the magneto-centrifugal mechanism, i.e., launched sub-Alfvénic and subsequently supersedes in the Alfvén and the fast magnetosonic speed. However, because we also have strong amplification of the toroidal field, the collimation process is very rapid (in terms of spatial scales). The Alfvén surface is rather close to the disk surface where the jet is launched. As a consequence, magneto-centrifugal acceleration can happen only along a short distance and the final speed remains rather low.

This is in particular true for the simulations with higher Coriolis number (and therefore stronger amplification of the magnetic field). The Alfvén surface moves further down to the disk surface. This is a very interesting effect. These jets are less efficient concerning the Blandford-Payne acceleration mechanism, but super efficient concerning the Blandford-Payne collimation mechanism. Note that the latter is indeed a consistent result as the material along collimated field lines cannot be accelerated magneto-centrifugally anymore.

In summary, we find that our consistent feedback model that quenches also the disk diffusivity strongly impacts the launching process. This holds in particular for

a weak dynamo (low Coriolis number $\Omega^* = 1$), because of the magnetic field reversals that are induced in the jet launching region and also the intermittent disruption of the jet followed by the production of a flare. However, even for high Coriolis numbers, when the differences are less pronounced, the jet structure is severely affected by this new feedback model, as acceleration decreases and collimation increases. One may hypothesize about a "critical" or "optimal" Coriolis number for the dynamo that can produce the fastest jets. However, this issue need further detailed analysis, which is beyond the scope of this thesis.

So far we have investigate only thin Keplerian disks (i.e., neglecting the non-diagonal components of the dynamo tensor). The differences we find by applying a small Coriolis number (representing a small effect of the rotation on the turbulence) suggest that we may expect even more structured and probably unstable jets that are produced by *thicker* accretion disks.

7.5 Summary

In extension of previous works on mean-field dynamo-driven jets (see Stepanovs, Fendt, and Sheikhnezami 2014), in this chapter we have essentially investigated the feedback of the dynamo-generated magnetic field on the dynamo activity and the disk diffusivity. This is a further step towards a consistent numerical modeling of mean-field disk dynamos.

In summary we have applied (i) different quenching models for the mean-field dynamo, and (ii) an analytically derived formalism for the mean-field dynamo and turbulent diffusivity, that consistently incorporates the suppression of turbulence by a strong and ordered magnetic field.

The following summarizes our approaches and results.

1) We have numerically investigated how different dynamo quenching models affect the magnetic field evolution and thus the jet launching process. More specifically, we compared the most common quenching strategies (Brandenburg and Subramanian, 2005; Stepanovs, Fendt, and Sheikhnezami, 2014) with the analytical model of Ruediger and Kichatinov (1993). The latter model has the advantage to be a more consistent approach, based on an analytical model of turbulent dynamo theory.

2) Essentially, we find that a stronger feedback by the magnetic field on the dynamo leads to a saturation of the magnetic field that is generated by the dynamo at lower disk magnetization. On the other hand, the so-called standard quenching or the diffusive quenching lead to a stronger saturated magnetic field. Nevertheless, the launching process and the jet structure that emerges are affected by the possible evolution of zones where dynamo activity is absent, and that even for similar states of the disk magnetization.

3) While the diffusive quenching model typically leads to a very stable disk-jet connection, just because of the continuous production of large-scale magnetic flux, the strong coupling in the model between the disk magnetization and the magnetic diffusivity, in combination with the absence of a quenching term of the dynamo tensor, may potentially lead to unphysically high values of diffusivity. This problem has been solved by applying a more consistent quenching model on the dynamo and a diffusivity model where $\alpha_{ss} \propto \sqrt{\mu_D}$.

4) In agreement with previous studies, when we apply a feedback only on the dynamo, we recover an interrelation between the disk magnetization and the outflow speed regardless of the Coriolis number (i.e., the strength of the dynamo) or the feedback model. While the feedback model plays a key role for in the saturation of the magnetic field, the relations between the inflow-outflow parameters seems to be independent of the dynamo/diffusivity model applied. This interrelation holds only when no quenching of the magnetic diffusivity is applied (see point 8 of this section).

5) We applied and investigated the effects of a more consistent quenching model which encompasses the suppression of the turbulence by a strong ordered magnetic field, for both the dynamo tensor (Ruediger and Kichatinov, 1993) and the magnetic diffusivity (Kitchatinov, Pipin, and Ruediger, 1994; Rüdiger et al., 1994). Such an approach has never been applied in the context of jet launching by dynamo-generated magnetic fields.

6) We found that, in the early evolutionary stages, the jet is driven by the magnetic pressure. Once the magnetic field has saturated in the inner disk region, and the magnetic loops are opened up and their central part has diffused outwards, the magneto-centrifugal Blandford-Payne outflow is produced.

7) We found that, by applying a consistent turbulence quenching model, reconnection processes lead to the formation of flux ropes (with opposite magnetic field polarity respect to the disk magnetic field) that are accreted and disrupt the jet. As a consequence, the magnetic field is re-amplified in the launching accretion disk region, leading to a very fast intermittent ejection.

8) When applying the quenching model that consistently quenches dynamo and diffusivity, for higher Coriolis numbers, we do not find the established interrelation between jet speed and disk magnetization. Instead, the high Coriolis number is associated with a more collimated jet. The strong toroidal field induced leads to rather short acceleration distances, such that these jets gain only little speed, but a high degree of collimation.

Chapter 8

Conclusions and Outlooks

In this thesis we have investigated the launching of collimated outflows from dynamo-resistive accretion disks in the context of the non-relativistic MHD approximation. The mean-field dynamo is a potential key process to recover the magnetic field necessary in order to trigger the launching mechanisms (R. D. Blandford and Znajek, 1977; R. D. Blandford and Payne, 1982; Lynden-Bell, 1996).

We implemented the mean-field dynamo in the MHD code PLUTO (Mignone, Bodo, Massaglia, et al., 2007) in order to incorporate the large scale consequences of the MRI (Steven A. Balbus and John F. Hawley, 1991). We have then tested several dynamo and diffusivity models in order to recover a more consistent formulation of both turbulent processes.

In this chapter, we summarize the major results presented in the previous chapters of this thesis and we briefly discuss possible future developments in terms of both numerical schemes and numerical simulations.

8.1 Summary

In Chapter 4 we have investigated the accuracy, stability and robustness of selected solutions to the Riemann problem for the Relativistic MHD equations. While the HLL represents the easiest algorithm to implement and the best choice in terms of stability, its lack of intermediate waves makes it a very diffusive solver, unable to fully capture the contact or Alfvén discontinuities.

On the other hand, the more (computationally) expensive HLLD solver showed great accuracy in all the tests conducted, making it the most desirable choice in order to perform accurate and more consistent simulations.

When the HLLD scheme becomes brittle (e.g., in the case of very strong magnetization), some possible backup options have been investigated. In particular, we found in the GFORCE and the HLLC approaches two viable alternatives to the HLLD formulation because of their improved accuracy (compared to the HLL solver) and their stability.

In Chapter 5 we applied for the first time a non-isotropic accretion disk dynamo in the context of jet launching simulations. Since, in principle, the dynamo tensor is not isotropic, a different ratio between the different dynamo components can lead to different properties of the disk outflow.

In particular we found that the $\phi-$component of the dynamo tensor (here assumed to be diagonal since we only worked with thin accretion disks) is strongly

correlated with the amplification of the toroidal field. A weaker α_ϕ leads to a weaker amplification of the poloidal magnetic field, which saturates at a lower value.

On the other hand, the two other dynamo components strongly affect the topology of the dynamo-amplified magnetic field. The strength of the radial and angular components leads to the presence/absence of the so-called "dynamo inefficient zones", i.e., zones where the magnetic field is not amplified by the dynamo. The formation of the dynamo inefficient zones is strongly correlated with the presence of antialigned magnetic loops, which affect the accretion process if close enough to the inner disk regions.

In Chapter 6 we took a step further and we applied a consistent dynamo and diffusivity. In particular the strength and anisotropy of η and α naturally descend from analytical calculation of turbulence, all the diffusivity and dynamo components are related to one single parameter, the Coriolis number Ω^*.

This new approach confirms the previous dynamo simulations, and it shows that the component α_θ is overestimated in the case of a scalar dynamo. A non-isotropic dynamo leads to a more stable evolution of the disk-jet system in presence of a non-radial magnetic seed field.

By investigating the effect of different Coriolis numbers, we recovered the interrelation between disk magnetization and jet speed found in the non-dynamo simulations. In particular a weaker dynamo leads to a weaker disk magnetization and therefore to a slower jet. We also found that for low Coriolis numbers dynamo inefficient zones are formed in the accretion disks, in agreement with the previous dynamo simulations. These dynamo inefficient zones affect the accretion-ejection process and the collimation of the launched jet.

In Chapter 7 we investigated the non-linearity of the dynamo tensor, i.e., the feedback of the magnetic field on the dynamo. As a first step we have investigated several feedback methods which prevent the endless amplification of the magnetic field because of the mean-field dynamo action. Despite several options to parametrize a mean-field dynamo and turbulent diffusivity being developed in the literature, so far, a consistent numerical treatment of the feedback has never been adopted in the context of the jets launching from a resistive and dynamo-active accretion disk. More specifically, we compared the most common isotropic quenching strategies with a more consistent non-isotropic analytical model.

We found that, as expected, the feedback models strongly affect the amplification and the saturation of the magnetic field. A diffusive quenching, which does not apply a direct quenching on the dynamo, leads to a stronger disk magnetization, while the standard feedback model (the most simple approach for an isotropic quenching model) and the analytical non-isotropic feedback model considered both led to a weaker saturation of the magnetic field. Nevertheless, the feedback models affect not only the magnitude but also the topology of the magnetic field, i.e., the presence or absence of the dynamo inefficient zones.

Though the magnetic field strongly depends on the feedback model, we found that the main jet properties, recovered at first by the non-dynamo launching simulations, remain unaltered. A clear interrelation, when applying only a dynamo feedback model, is recovered even if the magnetic field saturates at different magnitudes.

The last portion of this thesis was the study of a consistent feedback model, able to encompass the suppression of both mean-field dynamo and magnetic diffusivity because of the large-scale magnetic field. Since both dynamo and diffusivity share a turbulent origin, the suppression of the latter because of a strong ordered magnetic field should affect both quantities.

We found that the jet is, at first, driven by the magnetic pressure, while at later stages the magnetocentrifugal mechanism takes place. For low Coriolis numbers, we also find a reversal of the magnetic field which is associated with the production of intermittent flares. Although the disk-jet system tends (at $t \gtrsim 15000$) to a quasi-steady state, the field reversal and the intermittent launching process represent a very interesting deviation from a steady state that descend naturally from the dynamo and diffusivity models employed.

We also compared different Coriolis numbers, finding that the interrelation between the disk magnetization and the jet speed is not present anymore. For this model, the Coriolis number strongly affects the jet collimation (rather than the jet speed) because of the strong toroidal field.

8.2   Outlook

A more consistent model of the mean-field dynamo and the magnetic diffusivity in the context of jet launching simulations seems to be a very promising aspect to consider in order to have a full understanding on how astrophysical jets are created and maintained. However, there is a number of ways how the current model can be further improved.

So far we have investigated thin Keplerian disks with fixed thermal (and therefore geometrical) disk height. Such assumption allows us to neglect the non-diagonal component of the dynamo tensor (which are proportional to the ratio between the radius and the disk height, H/R). However, we expect that the variety of disks found around astrophysical objects, may play a key role in the launching process. The influence of the disk height and, consequently, of the non-diagonal components of the dynamo tensor, should be investigated.

Another major change in our simulations would be the extension to the lower hemisphere or to full 3D simulations. Although we expect no substantial changes in the dynamo action, the dynamics of the disk (and therefore of the launched jet) would be strongly affected. In particular such extension would break the assumption of symmetry along the equatorial plane and all its consequences (e.g., a vanishing toroidal field along the disk midplane). Moreover, the absence of symmetry in the accretion disks (which is a plausible scenario) may be able to affect the action of the mean-field dynamo and, ultimately, the properties of the jet formation process. The extension to a full 3D setup would probably require a deep investigation of the boundaries at the inner disk and coronal region. However, the plasma instabilities that are characteristic of a three-dimensional setup would allow use to perform even more realistic and consistent simulations.

In the current work we have adopted some standard numerical algorithms in order to model the set of equations, such as the HLL or the HLLC Riemann solvers. Such numerical schemes do not require nor provide any information concerning the Alfvén waves, which are strongly affected by the presence of the dynamo term. In

particular, the existence of a full set of real eigenvalues (associated with the plasma waves) is not guaranteed, leading to a partial loss of hyperbolicity. The development of numerical schemes suited for these kind of problems represents an unavoidable step in order to perform high resolution-high accuracy simulations. Moreover, genuinely 4th order schemes which run on GPU are becoming available, allowing the scientific community to perform more accurate simulations at reduced computational cost. The possibility to have a fully 3D highly resolved accretion disk (and consequently the launched jet) arises also from such numerical and computational improvements.

Alongside the numerical improvement, several physical processes can be incorporated. To our knowledge, there is no MHD code that includes all the turbulent processes influenced by rotation, like, e.g., diffusivity, dynamo, heat conductivity and viscosity. As for the dynamo and the diffusivity, other physical processes may be relevant in order to investigate the stability of the launched jet, as well as the jet properties (e.g., speed, collimation or magnetization).

Finally, one must bear in mind that a full understanding requires the comparison between numerical simulations and observations. The investigation of the emission spectrum can be performed in several ways. A fully radiative closure would certainly be the most consistent option. However, such a model would require a significant effort in order to derive the correct set of equations and to implement it in a numerical code. The radiation spectrum can also be derived through a radiation transport code, which would not take into account the interplay between matter and radiation as the system evolves, but it can give us a general comparison between numerical simulations and observations. Another possibility is to include Lagrangian particles to the setup, whose spectrum would evolve in time by solving the relativistic cosmic ray transport equation. Such an approach has been recently adopted in order to understand the properties of astrophysical jets and it can help us to understand emission processes in the presence of shocks within the jet. High resolution simulations with radiation transfer should allow us to compare the simulated spectra with that observed from real astrophysical objects.

Appendix A

Test Simulations and Comparison to the Literature

In order to validate our implementation of the mean-field dynamo tensor in the version 4.3 of PLUTO, we have also performed comparison simulations to the reference simulation of Fendt and Gaßmann (2018), now restricted to one hemisphere.

Note that while in Stepanovs, Fendt, and Sheikhnezami (2014) and Fendt and Gaßmann (2018) the dynamo term was simply coupled with the magnetic diffusivity, here, because of its hyperbolic nature, the α-tensor is coupled with the standard hyperbolic MHD flux terms, with a correction due to the solenoidal condition of the magnetic field. Some minor differences in the magnetic field evolution seem to arise from the different implementation schemes, however, the overall evolution of the system shows very small differences in the strength of the physical processes at work.

Our simulation runs till $t = 30000$, corresponding to $\simeq 5000$ inner disk rotations. Figure A.1 shows the evolution of the density and of the magnetic field lines. We may distinguish three different zones of evolution – the innermost disk, the outer disk, and the corona. The temporal evolution is in very good agreement with Fendt and Gaßmann (2018), evolving the same features.

Throughout the inner disk region the magnetic field lines have the typical open field lines inclined with respect to the disk surface. This configuration is particularly favorable for a Blandford-Payne-driven outflow. The outer disk region is filled with magnetic loops, which are pushed outwards by the magnetic pressure gradient and thereby diffusing through the disk until it is filled with magnetic energy and a local steady state is reached.

In difference to Fendt and Gaßmann (2018) we find that the poloidal magnetic energy saturates towards a somewhat level, but this is simply because our computational domain is smaller. Integrated over the whole disk Fendt and Gaßmann (2018) find a saturation magnitude of $\simeq 2 \times 10^{-3}$ (in code units), while here we reach a saturation value of $\simeq 1.2 \times 10^{-3}$ (assuming that the lower hemisphere follows the same evolution as the upper hemisphere).

On the other hand, the accretion and ejection rates saturate at similar magnitude, and also the accretion-ejection ratio agrees with our previous studies (Fendt and Gaßmann, 2018). This again strongly supports our conclusion that the different implementation schemes are identical.
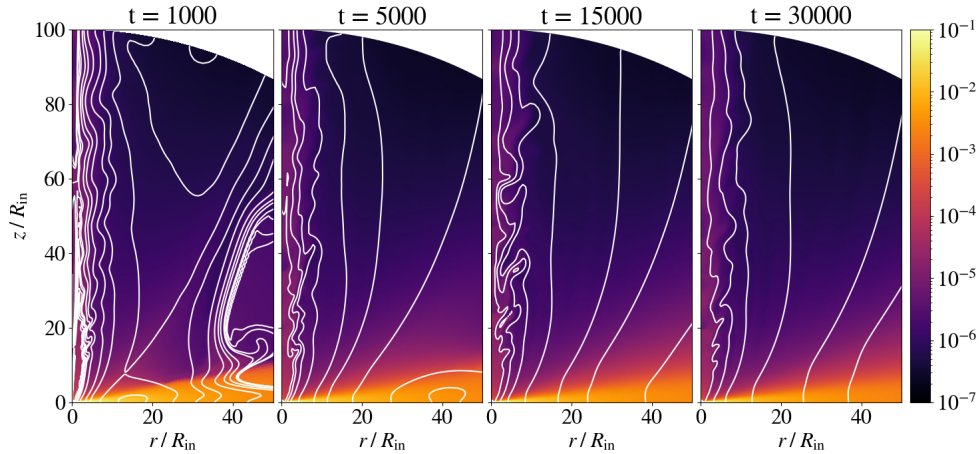
FIGURE A.1: Comparison simulation. Snapshots at different times for a simulation with the the reference parameters of Fendt and Gaßmann (2018), now performed with PLUTO 4.3. The color map shows the density while the white lines are contours of the vector potential (poloidal magnetic field lines).

A.1   The dynamo number

One way to examine the evolution of the dynamo action is to look at the time evolution of the dynamo number, see Equation (3.56). Dynamo quenching limits the dynamo number to a marginally sub-critical magnitude at which the alpha-dynamo is balanced by magnetic diffusivity. We point out that the critical dynamo number is not known *a priori*, but had to be derived from comparison of parameter studies. Furthermore, it tells us whether a particular disk region has reached a quasi-steady state. The evolution of the dynamo number is shown in Figure A.2 as a function of time and radius, respectively.

At $t = 0$ the dynamo number is almost infinite because of the weak magnetization, then it decreases starting from the inner radii and then reaching a quasi-steady state also in the outer regions. At $t = 5000$ we can distinguish two areas in the profile of the dynamo number. For $R < 60$, diffusive quenching has already lead to a field saturation. For larger radii the diffusivity still decreases as the toroidal magnetic field has not entirely engulfed the accretion disk.

At time $t = 15000$ the dynamo-generated magnetic loops are diffused to large radii and the whole system has reached a stable configuration. For all radii the dynamo number is somewhat below 6, which we consider as the critical dynamo number for this simulation setup. We note that this magnitude is similar to what Brandenburg and Subramanian (2005) have suggested, although the critical dynamo number depends on the geometry and other physical details of the simulation setup. Going even further in time we see no difference in the temporal evolution nor in the dynamo number. Thus, all simulations were performed, if not specified otherwise, till $t = 10000$.
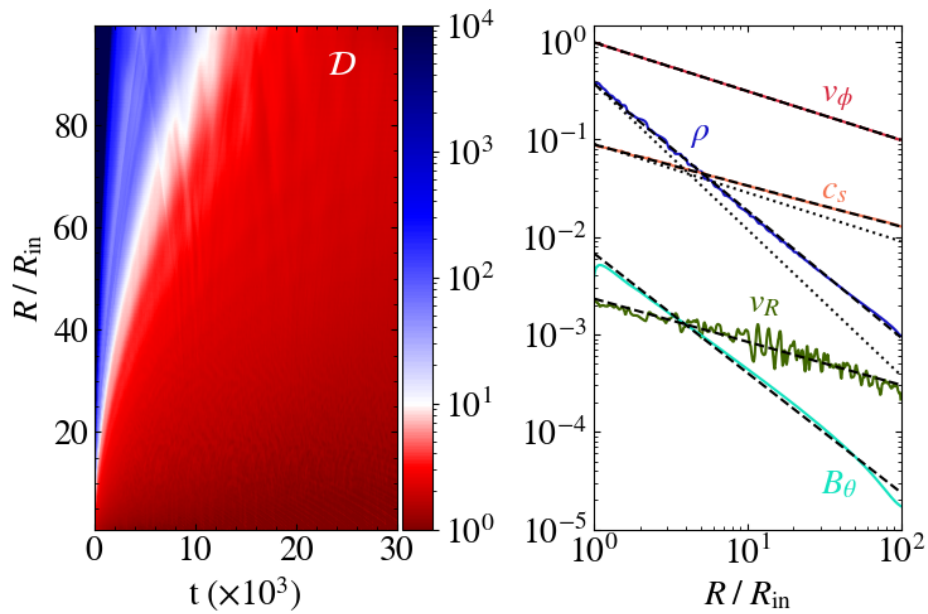
FIGURE A.2: Comparison simulation. Evolution of the dynamo number and MHD variables for a simulation of with the the reference parameters of Stepanovs, Fendt, and Sheikhnezami (2014). Shown is the evolution of the dynamo number as a function of time and radius (left) over time, and the profile of certain physical quantities along the disk mid-plane (right) at $t = 30000$. Colored lines indicate different physical quantities, while thin dashed lines show the initial power-law distribution. The thick dashed lines show the corresponding fit by a power-law.

A.2 Mid-plane quantities

Figure A.2 shows the distribution of specific physical quantities along the disk mid-plane, measured at $t = 30000$. This allows to compare our test simulations to the reference simulation of Stepanovs, Fendt, and Sheikhnezami (2014).

We have again fitted the simulation data points with a power law in order to extrapolate the power law index β_X and compare it with the radial distribution at $t = 0$. We find that the disk rotation remains Keplerian with $\beta_{v_\phi} = -1/2$. However, the radial profile of the density distribution changes substantially from $\beta_\rho = -3/2$ to $\beta_\rho = -4/3$ up to $R \simeq 30$, while for larger radii the power index is $\beta_\rho = -5/4$. As the total mass flux is conserved, the ejection of matter immediately changes the accretion rate over the disk and is thus related to the changes in the profiles of the mass fluxes. The radial (accretion) velocity follows a power law index $\beta_{v_R} = -2/5$. Since we are reaching a longer run time than Stepanovs, Fendt, and Sheikhnezami (2014), we are now able to get rid of the oscillations and also the reversal found by Stepanovs, Fendt, and Sheikhnezami (2014) in the outer disk regions (as their magnetic field was not yet diffused across the whole accretion disk).

The power-law coefficient of the sound speed changes during $t = 0$ and $t = 10000$ from $\beta_{\mathrm{cs}} = -1/2$ to $\beta_{\mathrm{cs}} = -3/7$, which tells us that the mean-field dynamo only slightly changes its strength as due to the disk sound speed through the disk-jet evolution (see Equation 3.41). This change does not lead to any strong net effect on the temporal evolution of the disk-jet system, therefore we again find difference to our previous results (Stepanovs, Fendt, and Sheikhnezami, 2014; Fendt and Gaßmann, 2018).

Also the angular magnetic field component B_θ follows the same power law, namely $\beta_{B_\theta} = -5/4$. Note, however, that we do not find the decrease in the outer disk regions ($R \geq 40$) as found in Stepanovs, Fendt, and Sheikhnezami (2014), simply because of our longer simulation time.

Overall, by quantifying essential dynamical properties of our simulation results, we find perfect agreement with the previous results that are based on a numerically different implementation of magnetic diffusivity and mean-field dynamo.

Appendix B

Resolution Study

A numerical study is incomplete without presenting a resolution study. This is done the in following where we discuss how our physical results depend on the numerical resolution applied. We compare the reference simulation of Chapter 6 (resolution [512 × 128]) with two simulation runs applying exactly the same physical parameters, but different resolution. We choose [1024 × 512] for a higher resolution run and [256 × 64] for a lower resolution run. The results are displayed in Figure B.1 where we show the density and poloidal magnetic field distribution and the evolution of the dynamo-generated poloidal magnetic energy.

First of all we notice that the reference resolution shows very small differences with the high resolution case, and this mostly in the initial evolutionary stages. The open field lines, favorable for the launching, in the inner disk region and the magnetic loops in the outer disk are present in all simulations, with almost no difference (see Figure B.1). This holds in particular for the evolution of the disk poloidal magnetic energy. On the other hand, for the low resolution run the differences persist also on the later stages, although the qualitative temporal evolution is the same of the reference case (see Figure B.1).

The differences in the evolution of the magnetic field are mostly related to the different numerical diffusivity, which is higher for lower resolution. Before the dynamo quenching by diffusivity has taken place, we believe that the numerical diffusivity quite contributes in the low resolution case, leading to a damping of the magnetic field amplification (a higher diffusivity lowers the dynamo number). However, at later times the *physical* magnetic diffusivity (which is triggered by the disk magnetization) becomes dominant and therefore the poloidal magnetic energy saturates around the same level (see Figure B.2).

Numerical diffusivity plays a key role in the dynamics of the disk-jet connection, e.g., in the efficiency of the accretion process, and also for the mass loading of the disk wind. Since in the low resolution case the field amplification slower, the saturation of the diffusivity level that allows to replenish (by accretion) the disk matter from the outer disk, happens on a longer timescale as well. Therefore, the disk accretion rate decreases for the lower resolution setup.

In summary, our simulation results are not completely resolution independent. However, the results of our reference simulation are very close to a higher resolution study, so a higher resolution would not lead to any improvement. In contrary, a lower resolution would affect the hydrodynamics of the system as well as the evolution of the magnetic field. Thus, we conclude that the resolution we chosen is in fact appropriate in order to capture the essential physics while keeping the computational low.
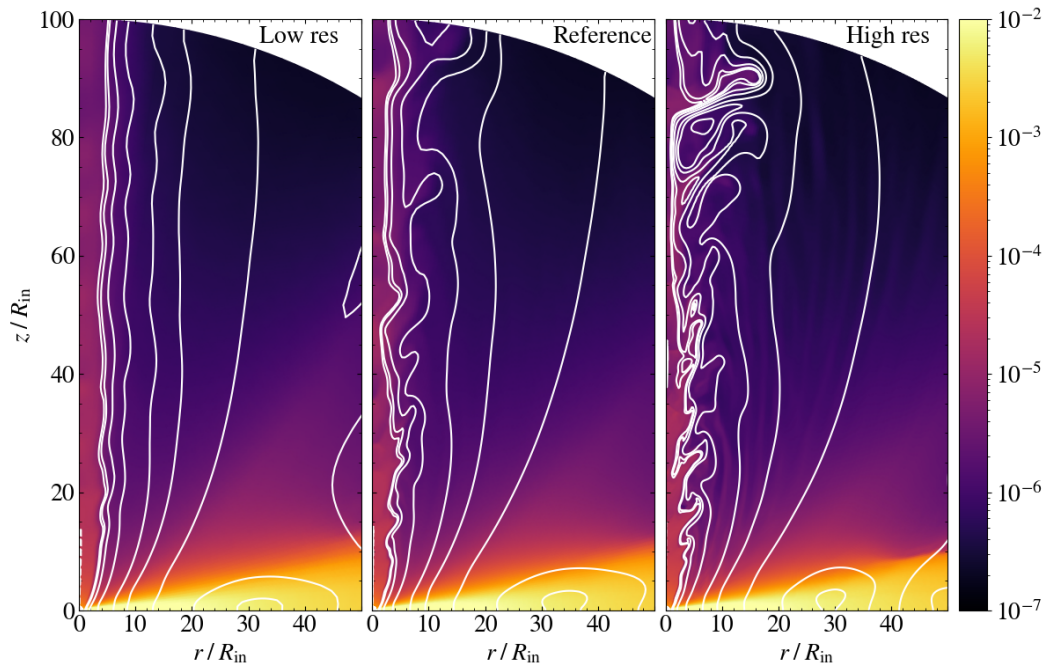
FIGURE B.1: Resolution study. Density distribution (color) and po-
loidal magnetic field (white lines) for simulations applying the refer-
ence parameters, but for different resolution at $t = 4000$.
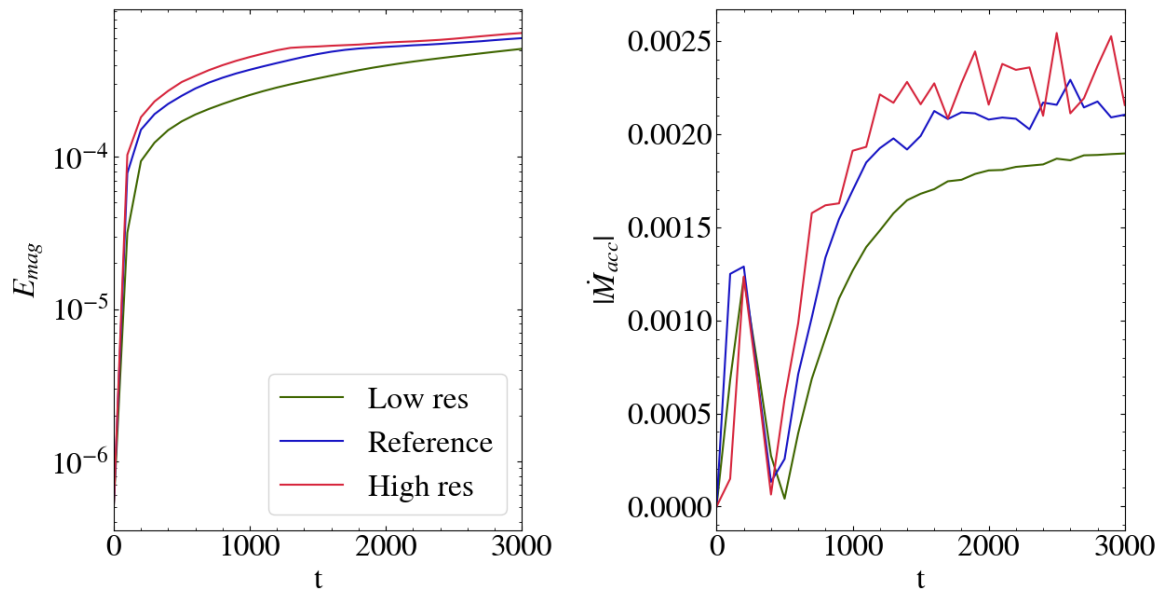
FIGURE B.2: Resolution study. Temporal evolution of the poloidal disk
magnetic energy (left panel) integrated from $R = 5$ to the outer bound-
ary, $R = 100$, and the accretion rate (right panel) computed at $R = 5$.

Appendix C

Contact and Alfvén Eigenvectors of Relativistic MHD

The eigenstructure of the RMHD equations has been studied by Anile and Pennisi (1987) and Anile (2005), and rewritten by S. S. Komissarov (1999), D. S. Balsara (2001), and Antón et al. (2010) in a more suited way for the numerical schemes. Our method of solution follows the approach of Antón et al. (2010), although the computation of the left eigenvectors slightly differs from their approach. For the sake of clarity, we summarize here the pertinent formulas. The most convenient way to compute the left and right eigenvectors is to use the so-called covariant variables $\tilde{\mathscr{U}} = (u^\mu, b^\mu, p, s)^T$. The eigenvector problem becomes

$$(\mathcal{A}^\mu \phi_\mu)\tilde{\mathbf{r}} = 0 \qquad \tilde{\mathbf{l}}_0(\mathcal{A}^\mu \phi_\mu) = 0. \tag{C.1}$$

The vector $\phi_\mu = (-\lambda, 1, 0, 0)$ describes the normal to the characteristic hypersurface, while the matrices $\mathcal{A}^\mu$ are defined by

$$\mathcal{A}^\mu = \begin{pmatrix} w_T u^\mu \delta^\alpha_\beta & -b^\mu \delta^\alpha_\beta + P^{\alpha\mu} b_\beta & l^{\alpha\mu} & 0^\alpha \\ b^\mu \delta^\alpha_\beta & -u^\mu \delta^\alpha_\beta & f^{\mu\alpha} & 0^\alpha \\ \rho h \delta^\mu_\beta & 0_\beta & u^\mu/c_s^2 & 0 \\ 0_\beta & 0_\beta & 0 & u^\mu \end{pmatrix}, \tag{C.2}$$

where the index $\alpha = [0,1,2,3]$ indicates the rows and the index $\beta = [0,1,2,3]$ indicates the columns. The quantities introduced in Equation (C.2) are $P^{\alpha\mu}_\beta = \jmath^{\alpha\mu} + 2u^\alpha u^\mu$, $l^{\alpha\mu} = (\rho h \jmath^{\alpha\mu} + (\rho h - b^2/c_s^2)u^\alpha u^\mu)/(\rho h)$, $f^{\alpha\mu} = (u^\mu b^\alpha/c_s^2 - u^\alpha b^\mu)/(\rho h)$, while c_s is the sound speed. As pointed by Koldoba, Kuznetsov, and Ustyugova (2002) and Antón et al. (2010), the ortonormalization of the eigenvectors is provided by

$$\tilde{\mathbf{l}}_0(\lambda_1)\mathcal{A}^0\tilde{\mathbf{r}}(\lambda_2) = \tilde{\mathbf{l}}(\lambda_1)\tilde{\mathbf{r}}(\lambda_2) = \delta^{\lambda_1}_{\lambda_2}. \tag{C.3}$$

Because of the degeneracies of the RMHD, we renormalized the left and right eigenvectors as already done by Antón et al. (2010). We start with the right eigenvector associated to the entropy wave,

$$\tilde{\mathbf{r}}_e = (0^\alpha, 0^\alpha, 0, 1)^T. \tag{C.4}$$

In order to compute the right Alfvén eigenvectors we need some intermediate quantities, as

$$
\begin{aligned}
\alpha_1^\mu &= \gamma(v^z, \lambda_a v^z, 0, 1 - \lambda_a v^x), \\
\alpha_2^\mu &= -\gamma(v^y, \lambda_a v^y, 1 - \lambda_a v^x, 0),
\end{aligned}
\tag{C.5}
$$

and

$$
\begin{aligned}
g_1 &= \frac{1}{\gamma}\left(B^y + \frac{\lambda_a v^y}{1 - \lambda_a v^x}B^x\right), \\
g_2 &= \frac{1}{\gamma}\left(B^z + \frac{\lambda_a v^z}{1 - \lambda_a v^x}B^x\right),
\end{aligned}
\tag{C.6}
$$

where, if $g_1 = g_2 = 0$, we follow the prescription $g_1 = g_2 = 1$. The explicit form of the right Alfvén eigenvectors becomes

$$
\tilde{\mathbf{r}}_{a,\pm} = (f_1 \alpha_1^\mu + f_2 \alpha_2^\mu, \mp\sqrt{w_T}(f_1 \alpha_1^\mu + f_2 \alpha_2^\mu), 0, 0)^T,
\tag{C.7}
$$

where

$$
f_{1,2} = \frac{g_{1,2}}{\sqrt{g_1^2 + g_2^2}}.
\tag{C.8}
$$

The normalized left eigenvectors in covariant variable are computed using Equation (C.1), which leads to

$$
\tilde{\mathbf{l}}_e = (0^\alpha, 0^\alpha, 0, 1),
\tag{C.9}
$$

for the entropy eigenvector, and

$$
\tilde{\mathbf{l}}_{a,\pm} = N\left(
\begin{array}{c}
(w_T \gamma \pm b^0 \sqrt{w_T})(f_1 \alpha_{1\mu} + f_2 \alpha_{2\mu}) \\
-(b^0 \pm \sqrt{w_T}\gamma)(f_1 \alpha_{1\mu} + f_2 \alpha_{2\mu}) + (f_1 \alpha_1^0 + f_2 \alpha_2^0)b_\mu \\
f_1 \alpha_1^0 + f_2 \alpha_2^0 \\
0
\end{array}
\right)^T,
\tag{C.10}
$$

for the Alfvén eigenvectors. The renormalization factor N takes the form

$$
N = \frac{\sqrt{w_T}}{g_1^2 + g_2^2}(N_1 + N_2 + N_3),
\tag{C.11}
$$

where

$$
\left\{
\begin{aligned}
N_1 &= (B^z v^y - B^y v^z)^2[2(\lambda^2 - 1)\sqrt{w_T}\gamma + b^0 \sqrt{w_T}(2\lambda^2 - 1) \mp \lambda b^x], \\
N_2 &= 2(\sqrt{w_T}\gamma \pm b^0)(\gamma - \lambda u^x)^2(g_1^2 + g_2^2), \\
N_3 &= (B^y v^z - B^z v^y)(\gamma - \lambda u^x)(b^z g_1 - b^y g_2).
\end{aligned}
\right.
\tag{C.12}
$$

This normalization is well defined through the RMHD degeneracies.

In order to include the entropy and Alfvén waves in the HLLEM solver we have to compute the normalized eigenvectors in conserved variables. The conserved eigenvectors are computed as follows:

$$
\mathbf{R} = \left(\frac{\partial \mathscr{U}}{\partial \tilde{\mathscr{U}}}\right)\tilde{\mathbf{r}} \qquad \mathbf{L} = \tilde{\mathbf{l}}\left(\frac{\partial \tilde{\mathscr{U}}}{\partial \mathscr{U}}\right).
\tag{C.13}
$$

The transformation matrix for the right eigenvectors has a straightforward explicit form:

$$
\left(\frac{\partial \mathcal{U}}{\partial \tilde{\mathcal{U}}} \right) =
\begin{pmatrix}
\rho & 0^j & 0 & 0^j & \rho_p \gamma & \rho_s \gamma \\
w_T u^i & w_T \gamma \delta^{ij} & A^i & M^{ij} & w_p \gamma u^i & w_s \gamma u^i \\
b^i & -b^0 \delta^{ij} & -u^i & \gamma \delta^{ij} & 0 & 0 \\
2 w_T \gamma - \rho & 0^j & F & C^j & G & w_s
\end{pmatrix},
\tag{C.14}
$$

where the intermediate quantities are

$$
\begin{aligned}
M^{ij} &= 2 b^j \gamma u^i - b^0 \delta^{ij} & A^i &= -2 b^0 \gamma u^i - b^i, \\
C^j &= 2 b^j \gamma^2 - b^j & F &= -2 b^0 \gamma^2 - b^0, \\
G &= w_p \gamma^2 - 1 - \rho_p \gamma,
\end{aligned}
\tag{C.15}
$$

while the partial derivatives are written in a more compact form

$$
\begin{aligned}
\rho_s &= \left(\frac{\partial \rho}{\partial s} \right)_p = -\frac{\rho}{s\Gamma} & w_s &= \left(\frac{\partial \rho h}{\partial s} \right)_p = -\frac{\rho}{s\Gamma}, \\
\rho_p &= \left(\frac{\partial \rho}{\partial p} \right)_s = \frac{\rho}{\Gamma p} & w_p &= \left(\frac{\partial \rho h}{\partial p} \right)_s = \frac{\rho}{\Gamma p} + \frac{\Gamma}{\Gamma - 1},
\end{aligned}
\tag{C.16}
$$

assuming an ideal equation of state. The conversion to the conserved variables yields

$$
\mathbf{R}_e = -\frac{D}{s\Gamma} (1, u^x, u^y, u^z, \gamma - 1, 0, 0, 0)^T,
\tag{C.17}
$$

for the entropic eigenvector, and

$$
\mathbf{R}_{a,\pm} = f_1 \mathbf{V}_{a,1,\pm} - f_2 \mathbf{V}_{a,2,\pm},
\tag{C.18}
$$

for the Alfvén eigenvectors, where

$$
\mathbf{V}_{a,1,\pm} =
\begin{pmatrix}
\rho u^z \\
2 u^z (w_T u^x \pm \sqrt{w_T} b^x) \\
w_T u^y u^z \pm \sqrt{w_T} b^y u^z \\
w_T [\gamma^2 + (u^z)^2 - (u^x)^2] \pm \sqrt{w_T} (b^z u^z + b^0 \gamma - b^x u^x) \\
0 \\
b^y u^z \pm \sqrt{w_T} u^y u^z \\
-b^y u^y \mp \sqrt{w_T} [1 + (u^y)^2] \\
2 u^z (w_T \gamma \pm \sqrt{w_T} b^0) - \rho u^z
\end{pmatrix},
\tag{C.19}
$$

and

$$
\mathbf{V}_{a,2,\pm} =
\begin{pmatrix}
\rho u^y \\
2u^y(w_T u^x \pm \sqrt{w_T} b^x) \\
w_T[\gamma^2 + (u^y)^2 - (u^x)^2] \pm \sqrt{w_T}(b^y u^y + b^0 \gamma - b^x u^x) \\
w_T u^y u^z \pm w_T b^z u^y \\
0 \\
-b^z u^z \pm \sqrt{w_T}[1 + (u^z)^2] \\
b^z u^y \pm w_T u^y u^z \\
2u^y(w_T \gamma \pm \sqrt{w_T} b^0) - \rho u^y
\end{pmatrix}.
\tag{C.20}
$$

The computation of the transformation matrix is made, as in Antón et al. (2010), in two steps. The first step is to convert the eigenvectors in primitive variables $\bar{\mathcal{V}} = (u^x, u^y, u^z, b^x, b^y, b^z, p, \rho)$,

$$
\mathbf{l} = \tilde{\mathbf{l}}\left(\frac{\partial \tilde{\mathcal{U}}}{\partial \bar{\mathcal{V}}}\right),
\tag{C.21}
$$

while, in the second step we recover directly the scalar product $\mathbf{L}_* \cdot (\mathcal{U}_R - \mathcal{U}_L)$, which is computed taking the scalar product between the primitive eigenvectors $\tilde{\mathbf{l}}_*$ and the solution of the linear system

$$
\left(\frac{\partial \mathcal{U}}{\partial \bar{\mathcal{V}}}\right)\mathbf{X} = \mathcal{U}_R - \mathcal{U}_L,
\tag{C.22}
$$

where $\mathbf{X}$ is the unknown vector. The system of Equation (C.22) is solved through a standard LU decomposition algorithm (Press et al., 1992). The first transformation matrix has the form

$$
\left(\frac{\partial \tilde{\mathcal{U}}}{\partial \bar{\mathcal{V}}}\right) =
\begin{pmatrix}
v^j & 0^j & 0 & 0 \\
\delta^{ij} & 0^{ij} & 0 & 0 \\
B^j & u^j & 0 & 0 \\
\dfrac{\partial b^i}{\partial u^j} & \dfrac{\partial b^i}{\partial B^j} & 0 & 0 \\
0^j & 0^j & 1 & 0 \\
0^j & 0^j & \left(\dfrac{\partial s}{\partial p}\right)_\rho & \left(\dfrac{\partial s}{\partial \rho}\right)_p
\end{pmatrix},
\tag{C.23}
$$

where

$$
\begin{aligned}
\frac{\partial b^j}{\partial u^i} &= v^i B^j - B^i v^j \gamma^{-2} - (\mathbf{v} \cdot \mathbf{B})(v^i v^j - \delta^{ij}), \\
\frac{\partial b^j}{\partial B^i} &= \gamma^{-1}(u^i u^j + \delta^{ij}),
\end{aligned}
\tag{C.24}
$$

and

$$
\left(\frac{\partial s}{\partial \rho}\right)_p = \frac{s}{p} \qquad \left(\frac{\partial s}{\partial p}\right)_\rho = -\frac{s\Gamma}{\rho}.
\tag{C.25}
$$

A difference between our approach and the one of Antón et al. (2010) is that, since

the conversion matrix is less straightforward, we do not provide an analytical expression for the left eigenvectors in primitive variables. On the other hand, this approach, since it converts immediately from the covariant magnetic field to the laboratory magnetic field, the latter step is much easier to compute.

The explicit form of the latter transformation matrix is

$$
\left(\frac{\partial \mathcal{U}}{\partial \bar{\mathcal{V}}} \right) =
\begin{pmatrix}
\rho v^j & 0^j & 0 & \gamma \\
\dfrac{\partial S^i}{\partial u^j} & \dfrac{\partial S^i}{\partial B^j} & \dfrac{\Gamma}{\Gamma - 1}\gamma u^i & \gamma u^i \\
0^{ij} & \delta^{ij} & 0^i & 0^i \\
\dfrac{\partial E}{\partial u^j} & \dfrac{\partial E}{\partial B^j} & \dfrac{\Gamma}{\Gamma - 1}\gamma^2 - 1 & \gamma(\gamma - 1)
\end{pmatrix} ,
\tag{C.26}
$$

where the partial derivatives are

$$
\begin{aligned}
\frac{\partial S^i}{\partial u^j} &= (\rho h - \frac{B^2}{\gamma^2})v^i u^j - \frac{B^i B^j}{\gamma} + \frac{B^i v^j}{\gamma}(\mathbf{v} \cdot \mathbf{B}) + (Dh + \frac{B^2}{\gamma})\delta^{ij}, \\
\frac{\partial S^i}{\partial B^j} &= 2v^i B^j - B^i v^j - (\mathbf{v} \cdot \mathbf{B})\delta^{ij}, \\
\frac{\partial E}{\partial u^j} &= 2u^j \rho h - \rho v^j + \frac{v^j B^2 - B^j(\mathbf{v} \cdot \mathbf{B})}{\gamma} - [v^2 B^2 - (\mathbf{v} \cdot \mathbf{B})^2]\frac{v^j}{\gamma}, \\
\frac{\partial E}{\partial B^j} &= B^j(1 + v^2) - v^j(\mathbf{v} \cdot \mathbf{B}).
\end{aligned}
\tag{C.27}
$$

We point out that the system has a trivial solution in the magnetic field components, therefore it can be reduced to 5 unknown values in order to increase its speed and performance. Although the last two steps are performed numerically, the orthonormalization of the conserved eigenvectors is preserved up to machine accuracy.

List of Publications

1. **Mattia Giancarlo**, Fendt Christian. Jets from Accretion Disk Dynamos: Consistent Quenching Modes for Dynamo and Resistivity, Submitted to ApJ

2. **Mattia Giancarlo**, Mignone Andrea. A comparison of Approximate non-Linear Riemann Solvers for Relativistic MHD, MNRAS,512,581

3. **Mattia Giancarlo**, Fendt Christian. Magnetohydrodynamic Accretion–Ejection: Jets Launched by a Nonisotropic Accretion-disk Dynamo. II. A Dynamo Tensor Defined by the Disk Coriolis Number, ApJ,900,60

4. **Mattia Giancarlo**, Fendt Christian. Magnetohydrodynamic Accretion–Ejection: Jets Launched by a Nonisotropic Accretion-disk Dynamo. I. Validation and Application of Selected Dynamo Tensorial Components, ApJ,900,59

Bibliography

Alfvén, H. (1942). "Existence of Electromagnetic-Hydrodynamic Waves". In: *Nature* 150.3805, pp. 405–406. DOI: 10.1038/150405d0.

Anile, A. M. (2005). *Relativistic Fluids and Magneto-fluids*.

Anile, A. M. and S. Pennisi (1987). "On the mathematical structure of test relativistic magnetofluiddynamics". en. In: *Annales de l'I.H.P. Physique théorique* 46.1, pp. 27–44. URL: http://www.numdam.org/item/AIHPA_1987__46_1_27_0.

Antón, L. et al. (2010). "Relativistic Magnetohydrodynamics: Renormalized Eigenvectors and Full Wave Decomposition Riemann Solver". In: *ApJ Supplement* 188.1, pp. 1–31. DOI: 10.1088/0067-0049/188/1/1.

Antonucci, R. R. J. and J. S. Ulvestad (1985). "Extended radio emission and the nature of blazars." In: *ApJ* 294, pp. 158–182. DOI: 10.1086/163284.

Atteia, J. -L. and K. Hurley (1986). "Extragalactic gamma-ray bursts". In: *Advances in Space Research* 6.4, pp. 39–43. DOI: 10.1016/0273-1177(86)90235-8.

Avara, M. J., J. C. McKinney, and C. S. Reynolds (2016). "Efficiency of thin magnetically arrested discs around black holes". In: *MNRAS* 462.1, pp. 636–648. DOI: 10.1093/mnras/stw1643.

Bacchini, F. et al. (2019). "Generalized, Energy-conserving Numerical Simulations of Particles in General Relativity. II. Test Particles in Electromagnetic Fields and GRMHD". In: *ApJ Supplement* 240.2, 40, p. 40. DOI: 10.3847/1538-4365/aafcb3.

Backus, G. (1958). "A class of self-sustaining dissipative spherical dynamos". In: *Annals of Physics* 4.4, pp. 372–447. DOI: 10.1016/0003-4916(58)90054-X.

Baczko, A. -K. et al. (2016). "A highly magnetized twin-jet base pinpoints a supermassive black hole". In: *A&A* 593, A47, A47. DOI: 10.1051/0004-6361/201527951.

Bai, X., D. Caprioli, et al. (2015). "Magnetohydrodynamic-particle-in-cell Method for Coupling Cosmic Rays with a Thermal Plasma: Application to Non-relativistic Shocks". In: *ApJ* 809.1, 55, p. 55. DOI: 10.1088/0004-637X/809/1/55.

Bai, X. and J. M. Stone (2013). "Local Study of Accretion Disks with a Strong Vertical Magnetic Field: Magnetorotational Instability and Disk Outflow". In: *ApJ* 767.1, 30, p. 30. DOI: 10.1088/0004-637X/767/1/30.

Balbus, Steven A. and John F. Hawley (1991). "A Powerful Local Shear Instability in Weakly Magnetized Disks. I. Linear Analysis". In: *ApJ* 376, p. 214. DOI: 10.1086/170270.

Bally, J. (2007). "Jets from young stars". In: *Astrophysics and Space Science* 311.1-3, pp. 15–24. DOI: 10.1007/s10509-007-9531-7.

Bally, J. and C. J. Lada (1983). "The high-velocity molecular flows near young stellar objects". In: *ApJ* 265, pp. 824–847. DOI: 10.1086/160729.

Bally, J., B. Reipurth, and C. J. Davis (2007). "Observations of Jets and Outflows from Young Stars". In: *Protostars and Planets V*. Ed. by Bo Reipurth, David Jewitt, and Klaus Keil, p. 215.

Bally, J., J. Walawender, and B. Reipurth (2012). "Deep Imaging Surveys of Star-forming Clouds. V. New Herbig-Haro Shocks and Giant Outflows in Taurus". In: *Astronomical Journal* 144.5, 143, p. 143. DOI: 10.1088/0004-6256/144/5/143.

Balsara, D. S. (2001). "Total Variation Diminishing Scheme for Relativistic Magneto-hydrodynamics". In: *ApJ Supplement* 132, pp. 83–101. DOI: 10.1086/318941.

— (2010). "Multidimensional HLLE Riemann solver: Application to Euler and magnetohydrodynamic flows". In: *Journal of Computational Physics* 229.6, pp. 1970–1993. DOI: 10.1016/j.jcp.2009.11.018.

— (2017). "Higher-order accurate space-time schemes for computational astrophysics—Part I: finite volume methods". In: *Living Reviews in Computational Astrophysics* 3.1, 2, p. 2. DOI: 10.1007/s41115-017-0002-8.

Balsara, D. S. and J. Kim (2016). "A subluminal relativistic magnetohydrodynamics scheme with ADER-WENO predictor and multidimensional Riemann solver-based corrector". In: *Journal of Computational Physics* 312, pp. 357–384. DOI: 10.1016/j.jcp.2016.02.001.

Balsara, D. S. and D. S. Spicer (1999). "A Staggered Mesh Algorithm Using High Order Godunov Fluxes to Ensure Solenoidal Magnetic Fields in Magnetohydrodynamic Simulations". In: *Journal of Computational Physics* 149.2, pp. 270–292. DOI: 10.1006/jcph.1998.6153.

Bardou, A. et al. (2001). "The effects of vertical outflows on disk dynamos." In: *A&A* 370, pp. 635–648. DOI: 10.1051/0004-6361:20010267.

Beck, R. (2015). "Magnetic fields in spiral galaxies". In: *A&A Rev.* 24, 4, p. 4. DOI: 10.1007/s00159-015-0084-4.

Beckwith, K., J. F. Hawley, and J. H. Krolik (2008). "The Influence of Magnetic Field Geometry on the Evolution of Black Hole Accretion Flows: Similar Disks, Drastically Different Jets". In: *ApJ* 678.2, pp. 1180–1199. DOI: 10.1086/533492.

Beckwith, K. and J. M. Stone (2011). "A Second-order Godunov Method for Multidimensional Relativistic Magnetohydrodynamics". In: *ApJ Supplement* 193, 6, p. 6. DOI: 10.1088/0067-0049/193/1/6.

Bellan, P. M. (2006). *Fundamentals of Plasma Physics*.

Belloni, T. et al. (2005). "The evolution of the timing properties of the black-hole transient GX 339-4 during its 2002/2003 outburst". In: *A&A* 440.1, pp. 207–222. DOI: 10.1051/0004-6361:20042457.

Bendre, A. B. et al. (2020). "Turbulent transport coefficients in galactic dynamo simulations using singular value decomposition". In: *MNRAS* 491.3, pp. 3870–3883. DOI: 10.1093/mnras/stz3267.

Beresnyak, A. (2012). "Universal Nonlinear Small-Scale Dynamo". In: *Phys. Rev. Lett.* 108.3, 035002, p. 035002. DOI: 10.1103/PhysRevLett.108.035002.

Birdsall, C.K. and A.B. Langdon (2004). *Plasma Physics via Computer Simulation*. Series in Plasma Physics and Fluid Dynamics. Taylor & Francis. URL: https://books.google.de/books?id=S2lqgDTm6a4C.

Blackman, E. G. and H. Ji (2006). "Laboratory plasma dynamos, astrophysical dynamos and magnetic helicity evolution". In: *MNRAS* 369.4, pp. 1837–1848. DOI: 10.1111/j.1365-2966.2006.10431.x.

Blandford, R. D. (1976). "Accretion disc electrodynamics - a model for double radio sources." In: *MNRAS* 176, pp. 465–481. DOI: 10.1093/mnras/176.3.465.

Blandford, R. D. and D. G. Payne (1982). "Hydromagnetic flows from accretion disks and the production of radio jets." In: *MNRAS* 199, pp. 883–903. DOI: 10.1093/mnras/199.4.883.

Blandford, R. D. and M. J. Rees (1974). "A "twin-exhaust" model for double radio sources." In: *MNRAS* 169, pp. 395–415. DOI: 10.1093/mnras/169.3.395.

Blandford, R. D. and R. L. Znajek (1977). "Electromagnetic extraction of energy from Kerr black holes." In: *MNRAS* 179, pp. 433–456. DOI: 10.1093/mnras/179.3.433.

Bodo, G. et al. (2014). "On the Convergence of Magnetorotational Turbulence in Stratified Isothermal Shearing Boxes". In: *ApJ Letters* 787.1, L13, p. L13. DOI: 10.1088/2041-8205/787/1/L13.

Bonanno, A., L. Rezzolla, and V. Urpin (2003). "Mean-field dynamo action in protoneutron stars". In: *A&A* 410, pp. L33–L36. DOI: 10.1051/0004-6361:20031459.

Boneva, D. V. et al. (2021). "Magnetic fields in the accretion disks for various inner boundary conditions". In: *A&A* 652, A38, A38. DOI: 10.1051/0004-6361/202038680.

Borges, R. et al. (2008). "An improved weighted essentially non-oscillatory scheme for hyperbolic conservation laws". In: *jcp* 227.6, pp. 3191–3211. DOI: 10.1016/j.jcp.2007.11.038.

Brandenburg, A., A. Nordlund, et al. (1995). "Dynamo-generated Turbulence and Large-Scale Magnetic Fields in a Keplerian Shear Flow". In: *ApJ* 446, p. 741. DOI: 10.1086/175831.

Brandenburg, A. and K. Subramanian (2005). "Astrophysical magnetic fields and nonlinear dynamo theory". In: *Physics Reports* 417.1-4, pp. 1–209. DOI: 10.1016/j.physrep.2005.06.005.

Bucciantini, N. and L. Del Zanna (2013). "A fully covariant mean-field dynamo closure for numerical 3 + 1 resistive GRMHD". In: *MNRAS* 428.1, pp. 71–85. DOI: 10.1093/mnras/sts005.

Bugli, M., L. Del Zanna, and N. Bucciantini (2014). "Dynamo action in thick discs around Kerr black holes: high-order resistive GRMHD simulations." In: *MNRAS* 440, pp. L41–L45. DOI: 10.1093/mnrasl/slu017.

Burnham, S. W. (1890). "Note on Hind's Variable Nebula in Taurus". In: *MNRAS* 51, p. 94. DOI: 10.1093/mnras/51.2.94.

Cabrit, S. and P. Andre (1991). "An Observational Connection between Circumstellar Disk Mass and Molecular Outflows". In: *ApJ Letters* 379, p. L25. DOI: 10.1086/186145.

Campbell, C. G. (1999). "Launching of accretion disc winds along dynamo-generated magnetic fields". In: *MNRAS* 310.4, pp. 1175–1184. DOI: 10.1046/j.1365-8711.1999.03073.x.

— (2009). "The stability of accretion discs with inflow driven purely by magnetic winds". In: *MNRAS* 392.1, pp. 271–280. DOI: 10.1111/j.1365-2966.2008.14035.x.

Carilli, C. L. and P. D. Barthel (1996). "Cygnus A". In: *A&A Rev.* 7.1, pp. 1–54. DOI: 10.1007/s001590050001.

Casse, F. and J. Ferreira (2000). "Magnetized accretion-ejection structures. IV. Magnetically-driven jets from resistive, viscous, Keplerian discs". In: *A&A* 353, pp. 1115–1128.

Casse, F. and R. Keppens (2002). "Magnetized Accretion-Ejection Structures: 2.5-dimensional Magnetohydrodynamic Simulations of Continuous Ideal Jet Launching from Resistive Accretion Disks". In: *ApJ* 581.2, pp. 988–1001. DOI: 10.1086/344340.

— (2004). "Radiatively Inefficient Magnetohydrodynamic Accretion-Ejection Structures". In: *ApJ* 601.1, pp. 90–103. DOI: 10.1086/380441.

Chabrier, G. and M. Küker (2006). "Large-scale α^2-dynamo in low-mass stars and brown dwarfs". In: *A&A* 446.3, pp. 1027–1037. DOI: 10.1051/0004-6361:20042475.

Chang, P., A. Spitkovsky, and J. Arons (2008). "Long-Term Evolution of Magnetic Turbulence in Relativistic Collisionless Shocks: Electron-Positron Plasmas". In: *ApJ* 674.1, pp. 378–387. DOI: 10.1086/524764.

Charbonneau, P. (2014). "Solar Dynamo Theory". In: *Annu. Rev. Astron. Astrophys* 52, pp. 251–290. DOI: 10.1146/annurev-astro-081913-040012.

Chiuderi, C. and M. Velli (2015). *Basics of Plasma Astrophysics*.

Colella, P. and Paul R. Woodward (1984). "The Piecewise Parabolic Method (PPM) for Gas-Dynamical Simulations". In: *Journal of Computational Physics* 54, pp. 174–201. DOI: 10.1016/0021-9991(84)90143-8.

Courant, R., K. Friedrichs, and H. Lewy (1928). "Über die partiellen Differenzengleichungen der mathematischen Physik". In: *Mathematische Annalen* 100, pp. 32–74. DOI: 10.1007/BF01448839.

Cowling, T. G. (1933). "The magnetic field of sunspots". In: *MNRAS* 94, pp. 39–48. DOI: 10.1093/mnras/94.1.39.

Curiel, S. et al. (2006). "Large Proper Motions in the Jet of the High-Mass YSO Cepheus A HW2". In: *ApJ* 638.2, pp. 878–886. DOI: 10.1086/498931.

Curtis, H. D. (1918). "Descriptions of 762 Nebulae and Clusters Photographed with the Crossley Reflector". In: *Publications of Lick Observatory* 13, pp. 9–42.

Davies, B. et al. (2010). "The circumstellar disc, envelope and bipolar outflow of the massive young stellar object W33A". In: *MNRAS* 402.3, pp. 1504–1515. DOI: 10.1111/j.1365-2966.2009.16077.x.

Davis, S. W., J. M. Stone, and M. E. Pessah (2010). "Sustained Magnetorotational Turbulence in Local Simulations of Stratified Disks with Zero Net Magnetic Flux". In: *ApJ* 713.1, pp. 52–65. DOI: 10.1088/0004-637X/713/1/52.

De Villiers, J. (2006). "Accretion Disks in Large-scale Magnetic Fields". In: *arXiv e-prints*, astro-ph/0605744, astro–ph/0605744.

De Villiers, J., J. F. Hawley, and J. H. Krolik (2003). "Magnetically Driven Accretion Flows in the Kerr Metric. I. Models and Overall Structure". In: *ApJ* 599.2, pp. 1238–1253. DOI: 10.1086/379509.

De Villiers, J., J. F. Hawley, J. H. Krolik, and S. Hirose (2005). "Magnetically Driven Accretion in the Kerr Metric. III. Unbound Outflows". In: *ApJ* 620.2, pp. 878–888. DOI: 10.1086/427142.

Dedner, A. et al. (2002). "Hyperbolic Divergence Cleaning for the MHD Equations". In: *Journal of Computational Physics* 175.2, pp. 645–673. DOI: 10.1006/jcph.2001.6961.

Del Zanna, L. and N. Bucciantini (2002). "An efficient shock-capturing central-type scheme for multidimensional relativistic flows. I. Hydrodynamics". In: *A&A* 390, pp. 1177–1186. DOI: 10.1051/0004-6361:20020776.

Del Zanna, L., N. Bucciantini, and P. Londrillo (2003). "An efficient shock-capturing central-type scheme for multidimensional relativistic flows. II. Magnetohydrodynamics". In: *A&A* 400, pp. 397–413. DOI: 10.1051/0004-6361:20021641. eprint: `astro-ph/0210618`.

Del Zanna, L., N. Tomei, et al. (2022). "General Relativistic Magnetohydrodynamics Mean-Field Dynamos". In: *Fluidika* 7.2, p. 87. DOI: `10.3390/fluids7020087`.

Del Zanna, L., O. Zanotti, et al. (2007). "ECHO: a Eulerian conservative high-order scheme for general relativistic magnetohydrodynamics and magnetodynamics". In: *A&A* 473, pp. 11–30. DOI: `10.1051/0004-6361:20077093`.

Dhang, P. et al. (2020). "Characterizing the dynamo in a radiatively inefficient accretion flow". In: *MNRAS* 494.4, pp. 4854–4866. DOI: `10.1093/mnras/staa996`.

Dhawan, V., I. F. Mirabel, and L. F. Rodríguez (2000). "AU-Scale Synchrotron Jets and Superluminal Ejecta in GRS 1915+105". In: *ApJ* 543.1, pp. 373–385. DOI: `10.1086/317088`.

Donat, R. and A. Marquina (1996). "Capturing Shock Reflections: An Improved Flux Formula". In: *Journal of Computational Physics* 125.1, pp. 42–58. DOI: `10.1006/jcph.1996.0078`.

Dopita, M. A., R. D. Schwartz, and I. Evans (1982). "Herbig-Haro objects 46 and 47: evidence for bipolar ejection from a young star." In: *ApJ Letters* 263, pp. L73–L77. DOI: `10.1086/183927`.

Dumbser, M. and D. S. Balsara (2016). "A new efficient formulation of the HLLEM Riemann solver for general conservative and non-conservative hyperbolic systems". In: *Journal of Computational Physics* 304, pp. 275–319. DOI: `10.1016/j.jcp.2015.10.014`.

Dyda, S. et al. (2018). "Magnetic field amplification via protostellar disc dynamos". In: *MNRAS* 477.1, pp. 127–138. DOI: `10.1093/mnras/sty614`.

Edge, D. O. et al. (1959). "A survey of radio sources at a frequency of 159 Mc/s." In: *memras* 68, pp. 37–60.

Einfeldt, B. et al. (1991). "On Godunov-type methods near low densities". In: *Journal of Computational Physics* 92, pp. 273–295. DOI: `10.1016/0021-9991(91)90211-3`.

Elstner, D., G. Ruediger, and M. Schultz (1996). "The non-linear galactic dynamo. II. Oscillatory versus steady solutions." In: *A&A* 306, p. 740.

Falcke, H., E. Körding, and S. Markoff (2004). "A scheme to unify low-power accreting black holes. Jet-dominated accretion flows and the radio/X-ray correlation". In: *A&A* 414, pp. 895–903. DOI: `10.1051/0004-6361:20031683`.

Fan, Y. and F. Fang (2014). "A Simulation of Convective Dynamo in the Solar Convective Envelope: Maintenance of the Solar-like Differential Rotation and Emerging Flux". In: *ApJ* 789.1, 35, p. 35. DOI: `10.1088/0004-637X/789/1/35`.

Fath, E. A. (1909). "The spectra of some spiral nebulae and globular star clusters". In: *Lick Observatory Bulletin* 149, pp. 71–77. DOI: `10.5479/ADS/bib/1909LicOB.5.71F`.

Federrath, C. et al. (2014). "The Turbulent Dynamo in Highly Compressible Supersonic Plasmas". In: *ApJ Letters* 797.2, L19, p. L19. DOI: `10.1088/2041-8205/797/2/L19`.

Felker, K. G. and J. M. Stone (2018). "A fourth-order accurate finite volume method for ideal MHD via upwind constrained transport". In: *Journal of Computational Physics* 375, pp. 1365–1400. DOI: `10.1016/j.jcp.2018.08.025`.

Fender, R. (2001). "Powerful jets from black hole X-ray binaries in low/hard X-ray states". In: *MNRAS* 322.1, pp. 31–42. DOI: 10.1046/j.1365-8711.2001.04080.x.

Fendt, C. (2003). "Magnetically driven outflows from Jovian circum-planetary accretion disks". In: *A&A* 411, pp. 623–635. DOI: 10.1051/0004-6361:20034154.

— (2006). "Collimation of Astrophysical Jets: The Role of the Accretion Disk Magnetic Field Distribution". In: *ApJ* 651.1, pp. 272–287. DOI: 10.1086/507976.

— (2009). "Formation of Protostellar Jets as Two-Component Outflows from Star-Disk Magnetospheres". In: *ApJ* 692.1, pp. 346–363. DOI: 10.1088/0004-637X/692/1/346.

Fendt, C. and M. Cemeljić (2002). "Formation of protostellar jets - effects of magnetic diffusion". In: *A&A* 395, pp. 1045–1060. DOI: 10.1051/0004-6361:20021442.

Fendt, C. and D. Elstner (1999). "Long-term evolution of a dipolar-type magnetosphere interacting with an accretion disk". In: *A&A* 349, pp. L61–L64.

— (2000). "Long-term evolution of a dipole type magnetosphere interacting with an accretion disk. II. Transition into a quasi-stationary spherically radial outflow". In: *A&A* 363, pp. 208–222.

Fendt, C. and D. Gaßmann (2018). "Bipolar Jets Launched by a Mean-field Accretion Disk Dynamo". In: *ApJ* 855.2, 130, p. 130. DOI: 10.3847/1538-4357/aab14c.

Fendt, C. and S. Sheikhnezami (2013). "Bipolar Jets Launched from Accretion Disks. II. The Formation of Asymmetric Jets and Counter Jets". In: *ApJ* 774.1, 12, p. 12. DOI: 10.1088/0004-637X/774/1/12.

Ferreira, J. and F. Casse (2013). "On fan-shaped cold MHD winds from Keplerian accretion discs". In: *MNRAS* 428.1, pp. 307–320. DOI: 10.1093/mnras/sts012.

Ferreira, J. and G. Pelletier (1995). "Magnetized accretion-ejection structures. III. Stellar and extragalactic jets as weakly dissipative disk outflows." In: *A&A* 295, p. 807.

Fleming, T. and J. M. Stone (2003). "Local Magnetohydrodynamic Models of Layered Accretion Disks". In: *ApJ* 585.2, pp. 908–920. DOI: 10.1086/345848.

Fleming, T. P., J. M. Stone, and J. F. Hawley (2000). "The Effect of Resistivity on the Nonlinear Stage of the Magnetorotational Instability in Accretion Disks". In: *ApJ* 530.1, pp. 464–477. DOI: 10.1086/308338.

Flock, M., Th. Henning, and H. Klahr (2012). "Turbulence in Weakly Ionized Protoplanetary Disks". In: *ApJ* 761.2, 95, p. 95. DOI: 10.1088/0004-637X/761/2/95.

Franceschetti, K. and L. Del Zanna (2020). "General Relativistic Mean-Field Dynamo Model for Proto-Neutron Stars". In: *Universe* 6.6, p. 83. DOI: 10.3390/universe6060083.

Frank, A. et al. (2014). "Jets and Outflows from Star to Cloud: Observations Confront Theory". In: *Protostars and Planets VI*. Ed. by Henrik Beuther et al., p. 451. DOI: 10.2458/azu_uapress_9780816531240-ch020.

Fromang, S. (2013). "MRI-driven angular momentum transport in protoplanetary disks". In: *EAS Publications Series*. Ed. by P. Hennebelle and C. Charbonnel. Vol. 62. EAS Publications Series, pp. 95–142. DOI: 10.1051/eas/1362004.

Fromang, S., P. Hennebelle, and R. Teyssier (2006). "A high order Godunov scheme with constrained transport and adaptive mesh refinement for astrophysical magnetohydrodynamics". In: *A&A* 457.2, pp. 371–384. DOI: 10.1051/0004-6361:20065371.

Fromang, S., C. Terquem, and S. A. Balbus (2002). "The ionization fraction in α models of protoplanetary discs". In: *MNRAS* 329.1, pp. 18–28. DOI: 10.1046/j.1365-8711.2002.04940.x.

Fruchter, A. S. et al. (1999). "Hubble Space Telescope and Palomar Imaging of GRB 990123: Implications for the Nature of Gamma-Ray Bursts and Their Hosts". In: *ApJ Letters* 519.1, pp. L13–L16. DOI: 10.1086/312094.

Fryxell, B. et al. (2000). "FLASH: An Adaptive Mesh Hydrodynamics Code for Modeling Astrophysical Thermonuclear Flashes". In: *ApJ Supplement* 131.1, pp. 273–334. DOI: 10.1086/317361.

Gailitis, A. et al. (2000). "Detection of a Flow Induced Magnetic Field Eigenmode in the Riga Dynamo Facility". In: *Phys. Rev. Lett.* 84.19, pp. 4365–4368. DOI: 10.1103/PhysRevLett.84.4365.

Gammie, C. F. (1996). "Layered Accretion in T Tauri Disks". In: *ApJ* 457, p. 355. DOI: 10.1086/176735.

Gammie, C. F., J. C. McKinney, and G. Tóth (2003). "HARM: A Numerical Scheme for General Relativistic Magnetohydrodynamics". In: *ApJ* 589, pp. 444–457. DOI: 10.1086/374594. eprint: astro-ph/0301509.

Gammie, C. F., S. L. Shapiro, and J. C. McKinney (2004). "Black Hole Spin Evolution". In: *ApJ* 602.1, pp. 312–319. DOI: 10.1086/380996.

Gardiner, T. A. and J. M. Stone (2005). "An unsplit Godunov method for ideal MHD via constrained transport". In: *Journal of Computational Physics* 205.2, pp. 509–539. DOI: 10.1016/j.jcp.2004.11.016.

Giacomazzo, B. and L. Rezzolla (2006). "The exact solution of the Riemann problem in relativistic magnetohydrodynamics". In: *Journal of Fluid Mechanics* 562, pp. 223–259. DOI: 10.1017/S0022112006001145. eprint: gr-qc/0507102.

Godunov, S. K. (1959). "A difference method for numerical calculation of discontinuous solutions of the equations of hydrodynamics". In: *Mat. Sb. (N.S.)* 47(89).3, pp. 271–306.

Goldstein, A. et al. (2017). "An Ordinary Short Gamma-Ray Burst with Extraordinary Implications: Fermi-GBM Detection of GRB 170817A". In: *ApJ Letters* 848.2, L14, p. L14. DOI: 10.3847/2041-8213/aa8f41.

Gorosabel, J. et al. (2005). "The GRB 030329 host: a blue low metallicity subluminous galaxy with intense star formation". In: *A&A* 444.3, pp. 711–721. DOI: 10.1051/0004-6361:20052768.

Gottlieb, S., C. Shu, and E. Tadmor (Jan. 2001). "Strong Stability-Preserving High-Order Time Discretization Methods". In: *SIAM Review* 43.1, pp. 89–112. DOI: 10.1137/S003614450036757X.

Gressel, O. (2010). "A mean-field approach to the propagation of field patterns in stratified magnetorotational turbulence". In: *MNRAS* 405.1, pp. 41–48. DOI: 10.1111/j.1365-2966.2010.16440.x.

— (2013). "Dynamo Effects in Magnetorotational Turbulence with Finite Thermal Diffusivity". In: *ApJ* 770.2, 100, p. 100. DOI: 10.1088/0004-637X/770/2/100.

Gressel, O. and D. Elstner (2020). "On the spatial and temporal non-locality of dynamo mean-field effects in supersonic interstellar turbulence". In: *MNRAS* 494.1, pp. 1180–1188. DOI: 10.1093/mnras/staa663.

Gressel, O. and M. E. Pessah (2015). "Characterizing the Mean-field Dynamo in Turbulent Accretion Disks". In: *ApJ* 810.1, 59, p. 59. DOI: 10.1088/0004-637X/810/1/59.

— (2022). "Finite-time Response of Dynamo Mean-field Effects in Magnetorotational Turbulence". In: *ApJ* 928.2, p. 118. DOI: 10.3847/1538-4357/ac56dd. URL: https://doi.org/10.3847/1538-4357/ac56dd.

Guan, X. and C. F. Gammie (2009). "The Turbulent Magnetic Prandtl Number of MHD Turbulence in Disks". In: *ApJ* 697.2, pp. 1901–1906. DOI: 10.1088/0004-637X/697/2/1901.

Haro, G. (1952). "Herbig's Nebulous Objects Near NGC 1999." In: *ApJ* 115, p. 572. DOI: 10.1086/145576.

— (1953). "Hα Emission Stars and Peculiar Objects in the Orion Nebula." In: *ApJ* 117, p. 73. DOI: 10.1086/145669.

Harten, A., P. Lax, and B. Leer (1983). "On Upstream Differencing and Godunov-Type Schemes for Hyperbolic Conservation Laws". In: *SIAM Review* 25.1, pp. 35–61. DOI: 10.1137/1025002. URL: https://doi.org/10.1137/1025002.

Hartigan, P. et al. (2001). "Proper Motions of the HH 111 Jet Observed with the Hubble Space Telescope". In: *ApJ Letters* 559.2, pp. L157–L161. DOI: 10.1086/323976.

Hawley, J. F. and S. A. Balbus (1991). "A Powerful Local Shear Instability in Weakly Magnetized Disks. II. Nonlinear Evolution". In: *ApJ* 376, p. 223. DOI: 10.1086/170271.

Hawley, J. F., C. Fendt, et al. (Oct. 2015). "Disks and Jets. Gravity, Rotation and Magnetic Fields". In: *Space Science Reviews* 191.1-4, pp. 441–469. DOI: 10.1007/s11214-015-0174-7.

Hawley, J. F., S. A. Richers, et al. (2013). "Testing Convergence for Global Accretion Disks". In: *ApJ* 772.2, 102, p. 102. DOI: 10.1088/0004-637X/772/2/102.

Hazard, C., M. B. Mackey, and A. J. Shimmins (1963). "Investigation of the Radio Source 3C 273 By The Method of Lunar Occultations". In: *Nature* 197.4872, pp. 1037–1039. DOI: 10.1038/1971037a0.

Herbig, G. H. (1950). "The Spectrum of the Nebulosity Surrounding T Tauri." In: *ApJ* 111, p. 11. DOI: 10.1086/145232.

— (1951). "The Spectra of Two Nebulous Objects Near NGC 1999." In: *ApJ* 113, pp. 697–699. DOI: 10.1086/145440.

— (1952). "Emission-line Stars in Galactic Nebulosities". In: *jrasc* 46, p. 222.

Herzenberg, A. (1958). "Geomagnetic Dynamos". In: *Philosophical Transactions of the Royal Society of London Series A* 250.986, pp. 543–583. DOI: 10.1098/rsta.1958.0007.

Hind, J. R. (1852). "Auszug aus einem Schreiben des Herrn Hind an die Redaction". In: *Astronomische Nachrichten* 35, p. 371. DOI: 10.1002/asna.18530352505.

Hirose, S. et al. (2004). "Magnetically Driven Accretion Flows in the Kerr Metric. II. Structure of the Magnetic Field". In: *ApJ* 606.2, pp. 1083–1097. DOI: 10.1086/383184.

Ho, L. C., A. V. Filippenko, and W. L. W. Sargent (1997). "A Search for "Dwarf" Seyfert Nuclei. V. Demographics of Nuclear Activity in Nearby Galaxies". In: *ApJ* 487.2, pp. 568–578. DOI: 10.1086/304638.

Hogg, J. D. and C. S. Reynolds (2018). "The Influence of Accretion Disk Thickness on the Large-scale Magnetic Dynamo". In: *ApJ* 861.1, 24, p. 24. DOI: 10.3847/1538-4357/aac439.

Homan, D. C. (2012). "Physical Properties of Jets in AGN". In: *International Journal of Modern Physics Conference Series*. Vol. 8. International Journal of Modern Physics Conference Series, pp. 163–171. DOI: 10.1142/S2010194512004552.

Honkkila, V. and P. Janhunen (2007). "HLLC solver for ideal relativistic MHD". In: *Journal of Computational Physics* 223.2, pp. 643–656. DOI: 10.1016/j.jcp.2006.09.027.

Hughes, M. P. (1965). "Radio Brightness Contours of 3C273". In: *Nature* 207.4993, pp. 178–179. DOI: 10.1038/207178a0.

Hurley, K. et al. (1994). "Detection of a γ-ray burst of very long duration and very high energy". In: *Nature* 372.6507, pp. 652–654. DOI: 10.1038/372652a0.

Isherwood, L., Z. J. Grant, and S Gottlieb (2018). "Strong Stability Preserving Integrating Factor Runge–Kutta Methods". In: *SIAM Journal on Numerical Analysis* 56.6, pp. 3276–3307. DOI: 10.1137/17M1143290. URL: https://doi.org/10.1137/17M1143290.

Ivanova, T. S. and A. A. Ruzmaikin (1977). "A nonlinear magnetohydrodynamic model of the solar dynamo". In: *Soviet Astronomy* 21, pp. 479–485.

Ivers, D. J. and R. W. James (1984). "Axisymmetric Antidynamo Theorems in Compressible Non-Uniform Conducting Fluids". In: *Philosophical Transactions of the Royal Society of London Series A* 312.1520, pp. 179–218. DOI: 10.1098/rsta.1984.0060.

Jacquemin-Ide, J., J. Ferreira, and G. Lesur (2019). "Magnetically driven jets and winds from weakly magnetized accretion discs". In: *MNRAS* 490.3, pp. 3112–3133. DOI: 10.1093/mnras/stz2749.

Jansky, Karl G. (1933). "Radio Waves from Outside the Solar System". In: *Nature* 132.3323, p. 66. DOI: 10.1038/132066a0.

Jorstad, S. G. et al. (2005). "Polarimetric Observations of 15 Active Galactic Nuclei at High Frequencies: Jet Kinematics from Bimonthly Monitoring with the Very Long Baseline Array". In: *Astronomical Journal* 130.4, pp. 1418–1465. DOI: 10.1086/444593.

Käpylä, M. J. et al. (2016). "Multiple dynamo modes as a mechanism for long-term solar activity variations". In: *A&A* 589, A56, A56. DOI: 10.1051/0004-6361/201527002.

Kato, Y. (2007). "Magnetic-Tower Jet Solution for Launching Astrophysical Jets". In: *Astrophysics and Space Science* 307.1-3, pp. 11–15. DOI: 10.1007/s10509-006-9220-y.

Kato, Y., S. Mineshige, and K. Shibata (2004). "Magnetohydrodynamic Accretion Flows: Formation of Magnetic Tower Jet and Subsequent Quasi-Steady State". In: *ApJ* 605.1, pp. 307–320. DOI: 10.1086/381234.

Keppens, R. et al. (2003). "Adaptive Mesh Refinement for conservative systems: multi-dimensional efficiency evaluation". In: *Computer Physics Communications* 153.3, pp. 317–339. DOI: 10.1016/S0010-4655(03)00139-5.

Kim, J. and D. S. Balsara (2014). "A stable HLLC Riemann solver for relativistic magnetohydrodynamics". In: *Journal of Computational Physics* 270, pp. 634–639. DOI: 10.1016/j.jcp.2014.04.023.

King, A. R., J. E. Pringle, and M. Livio (2007). "Accretion disc viscosity: how big is alpha?" In: *MNRAS* 376.4, pp. 1740–1746. DOI: 10.1111/j.1365-2966.2007.11556.x.

Kitchatinov, L. L., V. V. Pipin, and G. Ruediger (1994). "Turbulent viscosity, magnetic diffusivity, and heat conductivity under the influence of rotation and magnetic field". In: *Astronomische Nachrichten* 315.2, pp. 157–170. DOI: 10.1002/asna.2103150205.

Klebesadel, R. W., I. B. Strong, and R. A. Olson (1973). "Observations of Gamma-Ray Bursts of Cosmic Origin". In: *ApJ Letters* 182, p. L85. DOI: 10.1086/181225.

Koide, S. (2003). "Magnetic extraction of black hole rotational energy: Method and results of general relativistic magnetohydrodynamic simulations in Kerr spacetime". In: *Phys. Rev. D* 67.10, 104010, p. 104010. DOI: 10.1103/PhysRevD.67.104010.

Koide, S., K. Shibata, and T. Kudoh (1998). "General Relativistic Magnetohydrodynamic Simulations of Jets from Black Hole Accretions Disks: Two-Component Jets Driven by Nonsteady Accretion of Magnetized Disks". In: *ApJ Letters* 495.1, pp. L63–L66. DOI: 10.1086/311204.

— (1999). "Relativistic Jet Formation from Black Hole Magnetized Accretion Disks: Method, Tests, and Applications of a General RelativisticMagnetohydrodynamic Numerical Code". In: *ApJ* 522.2, pp. 727–752. DOI: 10.1086/307667.

Koide, S., K. Shibata, T. Kudoh, and D. L. Meier (2002). "Extraction of Black Hole Rotational Energy by a Magnetic Field and the Formation of Relativistic Jets". In: *Science* 295.5560, pp. 1688–1691. DOI: 10.1126/science.1068240.

Koldoba, A. V., O. A. Kuznetsov, and G. V. Ustyugova (2002). "An approximate Riemann solver for relativistic magnetohydrodynamics". In: *MNRAS* 333.4, pp. 932–942. DOI: 10.1046/j.1365-8711.2002.05474.x.

Komissarov, S. S. (1999). "A Godunov-type scheme for relativistic magnetohydrodynamics". In: *MNRAS* 303, pp. 343–366. DOI: 10.1046/j.1365-8711.1999.02244.x.

— (2001). "Direct numerical simulations of the Blandford-Znajek effect". In: *MNRAS* 326.3, pp. L41–L44. DOI: 10.1046/j.1365-8711.2001.04863.x.

— (2002). "Time-dependent, force-free, degenerate electrodynamics". In: *MNRAS* 336.3, pp. 759–766. DOI: 10.1046/j.1365-8711.2002.05313.x.

— (2004). "General relativistic magnetohydrodynamic simulations of monopole magnetospheres of black holes". In: *MNRAS* 350.4, pp. 1431–1436. DOI: 10.1111/j.1365-2966.2004.07738.x.

— (2007). "Multidimensional numerical scheme for resistive relativistic magnetohydrodynamics". In: *MNRAS* 382.3, pp. 995–1004. DOI: 10.1111/j.1365-2966.2007.12448.x.

— (2009). "Blandford-Znajek Mechanism versus Penrose Process". In: *Journal of Korean Physical Society* 54.61, p. 2503. DOI: 10.3938/jkps.54.2503.

Komissarov, Serguei and Oliver Porth (June 2021). "Numerical simulations of jets". In: *New Astronomy Reviews* 92, 101610, p. 101610. DOI: 10.1016/j.newar.2021.101610.

Krasnopolsky, R., Z. Li, and R. Blandford (1999). "Magnetocentrifugal Launching of Jets from Accretion Disks. I. Cold Axisymmetric Flows". In: *ApJ* 526.2, pp. 631–642. DOI: 10.1086/308023.

Krause, F. and K. -H. Raedler (1980). *Mean-field magnetohydrodynamics and dynamo theory*.

Kulsrud, R. M. (Jan. 1999). "A Critical Review of Galactic Dynamos". In: *Annu. Rev. Astron. Astrophys* 37, pp. 37–64. DOI: 10.1146/annurev.astro.37.1.37.

Lada, C. J. (1985). "Cold outflows, energetic winds, and enigmatic jets around young stellar objects." In: *araa* 23, pp. 267–317. DOI: 10.1146/annurev.aa.23.090185.001411.

Larmor, J. (1919). "How could a Rotating Body such as the Sun become a Magnet?" In: *Report of the British Association for the Advancement of Science* 1, pp. 159–160.

Lebedev, S. V. et al. (2005). "Magnetic tower outflows from a radial wire array Z-pinch". In: *MNRAS* 361.1, pp. 97–108. DOI: 10.1111/j.1365-2966.2005.09132.x.

Lee, C. et al. (2018). "Unveiling a magnetized jet from a low-mass protostar". In: *Nature Communications* 9, 4636, p. 4636. DOI: 10.1038/s41467-018-07143-8.

LeVeque, R.J. et al. (1998). *Computational Methods for Astrophysical Fluid Flow: Saas-Fee Advanced Course 27. Lecture Notes 1997 Swiss Society for Astrophysics and Astronomy*. Saas-Fee Advanced Course. Springer Berlin Heidelberg. URL: https://books.google.de/books?id=ZdjImbOLi9gC.

Li, S. (2005). "An HLLC Riemann solver for magneto-hydrodynamics". In: *Journal of Computational Physics* 203.1, pp. 344–357. DOI: 10.1016/j.jcp.2004.08.020.

Lichnerowicz, A. (1976). "Shock waves in relativistic magnetohydrodynamics under general assumptions". In: *Journal of Mathematical Physics* 17, pp. 2135–2142. DOI: 10.1063/1.522857.

LIGO Scientific Collaboration and Virgo Collaboration (2017a). "GW170817: Observation of Gravitational Waves from a Binary Neutron Star Inspiral". In: *Phys. Rev. Lett.* 119.16, 161101, p. 161101. DOI: 10.1103/PhysRevLett.119.161101.

— (2017b). "GW170817: Observation of Gravitational Waves from a Binary Neutron Star Inspiral". In: *Phys. Rev. Lett.* 119.16, 161101, p. 161101. DOI: 10.1103/PhysRevLett.119.161101.

Liska, M., K. Chatterjee, et al. (2019). "H-AMR: A New GPU-accelerated GRMHD Code for Exascale Computing With 3D Adaptive Mesh Refinement and Local Adaptive Time-stepping". In: *arXiv e-prints*, arXiv:1912.10192, arXiv:1912.10192.

Liska, M., A. Tchekhovskoy, and E. Quataert (2020). "Large-scale poloidal magnetic field dynamo leads to powerful jets in GRMHD simulations of black hole accretion with toroidal field". In: *MNRAS* 494.3, pp. 3656–3662. DOI: 10.1093/mnras/staa955.

Liska, M. T. P. et al. (2022). "Formation of Magnetically Truncated Accretion Disks in 3D Radiation-Transport Two-Temperature GRMHD Simulations". In: *arXiv e-prints*, arXiv:2201.03526, arXiv:2201.03526.

Lister, M. L., M. H. Cohen, et al. (2009). "MOJAVE: Monitoring of Jets in Active Galactic Nuclei with VLBA Experiments. VI. Kinematics Analysis of a Complete Sample of Blazar Jets". In: *Astronomical Journal* 138.6, pp. 1874–1892. DOI: 10.1088/0004-6256/138/6/1874.

Lister, M. L. and A. P. Marscher (1997). "Statistical Effects of Doppler Beaming and Malmquist Bias on Flux-limited Samples of Compact Radio Sources". In: *ApJ* 476.2, pp. 572–588. DOI: 10.1086/303629.

Londrillo, P. and L. del Zanna (2004). "On the divergence-free condition in Godunov-type schemes for ideal magnetohydrodynamics: the upwind constrained transport method". In: *Journal of Computational Physics* 195.1, pp. 17–48. DOI: 10.1016/j.jcp.2003.09.016.

Lynden-Bell, D. (1996). "Magnetic collimation by accretion discs of quasars and stars". In: *MNRAS* 279.2, pp. 389–401. DOI: 10.1093/mnras/279.2.389.

— (2003). "On why discs generate magnetic towers and collimate jets". In: *MNRAS* 341.4, pp. 1360–1372. DOI: 10.1046/j.1365-8711.2003.06506.x.

Lynden-Bell, D. and C. Boily (1994). "Self-Similar Solutions up to Flashpoint in Highly Wound Magnetostatics". In: *MNRAS* 267, p. 146. DOI: 10.1093/mnras/267.1.146.

MacNeice, P. et al. (2000). "PARAMESH: A parallel adaptive mesh refinement community toolkit". In: *Computer Physics Communications* 126.3, pp. 330–354. DOI: 10.1016/S0010-4655(99)00501-9.

Maiolino, R. and G. H. Rieke (1995). "Low-Luminosity and Obscured Seyfert Nuclei in Nearby Galaxies". In: *ApJ* 454, p. 95. DOI: 10.1086/176468.

Markoff, S. et al. (2008). "Results from an Extensive Simultaneous Broadband Campaign on the Underluminous Active Nucleus M81*: Further Evidence for Mass-scaling Accretion in Black Holes". In: *ApJ* 681.2, pp. 905–924. DOI: 10.1086/588718.

Martí, J. M. (2015). "On the correction of conserved variables for numerical RMHD with staggered constrained transport". In: *Computer Physics Communications* 191, pp. 100–105. DOI: 10.1016/j.cpc.2015.02.004.

Martí, J. M. and E. Müller (2015). "Grid-based Methods in Relativistic Hydrodynamics and Magnetohydrodynamics". In: *Living Reviews in Computational Astrophysics* 1.1, 3, p. 3. DOI: 10.1007/lrca-2015-3.

Matt, S. and R. E. Pudritz (2005). "Accretion-powered Stellar Winds as a Solution to the Stellar Angular Momentum Problem". In: *ApJ Letters* 632.2, pp. L135–L138. DOI: 10.1086/498066.

Mattia, G. and C. Fendt (2020a). "Magnetohydrodynamic Accretion-Ejection: Jets Launched by a Nonisotropic Accretion-disk Dynamo. I. Validation and Application of Selected Dynamo Tensorial Components". In: *ApJ* 900.1, 59, p. 59. DOI: 10.3847/1538-4357/aba9d7.

— (2020b). "Magnetohydrodynamic Accretion-Ejection: Jets Launched by a Nonisotropic Accretion-disk Dynamo. II. A Dynamo Tensor Defined by the Disk Coriolis Number". In: *ApJ* 900.1, 60, p. 60. DOI: 10.3847/1538-4357/aba9d6.

— (2022). "Jets from Accretion Disk Dynamos: Consistent Quenching Modes for Dynamo and Resistivity". In: *Submitted to ApJ*.

Mattia, G. and A. Mignone (2022). "A comparison of Approximate non-Linear Riemann Solvers for Relativistic MHD". In: *MNRAS* 510.1, pp. 481–499. DOI: 10.1093/mnras/stab3373.

Mazets, E. P. et al. (1981). "Catalog of cosmic gamma-ray bursts from the KONUS experiment data". In: *Astrophysics and Space Science* 80.1, pp. 3–83. DOI: 10.1007/BF00649140.

McCorquodale, P. and P. Colella (2011). "A high-order finite-volume method for conservation laws on locally refined grids". In: *Communications in Applied Mathematics and Computational Science* 6. DOI: 10.2140/camcos.2011.6.1.

McKinney, J. C. (2006). "General relativistic magnetohydrodynamic simulations of the jet formation and large-scale propagation from black hole accretion systems". In: *MNRAS* 368.4, pp. 1561–1582. DOI: `10.1111/j.1365-2966.2006.10256.x`.

McKinney, J. C. and R. D. Blandford (2009). "Stability of relativistic jets from rotating, accreting black holes via fully three-dimensional magnetohydrodynamic simulations". In: *MNRAS* 394.1, pp. L126–L130. DOI: `10.1111/j.1745-3933.2009.00625.x`.

McKinney, J. C., L. Dai, and M. J. Avara (2015). "Efficiency of super-Eddington magnetically-arrested accretion". In: *MNRAS* 454.1, pp. L6–L10. DOI: `10.1093/mnrasl/slv115`.

McKinney, J. C. and C. F. Gammie (2004). "A Measurement of the Electromagnetic Luminosity of a Kerr Black Hole". In: *ApJ* 611.2, pp. 977–995. DOI: `10.1086/422244`.

McKinney, J. C. and R. Narayan (2007). "Disc-jet coupling in black hole accretion systems - I. General relativistic magnetohydrodynamical models". In: *MNRAS* 375.2, pp. 513–530. DOI: `10.1111/j.1365-2966.2006.11301.x`.

McKinney, J. C., A. Tchekhovskoy, and R. D. Blandford (2012). "General relativistic magnetohydrodynamic simulations of magnetically choked accretion flows around black holes". In: *MNRAS* 423.4, pp. 3083–3117. DOI: `10.1111/j.1365-2966.2012.21074.x`.

McKinney, J. C., A. Tchekhovskoy, A. Sadowski, et al. (2014). "Three-dimensional general relativistic radiation magnetohydrodynamical simulation of super-Eddington accretion, using a new code HARMRAD with M1 closure". In: *MNRAS* 441.4, pp. 3177–3208. DOI: `10.1093/mnras/stu762`.

Meegan, C. A. et al. (1995). "Do Gamma-Ray Burst Sources Repeat?" In: *ApJ Letters* 446, p. L15. DOI: `10.1086/187919`.

Melon Fuksman, J. D. and A. Mignone (2019). "A Radiative Transfer Module for Relativistic Magnetohydrodynamics in the PLUTO Code". In: *ApJ Supplement* 242.2, 20, p. 20. DOI: `10.3847/1538-4365/ab18ff`.

Merloni, A., S. Heinz, and T. di Matteo (2003). "A Fundamental Plane of black hole activity". In: *MNRAS* 345.4, pp. 1057–1076. DOI: `10.1046/j.1365-2966.2003.07017.x`.

Mészáros, P. (2001). "Gamma-Ray Bursts: Accumulating Afterglow Implications, Progenitor Clues, and Prospects". In: *Science* 291.5501, pp. 79–84. DOI: `10.1126/science.291.5501.79`.

Mignone, A. (2014). "High-order conservative reconstruction schemes for finite volume methods in cylindrical and spherical coordinates". In: *Journal of Computational Physics* 270, pp. 784–814. DOI: `10.1016/j.jcp.2014.04.001`.

Mignone, A. and G. Bodo (2005). "An HLLC Riemann solver for relativistic flows - I. Hydrodynamics". In: *MNRAS* 364, pp. 126–136. DOI: `10.1111/j.1365-2966.2005.09546.x`. eprint: `astro-ph/0506414`.

— (2006). "An HLLC Riemann solver for relativistic flows - II. Magnetohydrodynamics". In: *MNRAS* 368, pp. 1040–1054. DOI: `10.1111/j.1365-2966.2006.10162.x`. eprint: `astro-ph/0601640`.

Mignone, A., G. Bodo, S. Massaglia, et al. (2007). "PLUTO: A Numerical Code for Computational Astrophysics". In: *ApJ Supplement* 170.1, pp. 228–242. DOI: `10.1086/513316`.

Mignone, A., G. Bodo, B. Vaidya, et al. (2018). "A Particle Module for the PLUTO Code. I. An Implementation of the MHD-PIC Equations". In: *ApJ* 859.1, 13, p. 13. DOI: 10.3847/1538-4357/aabccd.

Mignone, A. and L. Del Zanna (2021). "Systematic construction of upwind constrained transport schemes for MHD". In: *Journal of Computational Physics* 424, 109748, p. 109748. DOI: 10.1016/j.jcp.2020.109748.

Mignone, A., M. Flock, and B. Vaidya (2019). "A Particle Module for the PLUTO Code. III. Dust". In: *ApJ Supplement* 244.2, 38, p. 38. DOI: 10.3847/1538-4365/ab4356.

Mignone, A. and Jonathan C. McKinney (2007). "Equation of state in relativistic magnetohydrodynamics: variable versus constant adiabatic index". In: *MNRAS* 378.3, pp. 1118–1130. DOI: 10.1111/j.1365-2966.2007.11849.x.

Mignone, A., P. Tzeferacos, and G. Bodo (2010). "High-order conservative finite difference GLM-MHD schemes for cell-centered MHD". In: *Journal of Computational Physics* 229.17, pp. 5896–5920. DOI: 10.1016/j.jcp.2010.04.013.

Mignone, A., M. Ugliano, and G. Bodo (2009). "A five-wave Harten-Lax-van Leer Riemann solver for relativistic magnetohydrodynamics". In: *MNRAS* 393, pp. 1141–1156. DOI: 10.1111/j.1365-2966.2008.14221.x. arXiv: 0811.1483.

Mignone, A., B. Vaidya, et al. (2020). "Particle-Gas Hybrid Schemes in the PLUTO Code". In: *Journal of Physics Conference Series*. Vol. 1623. Journal of Physics Conference Series, p. 012007. DOI: 10.1088/1742-6596/1623/1/012007.

Mignone, A., C. Zanni, et al. (2012). "The PLUTO Code for Adaptive Mesh Computations in Astrophysical Fluid Dynamics". In: *ApJ Supplement* 198.1, 7, p. 7. DOI: 10.1088/0067-0049/198/1/7.

Mimica, P. et al. (2009). "Spectral Evolution of Superluminal Components in Parsec-Scale Jets". In: *ApJ* 696.2, pp. 1142–1163. DOI: 10.1088/0004-637X/696/2/1142.

Mirabel, I. F. and L. F. Rodríguez (1994). "A superluminal source in the Galaxy". In: *Nature* 371.6492, pp. 46–48. DOI: 10.1038/371046a0.

— (1998). "Microquasars in our Galaxy". In: *Nature* 392.6677, pp. 673–676. DOI: 10.1038/33603.

— (1999). "Sources of Relativistic Jets in the Galaxy". In: *araa* 37, pp. 409–443. DOI: 10.1146/annurev.astro.37.1.409.

Miyoshi, T. and K. Kusano (2005). "A multi-state HLL approximate Riemann solver for ideal magnetohydrodynamics". In: *Journal of Computational Physics* 208.1, pp. 315–344. DOI: 10.1016/j.jcp.2005.02.017.

Moffatt, H. K. (1978). *Magnetic field generation in electrically conducting fluids*.

Monchaux, R. et al. (2007). "Generation of a Magnetic Field by Dynamo Action in a Turbulent Flow of Liquid Sodium". In: *Phys. Rev. Lett.* 98.4, 044502, p. 044502. DOI: 10.1103/PhysRevLett.98.044502.

Moss, D. and A. Shukurov (1996). "Turbulence and magnetic fields in elliptical galaxies." In: *MNRAS* 279.1, pp. 229–239. DOI: 10.1093/mnras/279.1.229.

Moss, D., D. Sokoloff, and V. Suleimanov (2016). "Dynamo generated magnetic configurations in accretion discs and the nature of quasi-periodic oscillations in accreting binary systems". In: *A&A* 588, A18, A18. DOI: 10.1051/0004-6361/201525944.

Mundt, R. and J. W. Fried (1983). "Jets from young stars." In: *ApJ Letters* 274, pp. L83–L86. DOI: 10.1086/184155.

Murphy, G. C., J. Ferreira, and C. Zanni (2010). "Large scale magnetic fields in viscous resistive accretion disks. I. Ejection from weakly magnetized disks". In: *A&A* 512, A82, A82. DOI: 10.1051/0004-6361/200912633.

Nathanail, A. et al. (2022). "Magnetic reconnection and plasmoid formation in three-dimensional accretion flows around black holes". In: *MNRAS*. DOI: 10.1093/mnras/stac1118.

Nauman, F. and E. G. Blackman (2015). "Sensitivity of the magnetorotational instability to the shear parameter in stratified simulations". In: *MNRAS* 446.2, pp. 2102–2109. DOI: 10.1093/mnras/stu2226.

Noble, Scott C. et al. (2006). "Primitive Variable Solvers for Conservative General Relativistic Magnetohydrodynamics". In: *ApJ* 641.1, pp. 626–637. DOI: 10.1086/500349.

Noh, W. F. (1987). "Errors for Calculations of Strong Shocks Using an Artificial Viscosity and an Artificial Heat Flux". In: *Journal of Computational Physics* 72.1, pp. 78–120. DOI: 10.1016/0021-9991(87)90074-X.

O'Sullivan, S. P. and D. C. Gabuzda (2009). "Magnetic field strength and spectral distribution of six parsec-scale active galactic nuclei jets". In: *MNRAS* 400.1, pp. 26–42. DOI: 10.1111/j.1365-2966.2009.15428.x.

Olivares, H. et al. (2019). "Constrained transport and adaptive mesh refinement in the Black Hole Accretion Code". In: *A&A* 629, A61, A61. DOI: 10.1051/0004-6361/201935559.

Ouyed, R. and R. E. Pudritz (1997). "Numerical Simulations of Astrophysical Jets from Keplerian Disks. I. Stationary Models". In: *ApJ* 482.2, pp. 712–732. DOI: 10.1086/304170.

Palenzuela, C. et al. (2009). "Beyond ideal MHD: towards a more realistic modelling of relativistic astrophysical plasmas". In: *MNRAS* 394.4, pp. 1727–1740. DOI: 10.1111/j.1365-2966.2009.14454.x.

Parker, E. N. (1955). "Hydromagnetic Dynamo Models." In: *ApJ* 122, p. 293. DOI: 10.1086/146087.

Parkin, E. R. and G. V. Bicknell (2013). "Global simulations of magnetorotational turbulence - I. Convergence and the quasi-steady state". In: *MNRAS* 435.3, pp. 2281–2298. DOI: 10.1093/mnras/stt1450.

Pelletier, G. and R. E. Pudritz (1992). "Hydromagnetic Disk Winds in Young Stellar Objects and Active Galactic Nuclei". In: *ApJ* 394, p. 117. DOI: 10.1086/171565.

Pencil Code Collaboration et al. (2021). "The Pencil Code, a modular MPI code for partial differential equations and particles: multipurpose and multiuser-maintained". In: *The Journal of Open Source Software* 6.58, 2807, p. 2807. DOI: 10.21105/joss.02807.

Penrose, R. and R. M. Floyd (1971). "Extraction of Rotational Energy from a Black Hole". In: *NPS* 229.6, pp. 177–179. DOI: 10.1038/physci229177a0.

Perri, B. et al. (2021). "Dynamical Coupling of a Mean-field Dynamo and Its Wind: Feedback Loop over a Stellar Activity Cycle". In: *ApJ* 910.1, 50, p. 50. DOI: 10.3847/1538-4357/abe2ac.

Pinilla, P. et al. (2016). "Can dead zones create structures like a transition disk?" In: *A&A* 596, A81, A81. DOI: 10.1051/0004-6361/201628441.

Piran, T. (2004). "The physics of gamma-ray bursts". In: *Reviews of Modern Physics* 76.4, pp. 1143–1210. DOI: 10.1103/RevModPhys.76.1143.

Ponomarenko, Y. B. (1973). "Theory of the hydromagnetic generator". In: *JAMTP* 14.6, pp. 775–778. DOI: 10.1007/BF00853190.

Porth, O., K. Chatterjee, et al. (2019). "The Event Horizon General Relativistic Magnetohydrodynamic Code Comparison Project". In: *ApJ Supplement* 243.2, 26, p. 26. DOI: 10.3847/1538-4365/ab29fd.

Porth, O., H. Olivares, et al. (2017). "The black hole accretion code". In: *Computational Astrophysics and Cosmology* 4.1, 1, p. 1. DOI: 10.1186/s40668-017-0020-2.

Porth, O., C. Xia, et al. (2014). "MPI-AMRVAC for Solar and Astrophysics". In: *ApJ Supplement* 214.1, 4, p. 4. DOI: 10.1088/0067-0049/214/1/4.

Press, W. H. et al. (1992). *Numerical recipes in C. The art of scientific computing.*

Price, P. A. et al. (2003). "The bright optical afterglow of the nearby γ-ray burst of 29 March 2003". In: *Nature* 423.6942, pp. 844–847. DOI: 10.1038/nature01734.

Pudritz, R. E. (1981a). "Dynamo Action in Turbulent Accretion Discs around Black Holes - Part Two - the Mean Magnetic Field". In: *MNRAS* 195, p. 897. DOI: 10.1093/mnras/195.4.897.

— (1981b). "Dynamo action in turbulent accretion discs around black holes. I - The fluctuations. II - The mean magnetic field". In: *MNRAS* 195, pp. 881–914. DOI: 10.1093/mnras/195.4.881.

Pudritz, R. E. and T. P. Ray (2019). "The Role of Magnetic Fields in Protostellar Outflows and Star Formation". In: *Frontiers in Astronomy and Space Sciences* 6, 54, p. 54. DOI: 10.3389/fspas.2019.00054.

Pudritz, R. E., C. S. Rogers, and R. Ouyed (2006). "Controlling the collimation and rotation of hydromagnetic disc winds". In: *MNRAS* 365.4, pp. 1131–1148. DOI: 10.1111/j.1365-2966.2005.09766.x.

Punch, M. et al. (1992). "Detection of TeV photons from the active galaxy Markarian 421". In: *Nature* 358.6386, pp. 477–478. DOI: 10.1038/358477a0.

Punsly, B., D. Balsara, et al. (2016). "Riemann solvers and Alfven waves in black hole magnetospheres". In: *Computational Astrophysics and Cosmology* 3.1, 5, p. 5. DOI: 10.1186/s40668-016-0018-1.

Punsly, B. and F. V. Coroniti (1990). "Relativistic Winds from Pulsar and Black Hole Magnetospheres". In: *ApJ* 350, p. 518. DOI: 10.1086/168408.

Puzzoni, E., A. Mignone, and G. Bodo (2021). "On the impact of the numerical method on magnetic reconnection and particle acceleration - I. The MHD case". In: *MNRAS* 508.2, pp. 2771–2783. DOI: 10.1093/mnras/stab2813.

Qian, Q., C. Fendt, and C. Vourellis (2018). "Jet Launching in Resistive GR-MHD Black Hole-Accretion Disk Systems". In: *ApJ* 859.1, 28, p. 28. DOI: 10.3847/1538-4357/aabd36.

Qiu, K. et al. (2019). "CO Multi-line Observations of HH 80-81: A Two-component Molecular Outflow Associated with the Largest Protostellar Jet in Our Galaxy". In: *ApJ* 871.2, 141, p. 141. DOI: 10.3847/1538-4357/aaf728.

Ray, T. et al. (2007). "Toward Resolving the Outflow Engine: An Observational Perspective". In: *Protostars and Planets V*. Ed. by Bo Reipurth, David Jewitt, and Klaus Keil, p. 231.

Ray, T. P. and J. Ferreira (2021). "Jets from young stars". In: *New Astronomy Reviews* 93, 101615, p. 101615. DOI: 10.1016/j.newar.2021.101615.

Rayburn, D. R. (1977). "A numerical study of the continuous beam model of extragalactic radio sources." In: *MNRAS* 179, pp. 603–617. DOI: 10.1093/mnras/179.4.603.

Reipurth, B., J. Bally, and D. Devine (1997). "Giant Herbig-Haro Flows". In: *Astronomical Journal* 114, p. 2708. DOI: 10.1086/118681.

Rekowski, M. v., G. Rüdiger, and D. Elstner (2000). "Structure and magnetic configurations of accretion disk-dynamo models". In: *A&A* 353, pp. 813–822.

Ressler, S. M. et al. (2015). "Electron thermodynamics in GRMHD simulations of low-luminosity black hole accretion". In: *MNRAS* 454.2, pp. 1848–1870. DOI: 10.1093/mnras/stv2084.

Rincon, F. (2019). "Dynamo theories". In: *Journal of Plasma Physics* 85.4, 205850401, p. 205850401. DOI: 10.1017/S0022377819000539.

Riols, A. and H. Latter (2018). "Magnetorotational instability and dynamo action in gravito-turbulent astrophysical discs". In: *MNRAS* 474.2, pp. 2212–2232. DOI: 10.1093/mnras/stx2455.

Ripperda, B., F. Bacchini, and A. A. Philippov (2020). "Magnetic Reconnection and Hot Spot Formation in Black Hole Accretion Disks". In: *ApJ* 900.2, 100, p. 100. DOI: 10.3847/1538-4357/ababab.

Ripperda, B., M. Liska, et al. (2022). "Black Hole Flares: Ejection of Accreted Magnetic Flux through 3D Plasmoid-mediated Reconnection". In: *ApJ Letters* 924.2, L32, p. L32. DOI: 10.3847/2041-8213/ac46a1.

Roe, P. L. (1986). "Characteristic-based schemes for the euler equations". In: *Annual Review of Fluid Mechanics* 18, pp. 337–365. DOI: 10.1146/annurev.fl.18.010186.002005.

Romero, G. E. et al. (2017). "Relativistic Jets in Active Galactic Nuclei and Microquasars". In: *Space Science Reviews* 207.1-4, pp. 5–61. DOI: 10.1007/s11214-016-0328-2.

Rüdiger, G. et al. (1994). "Dynamo models with magnetic diffusivity-quenching". In: *Geophysical and Astrophysical Fluid Dynamics* 78.1, pp. 247–259. DOI: 10.1080/03091929408226581.

Ruediger, G., D. Elstner, and T. F. Stepinski (1995). "The standard-accretion disk dynamo." In: *A&A* 298, p. 934.

Ruediger, G. and L. L. Kichatinov (1993). "Alpha-effect and alpha-quenching". In: *A&A* 269.1-2, pp. 581–588.

Ruiz, M. et al. (2012). "The role of the ergosphere in the Blandford–Znajek process". In: *Monthly Notices of the Royal Astronomical Society* 423.2, pp. 1300–1308. DOI: 10.1111/j.1365-2966.2012.20950.x. eprint: https://academic.oup.com/mnras/article-pdf/423/2/1300/2849453/mnras0423-1300.pdf. URL: https://doi.org/10.1111/j.1365-2966.2012.20950.x.

Ryan, B. R. et al. (2017). "Resolution Dependence of Magnetorotational Turbulence in the Isothermal Stratified Shearing Box". In: *ApJ* 840.1, 6, p. 6. DOI: 10.3847/1538-4357/aa6a52.

Sądowski, A., R. Narayan, et al. (2015). "Global simulations of axisymmetric radiative black hole accretion discs in general relativity with a mean-field magnetic dynamo". In: *MNRAS* 447.1, pp. 49–71. DOI: 10.1093/mnras/stu2387.

Sądowski, A., M. Wielgus, et al. (2017). "Radiative, two-temperature simulations of low-luminosity black hole accretion flows in general relativity". In: *MNRAS* 466.1, pp. 705–725. DOI: 10.1093/mnras/stw3116.

Salvesen, G. et al. (2016). "Accretion disc dynamo activity in local simulations spanning weak-to-strong net vertical magnetic flux regimes". In: *MNRAS* 457.1, pp. 857–874. DOI: 10.1093/mnras/stw029.

Sandage, A. (1965). "The Existence of a Major New Constituent of the Universe: the Quasistellar Galaxies." In: *ApJ* 141, p. 1560. DOI: 10.1086/148245.

Sano, T. et al. (2000). "Magnetorotational Instability in Protoplanetary Disks. II. Ionization State and Unstable Regions". In: *ApJ* 543.1, pp. 486–501. DOI: 10.1086/317075.

Scheuer, P. A. G. (1974). "Models of extragalactic radio sources with a continuous energy supply from a central object". In: *MNRAS* 166, pp. 513–528. DOI: 10.1093/mnras/166.3.513.

Schmidt, M. (1963). "3C 273 : A Star-Like Object with Large Red-Shift". In: *Nature* 197.4872, p. 1040. DOI: 10.1038/1971040a0.

Schmitt, J. L. (n.d.). "BL Lac identified as a Radio Source". In: *Nature* 218.5142 (), p. 663. DOI: 10.1038/218663a0.

Schober, J., D. Schleicher, S. Bovino, et al. (2012). "Small-scale dynamo at low magnetic Prandtl numbers". In: *Phys. Rev. E* 86.6, 066412, p. 066412. DOI: 10.1103/PhysRevE.86.066412.

Schober, J., D. Schleicher, C. Federrath, S. Glover, et al. (2012). "The Small-scale Dynamo and Non-ideal Magnetohydrodynamics in Primordial Star Formation". In: *ApJ* 754.2, 99, p. 99. DOI: 10.1088/0004-637X/754/2/99.

Schober, J., D. Schleicher, C. Federrath, R. Klessen, et al. (2012). "Magnetic field amplification by small-scale dynamo action: Dependence on turbulence models and Reynolds and Prandtl numbers". In: *Phys. Rev. E* 85.2, 026303, p. 026303. DOI: 10.1103/PhysRevE.85.026303.

Schober, J., D. R. G. Schleicher, C. Federrath, et al. (2015). "Saturation of the turbulent dynamo". In: *Phys. Rev. E* 92.2, 023010, p. 023010. DOI: 10.1103/PhysRevE.92.023010.

Schober, J., D. R. G. Schleicher, and R. S. Klessen (2013). "Magnetic field amplification in young galaxies". In: *A&A* 560, A87, A87. DOI: 10.1051/0004-6361/201322185.

Schultz, M., D. Elstner, and G. Ruediger (1994). "The non-linear galactic dynamo I. Field strength and vertical parity". In: *A&A* 286, pp. 72–79.

Schwartz, R. D. (1975). "T Tauri nebulae and Herbig-Haro nebulae: evidence for excitation by a strong stellar wind." In: *ApJ* 195, pp. 631–642. DOI: 10.1086/153364.

— (1977). "Evidence of star formation triggered by expansion of the Gum Nebula." In: *ApJ Letters* 212, pp. L25–L26. DOI: 10.1086/182367.

Seyfert, C. K. (1943). "Nuclear Emission in Spiral Nebulae." In: *ApJ* 97, p. 28. DOI: 10.1086/144488.

Shakura, N. I. and R. A. Sunyaev (1973). "Reprint of 1973A&A....24..337S. Black holes in binary systems. Observational appearance." In: *A&A* 500, pp. 33–51.

Sharda, P. et al. (2021). "Magnetic field amplification in accretion discs around the first stars: implications for the primordial IMF". In: *MNRAS* 503.2, pp. 2014–2032. DOI: 10.1093/mnras/stab531.

Sheikhnezami, S. et al. (2012). "Bipolar Jets Launched from Magnetically Diffusive Accretion Disks. I. Ejection Efficiency versus Field Strength and Diffusivity". In: *ApJ* 757.1, 65, p. 65. DOI: 10.1088/0004-637X/757/1/65.

Shi, J., J. H. Krolik, and S. Hirose (2010). "What is the Numerically Converged Amplitude of Magnetohydrodynamics Turbulence in Stratified Shearing Boxes?" In: *ApJ* 708.2, pp. 1716–1727. DOI: 10.1088/0004-637X/708/2/1716.

Shi, J., J. M. Stone, and C. X. Huang (2016). "Saturation of the magnetorotational instability in the unstratified shearing box with zero net flux: convergence in taller boxes". In: *MNRAS* 456.3, pp. 2273–2289. DOI: 10.1093/mnras/stv2815.

Shibata, K. and Y. Uchida (1985). "A magnetodynamic mechanism for the formation of astrophysical jets. I - Dynamical effects of the relaxation of nonlinear magnetic twists". In: *Astronomical Society of Japan* 37.1, pp. 31–46.

Shiokawa, H. et al. (2012). "Global General Relativistic Magnetohydrodynamic Simulations of Black Hole Accretion Flows: A Convergence Study". In: *ApJ* 744.2, 187, p. 187. DOI: 10.1088/0004-637X/744/2/187.

Shklovskii, I. S. (1953). In: *Akademiia Nauk SSSR Doklady* 90, p. 983.

Shu, F. et al. (1994). "Magnetocentrifugally Driven Flows from Young Stars and Disks. I. A Generalized Model". In: *ApJ* 429, p. 781. DOI: 10.1086/174363.

Sironi, L. and A. Spitkovsky (2014). "Relativistic Reconnection: An Efficient Source of Non-thermal Particles". In: *ApJ Letters* 783.1, L21, p. L21. DOI: 10.1088/2041-8205/783/1/L21.

Sironi, L., A. Spitkovsky, and J. Arons (2013). "The Maximum Energy of Accelerated Particles in Relativistic Collisionless Shocks". In: *ApJ* 771.1, 54, p. 54. DOI: 10.1088/0004-637X/771/1/54.

Snell, R. L., R. B. Loren, and R. L. Plambeck (1980). "Observations of CO in L 1551 : evidence for stellar wind driven shocks." In: *ApJ Letters* 239, pp. L17–L22. DOI: 10.1086/183283.

Sorathia, K. A. et al. (2012). "Global Simulations of Accretion Disks. I. Convergence and Comparisons with Local Models". In: *ApJ* 749.2, 189, p. 189. DOI: 10.1088/0004-637X/749/2/189.

Steenbeck, M. and F. Krause (1966). "Erklärung stellarer und planetarer Magnetfelder durch einen turbulenzbedingten Dynamomechanismus". In: *ZNTA* 21, p. 1285. DOI: 10.1515/zna-1966-0813.

— (1969a). "On the Dynamo Theory of Stellar and Planetary Magnetic Fields. I. AC Dynamos of Solar Type". In: *Astronomische Nachrichten* 291, pp. 49–84. DOI: 10.1002/asna.19692910201.

— (1969b). "On the Dynamo Theory of Stellar and Planetary Magnetic Fields. II. DC Dynamos of Planetary Type". In: *Astronomische Nachrichten* 291, pp. 271–286.

Stepanovs, D. and C. Fendt (2014). "Modeling MHD Accretion-Ejection—from the Launching Area to Propagation Scales". In: *ApJ* 793.1, 31, p. 31. DOI: 10.1088/0004-637X/793/1/31.

— (2016). "An Extensive Numerical Survey of the Correlation Between Outflow Dynamics and Accretion Disk Magnetization". In: *ApJ* 825.1, 14, p. 14. DOI: 10.3847/0004-637X/825/1/14.

Stepanovs, D., C. Fendt, and S. Sheikhnezami (2014). "Modeling MHD Accretion-Ejection: Episodic Ejections of Jets Triggered by a Mean-field Disk Dynamo". In: *ApJ* 796.1, 29, p. 29. DOI: 10.1088/0004-637X/796/1/29.

Stepinski, T. F. and E. H. Levy (1988). "Generation of Dynamo Magnetic Fields in Protoplanetary and Other Astrophysical Accretion Disks". In: *ApJ* 331, p. 416. DOI: 10.1086/166569.

— (1990). "Generation of Dynamo Magnetic Fields in Thin Keplerian Disks". In: *ApJ* 362, p. 318. DOI: 10.1086/169268.

Stirling, A. M. et al. (2001). "A relativistic jet from Cygnus X-1 in the low/hard X-ray state". In: *MNRAS* 327.4, pp. 1273–1278. DOI: 10.1046/j.1365-8711.2001.04821.x.

Stone, J. M., T. A. Gardiner, et al. (Sept. 2008). "Athena: A New Code for Astrophysical MHD". In: *ApJ Supplement* 178.1, pp. 137–177. DOI: 10.1086/588755. arXiv: 0804.0402 [astro-ph].

Stone, J. M. and M. L. Norman (1992). "ZEUS-2D: A Radiation Magnetohydrodynamics Code for Astrophysical Flows in Two Space Dimensions. II. The Magnetohydrodynamic Algorithms and Tests". In: *ApJ Supplement* 80, p. 791. DOI: 10.1086/191681.

Stone, J. M., K. Tomida, et al. (2020). "The Athena++ Adaptive Mesh Refinement Framework: Design and Magnetohydrodynamic Solvers". In: *ApJ Supplement* 249.1, 4, p. 4. DOI: 10.3847/1538-4365/ab929b.

Subramanian, K. (1998). "Can the turbulent galactic dynamo generate large-scale magnetic fields?" In: *MNRAS* 294, pp. 718–728. DOI: 10.1046/j.1365-8711.1998.01284.x.

Sur, S., A. Brandenburg, and K. Subramanian (2008). "Kinematic α-effect in isotropic turbulence simulations". In: *MNRAS* 385.1, pp. L15–L19. DOI: 10.1111/j.1745-3933.2008.00423.x.

Takano, T. et al. (1984). "High angular resolution CS (J=1-0) observations of the bipolar flow source near NGC 2071 : can the CS compact cloud collimate the flow ?" In: *ApJ Letters* 282, pp. L69–L71. DOI: 10.1086/184307.

Tchekhovskoy, A. and J. C. McKinney (2012). "Prograde and retrograde black holes: whose jet is more powerful?" In: *MNRAS* 423.1, pp. L55–L59. DOI: 10.1111/j.1745-3933.2012.01256.x.

Tchekhovskoy, A., R. Narayan, and J. C. McKinney (2011). "Efficient generation of jets from magnetically arrested accretion on a rapidly spinning black hole". In: *MNRAS* 418.1, pp. L79–L83. DOI: 10.1111/j.1745-3933.2011.01147.x.

Thorne, K0 S., R0 H. Price, and D0 A. MacDonald (1986). *Black holes: The membrane paradigm*.

Tobias, S. M. (2002). "The solar dynamo". In: *Philosophical Transactions of the Royal Society of London Series A* 360.1801, pp. 2741–2756. DOI: 10.1098/rsta.2002.1090.

Tomei, N. et al. (2020). "General relativistic magnetohydrodynamic dynamo in thick accretion discs: fully non-linear simulations". In: *MNRAS* 491.2, pp. 2346–2359. DOI: 10.1093/mnras/stz3146.

— (2021). "Are GRMHD Mean-Field Dynamo Models of Thick Accretion Disks SANE?" In: *Universe* 7.8, p. 259. DOI: 10.3390/universe7080259.

Torkelsson, U. and A. Brandenburg (1994). "Turbulent accretion disk dynamos ?" In: *A&A* 283, pp. 677–692.

Toro, E. (2009). *Riemann Solvers and Numerical Methods for Fluid Dynamics: A Practical Introduction.* DOI: 10.1007/b79761.

Toro, E. F., M. Spruce, and W. Speares (1994). "Restoration of the contact surface in the HLL-Riemann solver". In: *Shock Waves* 4, pp. 25–34. DOI: 10.1007/BF01414629.

Toro, E. F. and V. A. Titarev (2006). "MUSTA fluxes for systems of conservation laws". In: *Journal of Computational Physics* 216.2, pp. 403–429. DOI: 10.1016/j.jcp.2005.12.012.

Tzeferacos, P., A. Ferrari, et al. (2009). "On the magnetization of jet-launching discs". In: *MNRAS* 400.2, pp. 820–834. DOI: 10.1111/j.1365-2966.2009.15502.x.

— (2013). "Effects of entropy generation in jet-launching discs". In: *MNRAS* 428.4, pp. 3151–3163. DOI: 10.1093/mnras/sts266.

Tzeferacos, P., A. Rigby, A. Bott, et al. (2017). "Numerical modeling of laser-driven experiments aiming to demonstrate magnetic field amplification via turbulent dynamo". In: *Physics of Plasmas* 24.4, 041404, p. 041404. DOI: 10.1063/1.4978628.

Tzeferacos, P., A. Rigby, A. F. A. Bott, et al. (2018). "Laboratory evidence of dynamo amplification of magnetic fields in a turbulent plasma". In: *Nature Communications* 9, 591, p. 591. DOI: 10.1038/s41467-018-02953-2.

Uchida, Y. and K. Shibata (Jan. 1985). "Magnetodynamical acceleration of CO and optical bipolar flows from the region of star formation." In: *Astronomical Society of Japan* 37, pp. 515–535.

Urry, C. M0 and P0 Padovani (1995). "Unified Schemes for Radio-Loud Active Galactic Nuclei". In: *PASP* 107, p. 803. DOI: 10.1086/133630.

Vaidya, B., C. Fendt, et al. (2011). "Jet Formation from Massive Young Stars: Magnetohydrodynamics versus Radiation Pressure". In: *ApJ* 742.1, 56, p. 56. DOI: 10.1088/0004-637X/742/1/56.

Vaidya, B., A. Mignone, et al. (2018). "A Particle Module for the PLUTO Code. II. Hybrid Framework for Modeling Nonthermal Emission from Relativistic Magnetized Flows". In: *ApJ* 865.2, 144, p. 144. DOI: 10.3847/1538-4357/aadd17.

van Leer, B. (1974). "Towards the Ultimate Conservation Difference Scheme. II. Monotonicity and Conservation Combined in a Second-Order Scheme". In: *Journal of Computational Physics* 14.4, pp. 361–370. DOI: 10.1016/0021-9991(74)90019-9.

— (1977). "Towards the Ultimate Conservative Difference Scheme. III. Upstream-Centered Finite-Difference Schemes for Ideal Compressible Flow". In: *Journal of Computational Physics* 23.3, pp. 263–275. DOI: 10.1016/0021-9991(77)90094-8.

van Marle, A. J., F. Casse, and A. Marcowith (2018). "On magnetic field amplification and particle acceleration near non-relativistic astrophysical shocks: particles in MHD cells simulations". In: *MNRAS* 473.3, pp. 3394–3409. DOI: 10.1093/mnras/stx2509.

von Rekowski, B. and A. Brandenburg (2004). "Outflows and accretion in a star-disc system with stellar magnetosphere and disc dynamo". In: *A&A* 420, pp. 17–32. DOI: 10.1051/0004-6361:20034065.

von Rekowski, B., A. Brandenburg, et al. (2003). "Structured outflow from a dynamo active accretion disc". In: *A&A* 398, pp. 825–844. DOI: 10.1051/0004-6361:20021699.

Vourellis, C. and C. Fendt (2021). "Relativistic Outflows from a GRMHD Mean-field Disk Dynamo". In: *ApJ* 911.2, 85, p. 85. DOI: 10.3847/1538-4357/abe93b.

Vourellis, C., C. Fendt, et al. (2019). "GR-MHD Disk Winds and Jets from Black Holes and Resistive Accretion Disks". In: *ApJ* 882.1, 2, p. 2. DOI: 10.3847/1538-4357/ab32e2.

Walker, J. and S. Boldyrev (2017). "Magnetorotational dynamo action in the shearing box". In: *MNRAS* 470.3, pp. 2653–2658. DOI: 10.1093/mnras/stx1032.

Warnecke, J. and M. J. Käpylä (2020). "Rotational dependence of turbulent transport coefficients in global convective dynamo simulations of solar-like stars". In: *A&A* 642, A66, A66. DOI: 10.1051/0004-6361/201936922.

Watson, A. M. et al. (2007). "Multiwavelength Imaging of Young Stellar Object Disks: Toward an Understanding of Disk Structure and Dust Evolution". In: *Protostars and Planets V*. Ed. by Bo Reipurth, David Jewitt, and Klaus Keil, p. 523.

White, C. J. and F. Chrystal (2020). "The effects of resolution on black hole accretion simulations of jets". In: *MNRAS* 498.2, pp. 2428–2439. DOI: 10.1093/mnras/staa2423.

White, C. J., J. M. Stone, and C. F. Gammie (2016). "An Extension of the Athena++ Code Framework for GRMHD Based on Advanced Riemann Solvers and Staggered-mesh Constrained Transport". In: *ApJ Supplement* 225.2, 22, p. 22. DOI: 10.3847/0067-0049/225/2/22.

White, C. J., J. M. Stone, and E. Quataert (2019). "A Resolution Study of Magnetically Arrested Disks". In: *ApJ* 874.2, 168, p. 168. DOI: 10.3847/1538-4357/ab0c0c.

Woltjer, L. (1959). "Emission Nuclei in Galaxies." In: *ApJ* 130, p. 38. DOI: 10.1086/146694.

Woosley, S. E. and J. S. Bloom (2006). "The Supernova Gamma-Ray Burst Connection". In: *araa* 44.1, pp. 507–556. DOI: 10.1146/annurev.astro.43.072103.150558.

Woosley, S. E. and A. Heger (2006). "The Progenitor Stars of Gamma-Ray Bursts". In: *ApJ* 637.2, pp. 914–921. DOI: 10.1086/498500.

Yoon, D. et al. (2020). "Spectral and imaging properties of Sgr A* from high-resolution 3D GRMHD simulations with radiative cooling". In: *MNRAS* 499.3, pp. 3178–3192. DOI: 10.1093/mnras/staa3031.

Youdin, A. and A. Johansen (2007). "Protoplanetary Disk Turbulence Driven by the Streaming Instability: Linear Evolution and Numerical Methods". In: *ApJ* 662.1, pp. 613–626. DOI: 10.1086/516729.

Yuan, F. et al. (2009). "A magnetohydrodynamical model for the formation of episodic jets". In: *MNRAS* 395.4, pp. 2183–2188. DOI: 10.1111/j.1365-2966.2009.14673.x.

Zamaninasab, M. et al. (2014). "Dynamically important magnetic fields near accreting supermassive black holes". In: *Nature* 510.7503, pp. 126–128. DOI: 10.1038/nature13399.

Zanni, C., A. Ferrari, et al. (2007). "MHD simulations of jet acceleration from Keplerian accretion disks. The effects of disk resistivity". In: *A&A* 469.3, pp. 811–828. DOI: 10.1051/0004-6361:20066400.

Zanni, C. and J. Ferreira (2009). "MHD simulations of accretion onto a dipolar magnetosphere. I. Accretion curtains and the disk-locking paradigm". In: *A&A* 508.3, pp. 1117–1133. DOI: 10.1051/0004-6361/200912879.

— (2013). "MHD simulations of accretion onto a dipolar magnetosphere. II. Magnetospheric ejections and stellar spin-down". In: *A&A* 550, A99, A99. DOI: 10. 1051/0004-6361/201220168.

Zhang, S. N. et al. (1997). "Galactic black hole binaries: Multifrequency connections". In: *Proceedings of the Fourth Compton Symposium*. Ed. by Charles D. Dermer, Mark S. Strickman, and James D. Kurfess. Vol. 410. American Institute of Physics Conference Series, pp. 141–162. DOI: 10.1063/1.54121.

Acknowledgements

This is the first time I use the singular first person pronoun in this thesis. I have intentionally avoided that before because this PhD would have never been as it has been without the many amazing people I spent time with. However, I would really like to thank you all, therefore the "I".

The first person I want to thank is my advisor Christian Fendt for all the help during these years. I felt free, and at the same time like someone was guiding me in the right direction. Honestly, I could have never asked for a better advisor. I also want to thank the past and present members of the jet group, Christos Vourellis, Melis Yardimci and Ravi Pratap Dubey, for the help and the useful conversations. In this regard, a very special thank goes to Luca Ricci for our great discussions about astrophysical jets. I am also extremely grateful to my friends who have proofread parts of this thesis. More specifically, Luca Ricci, Jacob Isbell, Arshia Jacob and Antonietta Paolino for the English part and Chrostoph Engler for the German version of the abstract. I also want to thank Marco Scavino for saving me every time I need help with LaTeX since 2016.

The Max Planck Institute for Astronomy has been a great place during these years, despite a pandemic which has affected all our lives. The possibility to use their computational facilities made this PhD possible. Despite 2 of the 3 clusters I used are currently unavailable, their computational power helped me beyond imagination. Furthermore, I should thank the travel office, the housing office and the IT department for the great help received during those years.

I want to thank the members of my examination committee, Henrik Beuther, Matthias Bartelmann and especially Ralf Klessen who also agreed to act as the referee for this thesis.

The PLUTO community has been extremely kind to me, and gave me the possiblity to perform the simulations and use and adapt the PLUTO code. A very special thank is reserved to Andrea Mignone, but also to the other members I interacted with: Bhargav Vaidya, Dipanjan Mukherjee, David Melon Fuksman, Eleonora Puzzoni and Vittoria Berta. I would also thank Luca Del Zanna for the e-mail exchange during this time.

The time spent in Heidelberg was great not only from the scientific point of view, but also on the human side. I have met and interacted with so many great people that I will never be thankful enough for the great time spent together. I was very lucky to belong in a great IMPRS generation, and I want to thank in particular Jacob, Camille, Marcelo, Sam, Chris, Paz, Ismael, Greg, Caroline, Oli, Tom, Liz, Francesco and Misha. Without you the time spent in Heidleberg would have not been the same. A great thank goes to the people of student coffee, who made the lunch break so interesting and fun. Thank you Irina, Alex, Alex, Neven, Yulong, Arianna, Josha, Johanna, Felipe, Hector, Christos, Christian, Jonas, Sid, Giddi, Dhruv, Evert and Eric. Alongside my workmates there are all the people who I encountered in Germany and I had a great time with, especially during the pandemic. Thank you Dome, Nino, Rati, Bree, Matthias, Greta, Martina, Mohammed and Tony for being a part of my life.

I would like to thank my dear friends from Turin for the great time spent during the years and for keeping some of the best relationship a man could hope for. Thank

you Lorenzo, Fiammetta, Gwydyon, Crocco, Guasco, Linda, Cesare, Beppe, Patty, Salvo, Leo, Ivan, Bondi, Chiaretta, Giulia, Miro, Andre, Rossana, Korwin, Nic, Tom, Ilaria, Sara, Silvia, Davide, Marco.

I would have never even started writing a thesis without my parents and family. Thank you very much for your continuous support, for making me the person I am and for being a constant role model in my life.

Last but not least, I want to thank my amazing wife. Meeting you was the best thing ever happened in my life. I am looking forward to the days that will come and I am sure that with you they will be nothing but amazing.